

**Formulation of Porous Catalyst Supports: Formulation,
Manufacturing, Testing and Performance Modelling**

By

Andrea Celani

A thesis submitted to the School of Chemical Engineering of the

University of Birmingham for the degree of

DOCTORATE IN ENGINEERING EngD

School of Chemical Engineering

Faculty of Engineering

The University of Birmingham

B15 2TT, UK

UNIVERSITY OF
BIRMINGHAM

University of Birmingham Research Archive

e-theses repository

This unpublished thesis/dissertation is copyright of the author and/or third parties. The intellectual property rights of the author or third parties in respect of this work are as defined by The Copyright Designs and Patents Act 1988 or as modified by any successor legislation.

Any use made of information contained in this thesis/dissertation must be in accordance with that legislation and must be properly acknowledged. Further distribution or reproduction in any format is prohibited without the permission of the copyright holder.

Abstract

Catalysts have a significant role in industry and the optimization of their performances could have significant impact in terms of environmental and economic aspects. In addition to the selected active species, catalyst performances are also influenced by the structural characteristics of the catalyst support which impacts diffusion into the catalysts. For this reason, in recent years there has been an increasing interest in the use of ceramic foams as catalysts supports.

In this work, new formulations of directly foamed ceramic suspensions were developed. These presented benefits in terms of both environmental impact and pH operating window. The performances of the new amphiphiles were tested and they were then ranked in accordance with their hydrophobicity. Correlations between amphiphile hydrophobicity and foam structure were found giving an insight on how to tailor the initial formulation to obtain the desired foam structure.

Foams structure is also affected by its manufacturing process. An aerated stirred vessel was used to generate the foam and a Design of Experiment was carried out to determine the process parameters that effects foam structure. Foam structure (e.g. porosity and bubble size) was correlated to global mixing parameters and mixing regimes to understand the mixing conditions necessary to obtain the desired foam. In addition, foams rheological properties were correlated to its bubble size and bubble size distribution; this correlation could result in the use of rheological measurements as an at-line technique to control the foam structure.

The performances of foam supported catalysts were tested in different reactions such as Fischer Tropsch and methane oxidation. In both cases foam supported catalyst gave better performances in

respect to conventional ones. The improved performances were attributed to the lower diffusion resistance inside the catalyst particles.

To screen the performances of catalysts having different structures, a computational approach was used to simulate the methane oxidation reaction when foams with different porosities were used as supports. An in-house developed kinetic model was validated against experimental results acquired by SpaciMS technique. In addition, two different approaches (1D + 1D and CFD) were used to simulate the reaction in a monolithic reactor resulting in comparable profiles.

A 1D + 1D model was used to simulate the methane light-off curve and it was compared with the experimental results. The comparison showed that, upon selection of the right characterization technique to reconstruct the foam structure, it was possible to satisfactorily reproduce the experimental light-off curve. The developed model allows a faster screening of the performances of catalysts supported on ceramic foams having different structures resulting in a more economical and faster catalysts development.

Acknowledgment

I would like to acknowledge Liz Holt for her constant support and guidance in the first two years of my EngD. Our scientific discussions have always been interesting and challenging and have been fundamental for the success of this project. A big thanks to Prof. Hugh Stitt that has taken care of me in the last two years and has contribute to increase my knowledge in chemical engineering. Thanks to Dr Li Liu for her help with CFD simulations and a special thanks to Dr. Sam Wilkinson for introducing me to code writing and parameter estimation; the last chapter of this thesis would have not been completed without his help. Thanks to Prof. Stuart Blackburn and Prof. Mark Simmons for your comments, suggestions and for reviewing all my written work. Thanks to Dr. Richard Greenwood for the great effort that he puts in the EngD programs and for all the social events and drinks that we shared.

Thanks to the always growing Italian community at Johnson Matthey, you have brought a piece of our homeland in my everyday job. Thanks to Michele for your help in settling down, Alessandro, Mimmo and the two Giuseppi for the coffee breaks, the Saturday nights and for letting me feel part of a family. Thanks to Tom for you lifts during the first months of EngD, for the loughs in the office and for sharing this journey with me. Thanks to all the colleagues in JM for all the discussion (scientific and not) and a special thanks to JM analytical team that I bother a lot in the last month of my EngD.

Last but not least, thanks to my wife that has constantly supported me in this journey. Thanks for being always by my side despite the challenges that it brings. This big achievement would have

not been possible without you by my side as for any other remarkable thing that I have done in my life.

Index

List of Figures.....	12
List of Tables.....	18
List of Symbols.....	20
Chapter 1	27
Introduction	27
1.1 Introduction to catalysis	27
1.1.1 Effects of diffusion phenomena in heterogeneous catalysts performances.....	28
1.1.2 Effects of crystal size and crystal defect on heterogeneous catalysts performances	30
1.1.3 Effects of promoters on heterogeneous catalyst performances.....	32
1.1.4 Steps for the development of catalyst at industrial scale	34
1.2 Company Background.....	36
1.3 Business Case	39
1.4 Scope of the Investigation	40
1.5 Thesis Structure	41
Chapter 2	45
Formulation of Ceramic Foams.....	45
2.1 Introduction	45
2.2 Liquid Foams and Instability Processes	46
2.3 Surfactants Stabilized Foams	48
2.4 Particles Stabilized Foams.....	50
2.5 Materials and Methods	53
2.5.1 Materials.....	53
2.5.2 Suspension Preparation	54
2.5.3 Foaming and Foam Characterisation.....	54
2.5.4 Solid State-NMR	55
2.5.5 Surface Tension Measurements	56
2.5.6 Suspension Filtration and Supernatant UV-Vis Analysis	57
2.6 Amino Acids as Amphiphiles in Particles Stabilized Foams	57
2.6.1 Amino Acids Screening	58

2.6.2 Amino Acids-Particles Interaction: SS-NMR	62
2.6.3 Investigation of the Particles Adsorption at the Different Interfaces	65
2.6.4 Determination of Amino Acids Hydrophobicity	69
2.6.5 Influence of Amino Acids Hydrophobicity on Foam Properties	72
2.6.6 Determination of the Minimum Amphiphile Concentration	77
2.7 Conclusion	80
Chapter 3	82
Manufacturability of Ceramic Foams	82
3.1 Introduction	82
3.2 Stirred Vessel	82
3.2.1 Configuration of a Stirred Vessel	82
3.2.2 Flow Patterns in Stirred Vessel	84
3.2.3 Power Input in Stirred Vessels	85
3.3 Aerated Stirred Vessel	87
3.3.1 Configuration of an Aerated Stirred Vessel	87
3.3.2 Power Consumption in Aerated Stirred Vessel	89
3.3.3 Gas Hold-Up Correlations	92
3.3.4 Bubble Size in Aerated Stirred Vessels	94
3.4 Rheology	96
3.4.1 Introduction	96
3.4.2 Rheology Models	96
3.4.3 Rheometer	101
3.5 Materials and Methods	103
3.5.1 Materials	103
3.5.2 Suspension Preparation	104
3.5.3 Foaming and Foam Characterization	104
3.5.4 Design of Experiment (DoE)	106
3.6 Determination of the significant factors affecting foam properties	106
3.7 Correlation between Foam Density and Foam Porosity	110
3.8 Gas Hold-Up Correlations Applied to the Produced Foams	112
3.9 Bubble Size Correlations Applied to the Produced Foams	118

3.10 Rheological Characterization of the Produced Foams	122
3.11 Conclusion	131
Chapter 4	133
Testing of ceramic foam supported catalysts in Fischer-Tropsch Synthesis.....	133
4.1 Introduction	133
4.2 Fischer-Tropsch reaction and reactor technologies	134
4.3 Fischer-Tropsch proposed reaction mechanism	139
4.4 Effects of catalyst formulation on FTS	144
4.4.1 Effects of crystal size and crystallite distribution on FTS reaction.....	145
4.4.2 Effect of support material and pore structure on FTS reaction	146
4.4.3 Effects of acidity and surface modification of FTS	147
4.4.4 Effects of mass transport on FTS	147
4.5 Catalyst Characterization Techniques	149
4.5.1 X-Ray Diffraction (XRD)	149
4.5.2 N ₂ Physisorption.....	152
4.5.3 Chemisorption	155
4.5.3.1 Isothermal chemisorption	156
4.5.3.2 Temperature Programmed Desorption (TPD)	158
4.5.4 Mercury Intrusion Porosimetry (MIP)	161
4.5.5 Scanning Electron Microscope.....	163
4.6 Materials and Methods	166
4.6.1 Materials.....	166
4.6.2 Slurry preparation and foaming.....	166
4.6.3 Catalyst precursor preparation	167
4.6.4 Catalyst test	168
4.6.5 Catalyst Characterization	169
4.7 Catalytic Testing of Foam Supported Catalysts for FTS Applications	172
4.8 Conclusions	183
Chapter 5	185
1D + 1D Simulation of CH ₄ Oxidation in a Monolith Channel: Intrinsic Kinetic Model Validation against SpaciMS Experimental Results.....	185

5.1 Introduction	185
5.2 Proposed kinetic equations for catalysed CH ₄ oxidation	186
5.3 Diffusion in porous solids.....	191
5.4 SpaciMS Technique.....	195
5.5 Reactor Model	197
5.6 1D + 1D Modelling of CH ₄ Oxidation: Comparison of Model and Experimental Results...	200
5.7 Conclusions	209
Chapter 6	211
Validation of a new OpenFOAM CFD reactor model using SpaciMS experimental data and 1D + 1D simulations.....	211
6.1 Introduction	211
6.2 Computational Fluid Dynamic (CFD).....	213
6.3 CFD Model Validation	218
6.4 Conclusions	223
Chapter 7	225
Effects of Foam Structure on the CH ₄ Oxidation Reaction: Experimental and Computational Determination of CH ₄ Light-Off Curve.....	225
7.1 Introduction	225
7.2 Packed Bed Reactor Model	226
7.3 Computational determination of D _{eff} coefficient in porous solids: Pore Resolved Method..	229
7.4 Materials and Method.....	232
7.4.1 Materials.....	232
7.4.2 Foam and Alumina Pelletting.....	233
7.4.3 Catalyst Support Impregnation and Characterization	233
7.4.4 Catalyst Testing: CH ₄ Light-Off curve	234
7.5 Catalysts characterization results.....	236
7.6 Catalytic test of Pd/Al ₂ O ₃ catalysts for CH ₄ oxidation	241
7.7 Light-Off Curve Modelling	243
7.8 Conclusions	249
Chapter 8	251
Conclusions and Future Work.....	251
8.1 Conclusions	251

8.2 Future Work.....	255
References	258
Appendix I.....	282
Comparison between foam porosity values obtained by water pick-up and Mercury Intrusion Porosimetry.....	282
Appendix II.....	284
Confidence Interval of Mean Bubble Size Determined by Image Analysis.....	284
Appendix III	287
Publications and Presentations	287

List of Figures

Chapter 1

Figure 1. 1: Steps involved in a typical heterogeneous catalytic process [7].....	28
Figure 1. 2: Diagram of the surface described by the TSK model [23]	31
Figure 1. 3: Typical sequence of interactive tasks followed in a catalyst development [41]	34
Figure 1. 4: Johnson Matthey new pellet shape protected by patent WO2010029324 [42]	35

Chapter 2

Figure 2. 1: (a) anionic surfactant (sodium p-dodecylbenzenesulfonate) (b) cationic surfactant (hexadecyltrimethylammonium chloride) (c) non-ionic surfactant (Triton X-100).....	48
Figure 2. 2: Illustration of continuous-dispersed phase dependence on particles contact angle [46]	51
Figure 2. 3: Energy of attachment of colloidal particles at an air-water interface as a function of the contact angle for different particles radius [46].....	52
Figure 2. 4: 21 protenogenic α -amino acids classified depending on the properties of their side chains.	59
Figure 2. 5: DL-leucine solubility (■) and COOH dissociation (—)/NH ₂ protonation (—) as a function of pH (Solubility Data from [86])	61
Figure 2. 6: Foam porosity as a function of amphiphile concentration for foams obtained using different amino acid and amino acid concentrations. (♦) Phenylalanine, (■) Tryptophan, (▲) Leucine, (*) Valine, (●) Methionine, (—) Isoleucine. The black triangle in the leucine curve indicates the solubility limit point. DL-alanine and DL-tyrosine are not present in the graph since they did not give stable foams.	62
Figure 2. 7: SS-NMR spectra for phenylalanine modified TiO ₂ samples prepared at pH = 1 (—), pH = 4 (—) and pH = 10 (—).....	64
Figure 2. 8: Langmuir's isotherm for phenylalanine at the solid-liquid interface. Blue points represent experimental data while solid line represents the Langmuir's isotherm.....	67
Figure 2. 9: Experimental (symbols) equilibrium values of the interfacial tension as a function of the amphiphile bulk concentration. Solid line represents the fitted Langmuir-Szyszkowski equation.	68
Figure 2. 10: Comparison of the DL-Phenylalanine isotherms at the Gas-Liquid (—) and Solid-Liquid (—) interfaces	69
Figure 2. 11: Shape of an amino acid solution drop analysed by the shape analyser software.....	70
Figure 2. 12: Surface tension curves for amino acids solutions having different concentrations. (♦) Phenylalanine, (■) Tryptophan, (▲) Leucine, (●) Alanine, (*) Valine, (●) Methionine, (+) Tyrosine, (—) Isoleucine. The black point in the Leucine curve indicates that the solubility limit for the amino acid was reached.	71
Figure 2. 13: Maximum foam porosity as a function of the amino acid hydrophobicity index	74
Figure 2. 14: Bubbles size distribution comparison of foam produced using different phenylalanine concentrations. 0.18 M (—), 0.24 M (—)	75

Figure 2. 15: Sauter diameter as a function of the amino acids hydrophobicity index	77
Figure 2. 16: Surface tension measurement of 25% _{w/w} titania suspension having different phenylalanine concentrations	79

Chapter 3

Figure 3. 1: Characteristic dimensions of a cylindrical stirred vessel	83
Figure 3.2: Typical flow patterns generated by an axial (a) and a radial impeller (b) [112].....	84
Figure 3. 3: Typical Power Curve [123]	86
Figure 3. 4: Aerated Stirred Vessel	88
Figure 3. 5: Power curves for gassed agitators (D.T. = Disc Turbine, V.D. = Vaned Disc, P.B.T. = Pitch Blade Turbine) [112]	89
Figure 3. 6: Regimes of bubble flow: (a) and (b) flooded impeller, (c) loaded impeller, (d) complete gas dispersion, (e) gross recirculation of gas [136]	90
Figure 3. 7: Power curves at constant gas rate for Rushton turbines [136]	91
Figure 3. 8: Disk turbine regime map [137]	92
Figure 3. 9: Summary of fluids flow behaviour [107]	97
Figure 3. 10: Model to describe: (a) elastic fluids, (b) viscous fluids, (c) Kelvin-Voigt model for visco-elastic fluids [158]	100
Figure 3. 11: Different geometries used as sensor systems in rheometers: (a) Concentric cylinder (b) cone and plate (c) parallel plate [159]	101
Figure 3. 12: Scoping graphs for the 40 and 100 μm disks: (a) density graph for 40 μm plate, (b) porosity graph for 40 μm plate, (c) density graph for 100 μm plate, (d) porosity graph for 100 μm plate	107
Figure 3. 13: Foam Stability Assessment: (a) Freshly made high porosity foam (b) High porosity foam after 2 weeks (c) Freshly made low porosity foam (d) Low porosity foam after 2 weeks.	108
Figure 3. 14: Porosity of the dry foam as a function of the density of the wet foam	111
Figure 3. 15: Foam porosity as a function of the total volume of entrained gas	112
Figure 3. 16: Foam porosity as a function of the adimensional group (ReFrF_{lg}) for foams produced using different sparging times: $T=1'$ (●) and $T=20'$ (▲)	114
Figure 3. 17: Foam porosity as a function of mean energy dissipation for foams produces using different air entrainment times. $T=1'$ (●) and $T=20'$ (▲)	115
Figure 3. 18: Flow regimes at different impeller speed, impeller diameter and gas flow rate. (a) $D=4\text{ cm}$, $G=2\text{ L min}^{-1}$, $N=200\text{ rpm}$ (b) $D=4\text{ cm}$, $G=2\text{ L min}^{-1}$, $N=1000\text{ rpm}$ (c) $D=4\text{ cm}$, $G=20\text{ L min}^{-1}$, $N=200\text{ rpm}$ (d) $D=4\text{ cm}$, $G=20\text{ L min}^{-1}$, $N=1000\text{ rpm}$ (e) $D=9\text{ cm}$, $G=2\text{ L min}^{-1}$, $N=200\text{ rpm}$ (f) $D=9\text{ cm}$, $G=2\text{ L min}^{-1}$, $N=1000\text{ rpm}$ (g) $D=9\text{ cm}$, $G=20\text{ L min}^{-1}$, $N=200\text{ rpm}$ (h) $D=9\text{ cm}$, $G=20\text{ L min}^{-1}$, $N=1000\text{ rpm}$	116
Figure 3. 19: Flow regime map for the experimental system. (▲) Flooded, (■) Loaded, (●) Fully recirculated.	117
Figure 3. 20: Foam porosity as a function of the flow regime conditions for (a) 1 min air entrainment time (b) 20 min air entrainment time. The different flow regimes are represented as flooded (▲), loaded (■) and fully recirculated (●)	118

Figure 3. 21: Example of cross-sectional image for one of the produced foam: (a) optical microscope image, (b) thresholded image.....	119
Figure 3. 22: Bubble size distribution for the obtained foams	120
Figure 3. 23: d_{32}/D as a function of mean energy dissipation for (a) We (b) P_g/V . The different sparger pore size and impeller diameter are indicated as: 40, $D = 4$ cm (●); 40, $D = 9$ cm (◆); 100, $D = 4$ cm (▲); 100, $D = 9$ cm (■)	121
Figure 3. 24: d_{32}/D depending on the different flow regimes conditions for (a) 40 μ m sparging disk (b) 100 μ m sparging disk. The different flow regimes are represented as flooded (▲), loaded (■) and fully recirculated (●).....	122
Figure 3. 25: (a) Comparison of the upward rheology curve for the produced foams (b) Details of the upward (●) and downward (■) rheology curve for one of the produced foams	124
Figure 3. 26: Foam upward rheology curve: geometry comparison: (◆) Flat parallel plate, (■) Hatched parallel plate, (●) Rotor-vane geometry).....	125
Figure 3. 27: (a) first series of overlapping rheology curves (b) bubble size distribution of the foams overlapping in the first series (c) second series of overlapping rheology curves (d) bubble size distribution of the foams overlapping in the second series (e) third series of overlapping rheology curve (f) bubble size distribution of the foams overlapping in the third series.....	127
Figure 3. 28: Slip shear stress as a function of bubble size and distribution span	129
Figure 3. 29: Amplitude sweep curve for one of the produced foams: (●) G' , (■) G''	130

Chapter 4

Figure 4. 1: Andreson-Shulz-Flory Distribution [184].....	136
Figure 4. 2: Possible reactors for the FTS: (a) slurry bubble column reactor; (b) multi-tubular trickle bed reactor; (c) circulating; (d) fluidized-bed reactor [G: gas, L: liquid] [188].....	137
Figure 4. 3: Surface carbide mechanism. The rate determining steps (R.D.S.) are indicated in the scheme [196].....	140
Figure 4. 4: Surface enol mechanism. The rate determining steps (R.D.S.) are indicated in the scheme [196].....	141
Figure 4. 5: CO insertion mechanism. The rate determining steps (R.D.S.) are indicated in the scheme [196].....	142
Figure 4. 6: Alkenyl chain growth mechanism [200].....	143
Figure 4. 7: Thermal transformation sequence of the aluminium hydroxides [214].....	146
Figure 4. 8: X-Ray diffractometer schematic [228]	151
Figure 4. 9: Stages involved in the physisorption process [230].....	152
Figure 4. 10: Different types of adsorption isotherms [231]	153
Figure 4. 11: Chemisorption isotherms for different values of the constant b [235].	157
Figure 4. 12: Schematic representation of the Temperature Programmed Desorption instrument [237].	159
Figure 4. 13: Example of a TPD curve [237]	160
Figure 4. 14: Schematic of a Mercury Intrusion Penetrometer [241].....	162
Figure 4. 15: Mercury Intrusion Porosimetry intrusion/extrusion curve [239]	162

Figure 4. 16: Schematic representation of a SEM (BSE = backscattered electrons, SE = secondary electrons, X = X-Rays, CRT = cathode-ray tube) [243].....	164
Figure 4. 17: Schematic of the test rig used for the catalyst testing	168
Figure 4. 18: Supports used in FTS test: (a) conventional titania spheres (b) titania foam	172
Figure 4. 19: N ₂ Physisorption (a) and mercury intrusion porosimetry (b) curves for the spheres (—) and foam (*) supported catalysts respectively	174
Figure 4. 20: SEM images of the samples cross sectional area: (a) foam support, (b) sphere support, (c) detail of the sphere cross section.....	175
Figure 4. 21: NH ₃ -TPD of conventional (—) and foam (—) catalyst supports.....	176
Figure 4. 22: Linear relationship between CH ₄ selectivity and C ₅₊ selectivity	179
Figure 4. 23: C ₅₊ Selectivity as a function of different catalyst properties: (a) Co crystal size (b) Co metal area (c) Foam porosity (d) Metal dispersion (e) N ₂ Physisorption pore diameter (f) BET surface area (g) N ₂ Physisorption pore volume (h) MIP Intrusion volume (i) MIP Median pore diameter. (●) Phe-Titania Foam (●) Val-Titania Foam (●) Leu-Titania Foam.....	181
Figure 4. 24: C ₅₊ selectivity as a function of the proposed parameter ϕ	182

Chapter 5

Figure 5. 1: SpaciMS schematic	196
Figure 5. 2: Schematic of a washcoated monolith; grey area represents the catalytic washcoat. Detail of the monolith shows the boundary conditions for the washcoat layer.....	198
Figure 5. 3: Comparison among model results obtained using both the Bosanquet (Mod-Bos) and the Wakao Smith (Mod-WS) correlation and the experimental results for the CH ₄ oxidation reaction conducted at 450 °C and in dry feed. The different species are represented by: (—) CH ₄ Exp, (—●) CH ₄ Mod-WS, (●) CH ₄ Mod-Bos; (—) CO ₂ Exp, (—●) CO ₂ Mod-WS, (●) CO ₂ Mod-Bos; (—) Temp Exp, (—●) Temp Mod-WS, (●) Temp Mod-Bos.....	202
Figure 5. 4: Comparison between model and experimental results for methane oxidation conducted at different operative conditions (a) dry feed, 400 °C (b) wet feed, 400 °C (c) dry feed, 425 °C (d) wet feed, 425 °C (e) dry feed, 450 °C (f) wet feed, 450 °C. The different species are represented by: (—) CH ₄ Exp., (—●) CH ₄ Mod., (—) CO ₂ Exp., (—●) CO ₂ Mod., (—) Temp. Exp., (—●) Temp. Mod.....	203
Figure 5. 5: Comparison between model and experimental results for the CH ₄ oxidation carried out at 400 °C and in wet feed in the case in which the water's enthalpy of adsorption is reduced by 5%. The different species are represented by: (—) CH ₄ Exp., (—●) CH ₄ Mod., (—) CO ₂ Exp., (—●) CO ₂ Mod., (—) Temp. Exp., (—●) Temp. Mod.	205
Figure 5. 6: Chemical species concentration profiles and temperature profile inside the washcoat (model at reactor length of 5 mm) for methane oxidation conducted at different operative conditions (a) dry feed, 400 °C (b) wet feed, 400 °C (c) dry feed, 425 °C (d) wet feed, 425 °C (e) dry feed, 450 °C (f) wet feed, 450 °C. The different species are represented by: (—●) CH ₄ , (—●) CO ₂ , (—●) Temp. Mod.	207
Figure 5. 7: 2D CH ₄ concentration profile within the washcoat and along the reactor channel for methane oxidation conducted at different operating conditions (a) dry feed, 400 °C (b) wet feed,	

400 °C (c) dry feed, 425 °C (d) wet feed, 425 °C (e) dry feed, 450 °C (f) wet feed, 450 °C. The different colours of the surface plot indicates areas at different CH₄ concentration: ■ 0-0.1 % vol., ■ 0.1-0.2 % vol., ■ 0.2-0.3 % vol., ■ 0.3-0.4 % vol.,..... 208

Chapter 6

Figure 6. 1: Sequence followed to generate the mesh	219
Figure 6. 2: CH ₄ trend comparison when different mesh sizes where used to model CH ₄ oxidation: (—) 1 Cell, (—) 2 Cells, (●) 6 Cells.	220
Figure 6. 3: CH ₄ concentration profile along the monolith channel for CH ₄ oxidation carried out at different operative conditions: (a) 400 °C and dry feed, (b) 400 °C and wet feed, (c) 425 °C and dry feed, (d) 425 °C and wet feed, (e) 450 °C and dry feed, (f) 450 °C and wet feed	221
Figure 6. 4: Comparison among CH ₄ concentration profile along the monolith channel for CH ₄ oxidation carried out at different operative conditions: (a) 400 °C and dry feed, (b) 400 °C and wet feed, (c) 425 °C and dry feed, (d) 425 °C and wet feed, (e) 450 °C and dry feed, (f) 450 °C and wet feed. The different species are represented by: (—) CH ₄ Exp., (—●) CH ₄ 1D + 1D, (●) CH ₄ OpenFOAM, (—) CO ₂ Exp., (—●) CO ₂ 1D + 1D, (●) CO ₂ OpenFOAM, (—) Temp. Exp., (—●) Temp. 1D + 1D, (●) Temp. OpenFOAM	222

Chapter 7

Figure 7. 1: Schematic of a packed bed reactor with detailed representation of the pellet boundaries.....	227
Figure 7. 2: Example of the method used for the generation of the porous structure using the ICT Prague DEM code [321]	230
Figure 7. 3: Example of diffusion simulation output	232
Figure 7. 4: Schematic of the test rig used for the determination of the CH ₄ light-off curve	235
Figure 7. 5: Catalyst supports before grounding: 1-75% Al ₂ O ₃ foam, 2-95% Al ₂ O ₃ foam, 3-Al ₂ O ₃ pellet, 4-Al ₂ O ₃ foam pellet	236
Figure 7. 6: (a) N ₂ -Isotherm of adsorption, (b) pore size distribution for the different samples: (—) Foam 77%, (—) Foam 95%, (—) Foam Pellet, (—) Alumina Pellet.	237
Figure 7. 7: (a) Mercury intrusion/extrusion curve, (b) Pore size distribution for the different samples: (—) Foam 77%, (—) Foam 95%, (—) Foam Pellet, (—) Alumina Pellet	237
Figure 7. 8: SEM images of the cross section of the four samples.....	239
Figure 7. 9: XRD images of the foam samples: (a) 2D image of the 95% foam, (b) 3D reconstructed image of a 95% foam Region of Interest (ROI), (c) 2D image of the 85% foam, (d) 3D reconstructed image of an 85% foam ROI	240
Figure 7. 10: Light-off curve for (a) foam supported and (b) pellet supported catalyst for both dry and wet feed: (—) 95% Foam-Dry, (—) 77% Foam-Dry, (●) 95% Foam-Wet, (●) 77% Foam-Wet, (—) 95% Al ₂ O ₃ pellet-Dry, (—) Foam pellet-Dry, (●) 95% Al ₂ O ₃ pellet-Wet, (●) Foam pellet-Wet	242

Figure 7. 11: Foam supported and pelleted supported samples, light off curves comparison: (—) 95% Foam-Dry, (—) 77% Foam-Dry, (●) 95% Foam-Wet, (●) 77% Foam-Wet, (—) 95% Al ₂ O ₃ pellet-Dry, (—) Foam pellet-Dry, (●) 95% Al ₂ O ₃ pellet-Wet, (●) Foam pellet-Wet.....	243
Figure 7. 12: Comparison among experimental and model results. (a) 95% foam: (—) Exp., (—●) Mod. Wakao-Smith, (●) Mod. PMS. (b) 77% foam: (—) Exp., (—●) Mod. Wakao-Smith, (●) Mod. PMS.....	244
Figure 7. 13: Thermocouple position inside the micro-reactor	245
Figure 7. 14: Comparison among model light-off curve and both experimental curves with corrected and uncorrected bed temperature: (—) Exp., (—●) Mod., (●) Exp.-Corrected temperature.	246
Figure 7. 15: Comparison among model light off curves obtained using different macro-meso pores thresholds and both the corrected and uncorrected experimental ones: (—) Exp., (●) Exp.-Corrected temperature, (—●) Mod.-TS50, (■) Mod.-TS30, (▲) Mod.-TS25	248

Chapter 8

No figures

List of Tables

Chapter 1

No tables

Chapter 2

Table 2. 1: List of hydrophobic amino acids and corresponding pK_1 and pK_2 values [81]	60
Table 2. 2: Values of maximum surface concentration Γ_{\max} and parameter a for the different interfaces.....	68
Table 2. 3: Comparison between the amino acids hydrophobicity scale determined in this work and that proposed by Bull et al.	72
Table 2. 4: Hydrophobicity Index and maximum foam porosity obtained for each amino acid...	73
Table 2. 5: Hydrophobicity Index and Sauter diameter obtained for each amino acid	76
Table 2. 6: Comparison of amino acids solubility and cost.....	78
Table 2. 7: t_{Crit} and t_{Stat} values for surface tension pairs.....	80

Chapter 3

Table 3. 1: Half factorial design runs with factors levels and response values	108
Table 3. 2: Process parameters affecting foam properties.....	110
Table 3. 3: Summary of the foams properties divided by overlapping series	128

Chapter 4

Table 4. 1: Comparison of the performances of conventionally supported and foam supported catalysts in FTS	172
Table 4. 2: Summary of the characterization undertaken on the two samples	173
Table 4. 3: Comparison of the performances of conventionally supported and foam supported catalysts in FTS	177
Table 4. 4: Summary of the characterization undertaken on the two samples	178

Chapter 5

Table 5. 1: Summary of the commonly used kinetic expression for CH_4 oxidation [246]	187
Table 5. 2: Kinetic parameters estimated by Hurtado et al. for a Mars van Krevlen CH_4 oxidation mechanism with A_r and A_{O_2} in $\text{mol bar}^{-1} \text{min}^{-1} \text{g}^{-1}$, A_3 in $\text{mol min}^{-1} \text{g}^{-1}$, $A_{\text{H}_2\text{O}}$ in bar^{-1} and E_{a_r} , $E_{a_{\text{O}_2}}$, E_{a_3} and $\Delta H_{\text{H}_2\text{O}}$ in kJ mol^{-1}	189
Table 5. 3: Kinetic parameters estimated in-house for the kinetic model 4	190
Table 5. 4: Operating conditions of the different CH_4 oxidation reactions simulated and experimentally investigated.....	201
Table 5. 5: Summary of model parameters	201

Chapter 6

No tables

Chapter 7

Table 7. 1: Example test protocol used for testing 3% Pd/Al ₂ O ₃ catalysts	236
Table 7. 2: Summary of the N ₂ -physisorption and Mercury Intrusion Porosimetry results	238
Table 7. 3: Summary of the CO-Chemisorption and XRD analysis for the four samples	241
Table 7. 4: Foam samples characteristics	244
Table 7. 5: Comparison among the different macro and meso porosities values obtained when different macro/meso pore thresholds were selected.....	248

Chapter 8

No tables

List of Symbols

Symbol	Description	SI Units
A_i	Pre-exponential factor adsorption species i	$\text{m}^3 \text{mol}^{-1}$
A_m	Active metal surface area	m^2
A_r	Pre-exponential factor	s^{-1} (1 st order reactions)
A_t	Total surface area	m^2
a	Activity	-
a_{CS}	Cross sectional area of the probe molecule	m^2
a_L	Langmuir constant	mol m^{-3}
a_{MR}	Mean radii of the pores	m
a_s	Mass of solid sample	Kg
a_v	Washcoat specific area	m^2
C_p	Gas specific heat	$\text{J mol}^{-1} \text{K}^{-1}$
$C_{p,s}$	Solid specific heat	$\text{J mol}^{-1} \text{K}^{-1}$
c	Concentration	mol m^{-3}
c_{BET}	BET constant	-
D	Impeller diameter	m
D_{AB}	Binary diffusion coefficient	$\text{m}^2 \text{s}^{-1}$
D_c	Diffusion coefficient	$\text{m}^2 \text{s}^{-1}$
D_F	Fickian diffusion	$\text{mol m}^{-2} \text{s}^{-1}$
D_K	Knudsen diffusion coefficient	$\text{m}^2 \text{s}^{-1}$
D_M	Metal dispersion	-
D_{eff}	Effective diffusivity	$\text{m}^2 \text{s}^{-1}$
D_{ij}	Stefan-Maxwell diffusion coefficient	$\text{m}^2 \text{s}^{-1}$
D_p	Channel radial length	m
$D_{v0.1}$	Value at which below which 10% of the	-
$D_{v0.5}$	Value at which below which 50% of the distribution is present	-

$D_{v0.9}$	Value at which below which 90% of the distribution is present	-
D_w	Sum of wall thickness and channel radial length distribution is present	m
d	Diameter	m
d_p	Space between diffracting planes	m
d_{32}	Mean Sauter diameter	m
E	Energy to remove particles from the interface	kT
E_L	Heat of adsorption for second layer and higher	J mol ⁻¹
E_{ar}	Reaction activation energy	J mol ⁻¹ K ⁻¹
E_1	Heat of adsorption for the first layer	J mol ⁻¹
F_i	External body force	Kg m s ⁻²
F_{lg}	Gas flow number	-
Fr	Froude number	-
G	Elastic modulus	Pa
G_{MV}	Mass superficial velocity	m s ⁻¹
$G_{z,m}$	Mass transport Graetz number	-
$G_{z,t}$	Heat transfer Graetz number	-
G^*	Complex modulus	Pa
G'	Storage modulus	Pa
G''	Loss modulus	Pa
g	Gravitational acceleration	m s ⁻²
Hi	Strength of the hydrophilic group	-
h	Sensible enthalpy	J mol ⁻¹
h_t	Thermal convection coefficient	W m ⁻² K ⁻¹
I_{tot}	Total intrusion	m ³ Kg ⁻¹
J	Diffusion flux	mol m ⁻² s ⁻¹
\vec{J}_i	Diffusion flux of species i	mol m ⁻² s ⁻¹

j_m	Mass j factor	-
j_h	Heat j-factor	-
K	Shape factor	-
K_i	Adsorption constant for species i	$\text{m}^3 \text{mol}^{-1}$
K_P	Constant depending on system geometry	-
k	Consistency index	-
k_B	Boltzmann constant	$\text{m}^2 \text{Kg s}^{-2} \text{K}^{-1}$
k_{eff}	Effective thermal conductivity	$\text{W m}^{-1} \text{K}^{-1}$
k_g	Thermal conductivity of the gas	$\text{W m}^{-1} \text{K}^{-1}$
k_m	Film mass transfer coefficient	m s^{-1}
k_r	Rate constant	s^{-1} (1 st order reactions)
k_s	Mixer share rate constant	-
M	Metal loading	-
MW_h	Molecular weight of hydrophilic portion of the molecule	mol g^{-1}
MW_i	Molecular weight of species i	mol g^{-1}
M_d	Torque	N m
M_{GF}	Geometry factor	-
M_k	Sample raw moment	-
M_{surf}	Moles of metal on surface	mol m^2
M_{tot}	Moles of total metal	mol
n_{LG}	Number of lipophilic groups	-
N	Impeller speed	s^{-1}
Nu	Nusselt number	-
N_A	Avogadro's number	-
N_{CD}	Complete dispersion impeller speed	s^{-1}
N_F	Flooding impeller speed	s^{-1}
N_R	Recirculation impeller speed	s^{-1}
N_s	Active sites	-

n_{FB}	Flow behaviour index	-
n_{ads}	Adsorbed molecules	-
n_c	Carbon atoms	-
n_i	Stoichiometric coefficient	-
n_r	Stoichiometry of the adsorption reaction	-
n_0	Number density	-
P	Power	W
Pr	Prandtl number	-
P_s	Static pressure	Pa
P_g	Power of a gassed system	W
P_0	Power number	-
p	Equilibrium pressure	Pa
P_{PM}	Pressure of the probe molecule	Pa
p_0	Saturation pressure	Pa
Q_g	Gas flow rate	$m^3 s^{-1}$
R	Gas constant	$J mol^{-1} K^{-1}$
Re	Reynolds number	-
R_D	Maximum drop radius	m
R_0	Radius of the catalyst particles	m
r	Radius	m
r_k	Kelvin radius of a cylindrical pore	m
r_p	Mean pore radius	m
r_{pr}	Rate of propagation	$mol s^{-1}$
r_r	Rate of reaction	$mol m^{-3} s^{-1}$
r_t	Rate of termination	$mol s^{-1}$
S	Reactor surface area to volume ratio	m^{-1}
Sc	Schmidt number	-

Sh	Sherwood number	m
S_{BET}	Specific surface area	m^2
S_t	Total surface area	m^2
S^2	Variance	-
s	Adsorption cross section	m^2
T	Temperature	K
T_g	Temperature of gas	K
T_s	Temperature of solid	K
t	Time	s
u_i	Fluid velocity	$m\ s^{-1}$
u_z	Gas superficial velocity	$m\ s^{-1}$
V_{H_2O}	Volume of water picked-up	m^3
V_L	Liquid volume	m^3
V_{ads}	Volume of adsorbed probe molecule	m^3
V_{bed}	Bed volume	m^3
V_g	Molar volume of gas at standard conditions	m^3
V_m	Molar volume	m^3
V_{por}	Pore volume	$m^3\ Kg^{-1}$
v	Adsorbed gas quantity	m^{-1}
v_i	Special diffusion parameters	-
v_m	Monolayer adsorbed gas quantity	m^{-1}
v_l	Molar volume of the liquid	m^3
v_s	Superficial gas velocity	$m\ s^{-1}$
We	Weber number	-
W_n	Weight percent	-
W_s	Sample weight	Kg
W_0	Sample initial weight	Kg
x	Length	m

x_i	Considered coordinate	-
z	Reactor length	m
α	Chain growth probability	-
β	Line broadening at half maximum intensity	-
β_s	Shape factor	-
Γ	Concentration of molecule adsorbed at the interface	$\mu\text{mol m}^{-2}$
Γ_{max}	Maximum concentration of adsorbed specie	$\mu\text{mol m}^{-2}$
γ	Surface tension	N m^{-1}
γ_k	kinematic viscosity	$\text{m}^2 \text{s}^{-1}$
γ_0	Interfacial tension of amphiphile free interface	N m^{-1}
$\dot{\gamma}_A$	Average shear rate	s^{-1}
$\dot{\gamma}_{max}$	Max shear rate	s^{-1}
ΔH_i	Enthalpy of adsorption species i	$\text{J mol}^{-1} \text{K}^{-1}$
ΔH_{reaz}	Heat of reaction	J mol^{-1}
ΔP	Pressure difference	Pa
$\Delta \rho$	Density difference	Kg m^{-3}
ε	Average dissipation	W Kg^{-1}
ε_M	Macro-porosity	-
ε_g	Gas hold-up	-
ε_m	Meso-porosity	-
θ_B	Bragg angle	-
θ_C	Three phase contact angle	-
θ_M	Density of surface metal atoms	m^{-2}
θ_V	Fraction of available adsorption site	-
θ_i	Incident angle	-
λ_B	Beam wavelength	m
λ_k	Kolmogoroff's length scale	m

μ	Viscosity	Pa s
μ_i	Chemical potential of species i	J mol ⁻¹
ρ_c	Continuous phase density	Kg m ⁻³
ρ_s	Solid density	Kg m ⁻³
ρ_{sk}	Skeletal density of solid	Kg m ⁻³
σ	Interfacial tension	N m ⁻¹
σ_{12}	Scattering cross section	m ²
τ	Tortuosity	-
τ_c	Crystallite mean size	m
τ_{ij}	Stress tensor	Pa
τ_s	Shear stress	Pa
τ_y	Yield stress	Pa
Φ	Porosity	-
χ	Structural parameter	-
χ	Mole fraction	-
Ω_{12}	Collision integral	-
ω	Angular velocity	rad s ⁻¹
$[C_i]_{out}$	outlet concentration of the species i	mol m ⁻³
$[C_i]_{react}$	Concentration of reacted species i	mol m ⁻³

Chapter 1

Introduction

1.1 Introduction to catalysis

The use of catalytic processes has ancient roots but its origin is difficult to trace [1]. However, the word catalysis was firstly used by J.J. Berzelius in his report published in 1836. In his work, he reviewed the early findings on chemical changes in homogeneous and heterogeneous systems proposing the existence of a new force called “catalytic force” and he called “catalysis” the decomposition of species by this force [2]. This marked the beginning of a scientific approach to catalysis, and to chemical reaction in general, that eventually led to the birth of industrial catalysis. Nowadays catalytic reactions play an important role in many industrial processes such as the production of mineral acids (e.g. HNO_3 , H_2SO_4), petrochemicals, and polymers just to list a few. It is estimated that more than 50% of the chemicals produced today come from catalytic processes [3] and the demand for catalyst is expected to be around 20.6 billion \$ in 2018 [4].

The use of catalysts gives two main advantages: they increase the rate of reaction by providing a transitional state characterised by a lower energy barrier and they increase the selectivity towards desired products vs un-wanted ones [5]. Catalytic processes can be divided in homogeneous and heterogeneous ones. In the former the catalyst and the reactants/products are in the same phase (e.g. liquid, gas or solid) while in the latter the catalyst and the reactants/products are present in different phases (e.g. solid-liquid, gas-solid, etc.). Heterogeneous catalysts are most commonly characterized by active site (functional centres where specific reactions occur) dispersed on the support with the latter having different structural properties (e.g. surface area and porosity); exceptions to this description are for example perovskites catalysts where the synthesised powder

constitutes the active species [6]. This work focused on the development of new porous supports to be used in heterogeneous catalysis and thus attention will be focussed on this class of catalysts. In the next subsections, an introduction to the factors affecting the performances of supported heterogeneous catalysts is given. Due to the vastness of the subject, this introduction is by no mean exhaustive and the effects of different factors impacting catalyst performances will be discussed in more detail in the relevant chapters.

1.1.1 Effects of diffusion phenomena in heterogeneous catalysts performances

Different physical and chemical phenomenon are involved in heterogeneous catalysis; the typical steps occurring in a heterogeneous catalyst are schematised in Figure 1. 1.

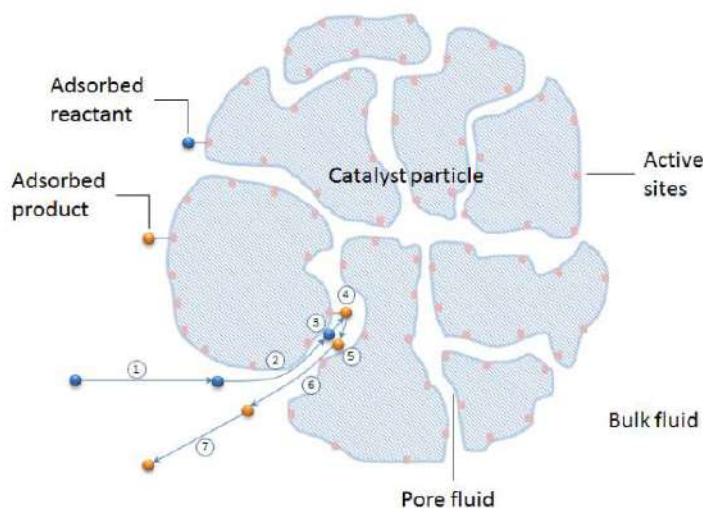


Figure 1. 1: Steps involved in a typical heterogeneous catalytic process [7]

The reactants firstly transfer from the bulk fluid to a catalyst particle (1), then internal diffusion in the catalyst pores occurs for the reactant to reach the active sites (2), the reactant adsorbs on the active site (3) so that the reaction can occur forming an adsorbed product (4), this then desorbs (5) and diffuses through the catalyst pores (6) and hence from the particles to the bulk fluid (7). It is

evident that in the case of heterogeneous catalysis the rate of reaction can depend on a series of physical phenomenon such as film diffusion resistance at the fluid film surrounding the particles, adsorption/desorption on/from the catalyst surface and pore diffusion resistance. The last is particularly relevant when considering internal diffusion limitations. In 1939, *Thiele* proposed a relationship between reaction rate and diffusion that took the name of Thiele modulus [8]. This value may be used for the determination of the effectiveness factor which express how much the reaction rate is lowered because of the pore resistance diffusion [3] and is defined as the ratio between the actual mean reaction rate within pores and the rate if not slowed by pore diffusion [3]. Catalyst effectiveness can be strongly influenced by the support shape and porosity; for example, the effectiveness of V_2O_5/TiO_2 catalysts used in NO conversion can vary between 0.01 and 0.3 when extruded-monolith and pellets are used respectively and can reach values up to unity in the case of wash-coated monolith; in addition, the effectiveness of such a catalyst can be substantially improved by introducing macro-porosity [9]. The effect of pore volume on catalyst performances was also observed in Fischer-Tropsch reaction; *Song and Li* showed that the mesopores (pore diameter comprised between 2 and 50 nm) of the support have an effect on the size of the active site particles with pore size of 6-10 nm giving catalyst with higher activities and selectivity toward the desired products [10]. *Li et al.* reported that the performance of Co catalyst in Fischer Tropsch were enhanced when supported on macroporous (pore diameter >50 nm) silica instead of non-macroporous silica; the authors concluded that the positive effect was due to the rapid transport of reactant and products when macropores were present [11]. Optimisation of the structure of catalyst support is receiving an increasing interest in different research areas. *Rao et al.* showed that PtRu catalysts, supported on low surface area carbon, present superior mass specific activities in methanol oxidation; the authors related this to the high PtRu utilisation and the facilitated diffusion

in macropores [12]. These are just few examples on how the structure of the catalyst support can be optimised to enhance the catalyst performances; further discussions on this topic will be presented in Chapter 4 and Chapter 7 of this work.

1.1.2 Effects of crystal size and crystal defect on heterogeneous catalysts performances

The size effect in catalyst particles has been studied since the infancy of catalytic research, for example, through studies of ultrafine particles and single-site catalysts [13] [14]. In the past, the size effect was only associated to an increase in the proportion of surface species and defects that in turn present a lower coordination number and hence are catalytically more active [15]. With the development of nanoscience it has become evident that, other than these size-dependent fractions of under-coordinated sites, electronic states of a metal nanoparticle could vary or even transition from a metallic state to a molecular one [16]. It is important to point out that the effects of different coordination environment and electronic state are not unidirectional but, the decrease in particle size, may either increase or decrease the activity of a given reaction. For example, the conversion of CO to CO₂ is significantly increased when the size of Au nanoparticles is decreased from ~6 nm to ~3 nm; this is due to the increase in the number of active sites in terms of Au atoms with a low coordination number [17]. By contrast, larger Pt nanoparticles exhibits a higher activity in the same reaction with the activation energy on 12 nm platinum particles being much lower than that of 1.7 nm particles; attributed to the stronger binding energy of smaller Pt particles and consequently to the lower desorption rate of CO molecules [18]. Other examples of reactions affected by particles size are the hydrogenation of unsaturated aldehydes catalysed by Au nanoparticles supported on TiO₂ [19] and the reduction of 4-nitrophenol to 4-aminophenol catalysed by cetyltrimethylammonium bromide-stabilised Au nanoparticles [20]; in both cases, an increase in

catalyst activity was observed reducing the particles size. It has been previously said that the presence of defects also affects the catalyst activity. In the 1920s *Kolles* [21] and *Stranski* [22] proposed the TSK (Terrace Step Kink) model. This states that the energy of an atom, positioned on a crystal surface, depends on its bonding to neighbouring atoms; depending on the atom positions, this will have a different number of neighbours. Considering a simple cubic surface, a kink atom has 3 neighbouring atoms, a step atom has 4 neighbouring atoms and a terrace atom has 5 neighbouring atoms. Figure 1. 2 shows a schematic diagram of the surface described by the TSK model.

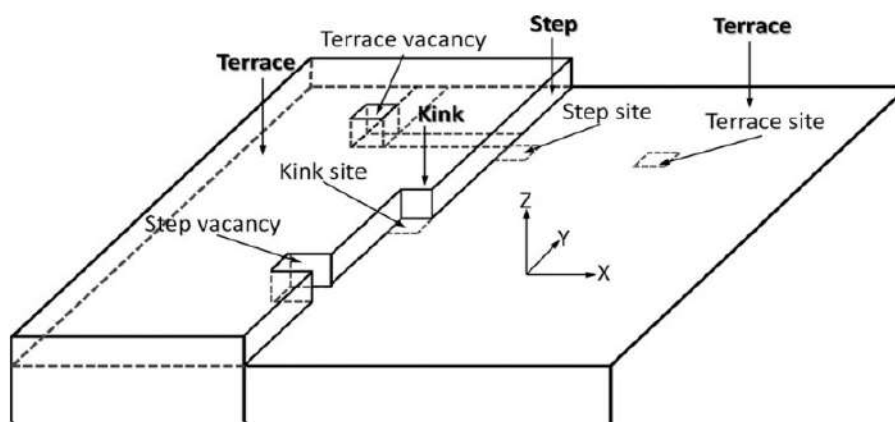


Figure 1. 2: Diagram of the surface described by the TSK model [23]

It has been postulated that, since step and kink atoms have fewer nearest neighbours than atoms in a flat surface, these are more reactive [24]. The lower surrounding electron density makes them more likely to bind adsorbates in order to make up for their electron density deficiency [25]. Many catalytic processes occurring on well-defined surfaces can be either defect favoured or terrace favoured. Defects can influence reactivity through geometric effects, due to the presence of surface atoms in favourable positions for catalytic promotion, or through electronic effects due to the alterations in electronic structure at defects [26]. *Spendelow et al.* reported that the oxidation of CO

at high coverage and low potential on Pt (111) in alkaline media is an example of a defect-favoured reaction in which the role of defects is to stabilise adsorbed OH. On the other hand, reduction of oxygen on Pt (111) in alkaline media serves as a model of a terrace favoured reaction in which defects are deactivated by strong localised adsorption of OH/O, leaving terrace sites as the active sites [26]. Another example of the beneficial effects of surface defects was given by *Wang et al.* who studied the dry dehydrogenation of alcohols on Cu (111) and Cu (110) model surfaces showing that the degree of hydrogenation can be increased by increasing the density of defect sites by roughening the surface via Ar^+ [27]. Although the beneficial effects of surface defects is frequently observed, this is not always the case. *Ford et al.* reported that the effect of defects may not be as important in surfaces that relax considerable from their ideal arrangement [25]. For example, the actual distance between the first and second layer of Pt (210) is 22% shorter than the ideal distance [28]; after surface relaxation, the electron density around a particular surface atom can be quite different from the electron density around the same atom in its ideal position making the defects effect less important. From these few examples it is evident that the effects of particles size and surface defects on the catalytic activity/selectivity are due to a combination of geometric and electronic effects. These can significantly vary depending on the reaction system under consideration and a compromise between geometric and electronic effects is usually required to optimise the catalyst performance.

1.1.3 Effects of promoters on heterogeneous catalyst performances

Promoters are added to heterogeneous catalysts to enhance activity, selectivity, lifetime or to ensure the structural integrity of the catalyst surface [29]. Al_2O_3 and K_2O are, for example, the promoters added in iron catalyst for ammonia synthesis. Al_2O_3 acts as a structural promoters and its main role

is to increase and stabilise the surface area of the catalyst; alumina, together with other oxidic materials, preferentially segregates the grain boundaries of the iron catalyst forming a physical barrier that prevents crystallites growth through sintering (reduction in catalyst surface area resulting from the aggregation of catalyst particles due to heat) [30]. Alumina also interacts with the potassium promoter reducing its loss from the surface. K_2O acts as an electronic promoter significantly increasing the low coverage N_2 adsorption coefficient, reducing the barrier to dissociation; thus enhancing the dissociative adsorption rate of N_2 [31] [32]. Potassium has a similar role in potassium promoted iron catalysts used in Fischer Tropsch synthesis; it enhances the adsorption and dissociation of CO [33] [34]. Similar promotion effects have been observed for the water gas shift reaction catalysed by cesium-promoted copper catalysts with cesium enhancing the rate of the reaction [33] [34] [35]. Apart from the electronic effects which aid adsorption/dissociation/desorption processes on the catalyst surface, there are two other ways in which promoters act to increase selectivity. It is known that the addition of chlorine compounds or NO_x in the oxidation of ethane to ethene oxide, using silver catalysts, significantly enhances the ethene oxide selectivity [36]. This is due to the suppression of non-selective homogeneous gas phase oxidation reactions. The addition of chlorine containing compounds has a similar effect in the oxidation of methane; also in this case this is due to the elimination of non-desired gas phase reactions [37]. Another way promoters can enhance catalyst selectivity is by blocking non-selective surface sites. For example, the addition of bismuth to supported platinum catalysts enhances the selectivity of oxidation reactions such as glycerol oxidation [38]. This is due to the bismuth atoms selectively blocking specific surface platinum sites. These few examples showed how promoters can be used to enhance catalyst activity and selectivity. These can act in a number of ways and, in

particular, complex interactions between structural and electronic effects can play an important role in enhancing the catalyst performances.

1.1.4 Steps for the development of catalyst at industrial scale

The previous sections have shown that the development of a new catalyst is not a trivial task. Once a promising research catalyst (laboratory scale) has been developed, several steps are required to obtain a technical catalyst (commercial scale). *Mitchell et al.* comprehensively described these steps in their review paper [39]; these are summarised in Figure 1. 3.

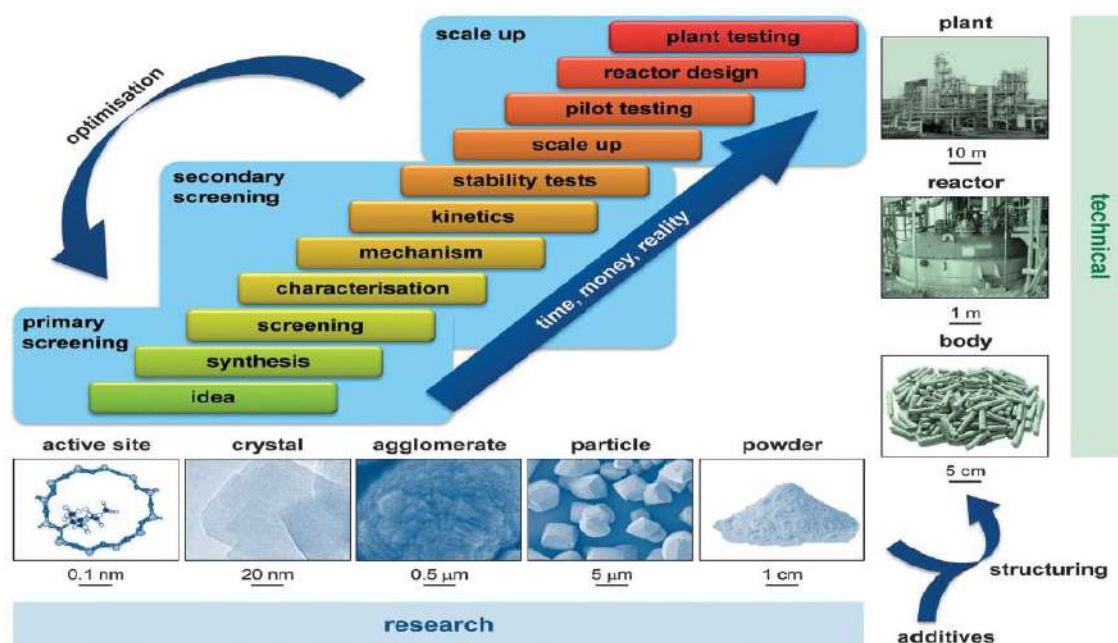


Figure 1. 3: Typical sequence of interactive tasks followed in a catalyst development [41]

Research catalyst is usually a single bulk or supported active phase in powder form while the technical catalysts, in addition to the active phase and support identified during the screening steps, includes a series of additives to complement physical (mass or heat transfer), chemical (functionality), or mechanical attributes. Another fundamental operation in the manufacturing of commercial catalysts is the unit operation known as forming in which powders are structured using

a specific method into macroscopic bodies (e.g. pelleting, extrusion, spray drying). Forming methods usually rely on powder agglomeration. Powder compaction is carried out on dry powders (pelleting) while wet (usually aqueous) powder is used for processes such as extrusion of pastes, granulation or as slurries for spray drying. Common elements to all the forming techniques are that the raw material must initially be refined to form a well-defined feed, the pre-mixtures must be agglomerated into “green” bodies of the required shape and finally, the shaped bodies must be hardened to satisfy the mechanical demands [39]. Due to the complexity of the forming step, it is evident that a support’s structure can be varied in several ways: selecting materials having different bulk properties (e.g. surface area), using different forming techniques to obtain the desired macrostructure (e.g. pelleting, extrusion, etc.) or controlling the catalyst after-treatment (e.g. calcination temperature) which affects both the porosity and the mechanical strength of the support. Johnson Matthey has a long and successful history in developing new structural catalyst supports; some examples include the patents US19880292002 and WO2010029324 granted to JM (still ICI in the case of the first patent) regarding the use of negative replica ceramic foams and a new shaped pellet (Figure 1. 4) as catalyst supports.

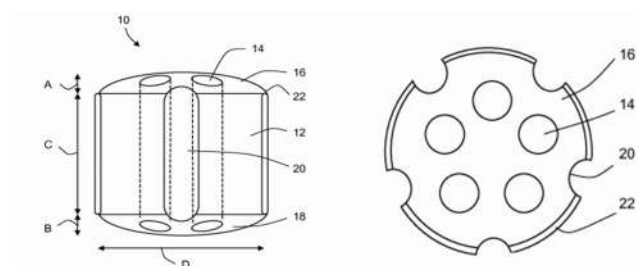


Figure 1. 4: Johnson Matthey new pellet shape protected by patent WO2010029324 [40]

Johnson Matthey has taken advantage in the development of computational techniques for the development of new catalyst shapes and structure. These were developed both in-house and through collaborations with leading institutions in the field such as, just to name a few, the

Worcester Polytechnic Institute, the Institute of Chemical Technology at Prague and the University of Leeds. From collaborations with the first institution pioneering Computational Fluid Dynamic studies regarding diffusion and reaction in packed bed reactor were carried out while, from collaborations with the second one, pore resolved models were used for multiscale simulations in order to understand the impact of catalyst structure on its performances; details of the specific publications will be given in Chapter 6 and Chapter 7 respectively. The work with Leeds by contrast was a very early example of a computational approach to loading catalyst pellets into tubes, enhancing the ability to investigate shape effects.

1.2 Company Background

Johnson Matthey plc (JM) is a leading speciality chemicals company with a core focus in catalysis, precious metals, process technologies and fine chemicals. Johnson Matthey is a UK registered FTSE 100 company operating in over 30 countries. As reported in their 2017 annual report, the company has an approximately 12,200 employees, revenue of £12.03 billion and an underlying profit before tax of £461.6 million [41]. As of October 2017, the company has four Sectors (or divisions):

- **Clean Air**, which supplies catalysts and technologies related to environmental applications such as catalysts for light and heavy duty vehicles, on-road and non-road diesel retrofit and stationary emission control systems (e.g. coal-fired power plants)
- **Efficient Natural Resources**, which supplies process catalysts and recycling capabilities; this division comprises:

- *Precious Metal Refining*: refining and recycling business which recovers platinum group metals (PGMs) from spent catalysts and other secondary materials and refines PGMs from global mining operations.
- *Precious Metal Management*: business including platinum marketing and distribution activities and market research services.
- *Noble Metal*: business leader in the fabrication and refining of a wide range of products made of platinum group metals (e.g. catalyst gauze for ammonia oxidation, advanced coating technology ceramics, sensors, etc.)
- *Advanced Glass Technology*: leader supplier of high performance materials to the automotive glass, electronic, tableware, advanced ceramics and technical glass.
- *Chemical Products*: manufacturer of minor metal compounds, organometallics and fine metal powders for high technology applications.
- *Syngas*: offers a range of catalysts and technology for ammonia, methanol, hydrogen, substitute natural gas and gas to liquid production. In addition, it includes the market leading KATALCO_{JM} and PURASPEC_{JM} catalyst ranges together with licensed process technologies.
- *Process Licensing and Technology*: develops chemical processes and technologies and licenses them for use in the oil, gas, petrochemical and biochemical industries.
- *Purification-Gas Processing*: provides absorbents and technologies used for the purification of natural gas, hydrocarbon gas and liquefied natural gas.
- *Diagnostic Services (Tracerco)*: provides measurement and diagnostic services for the oil and gas industry.

- *Chemical Catalysts*: catalysts for the petrochemical industry. In addition, it includes the market leading FORMOX™ process technology, catalysts and services for formaldehyde production.
- **Health**, which brings cost effective, niche treatments to the market. It includes:
 - *Custom Pharma Solutions*: provides a full range of dedicated drug development, scale-up and manufacturing services.
 - *Controlled Substances*: supplies an extensive range of controlled substances and opioids. This division includes Macfarlan Smith Ltd which is the world's leading manufacturer of opiate alkaloids.
 - *APIs and Life Cycle Management*: provides an extensive range of APIs.
- **New Markets** which focuses on areas adjacent to current interests and include:
 - *Batteries Technology*: develops advanced materials and technologies for high performance battery applications, and is the globally second in terms of cathode material manufacture.
 - *Catalysts*: dedicated to improving the efficiency of catalytic reactions for the manufacture of pharmaceuticals, fine and agro-chemicals.
 - *Fuel Cells*: world leader in the production of catalysed components for use in fuel cells and of membrane electrode assemblies.
 - *Atmosphere Control Technologies*: creates advanced technologies to extend the post-harvest life of fresh produce.
 - *Water Technologies*: provides high technology purification and decontamination products for a variety of industrial applications.

- *Medical Devices*: provides a complete range of capabilities in the fabrication of precious metals, alloys, Nitinol and engineered plastics.

1.3 Business Case

For Johnson Matthey, developing new porous supports and the assessment of their performance through experimental testing and computational methods is beneficial in several aspects:

- The developing of porous supports characterized by extensive macro-porosity allows improvements in catalyst effectiveness. It has been introduced in Section 1.1.1 that this catalyst property is particularly affected by the percentage of macro-pores. Higher catalyst effectiveness has three major advantages: allows to bring the cost down since less active species can be used, leads to a reduction of the reactor volume and, consequently, increases the sustainability of the process since less catalyst has to be disposed of or recycled.
- Design and optimization of the manufacturing process results in the understanding of how to control it in order to obtain the desired final product. In addition, it allows to manufacture the desired product in a time and cost effective way.
- Testing of different catalytic species supported on macro-porous supports allows identification of catalytic process in which the use of these supports is particularly beneficial. This puts JM in a position to enter such markets before its competitors.
- Develop modelling methodologies that can be applied to the investigation of catalyst having different porous structures. This results in a more efficient development time of new catalyst structure, decreasing the time to market of the product.

Development of both new support structures and modelling methodologies will give JM a commercial advantage in different area (e.g. syngas, emission control) over its competitors. An additional commercial benefit is that the development of these new materials will result in more sustainable processes, which is in line with Johnson Matthey vision for a cleaner and healthier world.

From an academic point of view, this work will provide a fundamental understanding of the chemistry and engineering involved in the formulation and manufacturing of these materials. Journal papers and conference presentations resulted from this project will be used to share this work with the scientific community.

1.4 Scope of the Investigation

This work has five major objectives and these are summarised below:

- **Developing new, more flexible and more sustainable ceramic foams formulations.** Ceramic foams, produced by direct foaming, commonly use carboxylic acids or amines to modify particles surface. These formulations present a limited pH operative window and, in addition, their use present environmental concerns.
- **Lie the basis for a fundamental understanding of foam manufacturing.** Initial ceramic slurries are usually mechanically frothed by a kitchen mixer; this approach limits the fundamental understanding of the manufacturing process and impedes its scale-up. Industrially applicable manufacturing methods will be used to understand the impact of different manufacturing parameters on the foam structure to gain a fundamental understating on foam manufacturing.

- **Testing of foam supported catalysts in different reaction systems.** Foam supported catalysts will be tested in reaction systems particularly relevant to Johnson Matthey business such as Fisher-Tropsch Synthesis and methane oxidation reaction; the advantage of using macro-porous supports over conventional ones will be assessed.
- **Develop reactor models to screen the performances of porous catalysts in different reactor configurations.** Time effective commercialisation of new catalysts can be facilitated using modelling tools. 1D + 1D models will be developed to screen the performances of catalysts in different reactor configurations such as monolith and packed bed reactors. Models results will be compared to experimental ones in order to confidently validate the developed models.
- **Compare different modelling approaches to understand the level of complexity necessary to effectively screen catalysts performances.** Two main comparisons will be carried out: 1D + 1D simulations against Computational Fluid Dynamic ones and the use of the Pore Resolved Model to determine the effective diffusivity of macro-porous materials against the use of the *Wakao-Smith* correlation. This will allow to have an understanding of the strengths and limitations of the different approaches and to identify the most suitable one depending on the level of accuracy required. Also in this case, the model results will be compared to experimental ones to have a clear benchmark against whom to compare them.

1.5 Thesis Structure

The main aims of this work have been summarised in the section above. A summary of their repartition among the thesis structure is given below:

- **Formulation of Ceramic Foams (Chapter 2).** Understanding the effect of the initial formulation on foam structure and developing more sustainable products is vital for the commercialization of such materials. In this chapter, amino acids will be used as alternative and more environmentally friendly amphiphiles for the modification of particle's surface properties. The effects of amino acids hydrophobicity on the foam structure will be investigated and relationships between amino acid hydrophobicity and foam structure will be derived. Amphiphile adsorption at the different interfaces (e.g. gas-liquid, liquid-solid) and minimum amphiphile concentration to be added will also be determined.
- **Manufacturability of Ceramic Foams (Chapter 3).** Developing scalable manufacturing process and understanding the effects of the foam manufacturing on its structural properties is fundamental for the industrial scale production of ceramic foams. In this chapter, an aerated stirred vessel will be used as an alternative to a kitchen mixer to mechanically froth the ceramic slurry. Design of Experiment will be carried out to assess the process parameters affecting foam structure. Foam properties such as porosity and bubble size will be correlated to global mixing parameters and vessel flow regimes giving an understanding of the operating conditions to be use to obtain the desired foam structure. Rheological properties of the produced foams will be measured and a correlation with foam bubble size and bubble size distribution will be proposed giving the foundation for the development of at-line rheology measurements to assess the structure of the produced foams.

- **Testing of ceramic foam supported catalysts in Fischer-Tropsch Synthesis (Chapter 4).** Fisher-Tropsch Synthesis (FTS) has a leading role in syngas reactions and its market is expected to grow in the next years; for this reason, improving the performances of FTS catalysts is of primary interest for Johnson Matthey. In this chapter, CoO catalyst supported on ceramic foams will be tested in Fischer-Tropsch Synthesis and their performances will be compared to those of conventionally supported ones (spheres). The role of support structure on the catalyst performances will be investigated.
- **1D + 1D Simulation of CH₄ Oxidation in a Monolith Channel: Intrinsic Kinetic Model Validation against SpaciMS Experimental Results (Chapter 5).** Johnson Matthey is particularly interested in CH₄ oxidation due to its role in emission control. For this reason, JM developed an in house kinetic model describing the methane oxidation reaction. To validate this kinetic model, a 1D + 1D reactor model will be built in Athena Visual Studio to describe the performances of a monolith reactor. The model results, obtained using JM kinetic model, will be compared to experimental results acquired by Ciaran Coney at Queen's University of Belfast. The comparison will allow to determine if the model well predicts the reactant/product profile along the reactor channel resulting in either model validation or rejection.
- **JMFoam Validation: use of SpaciMS data and 1D + 1D simulation to validate new Computational Fluid Dynamic capability (Chapter 6).** In recent years, Computational Fluid Dynamic simulations have gained a significant role in chemical engineering. Johnson Matthey, in collaboration with Tridiagonal Solutions, has developed a new CFD simulation package allowing diffusion and reaction simulation. To validate this software,

methane oxidation reactions conducted in a monolith reactor will be carried out and the results will be compared to those obtained experimentally and by 1D + 1D model. The validation of the new CFD capability will grow confidence on its use for predicting the performances of systems in which diffusion and reaction are involved.

- **Effects of Foam Structure on the CH₄ Oxidation Reaction: Experimental and Computational Determination of CH₄ Light-Off Curve (Chapter 7).** It has been previously said that methane oxidation is of particular interest for JM and the development of better-performing catalysts is an ongoing process. In this chapter, the performances of Pd catalysts supported on both foams, having different porosities, and conventional pellets will be assessed and compared; light-off curves will be acquired to determine the performances of such catalysts.

A 1D + 1D reactor model will be developed and the light-off curve of high and low porosity foams will be simulated. Two different approaches will be used and compared for the determination of the effective diffusivity, namely the *Wakao-Smith* correlation and the Pore Resolved Model (PMS). The aim of this comparison is to identify the benefits and limitations of each approach and to select the right one to be used at the macro-scale. This study will generate the foundation for the development of a reactor models that could be used to screen the performances of catalysts having different structures.

Chapter 2

Formulation of Ceramic Foams

2.1 Introduction

Ceramic foams have been receiving increasing attention due to their applicability in several technology fields. Amongst others, ceramic porous materials are used as refractory insulators, catalyst supports and filters for molten metals [42] [43]. Several techniques have been developed for the production of ceramic foams; these include replica techniques, sacrificial templating and direct foaming [44]. The replica technique consists in the impregnation of a natural (e.g. wood [45], coral [46]) or a synthetic template (e.g. polymer foam [47]) with a ceramic suspension. In order to obtain a thin ceramic coating on the template surface, the excess suspension is removed by passing the template through rollers. After drying and calcination, a ceramic positive replica of the template is obtained. Sacrificial templating uses a biphasic mixture of a template and ceramic slurry to generate the porous structure inside the ceramic body. The sacrificial material can be natural [48] or synthetic [49] and either in solid [50] or liquid form [51]. These are then either extracted or decomposed to form a negative replica of the sacrificial template in the ceramic material. Direct foaming is an ostensibly straightforward method for the production of ceramic foams. This method consists of the stabilization of liquid foams with particles. Air is directly entrained into the ceramic suspension causing the attachment of partially hydrophobic particles at the air/water interface, leading to stable foams [52]. Particles hydrophobization is realized through the addition of an amphiphile; namely a chemical that has a polar head which electrostatically interacts with the particles' surface and a hydrophobic tail that is directed toward the aqueous phase. In this chapter, the reader is introduced to liquid foams, their destabilization processes and the various systems used for their stabilization including the use of surfactants and particles. The materials, methods

and analytical techniques used during the experimentation are then described, the amphiphiles used in the literature are reviewed and a new class of amphiphiles is proposed. The effects of the different amphiphiles on the foam properties are illustrated; specifically, the effects of amphiphile concentration on foam porosity and bubble size distribution is presented in detail, then the particles-amphiphile interaction and the adsorption of the particles at the air-liquid interface are studied using different analytical techniques. The new amphiphiles are then ranked depending on the hydrophobicity of their side chain and a relation between amphiphiles hydrophobicity and foam structural properties is presented. Finally, the most economically viable amphiphile is selected and the minimum amphiphile concentration to obtain a stable foam is determined.

2.2 Liquid Foams and Instability Processes

Liquid foams are gas-liquid systems where the gas bubbles are dispersed in a continuous liquid phase and they account for most of the foam volume (>50%). Gas bubbles can be polyhedral or spherical in shape depending on the liquid fraction present. Dry foams (< 1-2% liquid fraction) tend to have polyhedral bubbles while wet foams (> 16% liquid fraction) are characterized by round bubbles. The equilibrium law that describes soap films was derived by *Plateau*; this states that three faces meet at angles of 120° and four edges join at angles of 109.47° at each vertex [53]. *Almgren and Taylor* stated that the geometry of a system is a consequence of energy minimization [54]. Foam energy can be expressed as bulk and surface energy; each film tries to minimize its area (in 3D) or its length (in 2D) [55]. Exploring this principle, in 1887, *Sir William Thomson (Lord Kelvin)* identified that a tetrakaidecahedron with curved faces is the unit cell that minimizes the surface area per unit volume and satisfies Plateau's law [56]. This was considered the most stable structure until 1994 when *Weaire and Phelan* demonstrated that a unit cell composed of six 14-

sided cells and two 12-sided cells had a surface area per unit volume 0.3% lower than the Kelvin structure [57]. Although the most stable foam structures are well known, foams undergo several physical processes that take place in order to reduce the overall system free energy; these include drainage, coalescence and Ostwald ripening [44]. Drainage is the separation of the gas and liquid phases due to gravity; liquid drainage mostly occurs through the Plateau borders (edge along which soap films meet is trees of 120°) [58] and, to a lesser extent, along the cell walls [59]. Coalescence consists of the association of neighbouring bubbles due to the instability of the thinned film after drainage. The stability of thin films depends on the attractive and repulsive interactions between bubbles; attractive Van der Waals forces are the main driving force for coalescence. This phenomenon can be contrasted with electrostatic and/or steric repulsive forces strong enough to overcome the attractive Van der Waals forces. This can be achieved by surfactant or particles attached at the gas-liquid interface; these two methods will be described in Sections 2.3 and 2.4 respectively. Ostwald ripening is due to the difference in Laplace pressure between bubbles of different sizes. The Laplace pressure arises from the curvature of the air-water interface and is described by:

$$\Delta P = \frac{2\gamma}{r} \quad (2.1)$$

where ΔP is the Laplace pressure, γ is the surface tension and r is the bubbles' radii [60]. The difference in Laplace pressure between bubbles causes a steady diffusion of gas molecules from smaller to larger bubbles through the liquid phase leading to bubble disproportionation. Although this last process cannot be completely prevented, the adsorption of surfactants can reduce the occurrence of this phenomenon by decreasing the surface tension.

2.3 Surfactants Stabilized Foams

Surfactants are surface active species that adsorb at the gas-liquid interface lowering the surface tension. These are amphiphilic species which are characterized by a polar hydrophilic head and a hydrophobic chain. They can be classified, depending on the nature of their functional group, as anionic, cationic or non-ionic surfactants; Figure 2. 1 shows an example of these classes of surfactants. It is notable that the classification depends on the net charge carried by the head group with anionic surfactants having a negative charge, cationic surfactants having a positive charge while non-ionic surfactants carry no charge.

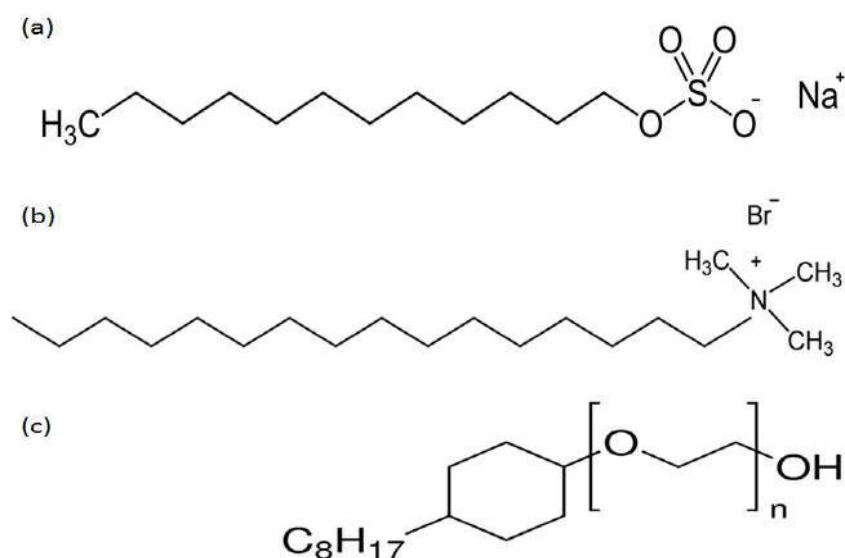


Figure 2. 1: (a) anionic surfactant (sodium *p*-dodecylbenzenesulfonate) (b) cationic surfactant (hexadecyltrimethylammonium chloride) (c) non-ionic surfactant (Triton X-100)

Surfactants can also be classified depending on their degree of hydrophilicity and can be identified by the Hydrophilic-Lipophilic Balance (HLB). Griffin proposed a mathematical relationship to determine the HLB [61]:

$$HLB = 20 \frac{MW_h}{MW} \quad (2.2)$$

where MW_h is the molecular weight of the hydrophilic portion of the molecule and MW is the molecular weight of the whole molecule. The disadvantage of this approach is that it does not account for the strength of the different hydrophilic groups. In 1957 *Davies* proposed an alternative formula for the calculation of the HLB:

$$HLB = 7 + \sum_{i=1}^m H_i - 0.475 n_{LG} \quad (2.3)$$

where H_i corresponds to the strength of the hydrophilic groups and n_{LG} is the number of lipophilic groups in the molecule [62]. The HLB can predict the surfactant properties. For example, molecules with HLB values greater than 10 are considered hydrophilic while the opposite is true for hydrophobic surfactants [63]. The nature of the surfactant can determine the disperse and continuous phase of the mixture; the packing of the surfactant at the gas-liquid interface determines the curvature of the surfactant monolayer toward the liquid or the gas [64]. Thus, for hydrophilic surfactants, the monolayer curves around air resulting in air-in-water dispersion (foam) while for more hydrophobic surfactants a water-in-air dispersion is obtained (mist). The adsorption of these species at the gas-liquid interface slows down the coalescence and disproportionation processes by reducing the gas-liquid interfacial energy. However, due to the low adsorption energy of surfactants (usually a few kTs) [65], the process is a dynamic equilibrium involving the continuous adsorption and desorption of surfactants. This prevents the long-term foam stabilization with a consequent foam collapse within a few minutes after foaming. Despite the low stability of surfactant-stabilized foams, the production of directly foamed ceramic foams using surfactant as the stabilizing agent has been attempted. This usually requires the use of a setting agent to consolidate the foam before the destabilization processes take place [44]. This can be achieved by in situ polymer setting, sol-gel setting or gelcast setting. *Wood et al.* patented a process where ceramic particles were

incorporated in organic solutions containing a precursor of polyurethane foams; the mixture was then foamed by in situ gas incorporation in presence of surfactant and the foam was consolidated by the thermosetting condensation reaction between the polyurethane precursors [66]. As previously mentioned, foam consolidation can be achieved using inorganic materials which exhibit sol-gel phase transition in liquid medium. For example, *Tomita et al.* used this approach to produce silica foams where air was mechanically frothed in the presence of surfactants [67]. The necessity to produce ceramic foams with a wide chemical composition led to the use of gelcasting methods. These require less organic materials with respect to the polymer setting technique reducing the extent of the pyrolysis step. In-situ free radical polymerization of acrylamide monomers was originally used by *Binner et al.* but the toxicity of the monomer and the necessity of an oxygen free atmosphere were the major disadvantages of this technique [68]. These drawbacks were overcome by replacing the original monomer with less harmful ones [69] or by using cross linkers which do not require an oxygen free atmosphere [70].

2.4 Particles Stabilized Foams

The use of colloidal particles to stabilize high energy interface has been used for more than a century. In 1907, *Pickering* proposed the use of solid particles that adsorb onto the interface between the two phases to stabilize it; these systems are called Pickering emulsions [71]. This concept has been recently applied to the stabilization of wet foams [72]. The attachment of particles at the interface is favourable when these present a partially hydrophobic character; in this case, part of the high energy solid-liquid area is substituted by a low energy solid-gas area due to the attachment of the particles at the air-liquid interface. Similarly to the HLB used for surfactant, the three-phase contact angle of the particles determines the dispersed and continuous phase of the

system [73]. This concept is illustrated in Figure 2. 2 where, depending on the contact angle value, either a foam or a mist is obtained.

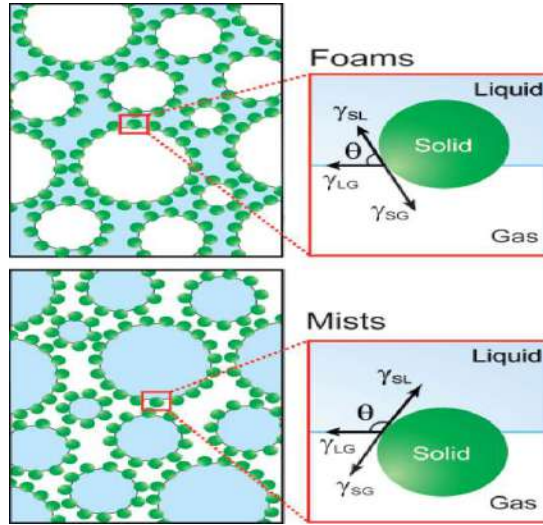


Figure 2. 2: Illustration of continuous-dispersed phase dependence on particles contact angle [44]

In particular, slightly hydrophobic particles present a contact angle $< 90^\circ$ and they remain predominantly in the liquid phase leading to the formation of foams, conversely, highly hydrophobic particles have contact angles $> 90^\circ$ and are mostly present in the gaseous phase resulting in mist formation. The three phase contact angle is also an important component in determining the energy of adsorption of the particles at the interface. Assuming that the particles are small enough so that the effect of gravity can be neglected (usually $< 1 \mu\text{m}$), the energy of adsorption at the interface can be expressed by:

$$E = \pi r^2 \gamma (1 \pm \cos \theta_c)^2 \quad (2.4)$$

where E is the energy required to remove the particles from the interface, r is the particles radius, γ is the interfacial tension and θ_c is the three phase contact angle. The sign inside the brackets is positive for the removal of the particles into air and negative for the removal into water. From (2.4)

it can be deduced that the maximum energy of adsorption is obtained when $\theta = 90^\circ$, at this contact angle value the energy can be as high as ~ 2500 kT [73]; the consequence of this high energy is that, contrarily to what is observed for surfactants, the particle adsorption can be considered irreversible leading to ultra-stable foams. This value rapidly falls at either side of $\theta = 90^\circ$ with $E < 10$ kT for $0^\circ < \theta < 20^\circ$ and $160^\circ < \theta < 180^\circ$. It has been previously mentioned that E also depends on the particle radius; Figure 2. 3 shows the energy of attachment of colloidal particles at an air-water interface as a function of the contact angle and for different particle radius.

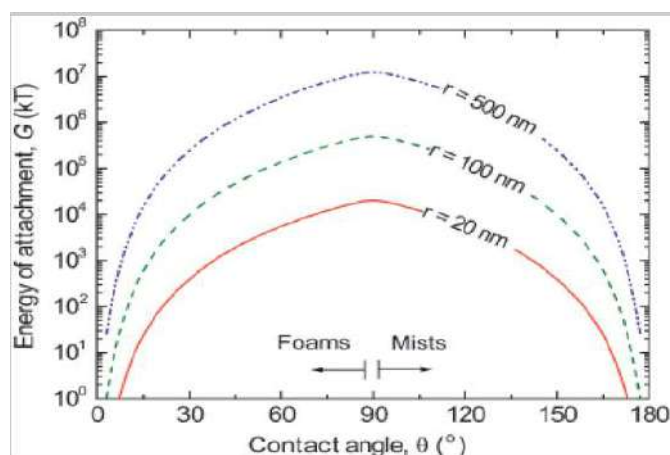


Figure 2. 3: Energy of attachment of colloidal particles at an air-water interface as a function of the contact angle for different particles radius [44]

It is clear from Figure 2. 3 that particles of the size comparable to common surfactants (< 0.5 nm in radius) present very low energy of attachment and may not be effective as stabilizers [73].

Partial particles' hydrophobization is usually realized by electrostatic interaction between the surface charged particles and small amphiphiles which adsorb with their polar group on the surface leaving the hydrophobic tail in contact with the liquid phase. Several classes of chemicals have been proposed as amphiphiles, these include, among others, carboxylic acids, amines and gallates [52]. The selection of the suitable amphiphile is largely governed by the particle's surface charge where carboxylic acids are used with positively charged particles, amines with negatively charged

particles and gallates with either positively charged or neutral particles. *Studart et al.* demonstrated that a minimum amphiphile concentration is necessary to impart enough hydrophobicity to the particles in order to promote their attachment at the air-water interface [74]. *Gonzenbach et al.* showed that the structural properties of the foam (e.g. porosity and bubble size) can be varied by changing the nature of the amphiphile and its concentration [52] [75].

Although the use of the previously mentioned amphiphiles is widely reported in the literature, their use is limited to a certain pH range dictated by the particle surface charge. In addition, many of these amphiphiles present acute toxicity limiting their usage at manufacturing scale. To overcome some of the mentioned limitations, a new class of amphiphiles is proposed in Section 2.6.

2.5 Materials and Methods

2.5.1 Materials

Fumed TiO₂ particles (grade AEROXIDE P25) were obtained from Evonik Industries (Essen, Germany). The supplier technical data sheet stated that the primary particles had a mean diameter of approximately 21 nm while their aggregates were several hundred nm in size. Density and surface area were 4 g cm⁻³ and 50 m² g⁻¹ respectively. The AEROXIDE P25 was characterized by an anatase/rutile ratio of 80/20 with both crystal structures having a tetragonal geometry.

The amino acids used to modify the particles surface were DL-alanine 99%, DL-valine 99%, DL-isoleucine 99%, DL-leucine 99%, DL-methionine 99%, DL-phenylalanine 99%, DL-tyrosine 98% and DL-tryptophan 99% (Alfa Aesar, Heysham, United Kingdom). Other chemical used in the experiments were demineralized water, 70%_{v/v} HNO₃ (Alfa Aesar, Heysham, United Kingdom) and 40%_{v/v} KOH solution prepared by dissolving potassium hydroxide pellets (Alfa Aesar, Heysham, United Kingdom) in demineralized water.

2.5.2 Suspension Preparation

Titania suspensions were prepared by stepwise addition of the powder to deionised water continuously stirred using an IKA EUROSTAR power control-visc overhead mixer. The pH of all suspensions was adjusted to electrostatically stabilise the particles. Titania particles are stable at pH either below 4 or above 7. To favour the dissolution of amino acids the pH was kept either below 2 or above 10 through the addition of small aliquots of 70%_{v/v} HNO₃ and 40%_{v/v} KOH respectively. The solid loading of titania suspensions was set to 25%_{w/w}. In a typical formulation, carried out at acid pH, 99.7 g of titania was added to 250 mL of demineralised water containing 50 mL of 5%_{v/v} HNO₃. After powder dispersion, the suspension pH was dropped below 2 through the addition of 5 mL of 70%_{v/v} HNO₃. Then an amino acid was added to the titania suspension to obtain the required concentration in the range 0.08 - 0.36 mol L⁻¹.

2.5.3 Foaming and Foam Characterisation

Foaming of 300 mL suspension was carried out using an overhead stirrer equipped with a gas inducing impeller [76]. The vessel diameter and impeller diameter were T = 12 cm and D = 6 cm respectively (D/T = 50%). The vessel was fitted with 4 baffles (B) 1 cm wide (B/T = 8.3%). Mixing was carried out at 2000 rpm for 20 minutes. The foam was dried under ambient conditions and then calcined in a Carbolite Furnace CWF at 600 °C for 4 hours. During the ramping step and for the first 45 minutes the furnace was purged under N₂ followed by air. The heating rate was 2 °C min⁻¹.

To determine the porosity of the calcined foam a water pick-up experiment was carried out. The initial weight of four foam samples was recorded then these were immersed in water and the weight of the wetted samples was recorded over a four day period. The average amount of water picked

up was determined by difference between the weight of the wet foam and the initial weight. From this value the foam porosity and pore volume were calculated. To validate the porosity values obtained by water pick up they were compared to those obtained by Mercury Intrusion Porosimetry giving comparable results; details of the comparison are presented in Appendix I. It is important to point out that both these techniques (e.g. water pick-up and mercury intrusion porosimetry) measure the open porosity of the sample since the measuring medium has to reach and fill the sample's pores.

Foam bubble size distribution was determined by acquiring optical microscope (Nikon Eclipse E200) images of the foam cross section. Bubble's diameters were obtained by analysing the acquired images with Fiji ImageJ 1.50a (Wayne Rasband, National Institute of Health, USA) [77]. The obtained diameters were corrected by dividing them by 0.79 to account for the random position of the bubbles during sample sectioning. The correction factor was determined by *Williams et al.*; they identified that the mean pore diameter determined from 2D images is 79% of the actual pore diameter. This factor was derived from numerical methods that they developed and described in order to correct the underestimated pore size obtained from 2-D cross section [78].

2.5.4 Solid State-NMR

Titania suspensions having pH of 0.8, 4 and 10 were prepared using the procedure described in Section 2.5.2. Titania particles were modified by the addition of 0.2 mol L⁻¹ of DL-phenylalanine. The suspensions were dried at ambient condition and then ground using mortar and pestle. The SS-NMR spectrum was acquired at a static magnetic field strength of 9.4 T ($\nu(1H) = 400.16$ MHz) on a Bruker Avance III console using a widebore Bruker 4 mm BB/1H WVT MAS probe and TopSpin 3.1 software. For ¹³C, the probe was turned to 100.63 MHz and the spectrum referenced

to the alanine CH₃ signal at 20.5 ppm. The powdered sample was packed into a zirconia MAS rotor with a Kel-F cap, with weighing before and after packing to obtain the sample mass. The rotor was spun using room-temperature purified compressed air. The total experiment time to acquire the spectrum was 18 hours. The spectrum was acquired using the cross polarisation (CP) method, in which magnetisation on ¹H nuclei is transferred to nearby ¹³C nuclei via the dipolar coupling. Magnetisation was transferred in a contact time of 1 ms. High power (100 W) SPINAL-64 decoupling was applied to the ¹H channel during acquisition.

2.5.5 Surface Tension Measurements

The surface tension of both suspensions and amino acid solutions was measured using the pendant drop method (Krüss Drop Shape Analyser, Hamburg, Germany). In this method, a drop of the solution under analysis is suspended from a needle. The shape of the drop results from the relationship between the surface tension and gravity. Using the drop shape analysis software, the solution surface tension can be determined using the following formula [79]:

$$\gamma = \frac{\Delta\rho g R^2}{\beta_s} \quad (2.5)$$

where γ is the surface tension in mN m⁻¹, $\Delta\rho$ is the density difference between the two phases in Kg m⁻³, g is the gravitational acceleration (9.81 m s⁻²), R is the maximum drop radius (m) and β_s is the shape factor. Suspensions were prepared using the procedure mentioned in Section 2.5.2 while amino acid solutions were prepared dissolving different amount of amino acids in 45 mL of demineralised water containing 5 mL of 70%_{v/v} HNO₃. The drop volumes were in the range 20 µL - 25 µL, depending on the surface tension of the sample. At least 5 drops for each sample were analysed to obtain an average value of the surface tension.

2.5.6 Suspension Filtration and Supernatant UV-Vis Analysis

To determine the amount of amino acid adsorbed at the particles surface, titania suspensions having different amino acid concentrations were prepared. 99.6 g of titania were stepwise dispersed in 300 mL of demineralised water. Amphiphile concentrations between 0.01 M and 0.125 M were dissolved in the suspension. To favour the amphiphile-particles interaction the modified suspensions were stirred at 200 rpm for 20 minutes using an overhead stirrer. The suspensions were then centrifuged at 3000 rpm for 90 minutes using a Falcon 6/300 centrifuge (MSE, London, United Kingdom). The supernatant was then separated from the solid residue. To remove finer particles still in suspension, the supernatant was filtrated using 0.1 μm PTFE membrane syringe filters (Whatman GE Healthcare, Amersham, United Kingdom). The filtrate was diluted ten times and the amino acid concentration was determined by UV-Vis. The UV-Vis spectra were recorded using a UV-1 Thermospectronic (Thermo Scientific, USA).

2.6 Amino Acids as Amphiphiles in Particles Stabilized Foams

In this section the use of amino acids as amphiphiles is proposed. These are environmentally friendly and they allow a wider pH operational window courtesy of the presence of both the carboxylic and the amino group on the same molecule resulting in the hydrophobization of both positively and negatively charged particles. Partial hydrophobization of TiO_2 particles was achieved by the addition of hydrophobic amino acids in suspension, air was then entrained and a stable foam was obtained. Foam porosity and bubble size were determined by water pick-up and SEM image analysis respectively. The amphiphile-particle interaction and the particles adsorption at the different interface were investigated by SS-NMR and UV-Vis respectively. Finally, the hydrophobicity of the different amino acids was determined by surface tension measurements.

2.6.1 Amino Acids Screening

Amino acids are organic compounds containing an amino group (-NH_2), a carboxylic group (-COOH) and a side chain specific to each amino acid. There are about 500 naturally occurring amino acids [80]; these can be classified according to the position of the amino group in alpha- (α), beta- (β), gamma- (γ) or delta- (δ). In this work, attention was focused on the alpha- amino acids and in particular on the 21 naturally occurring amino acids [81]; in these molecules the carboxylic and the amino groups are attached to the first carbon or alpha- (α) carbon. The selection of this class of amino acids was based on their lower cost relative to hydrophobic β -, γ - and δ - amino acids which makes them more economically suitable for the scale-up of the process in the future. Figure 2. 4 shows a classification of these amino acids according to the different properties of their side chain.

Amino Acids with Electrically Charged Side Chains				Special Cases				
Arginine	Histidine	Lysine	Aspartic Acid	Cysteine	Selenocysteine	Glycine	Proline	
Glutamic Acid								
Amino Acids with Hydrophobic Side Chain				Amino Acids with Polar Uncharged Side Chains				
Alanine	Valine	Isoleucine	Leucine	Methionine	Serine	Threonine	Asparagine	Glutamine
Phenylalanine	Tyrosine	Tryptophan						

Figure 2. 4: 21 protenigenic α -amino acids classified depending on the properties of their side chains.

As described in Section 2.4, in order to obtain stable foams, amphiphiles with a hydrophobic side chain are preferred. For this reason, only the amino acids classified as hydrophobic were tested; Table 2. 1 summarizes the pK_1 and pK_2 values for the selected amino acids.

Table 2. 1: List of hydrophobic amino acids and corresponding pK_1 and pK_2 values [82]

Amino Acid	Abbreviation	pK_1 (α -COOH)	pK_2 (α -NH ₂)
Alanine	Ala	2.4	9.7
Isoleucine	Ile	2.4	9.7
Leucine	Leu	2.4	9.6
Methionine	Met	2.3	9.2
Phenylalanine	Phe	1.8	9.1
Tryptophan	Trp	2.4	9.4
Tyrosine	Tyr	2.2	9.1
Valine	Val	2.3	9.6

To assess the performance of the different amino acids, titania suspensions, prepared as described in Section 2.5.2, were foamed using different amino acids and amino acid concentrations. At $pH < 2$ the titania surface is positively charged due to the presence of $-OH_2^+$ groups [83]. Under this conditions the dissociated fraction of $-COO^-$ groups present on the amino acids electrostatically interact with the titania surface. While at $pH < 2$, less than 20% of the carboxylic groups are dissociated; the low solubility of some of the amino acids made it necessary to work at such a low pH. Figure 2. 5 shows the change in solubility and functional group dissociation/protonation as a function of the pH for DL-leucine [84]. The graph shows a significant increase in amino acid solubility at low (<2) and high pH (>10) and a corresponding low degree of dissociation/protonation of the functional groups at these pH values.

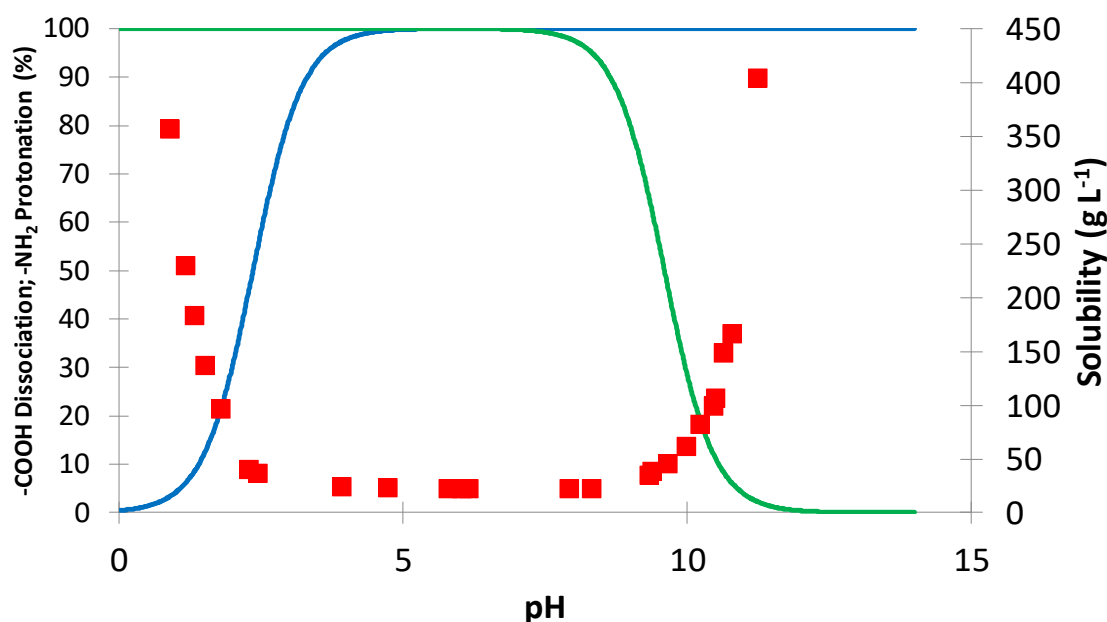


Figure 2. 5: DL-leucine solubility (■) and COOH dissociation (—)/NH₂ protonation (—) as a function of pH (Solubility Data from [84])

Figure 2. 6 shows the porosity of foams obtained using different amino acids and amino acid concentrations. The lines connecting the experimental points are served as a guide for the reader. With the sole exception of DL-methionine, an increase in porosity was observed when increasing the amphiphile concentration until a maximum value was reached, beyond which the porosity decreased. The initial increase in porosity was due to the higher concentration of amphiphile adsorbed on the particles' surface resulting in a higher particle hydrophobicity giving in turn more stable foams. A further increase in the amino acid concentration however led to saturation of the particles' surface by the amphiphile. This caused a reduction in electrostatic stabilization that, in turn, increased the suspension viscosity. The higher viscosity hindered the air entrainment resulting in lower foam porosity. This trend was not however observed for DL-methionine suggesting that the amino acid was either mostly adsorbed at the air-water interface or that the particles were already been saturated. In addition, different amino acids gave different values of maximum

porosity obtainable. This is a consequence of the different hydrophobicity of the amino acids' side chains. This aspect will be discussed in more detail in Section 2.6.4. The low hydrophobicity of both DL-alanine and DL-tyrosine side chains was presumed to be the major reason why these two amino acids were not able to give stable foams.

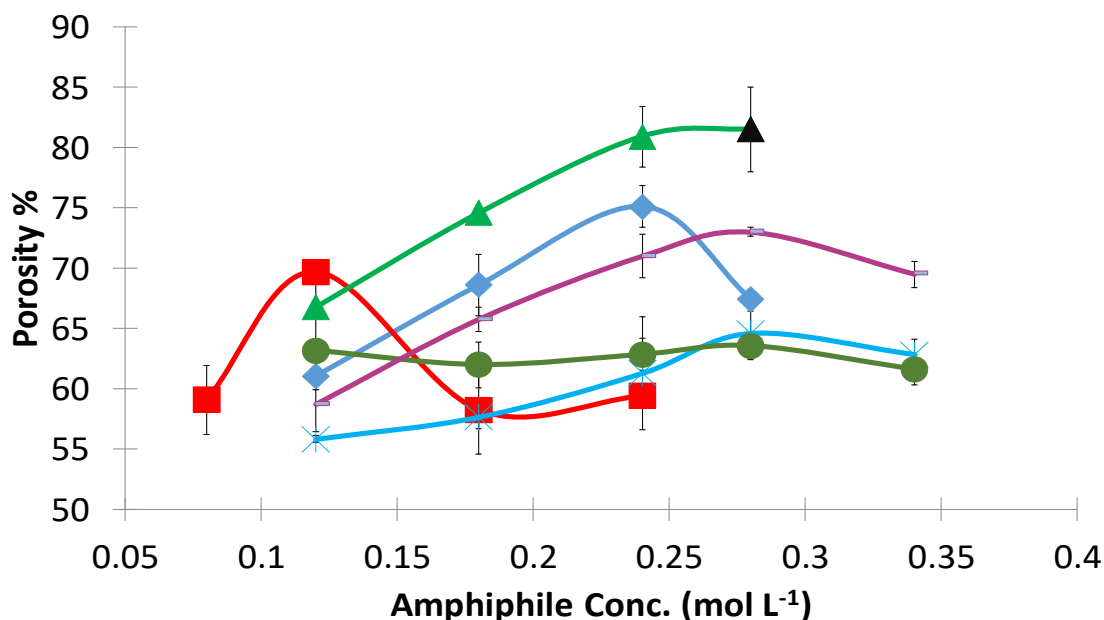


Figure 2. 6: Foam porosity as a function of amphiphile concentration for foams obtained using different amino acid and amino acid concentrations. (♦) Phenylalanine, (■) Tryptophan, (▲) Leucine, (*) Valine, (●) Methionine, (—) Isoleucine. The black triangle in the leucine curve indicates the solubility limit point. DL-alanine and DL-tyrosine are not present in the graph since they did not give stable foams.

2.6.2 Amino Acids-Particles Interaction: SS-NMR

In Section 2.6.1 it has been shown that amino acids can give stable foams in acidic conditions. It was theorized that these compounds would be capable of acting as amphiphiles even in basic conditions thanks to the presence of the amino group. It was assumed that the protonated fraction of -NH_3^+ groups could electrostatically interact with the -O^- groups present on the titania surface at basic pH [83]. To confirm this hypothesis, dried samples of functionalized titania were analysed by SS-NMR following the methodology reported in Section 2.5.4. When the amphiphile-particles

interaction occurred, a change in the electronic environment of the interacting functional group (e.g. carboxylic group or amino group) was expected, and consequently, of its chemical shift [85]. Specifically, when the amino acid interacts through the carboxylic group, a change in the peaks of the carboxylic carbon and, to a minor extent, of the α -carbon should be observed. Rather, when the amino acid adsorbs through the amino group a change in the peaks of the carboxylic, α - and β -carbons should be observed. Figure 2. 7 shows the spectra for the samples prepared at pH = 1, at pH = 4 and at pH = 10.

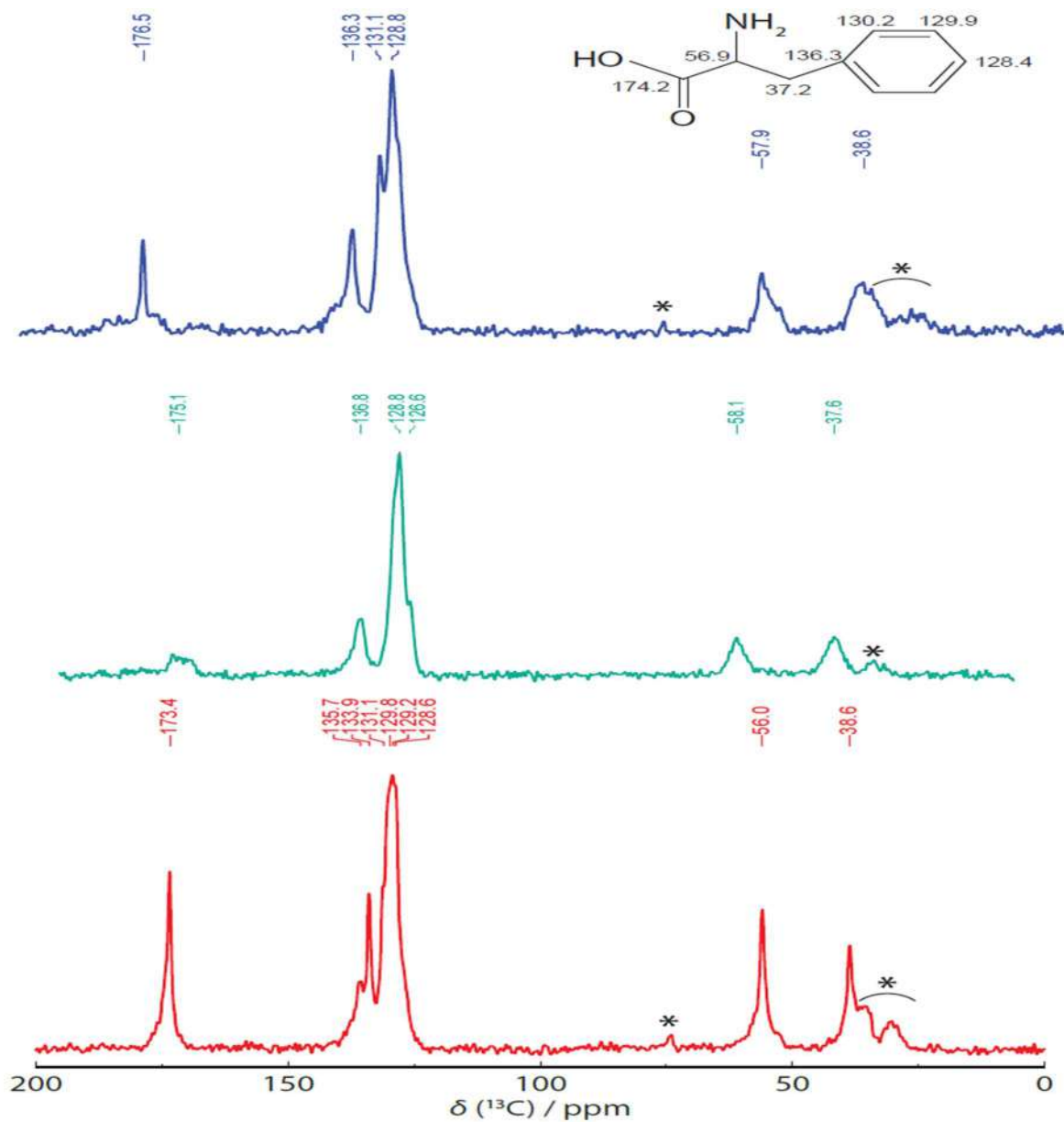


Figure 2. 7: SS-NMR spectra for phenylalanine modified TiO_2 samples prepared at pH = 1 (—), pH = 4 (—) and pH = 10 (—)

At pH = 1 less than 5% of the amino acid carboxylic group was dissociated so the particles-amphiphile interaction was assumed to be negligible. The chemical shift values relative to DL-phenylalanine carbons are reported next to each of them in the amino acid structure shown in Figure 2. 7; these were obtained from a database search and were relative to phenylalanine in solution. It should be noted that the chemical shifts observed for the solid sample were very close to the

solution data. In addition, the fact that the peaks were sharp suggested that no particle-amphiphile interaction was present. The spectrum for the solid sample prepared at pH 4 shows that the sharp peaks seen for the pH = 1 solution derived sample, and attributed to crystalline phenylalanine, are no longer present. The broadening of the carbonyl and α -carbon peaks indicates that the phenylalanine has a more amorphous structure. The spectrum of the basic solution derived sample shows sharp peaks for the aromatic and carbonyl sites, but peaks of the α - and β - carbons are broader. This implies a difference in the local environment of these sites, possibly a disordered distribution of environments or hindered mobility that could be an indication of an interaction between the titania and the phenylalanine amino group. Although titania is weakly paramagnetic ($\chi_{\text{mol}} = 74 \text{ m}^3 \text{ mol}^{-1}$), this is probably too weak an effect to cause the observed broadening. The changes in the α - and β - carbon peaks in basic conditions and the changes in the carbonyl and α -carbons peaks in acidic conditions confirm the interaction of the amino acid through the amino and the carboxylic group in basic and acid conditions respectively. This confirms the initially suggested capability of the amino acids of interacting with both positively and negatively charged particles extending, as a consequence, the pH operating range with respect to the amphiphiles commonly reported in the literature.

2.6.3 Investigation of the Particles Adsorption at the Different Interfaces

A fundamental aspect of foam formulation is understanding how the amino acid is distributed among the different interfaces. The presence of three phases (e.g. solid, liquid and gas) leads to three interfaces: solid-liquid, solid-gas and liquid-gas. The relative adsorption of the amphiphile on these interfaces affects the hydrophobic character of the modified particles [86]. It will be shown in Section 2.6.6 that, for several reasons, phenylalanine presents the best choice of amphiphile from

those studies in this work. It was therefore used as a representative example for the determination of the amphiphile adsorption at the different interfaces. In this work, attention was focused on firstly identifying the amount of amphiphile adsorbed at the particles surface (e.g. solid-liquid interface) and consequently determining the concentration of amino acid present as a free amphiphile in solution. Then, the amount of free amphiphile adsorbed at the liquid-gas interface was evaluated. The amount of amphiphile adsorbed at an interface can be described by an isotherm of adsorption which relates the amount of amphiphile adsorbed at the interface Γ to its bulk concentration c [87]. One of the most commonly used non-linear isotherms is that of *Langmuir* [88]:

$$\Gamma = \Gamma_{max} \frac{c}{c+a_L} \quad (2.6)$$

where a_L is the *Langmuir* constant [89] and Γ_{max} the maximum concentration of adsorbed amphiphile. The *Langmuir* isotherm is based on a lattice-type model with the assumptions that every adsorption site is equivalent (same energy of adsorption), that the probability for adsorption at an empty site is independent of the occupancy of neighbouring sites, that there are no interactions between the monomers and that no intermolecular forces act between the latter [90]. The adsorbed amount of amphiphile at the solid-liquid Γ_{SL} and gas-liquid Γ_{GL} interfaces could not be directly measured. First, the adsorption of amphiphile at the particles surface Γ_{SL} was determined by differential concentration determination of the amino acid in the supernatant of particulate suspensions, both before and after some equilibrating time as described in Section 2.5.6; Figure 2. 8 shows the experimental values fitted with the *Langmuir's* isotherm. The fitting parameters are reported in Table 2. 2. The increment of amphiphile adsorption to the solid-liquid interface Γ_{SL} with the increase in amphiphile concentration indicates the affinity of the amphiphile to the solid

surface. In Figure 2. 8 the typical plateau corresponding to the saturation of the solid-liquid interface cannot be observed since the solubility limit for the amino acid was reached before particle surface saturation.

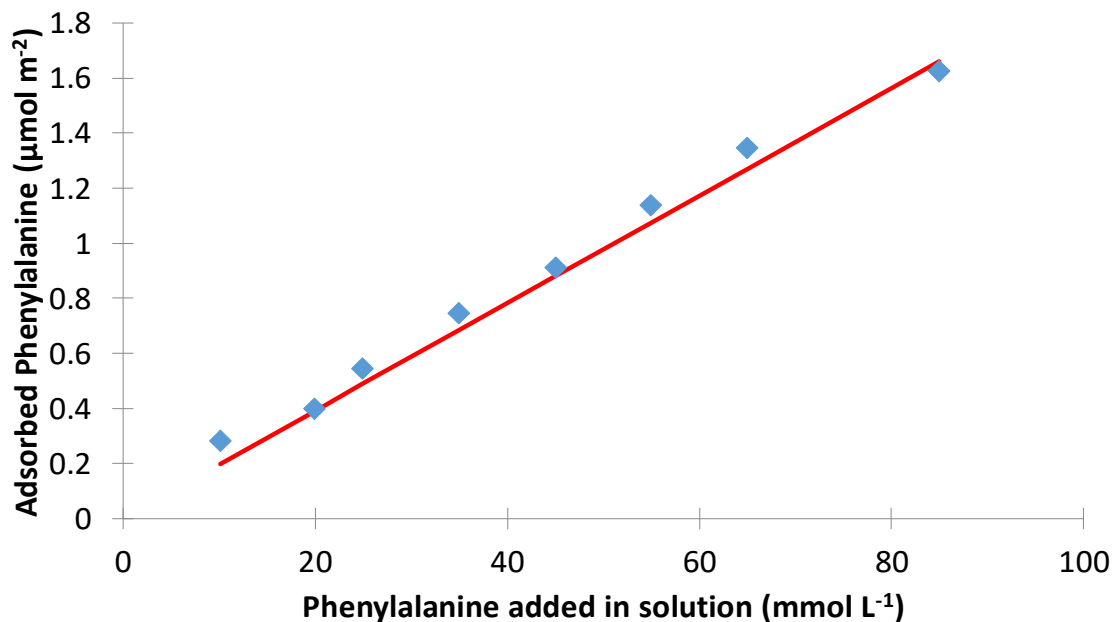


Figure 2. 8: Langmuir's isotherm for phenylalanine at the solid-liquid interface. Blue points represent experimental data while solid line represents the Langmuir's isotherm.

The adsorption at the gas-liquid interface Γ_{LG} was obtained from the surface tension γ of phenylalanine solutions, with different concentrations, using the *Langmuir-Szyszkowsky's* state equation [91] (2.7), which relates the equilibrium interfacial tension to the bulk amphiphile concentration c .

$$\gamma = \gamma_0 - RT\Gamma_{max} \ln \left(1 + \frac{c}{a_L} \right) \quad (2.7)$$

where γ_0 is the interfacial tension corresponding to the amino acid free interface and R and T are the gas constant and temperature respectively. The result, in Figure 2. 9, confirms that there is a progressive decrease in the surface tension with rising concentration of the amino acid. This

indicates the effective adsorption at the air liquid interface. From Figure 2. 9 it should be noted the absence of the plateau indicative of the critical micelle concentration (C.M.C.); this is due to the low solubility of phenylalanine at pH = 4.

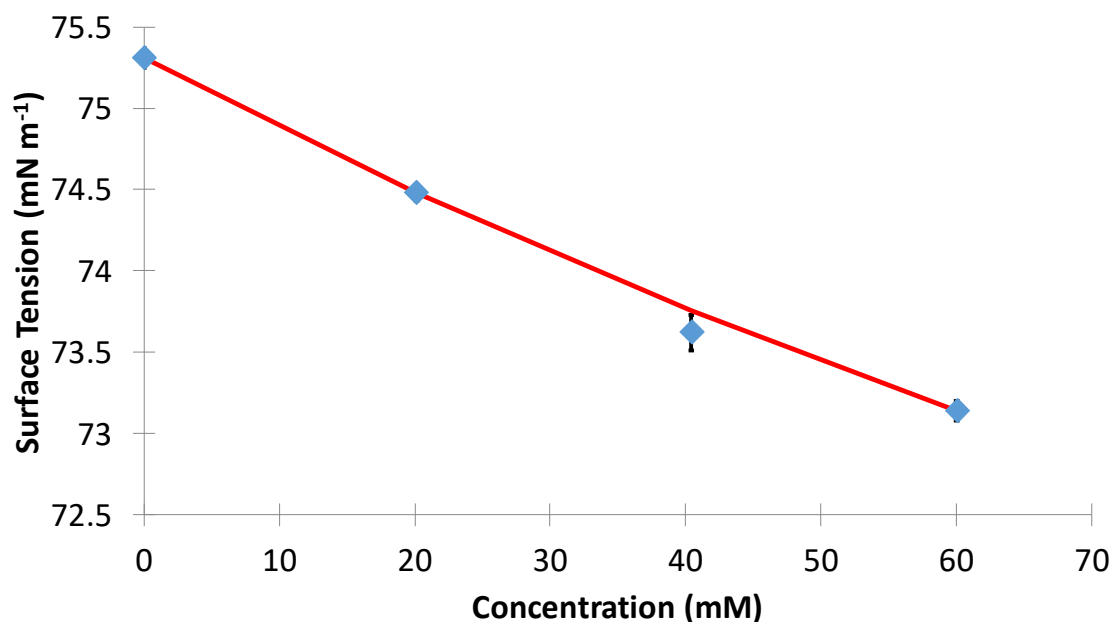


Figure 2. 9: Experimental (symbols) equilibrium values of the interfacial tension as a function of the amphiphile bulk concentration. Solid line represents the fitted Langmuir-Szyszkowski equation.

Fitting these data with the *Langmuir-Szyszkowski* equation allowed the values of Γ_{max} and a to be determined; these values are summarized in Table 2. 2. These were then substituted into the Langmuir isotherm equation for each amphiphile concentration giving the amount of amino acid adsorbed at the liquid-gas interface.

Table 2. 2: Values of maximum surface concentration Γ_{max} and parameter a for the different interfaces.

Solid-Liquid Interface		Gas-Liquid Interface	
Γ_{max} ($\mu\text{mol m}^{-2}$)	a_L (mol L^{-1})	Γ_{max} ($\mu\text{mol m}^{-2}$)	a_L (mol L^{-1})
4628	238	2.11	0.12

The surface concentration of the liquid-gas interface as a function of the bulk concentration of amphiphile as given by the Langmuir's isotherm is displayed in Figure 2. 10. The adsorption of the amphiphile increases monotonically with the bulk concentration but, again, surface saturation is not observed due to the low solubility of the amino acid. Comparing the isotherms at the two different interfaces it is possible to observe the preferential adsorption of the amphiphile on one interface or the other.

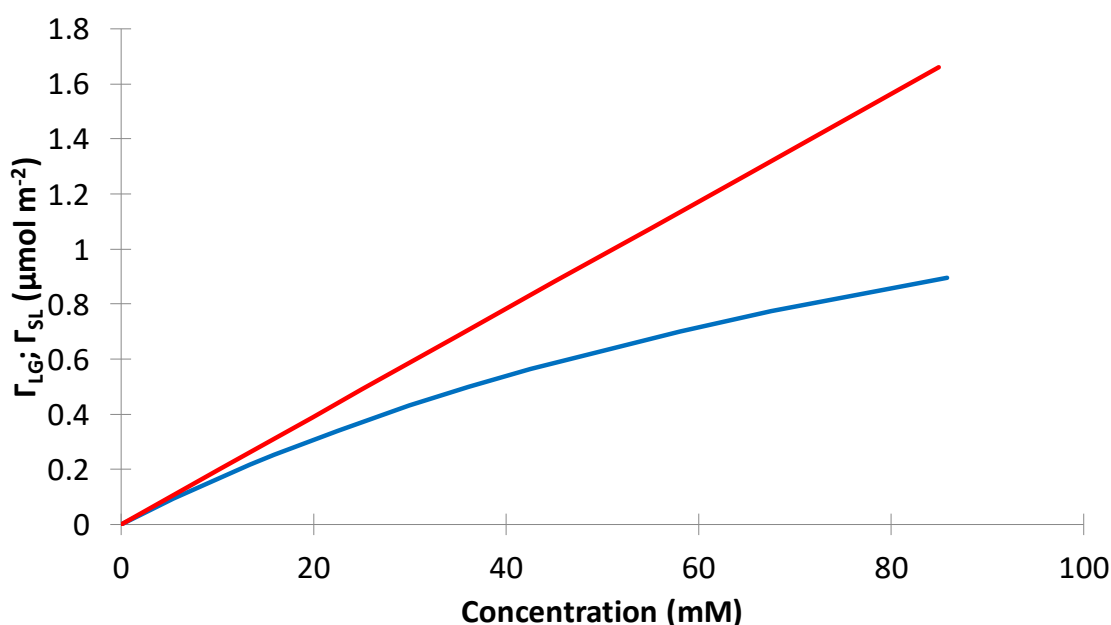


Figure 2. 10: Comparison of the DL-Phenylalanine isotherms at the Gas-Liquid (—) and Solid-Liquid (—) interfaces

At phenylalanine concentrations below 10 mM the amphiphile is equally distributed between the two interfaces while at higher concentrations the amino acid preferentially adsorbs at the solid-liquid interface with this trend becoming more and more pronounced as the concentration increases.

2.6.4 Determination of Amino Acids Hydrophobicity

In Section 2.6.1 it was hypothesized that the different maximum porosity observed in foams made using different amino acids as amphiphiles is due to their different hydrophobicity. Amino acids

hydrophobicity is usually classified in biological systems, where they are ranked based on the portion of internally and externally exposed fraction. In these scales, amino acids commonly found in the outer section of proteins are considered to be more hydrophilic and those commonly found in the inner part are considered to be more hydrophobic [92] [93]. Hydrophobicity scales for the free amino acids are present in the literature. The measurement of the surface tension of amino acid solution has been used to rank the amino acids based on their hydrophobicity [94]. *Bull et al.* showed that the gradient of the surface tension curve constitutes a hydrophobicity scale for the amino acids. Specifically, it was noted that the higher the gradient the higher the hydrophobicity. Although it was commented that expressing the hydrophobicity index in $\text{mN L m}^{-1} \text{ mmol}^{-1}$ is not an easy interpretation, this is not a concern for this study since the aim is to simply rank the amino acids based on their different hydrophobicity index (H.I.).

Surface tension measurements were carried out by the pendant drop method as described in Section 2.5.5. Figure 2. 11 shows a representative image of the shape of an amino acid solution drop analysed by the drop shape analysis software. The values of surface tension γ , shape factor β and drop volume are shown respectively on the left panel.



Figure 2. 11: Shape of an amino acid solution drop analysed by the shape analyser software

The surface tension of amino acid solutions with concentrations ranging from 0 to 1 M was measured; the results are presented in Figure 2. 12. The general trend of surface tension is a reduction in surface tension with increasing surfactant concentration. The surface tension maintains a constant value once the critical micelle concentration (C.M.C.) value is exceeded.

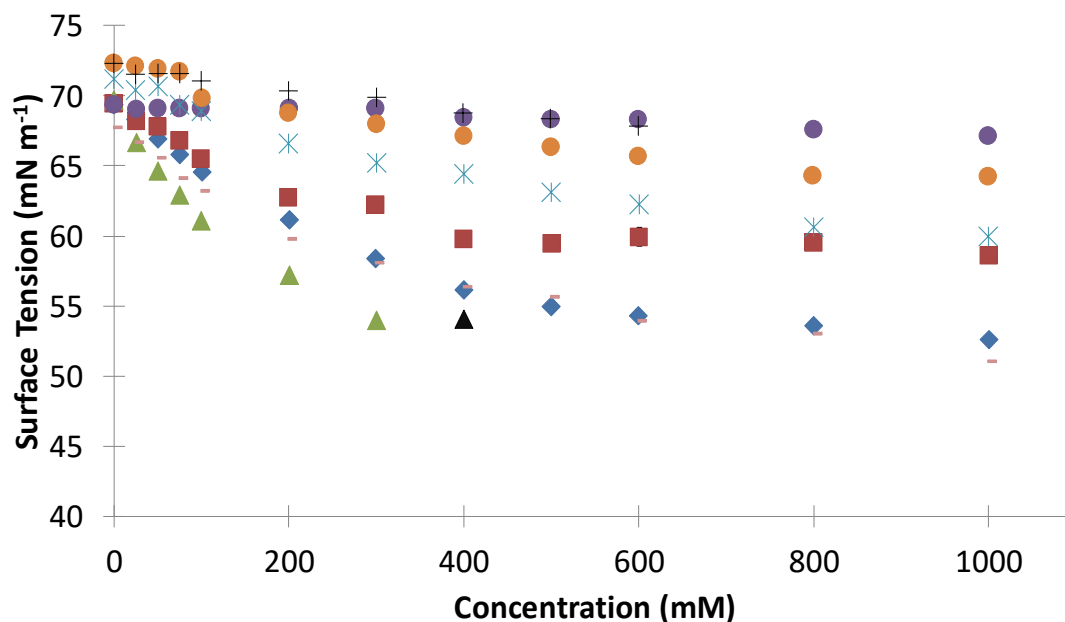


Figure 2. 12: Surface tension curves for amino acids solutions having different concentrations. (♦) Phenylalanine, (■) Tryptophan, (▲) Leucine, (●) Alanine, (*) Valine, (●) Methionine, (+) Tyrosine, (—) Isoleucine. The black point in the Leucine curve indicates that the solubility limit for the amino acid was reached.

The hydrophobicity index was established from the gradient of the linear section of the surface tension curve below the C.M.C.; Table 2. 3 compares the hydrophobicity scale measured in this work with that presented by *Bull et al.* [94].

Table 2. 3: Comparison between the amino acids hydrophobicity scale determined in this work and that proposed by Bull et al.


	Current Work	<i>Bull et al.</i>
	Leucine	Leucine
	Phenylalanine	Phenylalanine
	Isoleucine	Isoleucine
	Tryptophan	Tyrosine
	Valine	Tryptophan
	Methionine	Valine
	Tyrosine	Methionine
	Alanine	Alanine

Table 2. 3 shows that, with the sole exception of tyrosine, the two scales are in agreement. *Bull et al.* [94] used the differential capillary rise method, developed by *Jones and Ray* [95], to measure the amino acid solutions surface tension. The authors reported that great difficulty was encountered during the tyrosine surface tension measurement and that the slope value was subject to significant error; this could explain the observed difference in tyrosine position in the hydrophobicity scales.

2.6.5 Influence of Amino Acids Hydrophobicity on Foam Properties

The Hydrophobicity Indexes identified in the previous section were compared with the maximum foam porosities obtained when the different amino acids were used as amphiphiles. Table 2. 4 summarizes the H.I. and the maximum obtained porosity for the different amino acids.

Table 2. 4: Hydrophobicity Index and maximum foam porosity obtained for each amino acid.

**Due to the solubility limit of leucine it is not possible to state that the observed porosity corresponds to the maximum obtainable porosity.*

Amino Acid	Hydrophobicity Index (mN L m⁻¹ mmol⁻¹)	Porosity %
Leucine	0.84	81.52*
Phenylalanine	0.48	75.11
Isoleucine	0.40	73.01
Tryptophan	0.23	69.68
Valine	0.21	64.57
Methionine	0.12	63.58
Tyrosine	0.07	No Foaming
Alanine	0.02	No Foaming

Foaming was not observed for the titania materials under these conditions when tyrosine and alanine were used as amphiphiles. This may be due to the low hydrophobicity of the amino acids side chains that, in turn, were not capable of sufficiently reducing the hydrophilicity of titania particles. It has been shown in Figure 2. 6 and Figure 2. 12 that leucine reaches its solubility limit at a concentration of 400 mM. This concentration may not be sufficient to obtain the maximum particles' hydrophobization leading to uncertainty about the value of the maximum porosity. For this reason, the leucine point is not included in the maximum foam porosity as a function of the Hydrophobicity Index plot. It should be noted that there is a clear monotonic, possibly linear relationship between H.I. and maximum foam porosity ($R^2 = 0.90$) (Figure 2. 13).

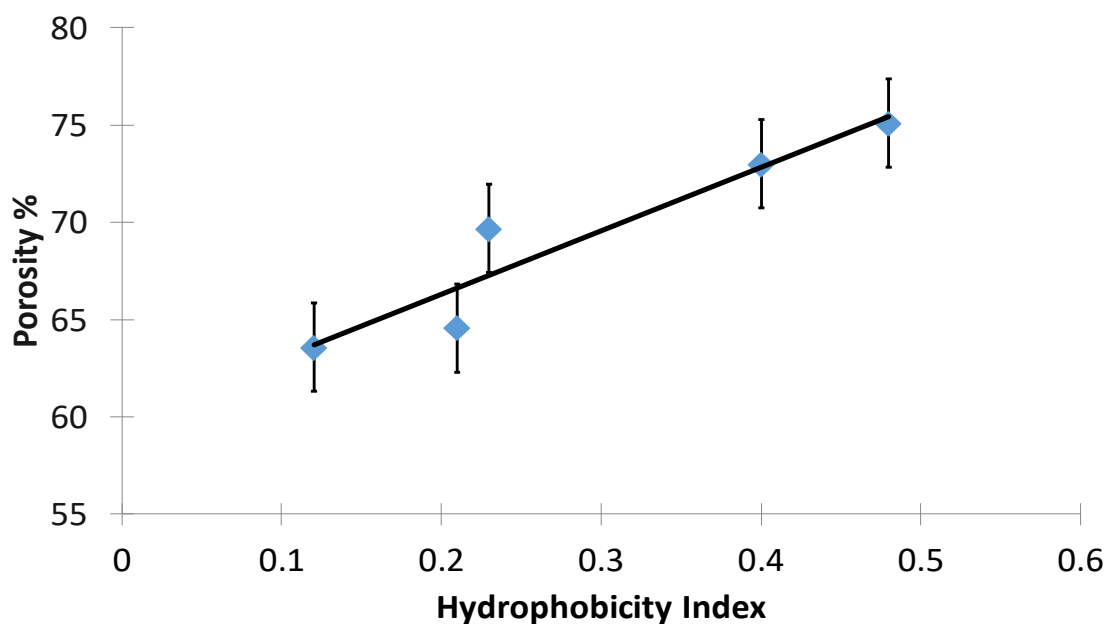


Figure 2. 13: Maximum foam porosity as a function of the amino acid hydrophobicity index

The effect of particle hydrophobicity on bubble size is extensively reported in the literature. In particular, *Gonzenbach et al.* showed that increasing the amphiphile concentration, and consequently the particle hydrophobicity, leads to a reduction in bubble size [75]. This was confirmed in the present study. Figure 2. 14 shows the bubble size distributions for titania foams obtained using phenylalanine concentration of 0.18 M and 0.24 M.

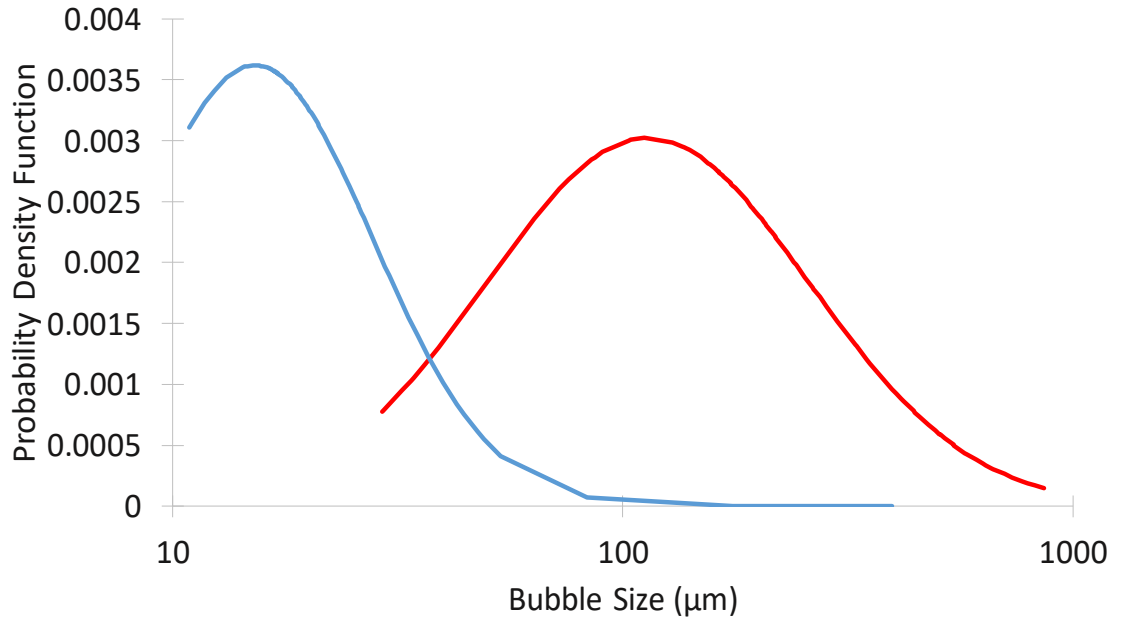


Figure 2. 14: Bubbles size distribution comparison of foam produced using different phenylalanine concentrations. 0.18 M (—), 0.24 M (—)

It can be observed from Figure 2. 14 that the distribution's mode shifts toward smaller bubble sizes when the amphiphile concentration is increased. In addition, the distribution narrows as the amphiphile concentration increases. This was determined by the calculation of the distribution span using the following equation [96]:

$$Span = \frac{D_{v0.9} - D_{v0.1}}{D_{v0.5}} \quad (2.8)$$

The span values are 2.58 and 1.50 for the distributions relative to foams obtained using an amphiphile concentration of 0.18 M and 0.24 M respectively; these values illustrate the narrowing of the distribution as the amphiphile concentration is increased.

The mean Sauter diameter (d_{32}) for the foams obtained using different amphiphiles and presenting the maximum porosity was determined using the following equation [97]:

$$d_{32} = \frac{\sum(n_i d_i^3)}{\sum(n_i d_i^2)} \quad (2.9)$$

Table 2. 5 presents the Hydrophobicity Index and the d_{32} values obtained for the different amino acids. As previously said, due to the limited solubility of leucine it was not possible to establish if the maximum particle hydrophobicity, and consequently the maximum porosity, was reached. For this reason, the mean Sauter diameter of foams using leucine as amphiphile was not determined.

Table 2. 5: Hydrophobicity Index and Sauter diameter obtained for each amino acid

Amino Acids	Hydrophobicity Index (mN L m⁻¹ mmol⁻¹)	d₃₂ (μm)
Phenylalanine	0.48	22
Isoleucine	0.40	286
Tryptophan	0.23	316
Valine	0.21	365
Methionine	0.12	381

It has been previously shown (Figure 2. 14) that an increase in particles hydrophobicity results in smaller bubble sizes. In that case the particles hydrophobicity was increased by augmenting the concentration of a given amphiphile. The same effect is expected when the particles hydrophobicity is changed varying the nature of the amphiphile; Table 2. 5 illustrates that the expected trend is followed. Figure 2. 15 plots the d_{32} values as a function of the amphiphile hydrophobicity index.

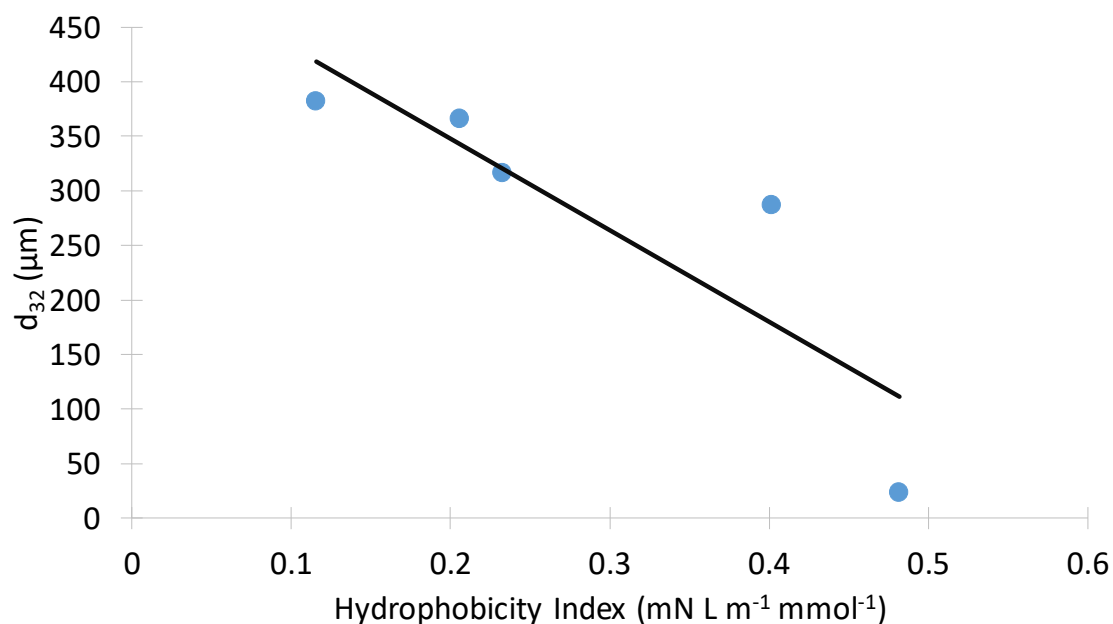


Figure 2. 15: Sauter diameter as a function of the amino acids hydrophobicity index

From Figure 2. 15 it can be seen that a monotonic relationship between mean bubble diameter and amphiphile hydrophobicity exists ($R^2 = 0.75$). These relationships confirm the role of particle hydrophobicity on foam properties and may allow a priori selection of the amino acid depending on the desired foam structure.

2.6.6 Determination of the Minimum Amphiphile Concentration

It has been shown in Section 2.5.1 that with the exception of DL-tyrosine and DL-alanine all the hydrophobic amino acids gave stable foams. The selection of the ideal amino acid, to be used as amphiphile, depends on its performances (e.g. possibility of obtaining a good range of porosities), solubility and price. In terms of performance, the amino acids that offer a wide porosity range are DL-leucine, DL-phenylalanine, DL-isoleucine and DL-tryptophan. The solubility and the cost of these amino acids are summarized in Table 2. 6.

Table 2. 6: Comparison of amino acids solubility and cost

Amino Acid	Solubility (g L⁻¹)	Cost (£/100 g)
Leucine	24.3	138.50
Phenylalanine	29.6	39.80
Isoleucine	41.2	154.50
Tryptophan	11.4	171.20

Both solubility and prices were obtained from the Sigma-Aldrich website (consulted on September 2016). The solubility values refer to solubility in water; these values were selected because, at industrial scale, foam production is unlikely to be carried out at such an acidic pH. In addition, the solubility rank is not expected to change with pH [98]. From Table 2. 6 it can be seen that phenylalanine is the amino acid that presents the lowest cost coupled with an acceptable solubility; for these reasons phenylalanine was selected as the model amphiphile to be used to gain a deeper insight into the foaming process. In particular, it was used to quantify the minimum amphiphile concentration necessary to observe the attachment of the modified particles at the air-water interface. This value was determined by surface tension measurement of 25%_{w/w} titania suspensions having different amino acid concentrations [99]. Figure 2. 16 shows the surface tension trend as a function of the DL-phenylalanine concentration.

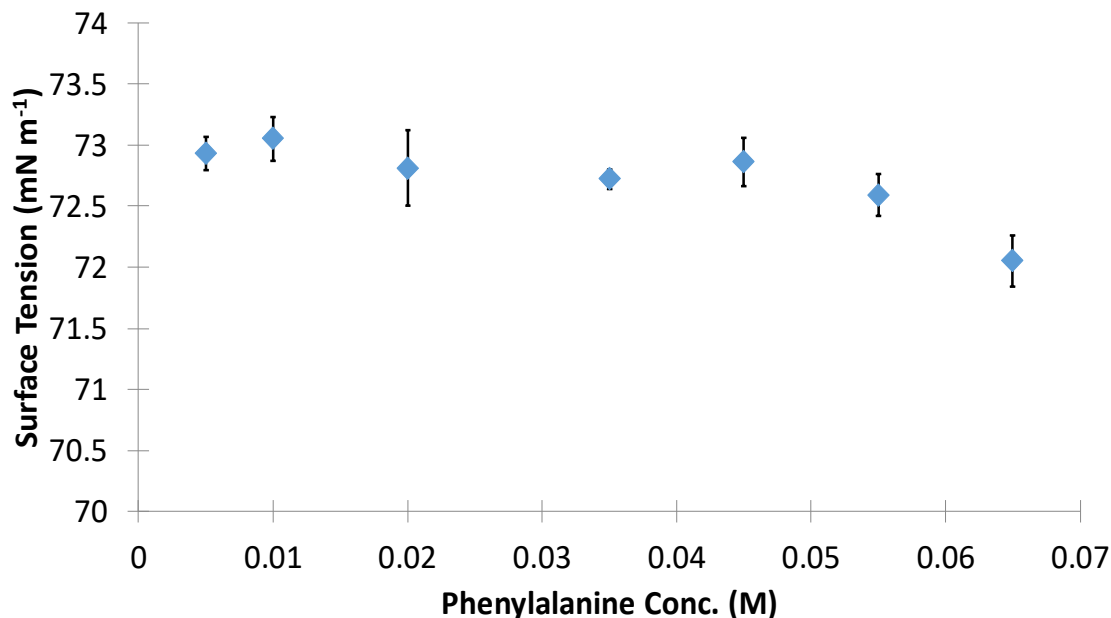


Figure 2. 16: Surface tension measurement of 25%_{w/w} titania suspension having different phenylalanine concentrations

The surface tension value is constant below a phenylalanine concentration somewhere in the range 0.045 to 0.055 M. After this point, the surface tension drops indicating that the modified particles start to attach at the air-water interface. The measurement of the surface tension of titania suspensions having phenylalanine concentrations higher than 0.065 M was not possible due to the formation of foams that prevented the formation of a drop. The equality of the surface tension values below 0.065 M was assessed by statistical analysis. The t-test for unequal variances populations was run on each pair of values [100]. The t-test was used to test the null hypothesis that the means of the two populations were equal. In order for the null hypothesis to be true, the tStat value has to lie between -tCrit and tCrit ($-t_{\text{Crit}} < t_{\text{Stat}} < t_{\text{Crit}}$); Table 2. 7 summarizes the tCrit and the tStat values for the tested surface tension pairs.

Table 2. 7: *t*Crit and *t*Stat values for surface tension pairs

Pair N°	Surface Tension Pairs (mN m ⁻¹)	<i>t</i> Crit	<i>t</i> Stat	Response
1	72.93 ± 0.14 (0.005 M) – 73.05 ± 0.18 (0.010 M)	2.31	-1.15	Equal
2	73.05 ± 0.18 (0.010 M) – 72.81 ± 0.31 (0.020 M)	2.45	1.49	Equal
3	72.81 ± 0.31 (0.020 M) – 72.72 ± 0.08 (0.035 M)	2.77	2.13	Equal
4	72.72 ± 0.08 (0.035 M) – 72.86 ± 0.20 (0.045 M)	2.57	-1.49	Equal
5	72.86 ± 0.20 (0.045 M) – 72.59 ± 0.17 (0.055 M)	2.31	2.35	Not Equal
6	72.59 ± 0.17 (0.055 M) – 72.05 ± 0.21 (0.065 M)	2.31	4.46	Not Equal
7	72.81 ± 0.31 (0.020 M) – 72.59 ± 0.17 (0.055 M)	2.45	1.41	Equal
8	72.81 ± 0.31 (0.020 M) – 72.05 ± 0.21 (0.065 M)	2.36	4.51	Not Equal

From Table 2. 7 it should be noted that pair N° 5 is the first one to present inequality between the two surface tension values but, from Figure 2. 16, it can be seen that the error bars for the surface tension values relative to a phenylalanine concentration of 0.02 M and 0.055 M overlap. For this reason, the t-test on these two values was carried out and from Table 2. 7 it can be observed that the difference between them is not significant. The surface tension for the 0.065 M suspension was compared to the surface tension values of both the 0.055 M and 0.02 M suspensions. In both cases, the difference between the two values was statistically significant indicating that a phenylalanine concentration of (0.060 ± 0.005) M is the minimum amount that has to be added to have attachment of the modified particles at the air-water interface. It has to be borne in mind that this concentration value is specific to the tested amino acid and operating conditions used. This value is affected by both the pH of the ceramic suspension, due to the different pKa values of the amino acids, and by the different hydrophobicity of the amino acids side chains.

2.7 Conclusion

In this chapter the use of hydrophobic α -amino acids as amphiphiles in the direct foaming technique has been illustrated. This class of amphiphile is more environmentally benign than those conventionally used and allows a wider pH operational window. It has been demonstrated that the amino acids adsorb at the particles' surface by either the carboxylic or amino group in acidic and

basic conditions respectively. In addition, the partition of a model amino acid (e.g. phenylalanine) between the solid-liquid and gas-liquid interfaces has been determined giving an insight into the distribution of the amino acid among the different interfaces. The tested amino acids have been classified accordingly to the hydrophobicity of their side chain. The amphiphile hydrophobicity index has been related to both the maximum porosity and the bubble size distribution of foams obtained when they are used as amphiphiles. Monotonic relationships have been observed in both cases with the possibility of a linear relationship in the case of porosity. These give a deeper insight into the role of amphiphile structure on the foam properties offering the possibility of tailoring them. Of the tested amino acids, DL-phenylalanine has been identified as the most suitable to be used due to its acceptable solubility and relatively low cost. For this amino acid, the minimum amphiphile concentration necessary to develop stable foams has been identified, however this value is specific to the tested amino acid since it depends on both pH and amino acid hydrophobicity. Although the effects of different formulations on the foam properties have been largely discussed and understood in this chapter, the structure of foamed materials is also affected by their manufacturing and processing. In the next chapter a deep study of the process parameters affecting the foam structural characteristics is reported in order to have a comprehensive understanding on how to tailor the structure of ceramic foam by controlling both their formulation and manufacturing process.

Chapter 3

Manufacturability of Ceramic Foams

3.1 Introduction

The formulation of ceramic foams and its consequent effects on their structure has been largely investigated in the literature and as part of this work; the same is not true for their manufacturing process and its effect on foams structure. In the literature, it is usually reported the use of a kitchen mixer [52] [75] [101] as a medium for the mechanical frothing of the initial ceramic slurry exposing evident limitations of process control and scale-up. Although different methods such as chemical decomposition [102] to generate gas and the use of pressurized vessels [103] or specific apparatus [104] for the entrainment of the gas in the ceramic slurry have been investigated, to the author's knowledge, a detailed study of the process parameters affecting the foam structure has not been conducted. In this chapter, a statistical approach is used to determine the relevant process parameters that affect the foam structure. In particular, an aerated stirred vessel was used to generate the foam and its properties (e.g. porosity, bubble size distribution and rheology) were measured giving an insight into the different mixing conditions to be used in order to obtain the desired foam. In the following sub-chapters, the reader is introduced to the basic aspects of mixing in a stirred vessel with a focus on the case of an aerated stirred vessel followed by an introduction to fluid rheology. Finally, the experimental system is described and the experimental results presented.

3.2 Stirred Vessel

3.2.1 Configuration of a Stirred Vessel

Mechanically agitated vessels are commonly used in the process industry with the general purpose of reducing inhomogeneity in order to achieve the desired process results [105] such as reduction

of solid non-uniformity in solid-liquid systems. A typical configuration for a stirred vessel is shown in Figure 3. 1 where T is the tank diameter, D is the impeller diameter, W is the impeller width, H is the filling level and C is the impeller clearance from the bottom.

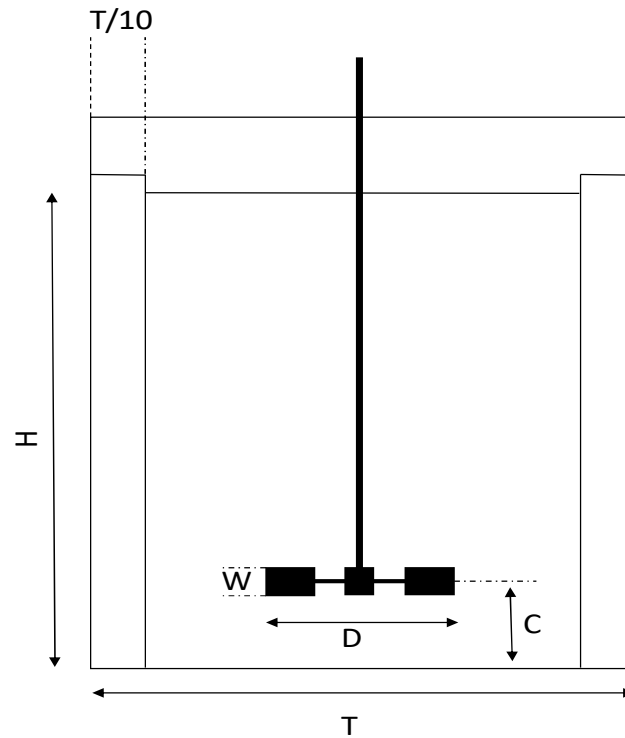


Figure 3. 1: Characteristic dimensions of a cylindrical stirred vessel

The guidelines for the stirred vessel sizing are usually: D/T should be between 0.3 and 0.5; this is recommended since impellers that are too small will not generate enough fluid movement while impellers that are too large will require much more power becoming less efficient. The H/T ratio should be around 1 for single impeller systems while the C/T is recommended to be around 0.20-0.25. The baffle width is usually $1/10$ of the tank diameter with four flat vertical baffles spread every 90° ; these are commonly used to disrupt the gross rotation of the fluid in the azimuthal direction.

3.2.2 Flow Patterns in Stirred Vessel

The flow patterns of a single-phase liquid in tanks agitated by different types of impellers have been extensively studied in the literature [106] [107] [108] [109]; the typical experimental techniques include the use of liquid tracer. The determination of the flow pattern inside the vessel is useful to establish the presence of “dead zones” which reduce the quality of the mixing; the typical flow patterns for a propeller (axial) and a disk turbine (radial) are represented in Figure 3.2 respectively.

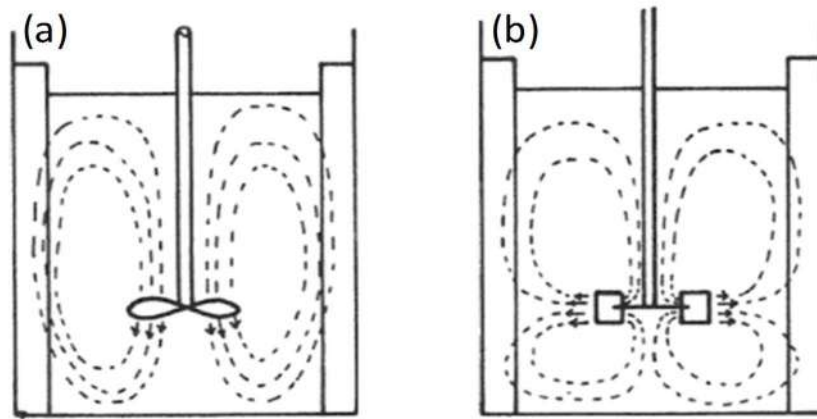


Figure 3.2: Typical flow patterns generated by an axial (a) and a radial impeller (b) [110]

The propeller generates an axial flow through the impeller and this may be upward or downward depending on the inclination of the blades [111] [112]; Figure 3.2 shows the pattern for a down-pumping impeller. Contrarily, the flat-bladed turbine produces a radial flow creating circulation zones at the top and bottom of the tank. Axial impellers are commonly used in solid dispersion due to their high pumping efficiency while radial impellers are used for gas dispersion due to a higher shear characteristic. The effects of different stirred vessel dimensions on the flow pattern has been largely investigated in the literature. *Jaworski et al.* [113], *Kresta et al.* [114] and *Amannullah et al.* [115] reported that a higher impeller position ($T/2$) can generate a larger fluid motion volume

in the mixing of high viscosity fluids. On the other side, *Nienow* [116], *Armenante et al.* [117] and *Montante et al.* [118] demonstrated that a lower impeller position is beneficial in the solid-liquid dispersion when a turbine impeller is used. Impeller geometrical parameters (e.g. impeller diameter, blade width and thickness) also have a significant impact on the fluid mixing; *Rutherford et al.* [119] showed that higher turbulence levels and lower mixing times were obtained when a thinner impeller was used while *Ameur et al.* [120] reported that an increase in blade size is beneficial to the enlargement of the well stirred region although this results in an increased power consumption due to the short distance between the impeller and the tank walls; this limits the flow around the agitator.

3.2.3 Power Input in Stirred Vessels

Consider a Newtonian liquid having density ρ and viscosity μ which is agitated by an impeller of diameter D and width W at a rotational speed N . The liquid is contained in a tank of diameter T and the liquid depth is H . The power requirement of the impeller P represents the rate of energy dissipation within the liquid and it depends upon the before-mentioned independent variables. The power requirement can be expressed as a function of a series of non-dimensional numbers as reported below [121]:

$$\frac{P}{\rho N^3 D^5} = fn \left\{ \frac{\rho N^2}{\mu}, \frac{N^2 D}{g}, \frac{T}{D}, \frac{W}{D}, \frac{H}{D}, etc. \right\} \quad (3.1)$$

where $P/\rho N^3 D^5$ is the power number P_0 , $\rho N D^2/\mu$ is the impeller Reynolds number Re and $N^2 D/g$ is the Froude number Fr . Fr is important only when gross vortexing exists, this is not the case if Re is less than approximately 300 and if baffles are used for $Re > 300$; in this case the power number only depends on the Re number and the geometrical ratio. The P_0 dependence on Re

number is usually plotted on a log-log graph giving the power curve for the system; Figure 3. 3 shows a typical power curve.

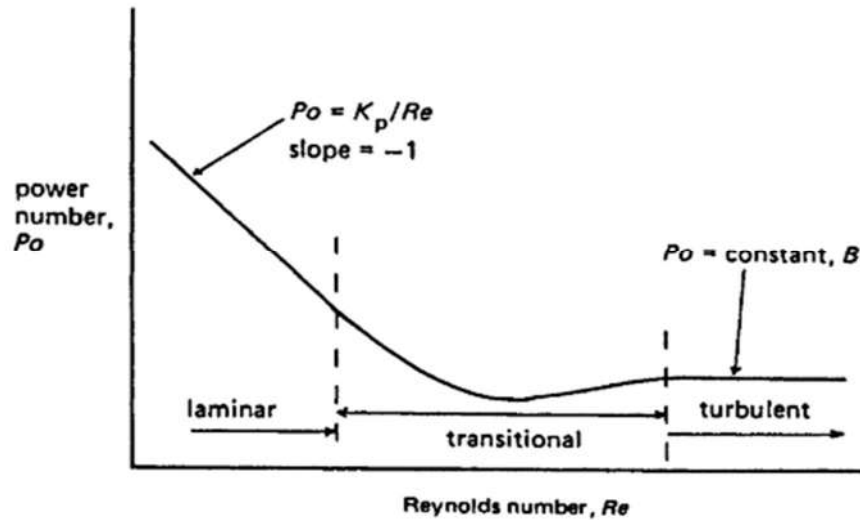


Figure 3. 3: Typical Power Curve [121]

From Figure 3. 3 it can be noted that in laminar regime ($Re < 10$) the slope of the curve is -1 and the following dependence exists:

$$P_0 = K_P / Re \quad (3.2)$$

where K_P is a constant depending only upon the system geometry; in this region the mixing is slow and only due to the velocity distribution in the vessel since the turbulence dispersion is absent. At high Reynolds numbers ($Re > 10000$) the flow is turbulent with rapid mixing due to the motion of turbulent eddies; in this region the power number assumes a constant value. In between the laminar and turbulent region, a transition zone exists in which no simple mathematical relationship between the power number and Re exists.

Metzner and Otto [122] showed that, in the case of non-Newtonian liquids, a simple relationship between Newtonian and non-Newtonian power consumption exists in the laminar regime. This is

based on the assumption that there is an average shear rate for a mixer which is directly proportional to the impeller speed:

$$\dot{\gamma}_A = k_s N \quad (3.3)$$

where k_s is the mixer shear rate constant. *Metzner and Otto* demonstrated that its value is relatively constant for a range of impeller speeds and fluid properties so an average value can be used for the calculation of the average shear rate. Using both an experimentally determined viscosity curve and the calculated average shear rate it is possible to obtain an apparent viscosity value; this can be used for the calculation of the Reynolds number and it can be directly used in the Newtonian power number-Reynolds number correlation.

3.3 Aerated Stirred Vessel

3.3.1 Configuration of an Aerated Stirred Vessel

This chapter is focused on the description of an aerated stirred vessel used for gas-liquid mixing but it is important to point out that this is not the only option. Some of the alternatives include bubble columns in which the gas is sparged into the liquid from the bottom of the vessel, static mixers in which the mixing energy derives directly for the fluid motion [123] [124] and plunging jets in which the gas is entrained into the liquid through a liquid jet [125]. Figure 3. 4 shows the schematic of an aerated stirred vessel.

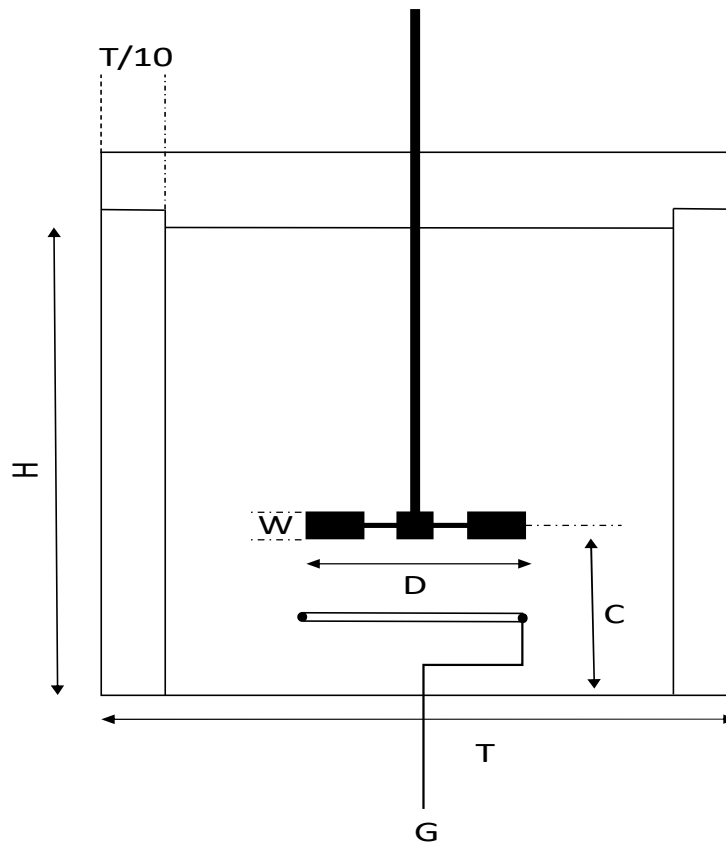


Figure 3. 4: Aerated Stirred Vessel

In the vessel depicted in Figure 3. 4 a gas sparger is posed underneath the impeller; this plays a key role in the gas dispersion. A Rushton disk turbine is traditionally used but hydrodynamic studies carried out by *Bruijn et al.* [126] and *van't Riet* [127] showed that agitators with concave blades rather than flat give flatter power curves (e.g. Scaba SRGT impeller [128]); up-flow pitch-blade impellers are also used since they present flat power characteristics. Self-inducing agitators are sometimes used [129]; these eliminate the need for recycle compressors but they are not very flexible since the rate of entrained gas depends on the impeller speed.

A typical configuration for a cylindrical aerated stirred vessel includes the use of four full baffles of width $T/10$, the sparging ring is placed below and nearer than $D/2$ to the agitator and the height of the dispersion, as in the case of a simple stirred vessel, should be $H = T$. Recommended agitators

are disk turbines with 18 flat blades or six concave blades having a diameter D comprised between $T/4$ and $T/2$ and mounted at a distance $C = T/4$ to $T/3$ from the vessel bottom [121].

3.3.2 Power Consumption in Aerated Stirred Vessel

In an aerated stirred vessel, the power absorbed by the gas-liquid system P_g is lower in respect to a simple stirred vessel due to the formation of gas cavities behind the impeller blades. This effect can be reduced using either concave blade impellers (e.g. Scaba SRGT) or up-pumping pitch blade impellers; Figure 3. 5 shows P_g/P as a function of the gas flow rate Q_g showing that concave blade impellers and up-flow pitch blade impellers present a flatter power profile.

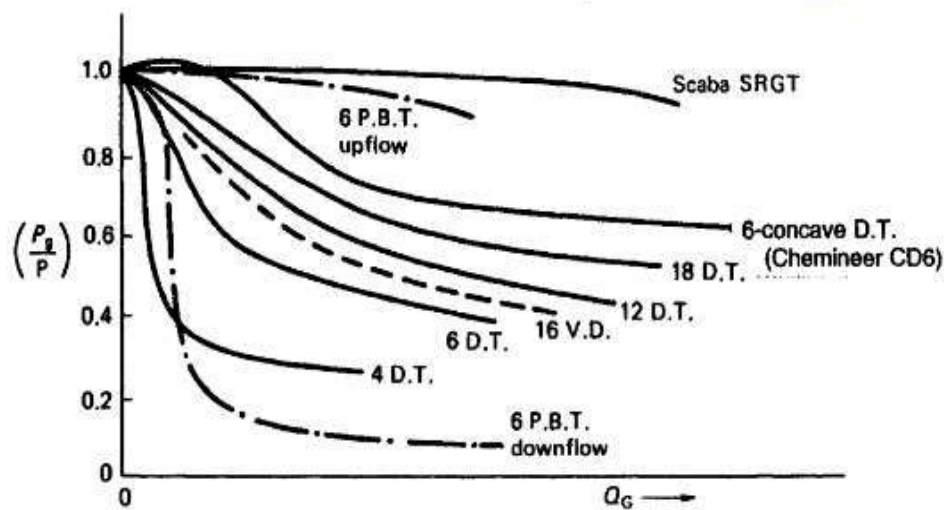


Figure 3. 5: Power curves for gassed agitators (D.T. = Disc Turbine, V.D. = Vaned Disc, P.B.T. = Pitch Blade Turbine) [110]

Several researchers attempted to correlate P_g to the system variables; *Calderbank* [130], *Michel and Miller* [131] and *Pharamond et al.* [132] derived empirical relations but these do not take into account the fluid mechanics in the impeller region and, for this reason, they are not recommended for use. *Greaves and Kobbacy* [133] produced empirical correlations that account for the different flow regimes and coalescence classifications but these were derived at very small scale and with a

limited range of configurations. *Nienow et al.* [134] correlated the P_g/P ratio to the different flow patterns obtained when the impeller speed N is increased and the gas flow rate Q_g is kept constant; Figure 3. 6 shows the different flow patterns presented.

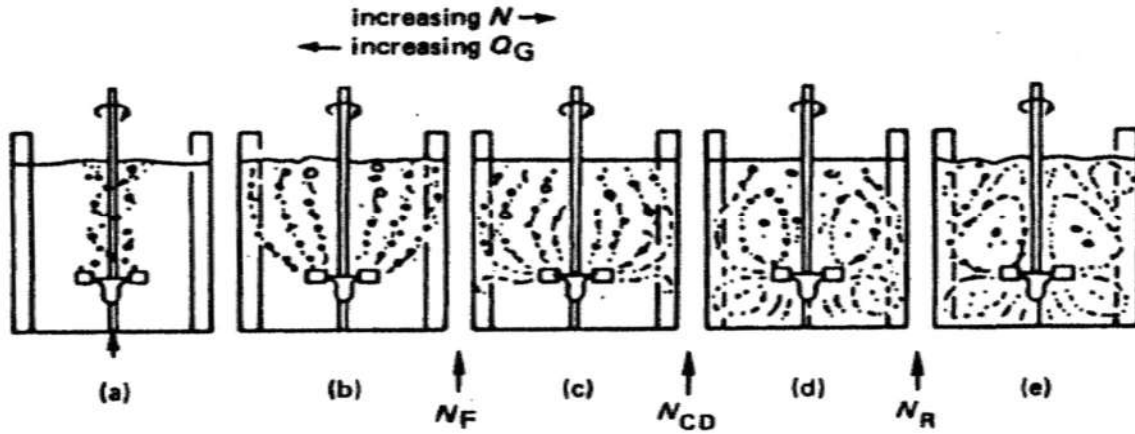


Figure 3. 6: Regimes of bubble flow: (a) and (b) flooded impeller, (c) loaded impeller, (d) complete gas dispersion, (e) gross recirculation of gas [134]

At low N (a and b) the gas passes through the agitator without dispersion and the liquid flows around the outer part of the blades; in this case the impeller is said to be flooded. As the impeller speed is increased beyond N_F the gas is captured by the vortex behind the blades and the impeller is said to be loaded; in this situation, the gas is dispersed and P_g decreases due to the formation of larger cavities. A further increase in N causes the cavities to change into “vortex” cavities. N_{CD} is the impeller speed at which the gas becomes completely dispersed in the whole vessel while at N_R gross recirculation of gas into the agitator sets in. The P_g/P trend at the different flow regimes is graphically represented in Figure 3. 7; the graph plots the gassed/un-gassed power ratio as a function of the gas flow number that is defined as follow:

$$F_{lG} = \frac{Q_g}{ND^3} \quad (3.4)$$

where Q_g is the gas flow rate, N is the impeller speed and D is the impeller diameter. The graph shows the change in the P_g/P ratio at different agitator speed; the trend can be explained by the occurrence of the flow regimes previously described at the different impeller speeds.

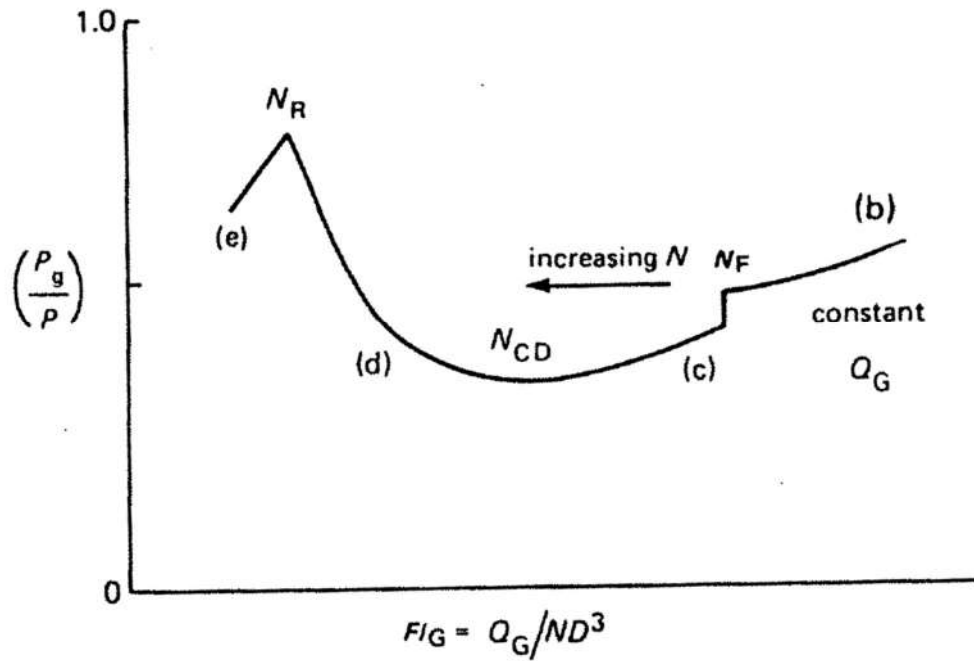


Figure 3. 7: Power curves at constant gas rate for Rushton turbines [134]

Smith *et al.* [135] produced a flow regime map for six blade disc turbine (Figure 3. 8); this uses the Froude and gas flow numbers to divide the operation spectra into areas in which the different flow regimes occur.

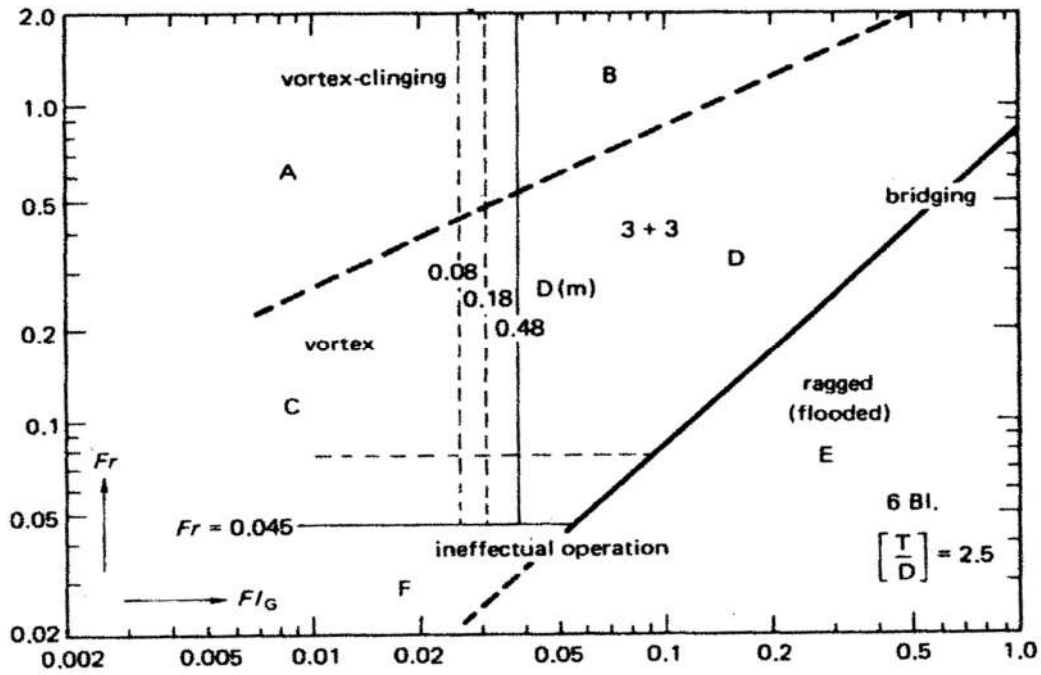


Figure 3. 8: Disk turbine regime map [135]

In the flow regime map can be noted, for example, that at high flow gas number and low Froude number the system is in a flooded regime; this map gives useful indications about the mixing regimes occurring in the aerated stirred mixer at different operative conditions. Similar maps have been produced for different impellers, for example, *Warmoeskerken et al.* [136] produced it for a six-blade concave turbine while *Nienow et al.* [134] derived one for multiple impellers.

3.3.3 Gas Hold-Up Correlations

Gas hold-up ε_g directly affects the mass transfer in gas-liquid systems and for this reason it has been extensively reported in the literature. Most early studies were conducted on small tanks and they show a significant divergence from the actual gas-hold up in larger stirred tanks [137]. Several correlations have been proposed. *Greaves and Barigou* [138] studied gas hold-up in large vessels (1 to 2.7 m) equipped with six blade disc turbines proposing the following correlation:

$$\varepsilon_g = 4.07(N)^{0.62}(Q_g)^{0.64}(D/T)^{1.39} \quad (3.5)$$

They observed that there is a wide divergence in prediction for different system configurations and operating conditions; they attributed this lack of agreement to the exclusion of dependence of the gas hold-up on the different flow regimes that could occur under different operating or geometric conditions.

Smith [139] used a similar system to *Greaves and Barigou* to predict the gas hold-up correlation; also in this case the extent of gas dispersion was attributed to the different flow regimes. The correlation suggested by *Smith* is illustrated below:

$$\varepsilon_g = 0.85(ReFrF_{lg})^{0.35}(D/T)^{1.39} \quad (3.6)$$

Smith proposed that, with the exception of small tanks ($T < 0.44$ m), gas hold-up can be predicted by the use of non-dimensional numbers.

Rewatkar et al. [140], in addition to the use of large vessels and six bladed pitched down-flow turbines, investigated the effects of different sparger types and positions on the gas hold-up proposing the following correlation:

$$\varepsilon_g = 3.54(D/T)^{2.08}(Fr)^{0.51}(F_{lg})^{0.43} \quad (3.7)$$

Despite the number of available correlations one of the most frequently used is the one based on the power dissipated approach:

$$\varepsilon_g \propto (P_g/V_L)^A v_s^B \quad (3.8)$$

where V_L is the liquid volume and v_s is the superficial gas velocity. Values of A and B range from 0.2 to 0.7 with the tendency for A to be higher for non-coalescing systems (e.g. solutions of electrolytes) compared to coalescing (e.g. pure liquids). *Whitton and Nienow* [141] proposed A and B values of 0.26 and 0.66 respectively while *Yawalkar et al.* [142] proposed values of 0.25 and 0.41 respectively. It is important to consider that the gas hold-up can be very different in real systems with respect to the case of pure liquids. In addition, bubble diameter may change due to adsorption, desorption and evaporation meaning that these correlations are not universally applicable. However, since ε_g is controlled by bubble size and the amount of recirculating gas which are function of (P_g/V) and v_s the basic form of (3.8) seems reasonable [121].

3.3.4 Bubble Size in Aerated Stirred Vessels

Different models to correlate the bubble size to the process variables have been suggested. *Kolmogoroff* proposed that the eddies in the turbulent flow give rise to different stresses depending on their size relative to the *Kolmogoroff* scale λ_k . The *Kolmogoroff* scale is expressed by:

$$\lambda_k = \left(\frac{\nu^3}{\varepsilon} \right)^{1/4} \quad (3.9)$$

where ν is the kinematic viscosity of the continuous phase and ε is the average dissipation usually

expressed as $\varepsilon = \frac{P}{V\rho}$ [143] [144] [145].

The turbulent eddies will give rise to different stresses depending on their size relative to the *Kolmogoroff* scale. Drop breakage will occur if the pressure across drop exceeds the pressure due to surface tension holding the drop together [146] (turbulent inertial break-up) and, for eddies sizes $\lambda \gg \lambda_k$, the following relationship is valid:

$$(d_d)_{max} = c \left(\frac{\sigma}{\rho_c} \right)^{0.6} \varepsilon^{-0.4} \quad (3.10)$$

where c is a constant, σ is the interfacial tension, ρ_c is the density of the continuous phase and ε is the mean energy dissipation rate. The equation above (3.10) can also be expressed in the form of dimensionless groups:

$$d_{32}/D = AWe^{-0.6} \quad (3.11)$$

where A in this case is $A = CP_0^{-0.4}$. The Weber number (We) is used for analysing the fluid flow when there is an interface between two different fluids with strongly curved surfaces and it is a measure of the relative importance of the fluid's inertia compared to its surface tension [147]; the Weber number in agitated vessel is expressed as:

$$We = \frac{\rho_c N^2 D^3}{\sigma} \quad (3.12)$$

where ρ_c is the density of the continuous phase, N is the impeller speed, D is the impeller diameter and σ is the interfacial tension. This theory was originally employed by *Hinze* for dilute liquid/liquid systems [148] and was later adopted for gas/liquid systems [149].

It is important to outline that, for bubbles smaller than λ_k , viscosity also has an effect on the fluctuating eddy velocity and the following relationship for the turbulent viscous break-up has been proposed by *Spro* [150]:

$$\frac{d_{max}(\mu_c \varepsilon \rho_c)^{1/2}}{\sigma f\left(\frac{\mu_d}{\mu_c}\right)} = const. \quad (3.13)$$

Correlations (3.10) and (3.11) satisfactorily correlate the effect of surface tension and agitation conditions on bubble/drop size in the case of liquid-liquid systems while discrepancies are observed

in the case of gas-liquid systems [151]. Acceptable correlations were obtained in gas-liquid systems where bubble coalescence was reduced (e.g. protein solutions) but, in every case, very different values of, both the correlating coefficient and the exponent, were required in order to predict the correct value of the mean bubble size [152] [153]. It has been suggested by *Machon et al.* [149] and *Nienow et al.* [154] that the different relationships are due to the fact that the Weber number only relates to bubble breakage while, in gas-liquid systems, bubble size is determined by a balance between breakage and coalescence. It is evident that, reducing the contribution of coalescence in the gas-liquid systems, leads to better predictions of the bubble size when the relationships (3.10) and (3.11) are used.

3.4 Rheology

3.4.1 Introduction

Rheology measurements find wide application in the process industry (e.g. food, polymer, catalysis) and, for this reason, it is not surprising that the structural properties of foams have been investigated by rheological measurements. Chapter 3.10 reports that wet ceramic foams present complex rheological behaviour and, for this reason, an introduction on the different rheological behaviours is given. Particular emphasis will be given to non-Newtonian fluids and the apparatus used to carry out rheological measurements will be briefly described.

3.4.2 Rheology Models

Fluids can be classified, according to their different flowing properties, into Newtonian and non-Newtonian. The latter have been classified, depending on the relationship between fluid viscosity and shear rate, into three groups: shear-thinning or pseudoplastic, shear-thickening or dilatant and

viscoelastic fluids; the latter include Bingham and Hershel-Bulkley fluids [105]. Figure 3. 9 depicts the different flow behaviour of fluids.

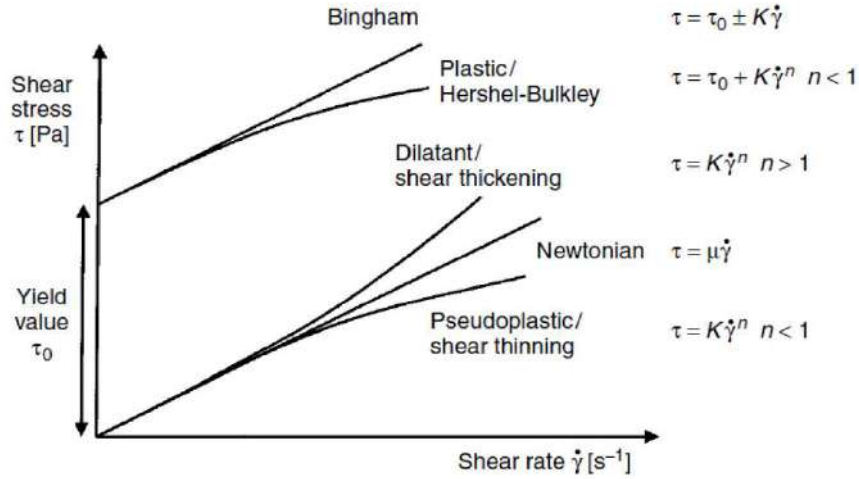


Figure 3. 9: Summary of fluids flow behaviour [105]

A description of the different flow behaviours is given below:

- **Newtonian.** Newtonian fluids obey Newton's law which is:

$$\tau = \mu \dot{\gamma} \quad (3.14)$$

where τ is the shear stress, μ is the viscosity and $\dot{\gamma}$ is the shear rate. In (3.14) the viscosity is assumed to be constant and independent of the shear rate. Although their viscosity is deformation rate or time independent, it varies with temperature and pressure. In addition, these fluids do not present any elastic properties or extensional anomalies; examples of Newtonian fluids are water, mineral oils and molasses [155].

- **Shear Thinning or Pseudoplastic.** Shear thinning fluids present a decrease in viscosity when the shear rate is increased from low to high levels; their behaviour can be described by different constitutive laws but power law is commonly used:

$$\tau = k\dot{\gamma}^{n_{FB}} \quad (3.15)$$

where τ is the shear stress, k is the fluid consistency index, $\dot{\gamma}$ is the shear rate and n_{FB} is the flow behaviour index; this assumes values less than 1 for shear thinning fluids. Materials that present this kind of behaviour are usually characterised by more than one phase, e.g. particles of irregular shape or droplets of one liquid dispersed in another. At rest, these materials maintain an irregular internal order and are characterized by an internal resistance against flow. As the shear rate is increased, the irregularly shaped particles can orientate in the direction of the flow or entangled polymeric chains can disentangle, stretch and eventually orientate themselves resulting in a viscosity reduction. For most fluids, this behaviour is reversible and, after a certain time-lag, they regain their high viscosity when the high shear is reduced or terminated [156].

- **Shear Thickening or Dilatant.** Shear thickening materials present an increase in viscosity as the shear rate is increased. As in the case of shear thinning fluids, their behaviour can be described by the power law (3.15) but, in this case, the flow behaviour index is greater than 1. Dilatant fluids are not common, and this behaviour is found, for example, in highly concentrated suspensions in which solid particles are mixed with liquids such as plasticizers to form plastisols. At low shear rate, the plasticizers act as a lubricant allowing an easy positional change of the particles [156]. At higher shear rates, particles will wedge others apart causing a volume increase and a consequent viscosity increase.
- **Viscoelastic.** These fluids are characterized by the presence of a yield-point. For shear stresses below the yield point, the inter-particle forces (e.g. polar forces, van der Waals forces, etc.) that build up in these materials are strong enough to prevent the positional

change of element of fluids giving them a solid character with an infinite viscosity. For shear stresses above the yield point, the outside forces are strong enough to overcome the network forces and the “solid” turns into a flowing fluid. These materials can be described by the following equation:

$$\tau = \tau_y + k\dot{\gamma}^n \quad (3.16)$$

where τ_y is the yield stress, k is the fluid consistency index and n is the flow behaviour index. Fluids are called Bingham fluids if $n = 1$, these present a Newtonian behaviour once the yield stress has been overcome while fluids for which $n < 1$ are called Herschel-Bulkley and present a pseudoplastic behaviour above the yield stress.

In Section 3.10 it will be shown that ceramic foams present a viscoelastic behaviour so a brief description on how to measure these properties will be given. Viscoelasticity can be investigated using an amplitude sweep test where the amplitude of the deformation (or shear stress) is varied while the frequency is kept constant. Purely elastic materials, can be described by a spring (Figure 3. 10-a) and their response to an oscillating strain can be expressed by the following stress function:

$$\tau = G\gamma_0 \sin(\omega t) \quad (3.17)$$

where τ is the shear stress, G is the elastic modulus, γ_0 is the maximum strain exerted on the spring, ω is the angular velocity and t is the time. In the case of elastic fluids, strain and stress are in-phase with each other with the strain and stress presenting their maximum at the same time. Purely viscous materials (Figure 3. 10-b), can be described by a dashpot and their response to an oscillating strain can be described by:

$$\tau = \eta\omega\gamma_0\cos(\omega t) \quad (3.18)$$

In this case the dashpot response of τ is 90° out of phase to the strain; whenever the strain in a dashpot is at its maximum the rate of change of the strain is zero. In a visco-elastic fluid, the phase shift angle δ between strain and stress is within the limits of $0 < \delta < 90^\circ$. Visco-elastic fluids can be described by the Kelvin-Voigt model (Figure 3. 10-c) which combines a dashpot and a spring in parallel; the equation of state to describe this model is the following:

$$\tau = G\gamma_0 \sin(\omega t) + \eta\omega\gamma_0\cos(\omega t) \quad (3.19)$$

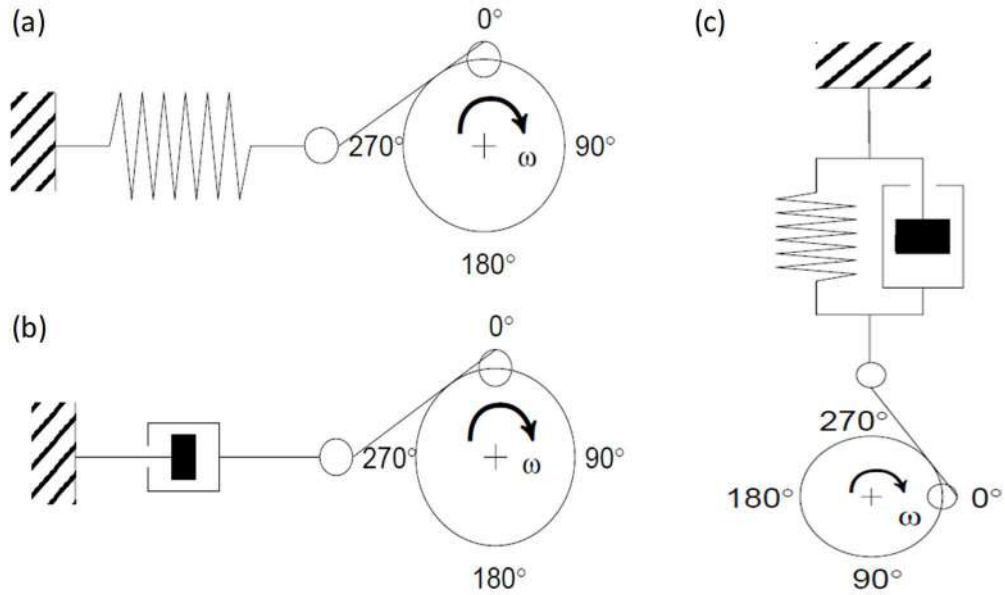


Figure 3. 10: Model to describe: (a) elastic fluids, (b) viscous fluids, (c) Kelvin-Voigt model for visco-elastic fluids [156]

Real visco-elastic fluids are obviously more complex than the Kelvin-Voigt model and it is common to use the term complex modulus G^* to describe them which represents the total resistance of the substance against the applied strain; this is defined as:

$$G^* = G' + iG'' = \tau_0(t)/\gamma_E(t) \quad (3.20)$$

where G' and G'' are the storage modulus and the loss modulus respectively. The storage modulus indicates that the stress energy is temporarily stored during the test but that it can be recovered afterwards while the loss modulus indicates that the energy which has been used to initiate the flow is irreversibly lost.

3.4.3 Rheometer

Rotational rheometers are one of the apparatus used for rheology measurements. Two basic alternatives are available: controlled stress and controlled shear rate. In the first one the stress input is controlled and the resulting shear rate is measured while the opposite is true for a control shear rate rheometer. Different sensor systems can be used in rheometers; Figure 3. 11 depicts the geometries commonly used in rotational rheometers.

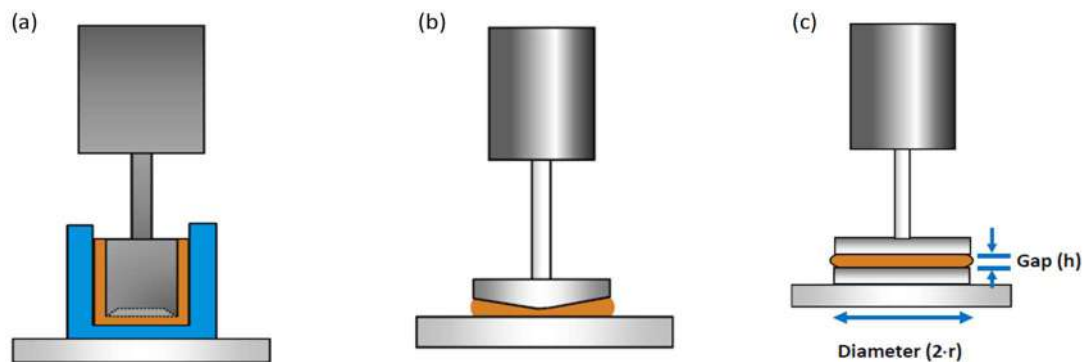


Figure 3. 11: Different geometries used as sensor systems in rheometers: (a) Concentric cylinder (b) cone and plate (c) parallel plate [157]

Concentric cylinders are commonly used for low to medium viscosity liquids, for unstable dispersions and slurries and to minimise the effects of evaporation but they require a high volume of sample and they are not suitable for the measurement of high viscosities.

Cone and plate geometries are used for measurement of low to high viscosity fluids and usually for unfilled samples. The cone is characterised by a shallow angle typically between 2° and 4° and it is

chosen in such a way that for any point of the cone surface, the ratio of angular speed and distance to the plate is constant resulting in a constant shear rate along the diameter of the cone. The tip of the cone should be in contact with the bottom plate but, to reduce the wear of the cone, this is usually truncated and the cone placed at a distance from the bottom plate equal to the extent of the truncation. Although the cone and plate geometry is ideal due to the constant shear rate across the cone diameter, the imposed fix cone-plate distance, due to the truncation, limits its use to unfilled samples.

Parallel plate geometries are the most widely used in the process industries due to their flexibility. This geometry was selected for the experimental work so details of the mathematical equations used to derive the shear rate and shear stress are given. In parallel plate systems, the gap between the plates can be varied allowing the measurement of particle containing fluids. The gap should not be smaller than 300 μm and not bigger than 3 mm otherwise measurement errors due to the nature of the sample cannot be avoided. The gap should be at least 10 times larger than the largest particles size. The shear rate of this systems is not uniform across the diameter of the plates and ranges from 0 at the plate centre to high shear rate values at the outer radius R of the plate; although this is not relevant during the measurement of Newtonian fluids, corrections must be introduced during the measurement of non-Newtonian ones. The max shear stress in parallel plates is expressed by the following equation:

$$\dot{\gamma}_{max} = M\Omega \quad (3.21)$$

where M is the geometry factor which is given by R/h , where R is the outer plate radius and h is the plates gap size, while Ω is expressed by:

$$\Omega = \frac{2\pi}{60} \quad (3.22)$$

where n is the rotor speed. The shear stress on the outer edge of the plate is related to the torque M_d and the geometry factor A by the following equation:

$$\tau = M_d A \quad (3.23)$$

where A is given by the following equation:

$$A = \frac{2}{\pi R^3} \quad (3.24)$$

As previously stated, in the case of non-Newtonian fluids the shear stress value must be corrected and the following equation is used [156]:

$$\tau = M_d A \left(\frac{3+n}{4} \right) \quad (3.25)$$

3.5 Materials and Methods

3.5.1 Materials

The fumed Al_2O_3 particles (AEROXIDE AluC) used in this study were obtained from Evonik Industries (Essen, Germany). The alumina was crystalline with a γ/δ - structure. Density and surface area were 50 g L^{-1} and $85\text{-}115 \text{ m}^2 \text{ g}^{-1}$ respectively.

Butyric acid was obtained from Alfa Aesar (Heysham, United Kingdom) and it was used to modify the particles' surface properties. $70\%_{\text{v/v}}$ HNO_3 (Alfa Aesar, Heysham, United Kingdom) and $40\%_{\text{v/v}}$ KOH solution, prepared by dissolving KOH pellets (Alfa Aesar, Heysham, United Kingdom) in demineralized water, were used to adjust the suspension's pH.

3.5.2 Suspension Preparation

Alumina suspensions were prepared by stepwise addition of the powder to an acidic solution continuously stirred using an overhead mixer. The pH of all suspensions was adjusted to electrostatically stabilize the particles. Alumina isoelectric point lies between 7 and 10 depending on the type of alumina [158]. The suspension solid loading and pH were set to 20%_{w/w} and 4.70 respectively. In a typical formulation 1.12 Kg of alumina was added to 4.425 L of demineralized water containing 75 mL of 70%_{v/v} HNO₃. Then, 155 mL of butyric acid was added to the suspension to modify the surface properties of the ceramic precursor. After amphiphile addition the suspension pH was adjusted to 3.50 through the addition of 40%_{v/v} KOH.

3.5.3 Foaming and Foam Characterization

Foaming of each 4.5 L suspension was carried out in a stainless steel vessel of 5 L volume, diameter T=175 mm, fitted with four baffles of width T/10. The vessel was equipped with a gas sparger at its bottom. Two different metal sintered sparging disks (ASCO Filtri s.r.l., Binasco, Italy) were used having an average pore size of 40 μm and 100 μm respectively; both disks had a diameter of 45 mm. During the foaming the slurry was agitated with an up-pumping impeller having diameter D comprised between 4 cm and 9 cm. Gas flow rate and gas sparging time were varied between 2-20 L min⁻¹ and 1-20 min respectively. The shaft torque was recorded by attaching a Binsfeld Engineering Inc. Torque Trak 10K strain gauge to the impeller shaft. The apparent density of the foam was determined by weighing a known volume of foam; the apparent density was obtained by dividing the sample mass by its apparent volume (volume of both the liquid and gas fraction). Some of the wet foam was stored in a sealed graduated container in order to assess the stability of the foam; the foam was left for two weeks and the change in volume was noted. The rest of the foam

was dried at 80 °C for 2 hours in a Carbolite Furnace CWF. Then it was calcined at 600 °C for 4 hours. During the ramping step and for the first 45 minutes the furnace was purged under N₂ while after the furnace was run under air; the heating rate was 2 °C min⁻¹. Foam porosity and bubble size was determined as described in Chapter 2.5.3.

Foam rheology was measured using an AR2000 rheometer (TA Instruments, Brusselsesteenweg, Belgium). Upward/downward rheology curves and viscoelasticity were measured with all measurements conducted at room temperature. In a typical rheology curve experiment the sample was firstly equilibrated for 2 min and then pre-sheared at 900 s⁻¹ for 30 s. In the upward ramp, the shear rate was increased from 10⁻³ s⁻¹ to 1000 s⁻¹, a log ramp mode was used with 10 points per decade acquired every 20 s. The same procedure was followed in the downward ramp where the shear rate was varied from 1000 s⁻¹ to 10⁻³ s⁻¹. To assess the viscoelasticity of the sample an oscillation experiment was carried out. The typical followed procedure included the equilibration of the sample for 2 min followed by a stress sweep step where the oscillation stress was varied from 0.1 Pa to 1000 Pa. The oscillation frequency was equal to 1 Hz and a log ramp mode was used to increase the stress value with 10 points per decade acquired also in this case. The rheological measurements were carried out using a 40 mm acrylic hatched parallel plate (geometry inertia = 1.56 μN m s²) with a gap set to 500 μm. To investigate the presence of slipping two additional geometries were employed: a 40 mm steel parallel plate (geometry inertia = 8.30 μN m s²) and a standard size vane-rotor with stator inner radius 15 mm and rotor outer radius 14 mm (geometry inertia = 2.44 μN m s²). The gap was set to 500 μm and 4000 μm when the parallel plate and the standard vane geometry were employed respectively.

3.5.4 Design of Experiment (DoE)

Before designing the full experimental series, scoping experiments were carried out to determine the factors' levels (range within which the different variables are changed) that gave a good range of foam porosity. Since the type of sparging disk is a categorical factor, the scoping experiments were replicated for both disks. In both cases the central points were repeated twice in order to assess the reproducibility of the experiment. A half factorial design with five factors and two levels was employed to screen the significance of the different factors. The screening design generated 16 runs to investigate the effect of the following independent factors: impeller diameter D (4-9 cm), impeller speed N (200-1000 rpm), gas flow rate G (2-20 L min⁻¹), sparging time t (1-20 min) and sparging disk mean pore size \bar{d} (40 and 100 μm). Foam porosity, foam density, foam stability and foam bubble size distribution were selected as responses; these were analysed using JMP 10 software (SAS Institute Inc.) in order to determine the significant factors affecting the foam properties.

3.6 Determination of the significant factors affecting foam properties

Scoping experiments were carried out to select the factors levels; due to the time consuming measurements involved in the determination of foam bubble size, foam porosity and foam density were chosen as the measured responses. Figure 3. 12 shows the obtained foam porosity and density for the two different sparging disks when the factors are set to their least forcing values (-1) (factors' values that led to the lowest foam porosity), most forcing values (1) (factors' values that led to the highest foam porosity) central point values (0) (factors' values in between the least forcing and most forcing values).

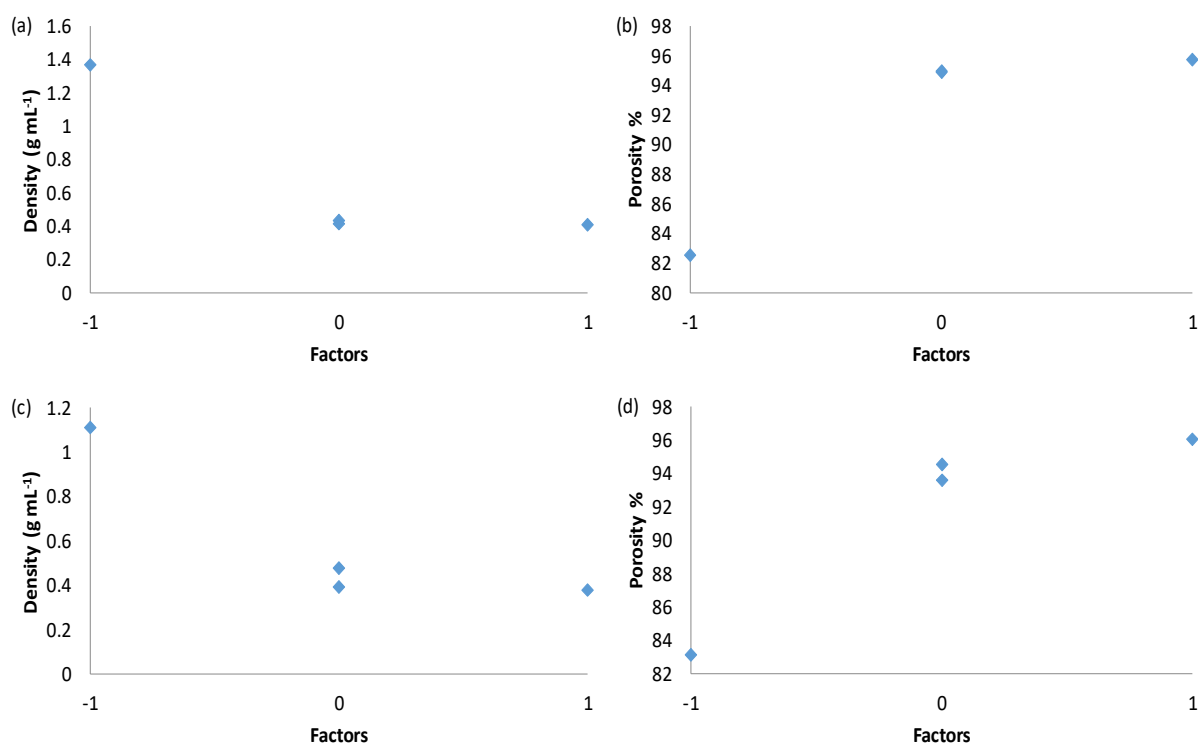


Figure 3. 12: Scoping graphs for the 40 and 100 μm disks: (a) density graph for 40 μm plate, (b) porosity graph for 40 μm plate, (c) density graph for 100 μm plate, (d) porosity graph for 100 μm plate

Figure 3. 12 shows that the selected factors levels led to a good range of porosity and density. In addition, in all cases the central points show good experimental reproducibility. The scoping graphs also suggest that the sparging disks' pore diameter does not significantly influence foam porosity and density since there is little variation in these values when the different disks are used.

Table 3. 1 summarizes the 16 runs with their different factors levels and responses in terms of foam porosity %, density (g mL^{-1}) and bubble size; the latter is expressed as mean Sauter diameter d_{32} (μm) [97]. Since foam stability was not affected by the process parameters, this response is not included in Table 3. 1 and will not be discussed further.

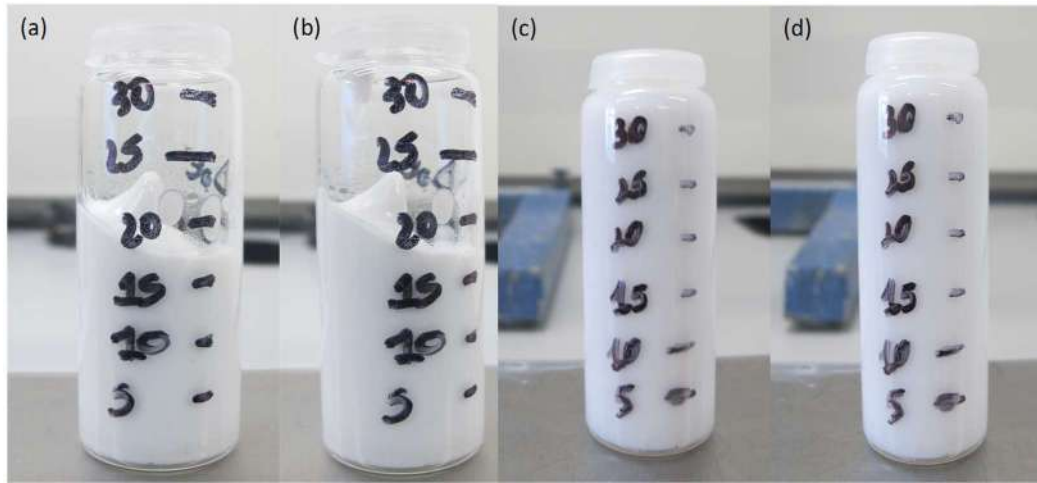


Figure 3. 13: Foam Stability Assessment: (a) Freshly made high porosity foam (b) High porosity foam after 2 weeks (c) Freshly made low porosity foam (d) Low porosity foam after 2 weeks

Figure 3. 13 shows that both high and low porosity foams do not present any volume variation after two weeks. This indicates that foam stability is exclusively affected by its formulation and it is independent on the foaming process.

Table 3. 1: Half factorial design runs with factors levels and response values

Run #	Air Flow Rate (L min ⁻¹)	Impeller Speed (RPM)	Sparging Time (min)	Impeller Diameter (cm)	Sintered Disk Mean Pore Size (μm)	Apparent Density (g cm ⁻³)	Open Porosity %	d ₃₂ (μm)
1	2	200	1	4	100	1.17	82.18	367
2	2	200	20	9	100	0.55	88.68	150
3	20	1000	1	9	40	0.8	88.65	96
4	20	1000	20	4	40	0.36	95.71	189
5	2	1000	1	4	40	0.91	83.42	236
6	2	1000	20	9	40	0.56	95.13	59
7	20	200	1	9	100	1.02	84.63	169
8	20	200	20	4	100	0.56	89.75	240
9	2	1000	20	4	100	0.86	89.71	91
10	20	200	1	4	40	1.02	83.24	331
11	20	200	20	9	40	0.58	91.32	175
12	2	1000	1	9	100	0.92	86.64	129
13	20	1000	20	9	100	0.3	96.71	86
14	20	1000	1	4	100	0.73	86.39	114
15	2	200	1	9	40	1.09	83.43	93
16	2	200	20	4	40	0.96	85.84	384

The responses summarized in Table 3. 1 were analysed using JMP 10 in order to determine the process factors that affects the foam properties. Table 3. 2 reports the factors affecting the considered foam properties. In the table are present five columns, in the first one the factors and the factor interactions are listed, the second column shows the contrast value that, in the case of an orthogonal design, is the same as the regression parameter estimates. The third column lists the Lenth t-ratio; this is obtained by the ratio between the contrast value (second column) and the Lenth's Pseudo-Standard Error (PSE). The latter is calculated by Lenth's method which identifies inactive effects from which it constructs an estimate of the residuals standard errors (PSE) [159]. The last two columns list the individual and simultaneous p-values respectively. The individual p-value is an indication of the significance of the considered factor; if the factor's individual p-value has a value lower than 0.05 this can be considered a significant factor. p-values are generated via a Monte Carlo simulation of 10000 runs of $n-1$ purely random values and Lenth's t-ratios are produced for each set. The p-value is the interpolated fractional position among these values in descending order. The simultaneous p-value is the interpolation along the $\max(|t|)$ of the $n-1$ values across the runs [160] [161].

Table 3. 2: Process parameters affecting foam properties

Density				
Parameter	Contrast	Length t-ratio	Individual p-Value	Simultaneous p-Value
Sparging Time	-0.183	-3.91	0.0074	0.0682
Air Flow Rate	-0.103	-2.20	0.0489	0.3726
Impeller Speed	-0.094	-2.01	0.0624	0.4768
Porosity				
Sparging Time	3.159	4.07	0.0063	0.0581
Impeller Speed	1.848	2.38	0.0367	0.2910
Air Flow Rate	1.568	2.02	0.0617	0.4712
Impeller Diameter	1.416	1.83	0.0830	0.5917
Bubble Size				
Impeller Speed	-209.491	-9.49	0.0004	0.0080
Impeller Diameter	-87.032	-3.94	0.0072	0.0660
Sparging Time & Air Flow Rate	-82.409	-3.73	0.0088	0.0792
Impeller Diameter & Sintered Disk	178.843	8.10	0.0004	0.0041

Sparging time, impeller speed and air flow rate are the factors affecting foam density and foam porosity while, confirming the scoping experiment, the porosity of the sparging disk does not influence these foam properties. Foam bubble size is governed by impeller speed, impeller diameter and a series of factors interactions including sparging time & air flow rate and impeller diameter & sintered disk. This study shows the significance of all the considered factors in shaping the structure of ceramic foams. Not all of them affect the same foam properties so the different factors could be selectively controlled in order to tailor the structure of the foam depending on the required application.

3.7 Correlation between Foam Density and Foam Porosity

The existence of a linear relationship between density and porosity of materials is well known [162]. Density of solid materials is usually measured by helium pycnometry. This technique more precisely measures the volume of the sample by gas displacement [163] [164]; the density of the sample is consequently obtained by dividing its mass by its volume. In this study the density of the

wet foam, measured as described in Chapter 3.5.3, is correlated to the porosity of the dry ceramic foam. Although this is not the conventional way to plot the porosity as a function of density, this method is a straightforward way to assess the porosity of the foam during its manufacture.

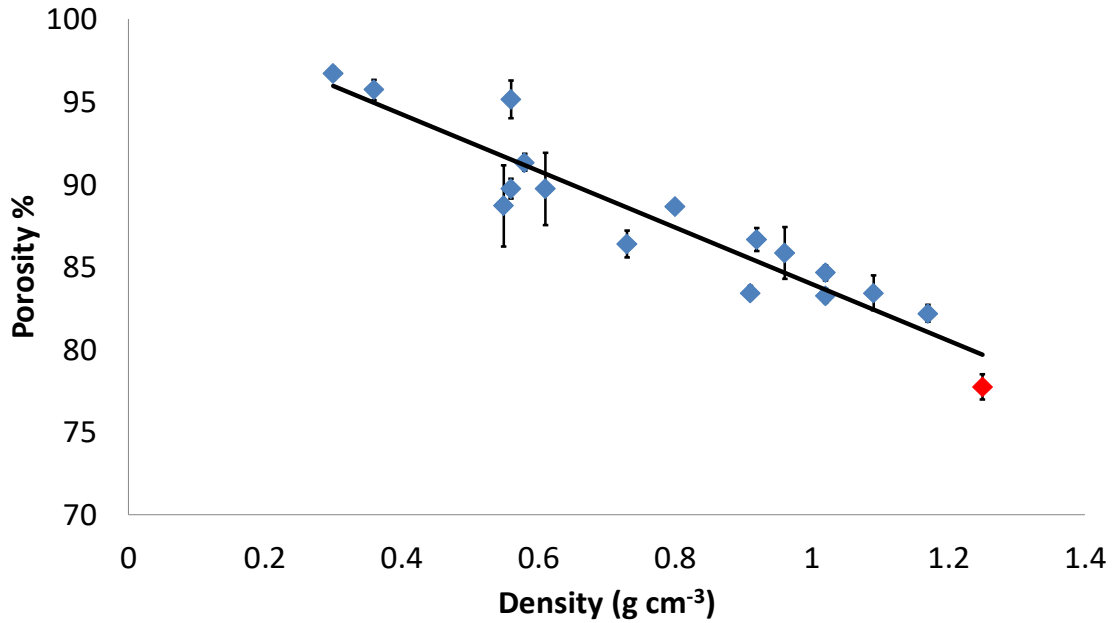


Figure 3. 14: Porosity of the dry foam as a function of the density of the wet foam

Figure 3. 14 shows the existence of a monotonic possibly linear relationship ($R^2 = 0.89$) between the porosity of the dry foam and the density of the wet foam. The red point in the graph refers to the porosity and density of the alumina ceramic slurry previous to air entrainment. Foam porosity is related to foam density by the following relationship:

$$Porosity \% = -17.17 * Density_{wet\ sample} (g/cc) + 101.12 \quad (3.26)$$

Although this relationship does not substitute more accurate techniques to measure porosity, it gives an indication of the foam porosity after treatment (e.g. drying and calcination). This relation is obviously valid only for the considered formulation since, as previously said, foam porosity is greatly affected by its formulation and after-treatment (e.g. drying and calcination).

3.8 Gas Hold-Up Correlations Applied to the Produced Foams

The dependence of foam porosity on the volume of entrained gas is obviously expected. Figure 3. 15 shows the foam porosity as a function of the total volume of entrained air; this was obtained by multiplying the gas flow rate by the sparging time.

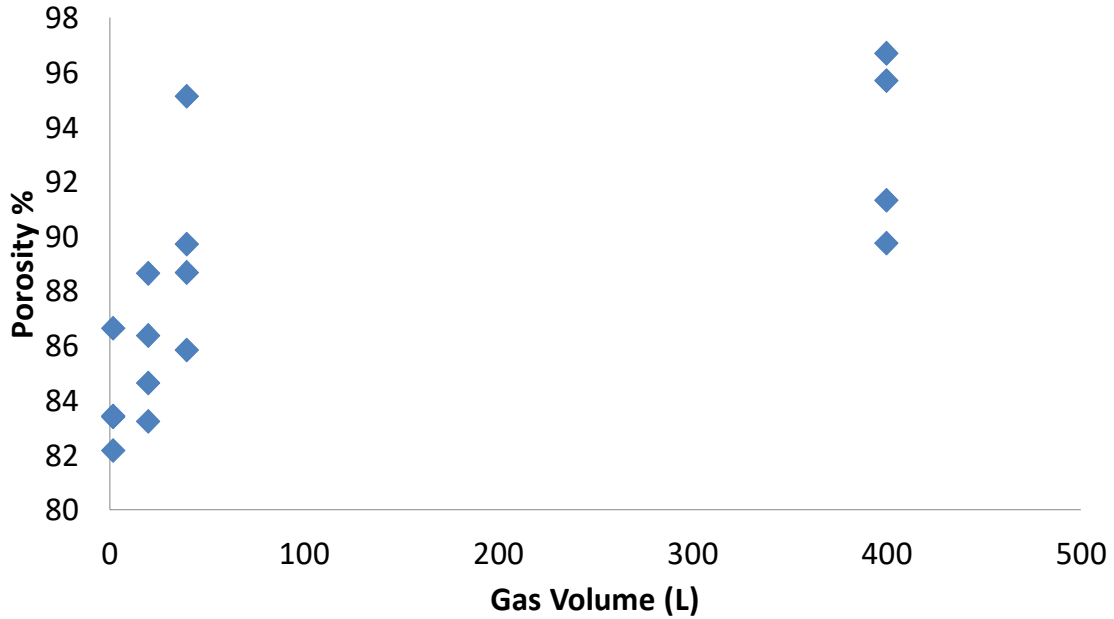


Figure 3. 15: Foam porosity as a function of the total volume of entrained gas

In the screening study (Section 3.6) it was established that the foam porosity is not only affected by the amount of entrained air; this is confirmed by Figure 3. 15 where foam produced entraining the same amount of air in the vessel present different porosities. In particular, impeller speed has been shown to have a significant impact on foam porosity with this effect probably related to the air entrainment observed during mixing. In principle, a parallelism between wet foam porosity and gas hold up in the aerated stirred vessel can be made. Several correlations between gas hold up and process parameters have been presented in Section 3.3.3. A similar approach has been applied to the case of wet foams where their porosities were correlated to a series of mixing parameters such as energy dissipation ($W m^{-3}$), Reynolds number (Re), Froude number (Fr) and gas flow number

(F_{lg}). It is important to point out that the correlations illustrated in Section 3.3.3 were obtained for pure gas-liquid systems in steady state conditions while, in the current study, a three-phase unsteady system (e.g. solid-gas-liquid) was present and divergences from the before-mentioned relationships are to be expected. It is important to remark that the flow conditions in the present study are low to mid transitional ($50 < Re < 1000$). Since correlations in this regime cannot be found in the literature, only the correlations from other regimes that gave the best fit are presented in this work. Correlations developed in the turbulent regime were found to give the best fit for the gas hold-up and bubble size correlations whilst, in the absence of a superior approach, the *Metzner - Otto* correlation was used to determine the impeller mean shear rate.

Figure 3. 16 shows the foam porosity as a function of the adimensional group ($ReFrF_{lg}$). Due to the transient nature of the system and the consequent change in the slurry's physical properties (e.g. density and viscosity), non-dimensional numbers such as the Reynolds number were calculated using the initial physical properties of the ceramic slurry. In addition, during the different experiments the impeller speed was varied subjecting the slurry to different shear rate; this resulted in different alumina slurry's viscosities due to its non-Newtonian nature. The average impeller shear rate was determined using the *Metzner and Otto* correlation (3.3); with the used impeller characterized by a mixer shear constant value of 12 [165]. The calculated average shear rates were used to determine the slurry viscosity by interpolation with the pre-determined initial slurry viscosity curve.

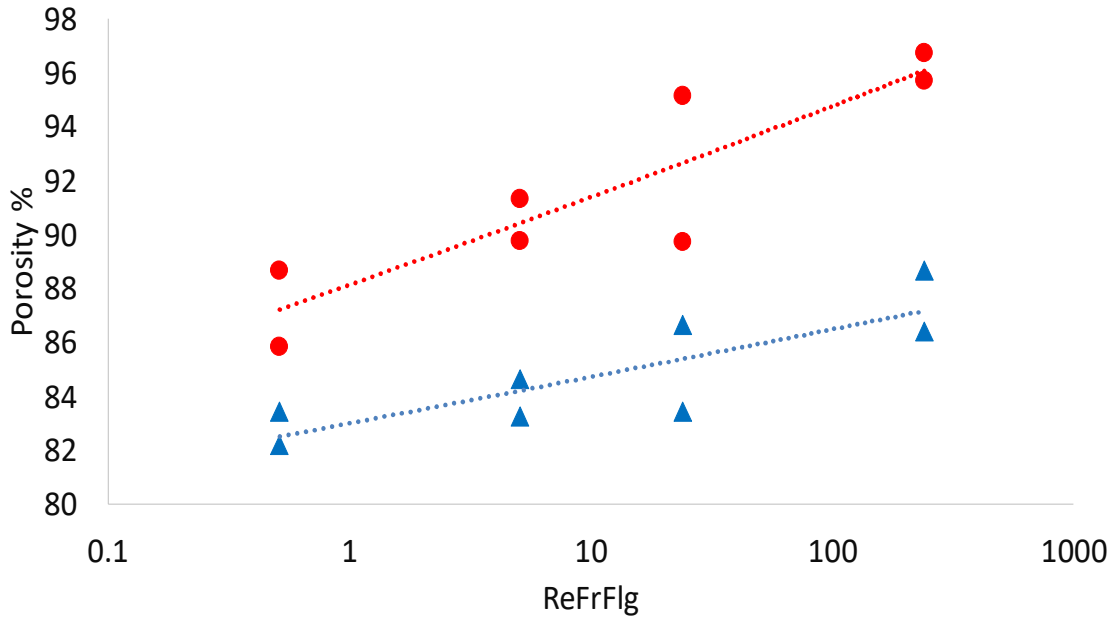


Figure 3. 16: Foam porosity as a function of the adimensional group ($ReFrF_{lg}$) for foams produced using different sparging times: $T=1'$ (●) and $T=20'$ (▲)

As a result of foam porosity being strongly affected by sparging time, different correlations were derived for foams produced using different entrainment times. Figure 3. 16 implies a monotonic correlation in all cases (R^2 equal to 0.80 and 0.69 for foam produced at 1' and 20' air entrainment time respectively) but, as expected, the exponent of the dimensionless group significantly differs from that proposed by *Smith* (3.6). It has been previously shown that the gas hold-up is more usefully expressed as a function of the mean power dissipation; Figure 3. 17 shows foam porosity as a function of the mean power dissipation for foams produced using different air entrainment times.

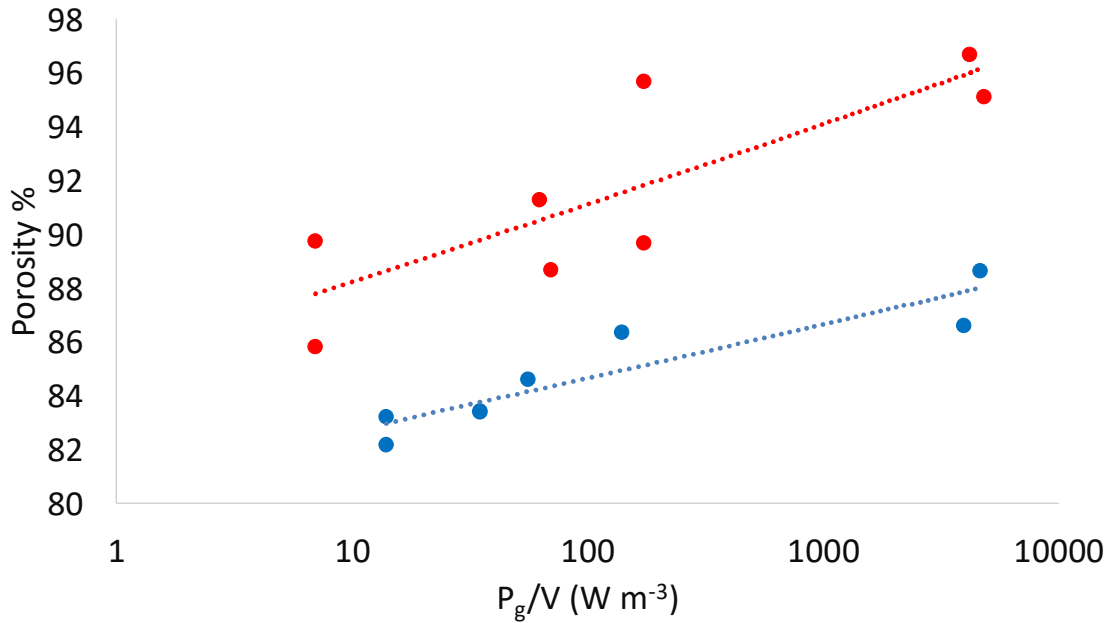


Figure 3. 17: Foam porosity as a function of mean energy dissipation for foams produces using different air entrainment times. $T=1'$ (●) and $T=20'$ (▲)

Monotonic relationships were found for the evaluated foams (R^2 equal to 0.68 and 0.85 for foam produced at 1' and 20' air entrainment time respectively) but again the exponent values were significantly different from the correlations determined for gas-liquid systems. In both the applied correlations, the exponent values were close to 0.3 while in this study the exponent values were in the range 0.012 ± 0.003 .

As previously mentioned, *Greaves and Barigou* [138] and *Smith* [137] suggest that gas hold-up depends on the different flow regimes present in the aerated stirred vessel; for this reason, the foam porosity was correlated to the different flow regimes present at the different experimental conditions. Since a flow-regime map for an up-pumping pitch blade turbine was not found in the literature, this was determined experimentally bearing in mind that the flow patterns presented in Section 3.3.2 are for gas-liquid systems. The presence of solid particles in the work undertaken here prevented the visual observation of the flow patterns; in addition, the change in the rheological

properties, due to foam formation, could lead to transient flow patterns. Despite the impossibility to exactly establish the flow regime in our system, an indication was obtained by using the experimental process parameters (e.g. impeller speed, impeller diameter and gas flow rate) in a particle free air-water system. From Figure 3. 18 it could be seen that, with the exception of case (b) where a loading pattern is observed, flooding is present when the smaller impeller is used (a, c-d); whereas increasing the gas flow rate a transition from a loaded to a recirculating regime is observed for the larger impeller (e-h).

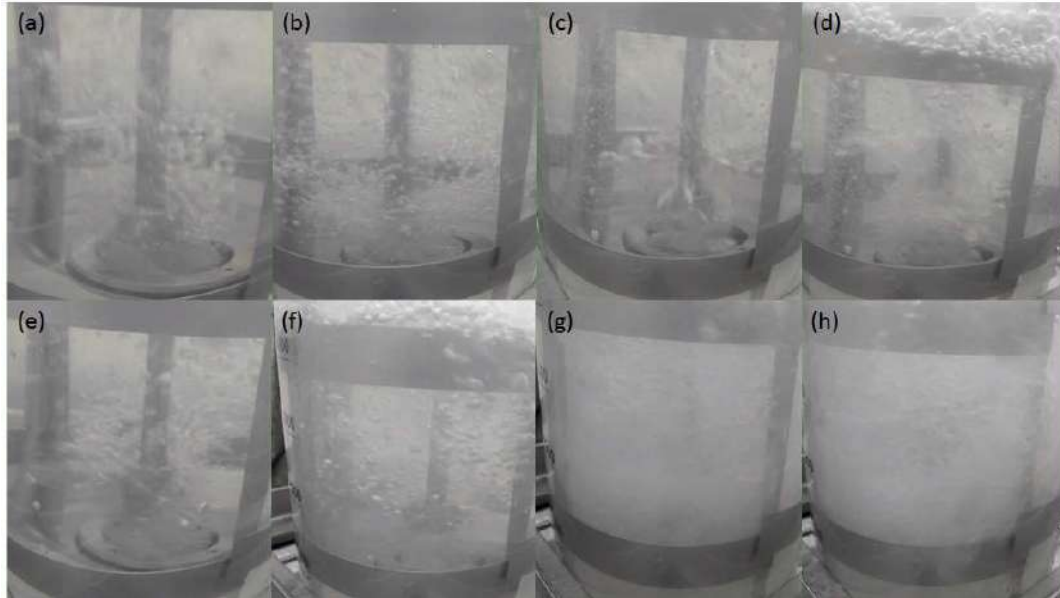


Figure 3. 18: Flow regimes at different impeller speed, impeller diameter and gas flow rate. (a) $D=4\text{ cm}$, $G=2\text{ L min}^{-1}$, $N=200\text{ rpm}$ (b) $D=4\text{ cm}$, $G=2\text{ L min}^{-1}$, $N=1000\text{ rpm}$ (c) $D=4\text{ cm}$, $G=20\text{ L min}^{-1}$, $N=200\text{ rpm}$ (d) $D=4\text{ cm}$, $G=20\text{ L min}^{-1}$, $N=1000\text{ rpm}$ (e) $D=9\text{ cm}$, $G=2\text{ L min}^{-1}$, $N=200\text{ rpm}$ (f) $D=9\text{ cm}$, $G=2\text{ L min}^{-1}$, $N=1000\text{ rpm}$ (g) $D=9\text{ cm}$, $G=20\text{ L min}^{-1}$, $N=200\text{ rpm}$ (h) $D=9\text{ cm}$, $G=20\text{ L min}^{-1}$, $N=1000\text{ rpm}$

From the visual observation of the different flow regimes, a flow regime map was drawn for the current system. The map makes use of the gas flow number (abscissa) and the Froude number (ordinate) to divide the experimental area in different regions where the mentioned regimes occur; these are represented by different colours where blue, red and green points represent flooded,

loaded and fully recirculated regimes respectively. The limited number of experiments did not allow absolute definition of transition regions between regimes; the map is illustrated in Figure 3.

19.

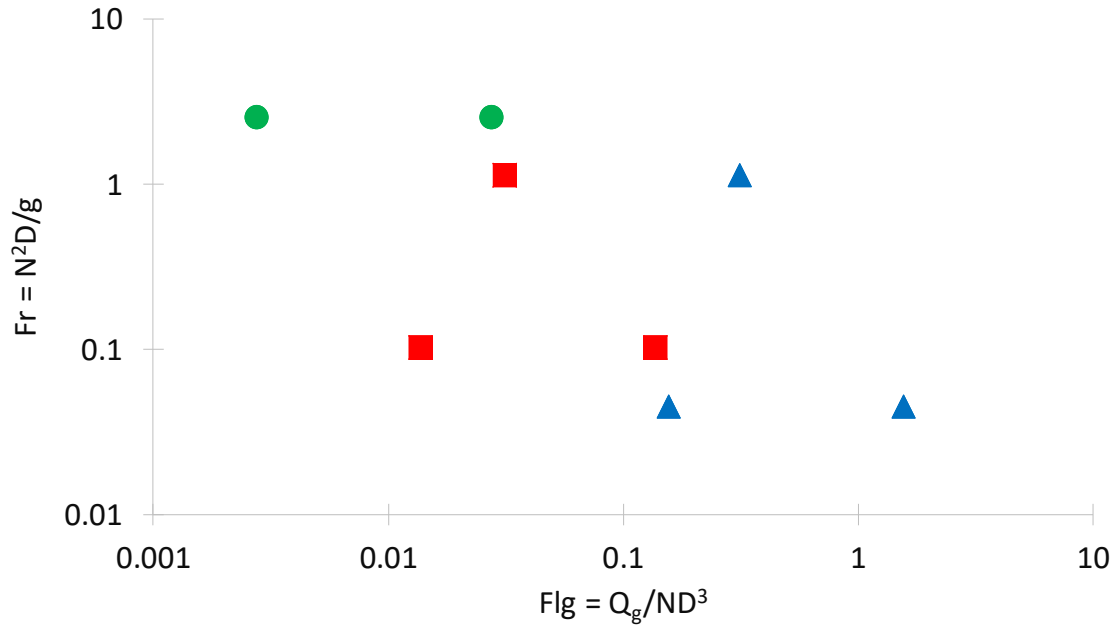


Figure 3. 19: Flow regime map for the experimental system. (▲) Flooded, (■) Loaded, (●) Fully recirculated.

Figure 3. 20 shows the foam porosity as a function of the different flow regimes; the different colours and shapes of the bars indicate the different flow regimes at which the specific foams were produced. Two different graphs were plotted for the short and long air entrainment time since this variable has an effect on the foam porosity.

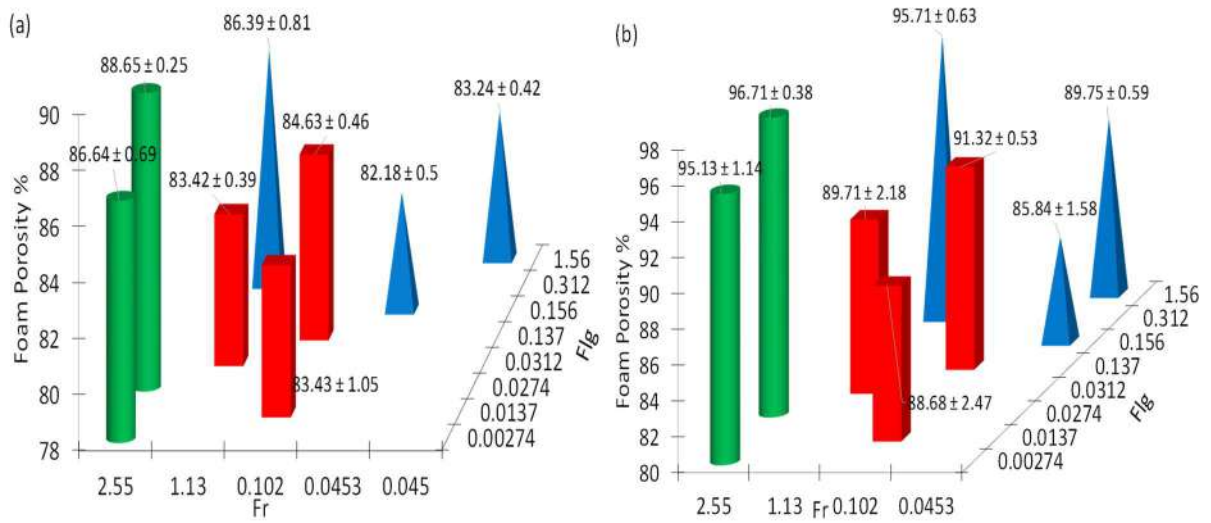


Figure 3. 20: Foam porosity as a function of the flow regime conditions for (a) 1 min air entrainment time (b) 20 min air entrainment time. The different flow regimes are represented as flooded (▲), loaded (■) and fully recirculated (●)

From the figures above, it can be noted that a similar trend is followed for both the short and long air entrainment time, with the highest porosity observed when the foam is produced in fully recirculated conditions. The only discrepancy from the expected trend is observed, for both air entraining times, when the foam is produced with process variables characterised by a Froude and Gas Flow number of 1.13 and 0.312 respectively. This could be to the high gas flow rate observed for a Gas Flow number of 0.312 and the air entrainment due to vortexes associated to a relatively high Froude number but, as previously mentioned, due to the nature of the investigated system discrepancies from a pure gas-liquid system are expected.

3.9 Bubble Size Correlations Applied to the Produced Foams

In Section 3.6 it was determined that the process parameters affecting the bubble size are impeller speed, impeller diameter, sparging time-air flow rate interaction and impeller diameter-sintered disk interaction. The bubble size distribution was determined by image analysis of the foam cross section; Figure 3. 21 (a) shows an example of the cross-sectional image of one of the produced

foam while Figure 3. 21 (b) shows the thresholded picture that was used to determine the bubble size; it should be noted that only the bubbles that were well in focus were analysed. Due to both the laborious image analysis and the limited amounts of available samples it was possible to analyse only ~100 bubbles per sample; the calculation of the standard deviation associated to each bubble size value is presented in detail in Appendix II.

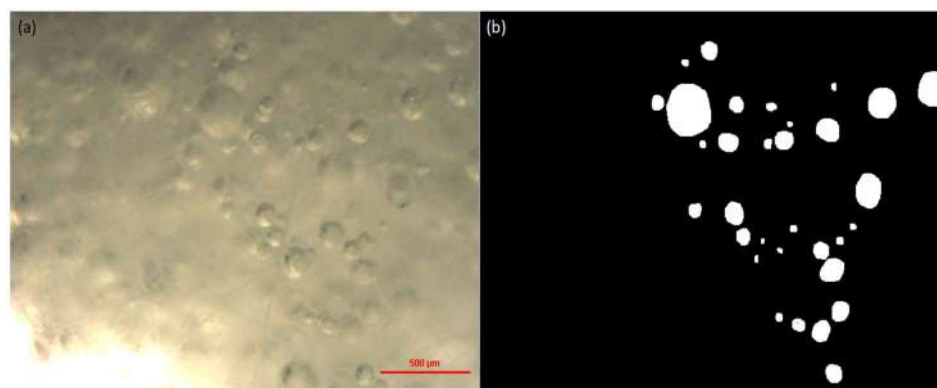


Figure 3. 21: Example of cross-sectional image for one of the produced foam: (a) optical microscope image, (b) thresholded image

The bubble size distribution obtained from the analysis of the cross-sectional images of all the produced foam is shown in Figure 3. 22.

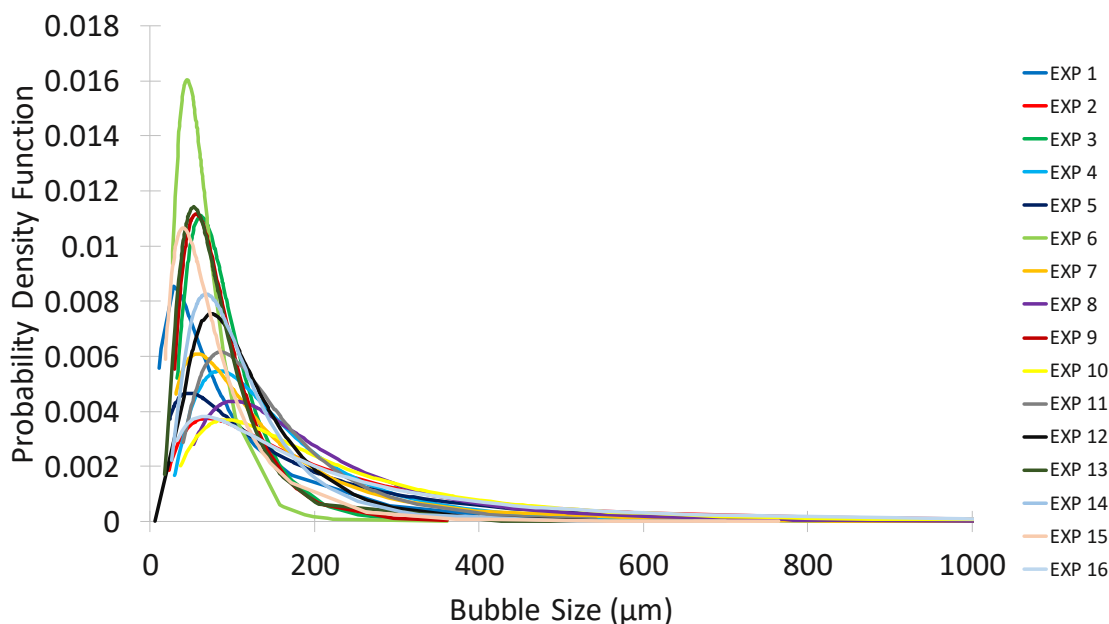


Figure 3. 22: Bubble size distribution for the obtained foams

The mean bubble size was expressed in terms of mean Sauter diameter calculated as reported in Section 2.6.5.

This was a three phases system so the direct imaging of the bubbles in the wet foam was not possible; consequently, the bubble size was determined by image analysis of the cross section of the dried and calcined foam. This could lead to uncertainties about the real size of the bubbles in the wet system. However, all measurements were made in the same way and thus the error would be systematic in nature allowing comparison between foams. The foam mean bubble size was plotted as a function of the mean energy dissipation and Weber number. It is worth noting that the correlations, as in the case of the gas hold-up correlations, refer to liquid-liquid systems or gas-liquid systems. In addition, as previously stated, the physical properties of the slurry changed over the duration of the experiment due to foam formation so the density and viscosity of the initial slurry were used for the calculation of the Weber number. Despite these considerations, it was expected that these relationships would describe the change in bubble size under different operating

conditions, although with some discrepancies in terms of the exponent values. Figure 3. 23 (a) and Figure 3. 23 (b) represent the d_{32}/D value as a function of the Weber number and mean energy dissipation respectively. Since the bubble size is affected by both the mean sparger pore size and the impeller diameter, bubble size of foams produced using two different spargers and different impeller diameters were plotted in two different series.

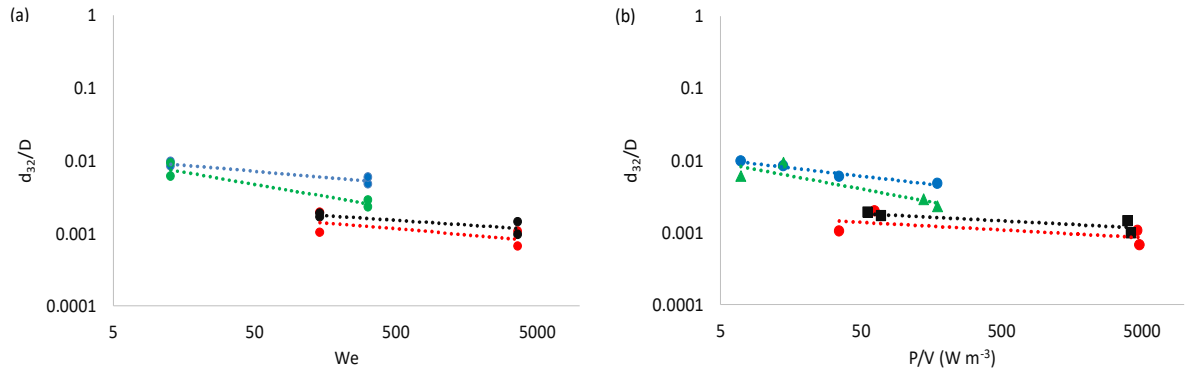


Figure 3. 23: d_{32}/D as a function of mean energy dissipation for (a) We (b) P_g/V . The different sparger pore size and impeller diameter are indicated as: 40, $D = 4$ cm (●); 40, $D = 9$ cm (◆); 100, $D = 4$ cm (▲); 100, $D = 9$ cm (■)

The figures above show that the experimental data are fitted by the relationships proposed in the literature but, as expected, different values of the mean energy dissipation and Weber number exponents are necessary to interpolate the data. The exponent assumes values ranging from 0.16 to 0.36; these values are not significantly different from the value observed by *Hu et al.* in systems where the presence of solvents strongly suppressed coalescence [166] [152]. The stability of the foams under consideration is due to the attachment of hydrophobic particles at the air-liquid interface that, in turn, prevents coalescence.

In Section 3.8, it was shown that the flow regime affects the porosity of the foam; a similar effect was expected for bubble size. Figure 3. 24 (a) and (b) shows the d_{32}/D as a function of the different flow regimes for the 40 μ m and 100 μ m disks respectively.

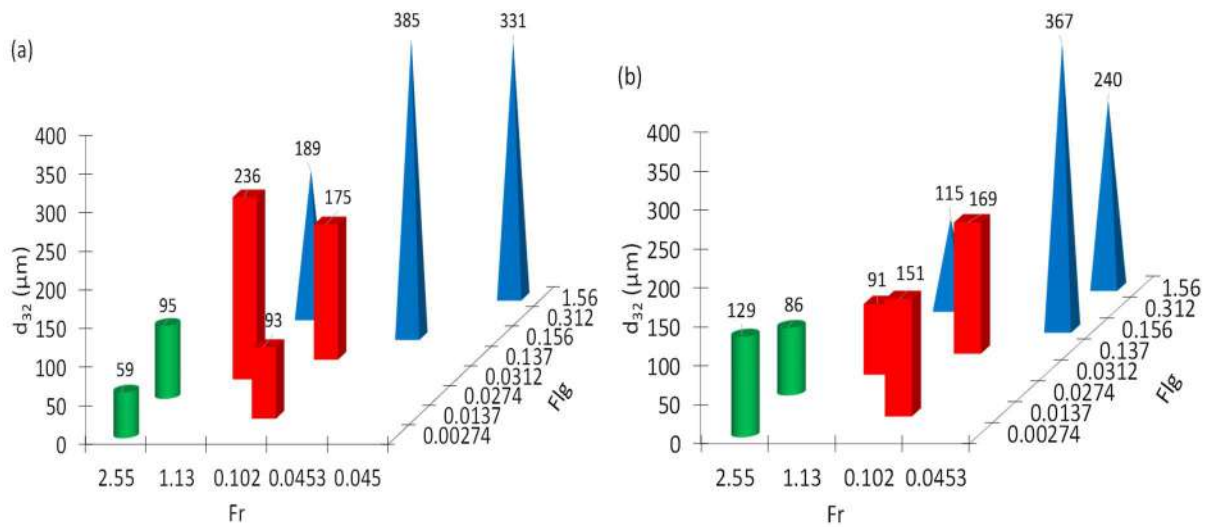


Figure 3. 24: d_{32}/D depending on the different flow regimes conditions for (a) 40 μm sparging disk (b) 100 μm sparging disk. The different flow regimes are represented as flooded (\blacktriangle), loaded (\blacksquare) and fully recirculated (\bullet)

From the figures above, it can be noted that a clear trend exists in both cases where the smaller bubbles are obtained in fully recirculated condition and bigger bubbles are progressively obtained when moving from loaded to flooded regime conditions. It is notable that, contrarily to what it would be expected, the smaller sparger size disk produces bigger bubbles for foams made at Flg higher than approximately 0.02. At high gas flow rates, a higher level of coalescence is expected in the small pores disk; this is mostly due to the closer proximity of the smaller pores and could result in the formation of initial bubbles bigger than those initially formed by the bigger pores sparger.

3.10 Rheological Characterization of the Produced Foams

The rheology of the foams was determined using the procedures described in Section 3.5.3. For all the sixteen foams an acrylic hatched parallel plate was used; Figure 3. 25 (a) shows the comparison between the upwards rheology curves obtained. There is a notable “kink” present in all the curves and, in addition, some of the curves perfectly overlap suggesting structural similarity among these

foams. Figure 3. 25 (b) exemplifies the upward (increasing shear rate) and downward (decreasing shear rate) rheology curve of one foam. It can be seen that, the downward curve does not reach the initial viscosity of the fresh foam suggesting that the structure of the foam is irreparably broken at the higher shear rates. In addition, the “kink” appears at lower shear rates in the down curve than the up curve. The different position of the “kink” could suggest a correlation with the foam structure but it was important to determine if such a feature is an artefact of the test procedure; it remained possible that, despite the top plate hatching, slipping could have occurred at the flat bottom plate.

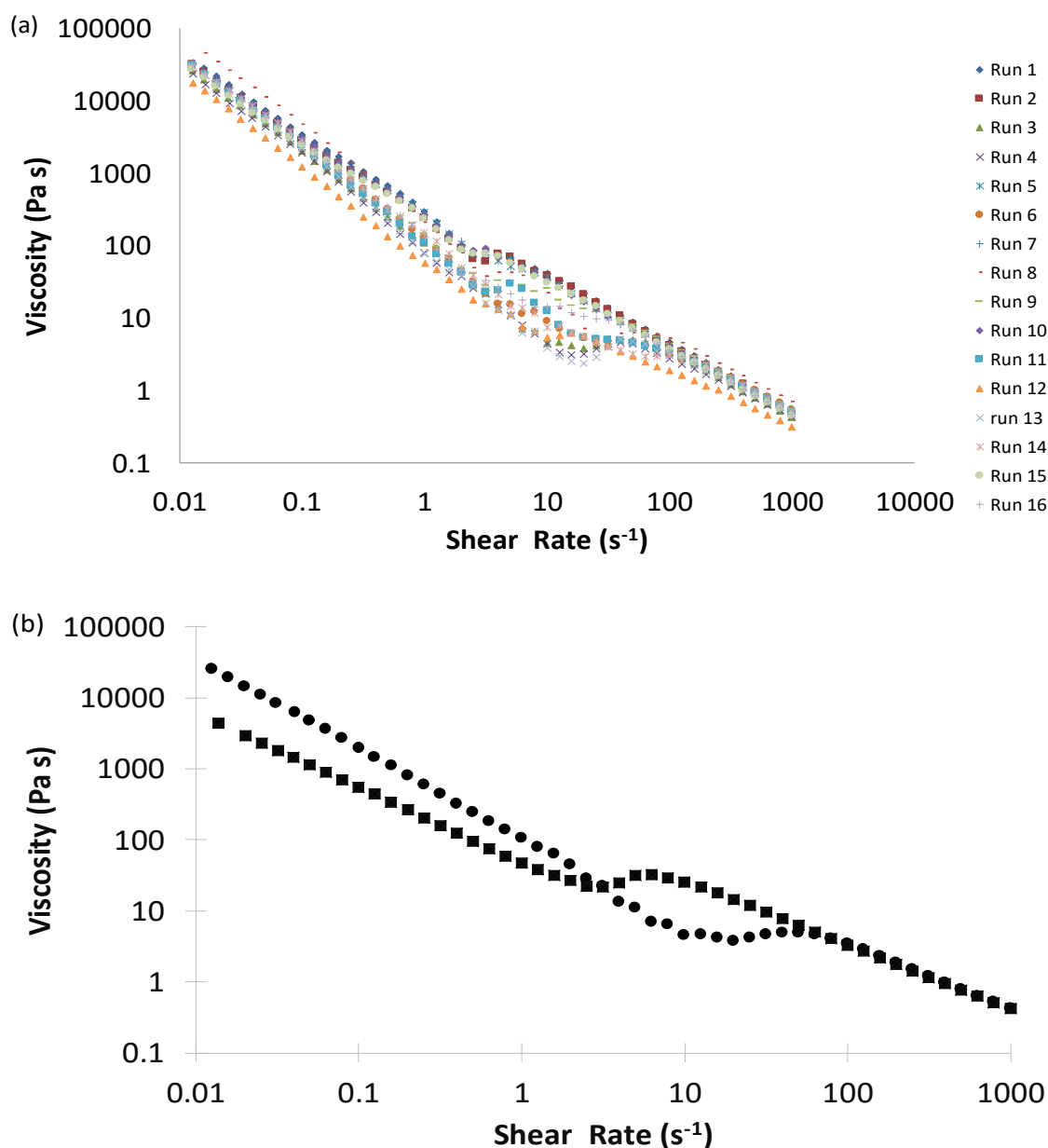


Figure 3. 25: (a) Comparison of the upward rheology curve for the produced foams (b) Details of the upward (●) and downward (■) rheology curve for one of the produced foams

To investigate the nature of the “kink” the rheology of a foam was measured using different geometries; in particular, a 40 mm steel plate, a 40 mm acrylic hatched plate and a standard rotor-vane geometry were employed. In this case, the foam was a 20%_{w/w} titania foam produced using

DL-phenylalanine as amphiphile. It was necessary to replace the amphiphile due to the larger volume required in the rotor-vane geometry which made difficult to work with butyric acid due to its unpleasant odour. Consequently, titania was used as ceramic precursor due to the better performances of phenylalanine as amphiphile when this powder was used. Although the measured system was different from the original foams, the aim of the comparison was to evaluate the nature of the observed “kink”.

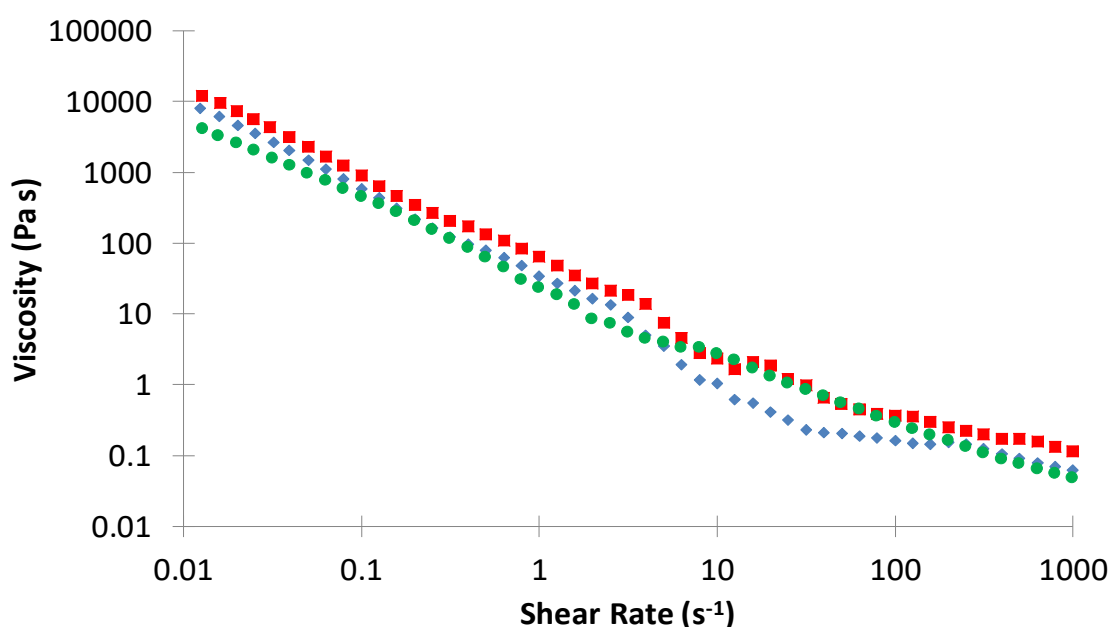


Figure 3. 26: Foam upward rheology curve: geometry comparison: (♦) Flat parallel plate, (■) Hatched parallel plate, (●) Rotor-vane geometry)

Figure 3. 26 shows the comparison among the upward rheology curves obtained following the testing procedure described in Section 3.5.3 but using the different geometries previously mentioned. It can be noted that the extent of the “kink” reduces moving from a flat parallel plate to a vane geometry suggesting that the observed feature is slip. Despite the fact that the geometry comparison would suggest that the best geometry to be used is a rotor-vane geometry, the odorous characteristic of butyric acid and the higher volume of sample required prevented the use of this

system. Once the nature of the “kink” was identified, its correlation with the structural properties of the foam were investigated. It can be assumed that the stabilized bubbles in ceramic foams behave like soft spheres, these, at high concentrations, exhibit viscoelastic and solid-like behaviour at low shear stress but yield and flow above a yield stress [167]. Slip of soft particles has been widely investigated in the literature; this occurs when particles are depleted from a solid surface giving a low viscosity boundary layer between the surface and the particles in the bulk of the suspension [168].

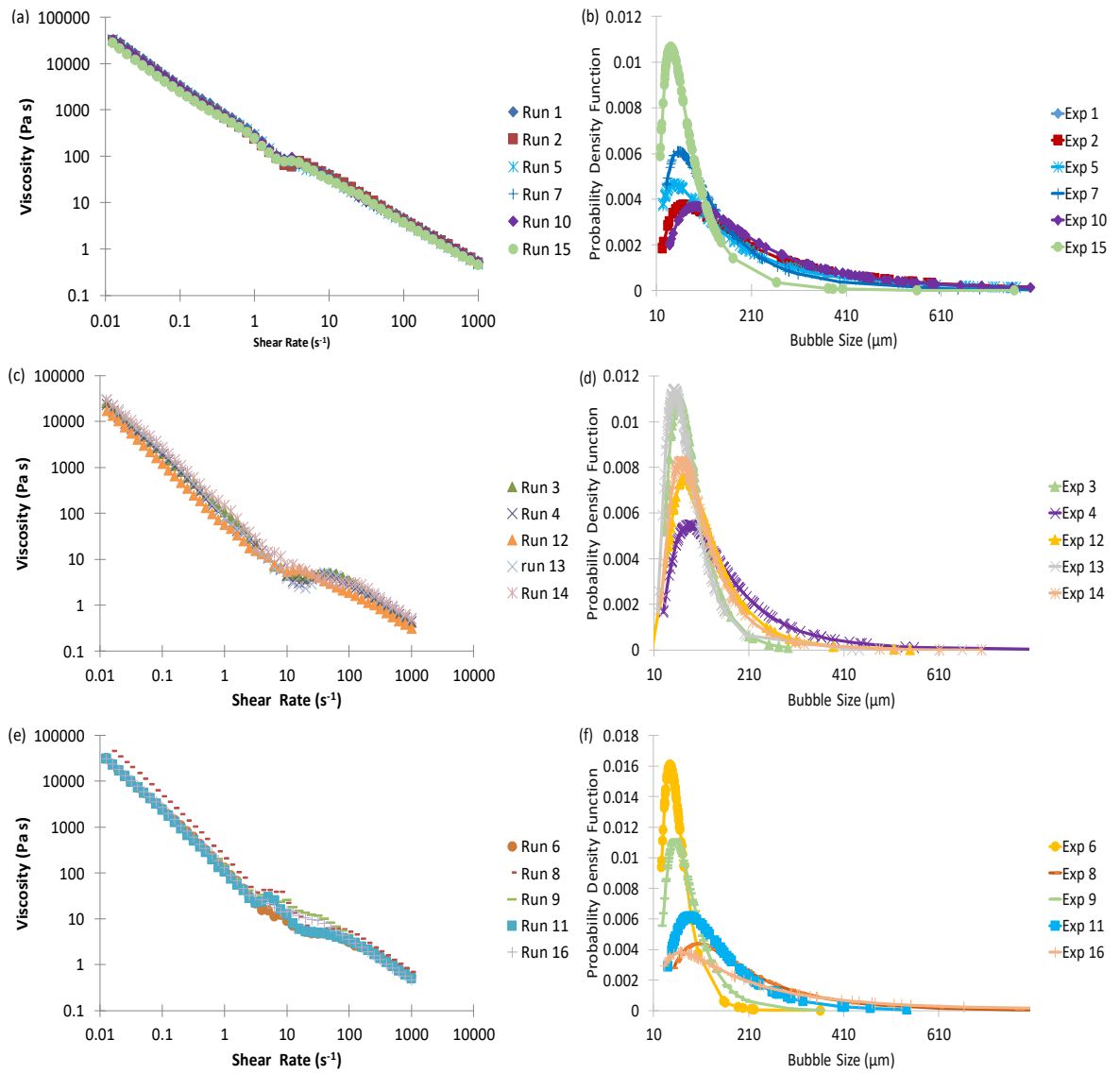


Figure 3. 27: (a) first series of overlapping rheology curves (b) bubble size distribution of the foams overlapping in the first series (c) second series of overlapping rheology curves (d) bubble size distribution of the foams overlapping in the second series (e) third series of overlapping rheology curve (f) bubble size distribution of the foams overlapping in the third series

Table 3. 3: Summary of the foams properties divided by overlapping series

	Exp.	d_{32} (μm)	Distribution Span	Shear Rate (s^{-1})	Shear Stress (Pa)
1 st Set	1	615.99	4.08	2.51	214.9
	2	1001.87	2.48	2.51	162.4
	5	635.84	5.08	2.51	195.0
	7	94.094	2.74	3.16	235.6
	10	1050.07	2.95	2.51	210.7
	15	432.17	1.62	2.51	173.1
Average		642.81	3.16	2.62	198.6
2 nd Set	3	164.09	1.56	9.99	44.89
	4	465.41	2.31	12.59	42.06
	12	278.64	1.50	10.01	53.59
	13	328.85	1.60	19.97	39.93
	14	391.27	1.70	12.59	73.58
Average		325.65	1.73	13.03	50.8
3 rd Set	6	182.58	1.26	5.01	70.82
	8	609.16	2.43	3.98	118.9
	9	199.33	1.89	3.98	89.33
	11	296.60	1.83	3.16	71.14
	16	1051.12	5.13	3.16	112.9
Average		467.76	2.51	3.86	92.6

Figure 3. 27 shows the sets of overlapping rheology curves and the bubble size distribution of the corresponding foams. Table 3. 3 summarizes the properties of the foam; the span values reported in the table refers to the width of the distribution and it was calculated as reported in Section 2.6.5.

It can be noted that slip occurs at different shear rate values in the three sets. In the first, slip appears at around 2.60 s^{-1} , in the second slip occurs at approximately 13.00 s^{-1} and in the third one slip occurs at around 3.90 s^{-1} . Although, the slip of the foams belonging to the same set occurs at very similar shear rates, due to the differences in viscosity among the compared foams, it is more indicative to compare the shear stresses at which slip occurs; these are summarized in Table 3. 3. Figure 3. 28 shows the dependence of the shear stress at which slips occurs on both bubbles size and distribution span.

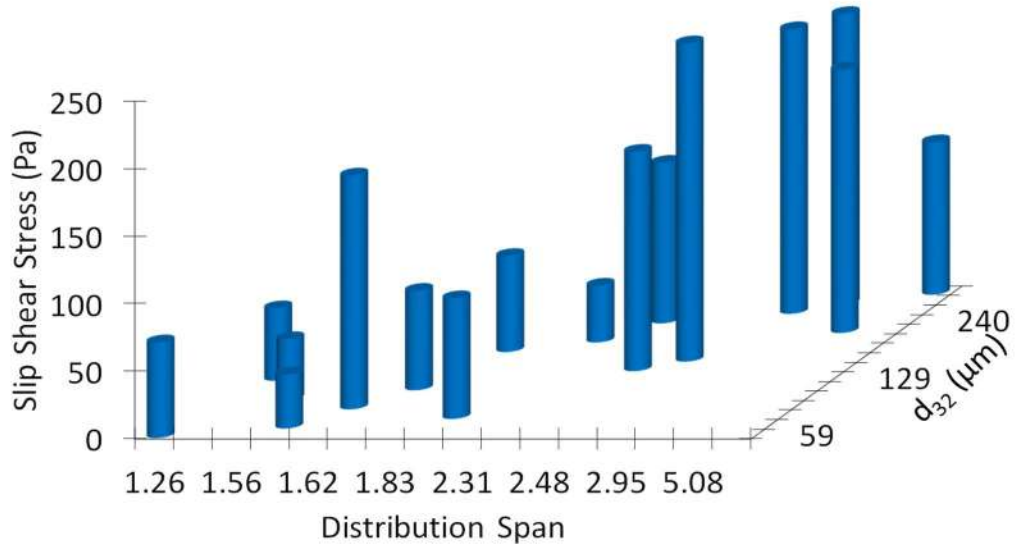


Figure 3. 28: Slip shear stress as a function of bubble size and distribution span

Figure 3. 28 shows that a higher shear stress is necessary to observe slip when bigger bubbles and larger distribution spans are present. These results show the dependence of slip on the structural properties of the foam. *Meeker et al.* proposed that slip in soft particle systems is based on an elastohydrodynamic lubrication (EHL) mechanism. EHL occurs when soft particles deform and develop flat facets at hard surface under shear. The increased effective area of the particles promotes hydrodynamic lubrication with the thickness of the slip layer depending on the balance between lift force and the repulsive forces generated by the tendency of the particles to regain sphericity; these forces are depending on the particles elastic modulus [169] [170]. The elastic modulus of bubbles can be described by the Gibbs elasticity term expressed as follow [171]:

$$G = 2 \frac{d\sigma}{d\ln A_t} \quad (3.27)$$

where σ is the gas-liquid interfacial tension and A_t is the total surface area of the bubble which is, in turn, radius dependent. Although it was not possible to determine the value of the elasticity

modulus due to the nature of the system, these relationships describe the dependence of slip on bubble size. Despite the artificial nature of the slip, it is interesting to outline its dependence on the structural characteristics of the foam.

The visco-elastic properties of the foams were tested following the testing procedure reported in Section 3.5.3. All the foams presented a similar trend so, for simplicity, only one representative oscillation curve is presented in Figure 3. 29.

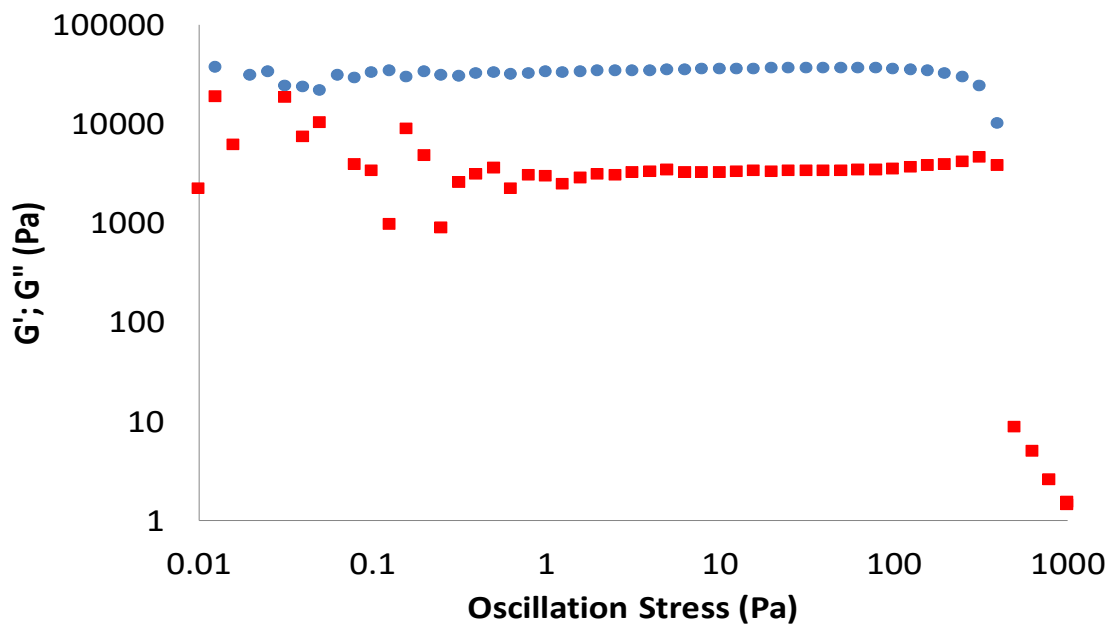


Figure 3. 29: Amplitude sweep curve for one of the produced foams: (●) G' , (■) G''

It should be noted that ceramic foams present quite an extensive linear viscoelastic region (LVER). In the LVER G' presents higher values with respect to G'' indicating that at deformations within the linear viscoelastic region ceramic foams behave more like an elastic solid. All the foams presented a LVER which extended beyond 100 Pa with the foam from experiment 8 extending to 500 Pa. The end of the LVER can be used as an indication of the maximum stress at which the foam can be subjected without destroying its structure. In fact, it has already been mentioned that particles stabilised foams behave like soft spheres giving a solid-like behaviour to the foam. It is

expected that, as the stabilized bubbles are broken, the foams behaves more like a viscous fluid. This aspect could be particularly relevant in the foam post-processing (e.g. extrusion or forming), where the material could be subjected to stresses higher than those experienced during its manufacture. In these operations knowing the maximum stress at which the foam can be subjected without destroying its structure is fundamental to retain the required product specifications.

3.11 Conclusion

In this chapter, the manufacturability of ceramic foams has been studied; in particular, the process parameters affecting the foam properties have been identified and include porosity and bubble size distribution. The effects of impeller speed, impeller diameter, gas flow rate, sparging time and sparging disk mean pore size have been investigated through design of experiment (DoE) in which foam density, foam porosity, foam stability and bubble size distribution were selected as responses. From the experimental work, it was established that foam stability is not dependent on its manufacturing process but is only affected by the initial ceramic slurry formulation. It was determined that sparging time, air flow rate and impeller speed are the major factors affecting foam density and porosity while impeller speed, impeller diameter and the interactions between sparging time and air flow rate and between impeller diameter and the mean pore diameter of sintered disk have an impact on bubble size. To facilitate the process scale-up, foam porosity and foam bubble size distribution were plotted as functions of different global mixing parameters. Correlations capable of describing the investigated system were not found in the literature; this is due to the transient flow behaviour of the investigated system and the change in its physical properties during the foaming. The system was better described by equations valid for turbulent systems and those were used to correlate foam porosity and bubble size to dimensionless numbers describing the

studied system. As expected, in both cases, differences in the exponent values were found compared to literature but the used relationships were well correlated by the experimental data. It is important to remark that, due to the complexity of the system and the number of assumptions made during the study, the new exponents are relevant exclusively for the current system and future work is necessary to identify a general correlation.

To fully characterize the structure of the foam, rheological measurements were carried out. Slip was observed in the rheological data whose onset was dependent on foam structure as measured by the mean Sauter diameter and distribution span. The viscoelastic properties of the foams were also investigated through an amplitude sweep test showing that foams behave more like viscoelastic solids with the end of the linear viscoelastic region occurring over 100 Pa.

This chapter highlighted the complexity of the manufacturing process of ceramic foams. Nonetheless, relationships proposed in the literature were shown to be able, upon adjustment of the exponents, to correlate the experimental data. This allows the manufacturing process to be tuned to the desired foam structure. The existence of a correlation between foam rheology and its structural properties, such as bubble size and distribution, could be the starting point to develop an at-line measurement to check the evolution of the foam structure during its manufacture.

Chapter 4

Testing of ceramic foam supported catalysts in Fischer-Tropsch Synthesis

4.1 Introduction

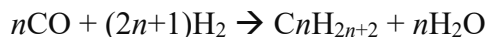
In the previous two chapters, the effects of both the formulation of the initial ceramic slurry and the effects of the process parameters on the foam structure have been described. In this chapter, the testing and comparison of foam and conventionally supported cobalt catalysts for Fischer-Tropsch synthesis (FTS) will be presented. FTS is a gas-to-liquid (GTL) process in which syngas is converted to hydrocarbons through the use of a catalyst [172] [173]. GTL processes have been increasing in interest since they allow the economic extraction of gas deposit located in areas where it is not economical to build a pipeline; liquid hydrocarbons are, in fact, more readily transported than methane. GTL processes also allow refineries to convert some of the flare gas (waste product) into valuable hydrocarbons. It is estimated in fact that over 150 billion cubic meters of natural gas are flared annually; this corresponds to approximately 30% of EU annual gas consumption [174]. GTL includes, among the others, the methane to methanol process where methane is converted in syngas and reacted to form methanol, the methanol to gasoline (MTG) where the methanol produced in the previous reaction is converted to gasoline and the methanol to olefins process (MTO) where methanol is converted in olefins which constitute the building blocks for several chemical process. As previously said, in this chapter attention is posed on the FTS. The process was invented by Franz Fischer and Hans Tropsch in 1923 while working at the Kaiser-Wilhelm-Institute for Coal Research (Mülheim, Germany), converting a mixture of carbon monoxide and hydrogen to hydrocarbons using an iron catalyst [175]. The first FTS pilot plant was built in Oberhausen (Germany) in 1934 while the first modern large-scale plant, with a production capacity

of 500 barrels per day (bpd), was operated by Sasol in South Africa in 1955 (Sasol I). Two other large-scale plants followed in 1980 (Sasol II) and 1982 (Sasol III), both with a capacity of 20,000 bpd [176]. Later, two plants operating on offshore methane were built in South Africa (Mossgas plant, now Petro SA) in 1992 and Malaysia (Shell Bintuli plant) in 1993 with production capacities of 20,000 and 15,000 bpd respectively. In 2005, a joint venture between Sasol and Qatar Petroleum (Oryx GTL) commissioned another GTL plant in Qatar in alliance with Chevron and produces 34,000 barrels per day. In 2011 the Shell Pearl GTL plant delivered the first commercial shipment while from 2012 it achieved full ramp-up; it is currently the world's largest GTL plant with a production of up to 140000 barrels per day. In the next sub-chapters, an introduction to FT chemistry, FTS processes and the proposed reaction mechanisms is given, then the role of catalyst formulation and mass transport on FTS performance is described. This is followed by a brief overview of the analytical techniques used to characterise the tested samples, then the experimental results are presented and discussed.

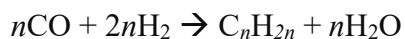
4.2 Fischer-Tropsch reaction and reactor technologies

In the Fischer-Tropsch reaction syngas is polymerised to produce various oligomers regularly distributed along the carbon number range. [177]. The main reactions are those leading to the formation of paraffin and olefin:

Paraffin formation:

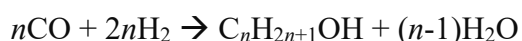


Olefin formation:



By-products formed during FTS are alcohols and carbon dioxide; these are formed in the following side reactions:

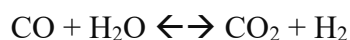
Alcohol production:



Boundouard reaction:



In the reactions showed above n is the carbon number and it depends on a number of factors such as the H_2/CO ratio in the syngas and the type of catalyst used; depending on these factors either paraffin or olefin formation predominates [178]. Paraffin formation is favoured by high H_2/CO ratios (natural gas derived syngas) and catalysts with strong hydrogenating abilities while olefin formation is favoured by low H_2/CO ratios (coal derived syngas) and a catalyst with lower hydrogenating abilities [179]. A by-product of FTS is water; its presence negatively affects syngas conversion, hydrocarbon selectivity and catalyst longevity [180]. Another reaction occurring during FTS is the Water Gas Shift reaction (WGS):



This reaction consumes CO and water (formed during FTS) and converts the reactants in hydrogen and carbon dioxide. WGS activity is high over potassium promoted iron catalysts; iron catalyst and the consequent WGS reaction are used to make-up the deficit of H_2 in coal derived syngas [181].

As previously said, FTS is a polymerisation reaction and its probability of chain growth is independent of chain length; therefore, selectivity to various hydrocarbon (notably carbon chain

length) can be predicted based on a simple statistical distribution calculated from chain growth probability. *Anderson, Shulz and Flory* (ASF distribution) proposed a chain polymerization model represented by the equation below [182]:

$$W_n = n(1 - \alpha)^2 \alpha^{n-1} \quad (4.1)$$

where W_n is the weight percent of a hydrocarbon containing n carbon atoms and α is the chain growth probability. The latter is expressed by (4.2) where r_p and r_t are the rate of propagation and termination respectively.

$$\alpha = \frac{r_p}{r_t + r_p} \quad (4.2)$$

A graphical representation of the product distribution is given in Figure 4. 1.

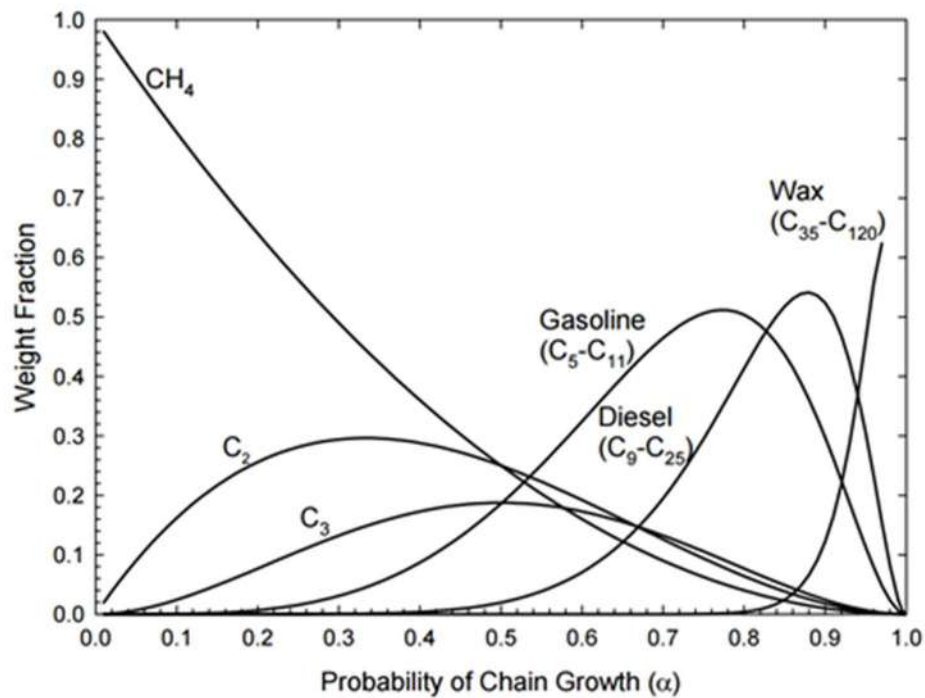


Figure 4. 1: Anderson-Shulz-Flory Distribution [182]

The ASF pattern always leads to a gradual decrease in selectivity with an increase in carbon number which limits the formation of desired middle distillates and heavy hydrocarbons (wax) [183] however, studies show that the ASF is seldom obeyed with common deviations being relatively high yield of methane and relatively low yield of ethane [184].

FTS is a highly exothermic reaction making the reactor design challenging; high temperatures in the reactor, in fact, leads to excessive methane yields, carbon deposition and catalyst loss due to particle fragmentation [185]. Three main reactor configurations have been used commercially: fixed bed, fluid bed and slurry bubble columns [186]; Figure 4. 2 shows a schematic of the three configurations.

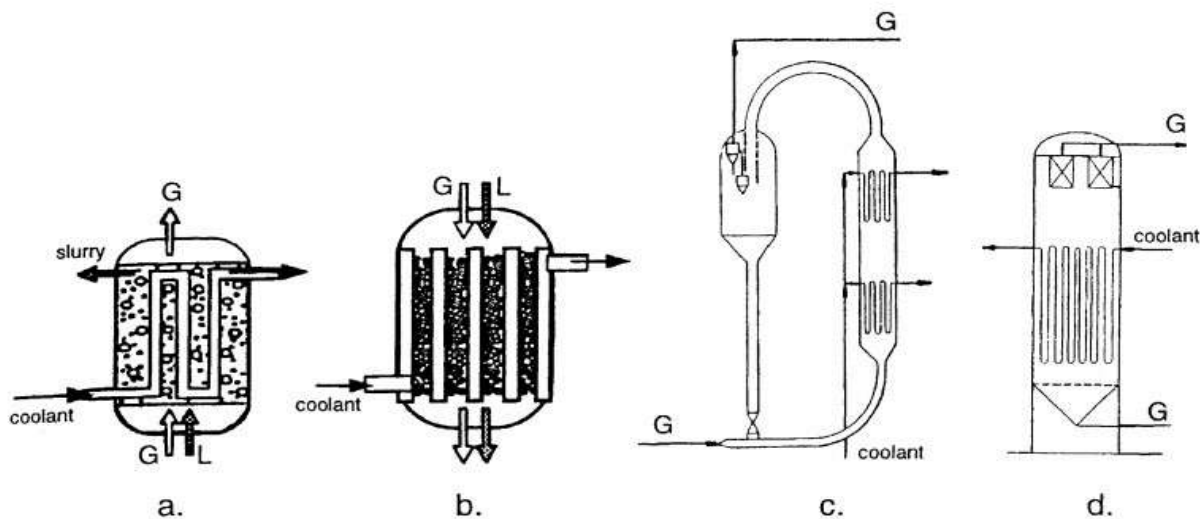


Figure 4. 2: Possible reactors for the FTS: (a) slurry bubble column reactor; (b) multi-tubular trickle bed reactor; (c) circulating; (d) fluidized-bed reactor [G: gas, L: liquid] [186]

The **fixed bed tubular reactor** (Figure 4. 2 b) is one of the most competitive technologies and is used at commercial scale by Sasol [187] and Shell [188]. This type of reactor operates at about 220 °C and 25-45 bar. Heat removal is achieved by utilising steam that is generated at the shell side of the reactor however, this is not really effective and results in axial and radial temperature profiles

in the tubes. This reactor configuration normally produces complex mixtures consisting of hydrocarbons ranging from methane to wax. To reduce the pressure drop in the tube, the use of catalyst particles of a few millimetres is necessary; this results in intra-particle diffusion limitation [188]. The major problems of fixed bed tubular reactors is the cost associated with their assembly and the fact that on-line changing of the catalyst is not permitted resulting in long down times of the reactor.

Another possibility is the use of **fluidised reactors**; these consist of a gas and solid phase and they can have either a fixed (Figure 4. 2 d) or a circulating bed (Figure 4. 2 c). In the first one the catalyst bed remains stationary and the gases pass upward through the bed while, in the second one, the catalyst is entrained in the fast moving gas stream. The Synthol reactor used by Sasol is a circulating bed reactor; in this set-up, a fine catalyst bed is entrained by a high velocity gas stream through a riser reactor. The catalyst is then separated from the effluent by cyclones and is then returned to the reactor inlet; two cooling zones are used in the riser to remove the heat of reaction. The main disadvantage of this configuration is that should any poison enter the reactor, the entire bed is poisoned.

The last reactor option is the **slurry bubble column reactor** (Figure 4. 2 a), in these three-phase reactors syngas is distributed from the bottom and rises through the slurry that consists of predominantly the FT wax product (high thermal capacity liquid) with the catalyst particles suspended in it. As the reaction proceeds, the heavy hydrocarbons form part of the slurry while gaseous products and water diffuse through the gas bubbles and are removed. In this configuration, if the slurry phase is sufficiently well mixed, it is possible to operate in isothermal conditions [189];

this results in the possibility of operating at higher temperature without the risk of catalyst degradation. Higher reactor temperatures results in higher CO conversion to products.

4.3 Fischer-Tropsch proposed reaction mechanism

The FTS reaction mechanism has been a topic of much debate since a mechanism was first proposed by *Fischer and Tropsch* in their original paper [190]. A key point of contention is whether the chemisorbed CO first dissociates into C and O atoms. In general, it is recognised that the FT reaction follows the sequence of reactant adsorption, chain initiation, chain growth, product desorption and re-adsorption of reactive products and further reaction. Initially, *Fischer and Tropsch* proposed the formation and hydrogenation of metal carbides to give methylene groups (CH_2) on the surface of the metal which then polymerise to yield the observed products [190]. This mechanism takes the name of **surface carbide mechanism** and is illustrated in Figure 4. 3. This mechanism was supported by *Craxford and Rideal* who proposed that CO is adsorbed onto the metal surface and, in the presence of hydrogen, dissociates and subsequently forms water and chemisorbed carbon; the latter is subsequently hydrogenated to form chemisorbed CH_2 which oligomerises to produce higher hydrocarbons [191]. *Browning and Emmett* recognized that the surface carbide mechanism was inconsistent with thermodynamic data for the formation of hydrocarbons by carbide hydrogenation at the reaction temperature [192] while *Evans and Nash* pointed out that the mechanism did not explain the formation of oxygenated products [193].

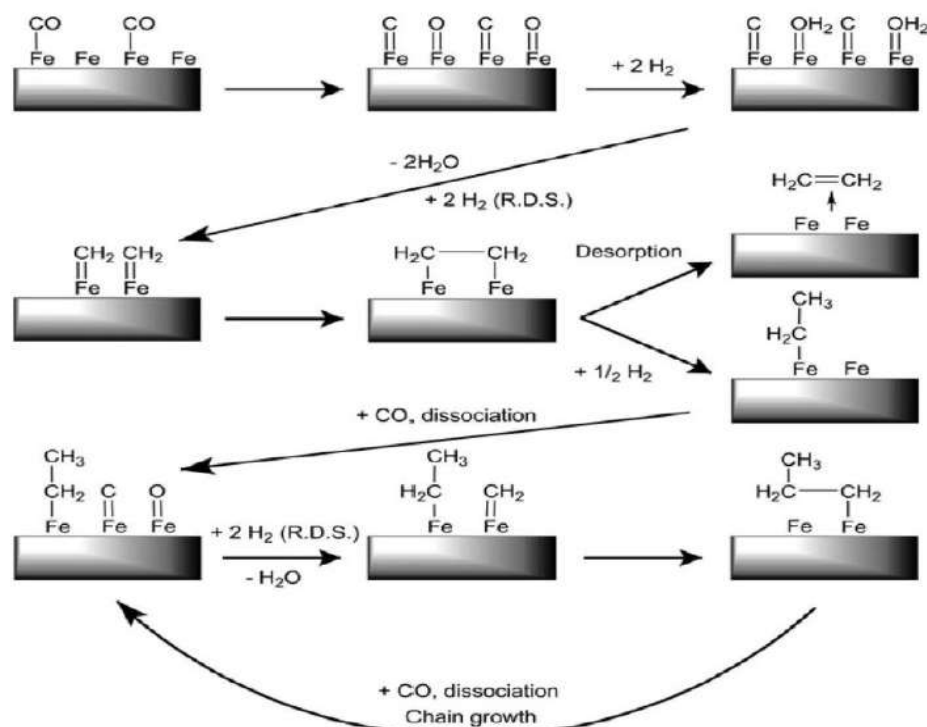


Figure 4. 3: Surface carbide mechanism. The rate determining steps (R.D.S.) are indicated in the scheme [194]

Kummer *et al.* proposed the **surface enol mechanism** in which the chain grows by undissociative chemisorption of CO which then reacts with adsorbed hydrogen to form enolic (HCOH) units; chain growth is then obtained by a combination of surface polymerization, condensation and water elimination steps using adjacent groups (Figure 4. 4) [195]. Hall *et al.* added ^{14}C -labelled alcohols or alkenes to the syngas feed. The distribution of the stable isotopically labelled products was analysed and showed that the added alkenes or alcohols were able to initiate chain growth. This was confirmed by the fact that when 1% ^{14}C marked ethylene was added to syngas and passed, at 1 atm, over an iron catalyst about 12% of the hydrocarbon formed from ethylene. The percentage increased to 50% when 1.5% marked propanol or propionaldehyde were added to the synthesis stream [196].

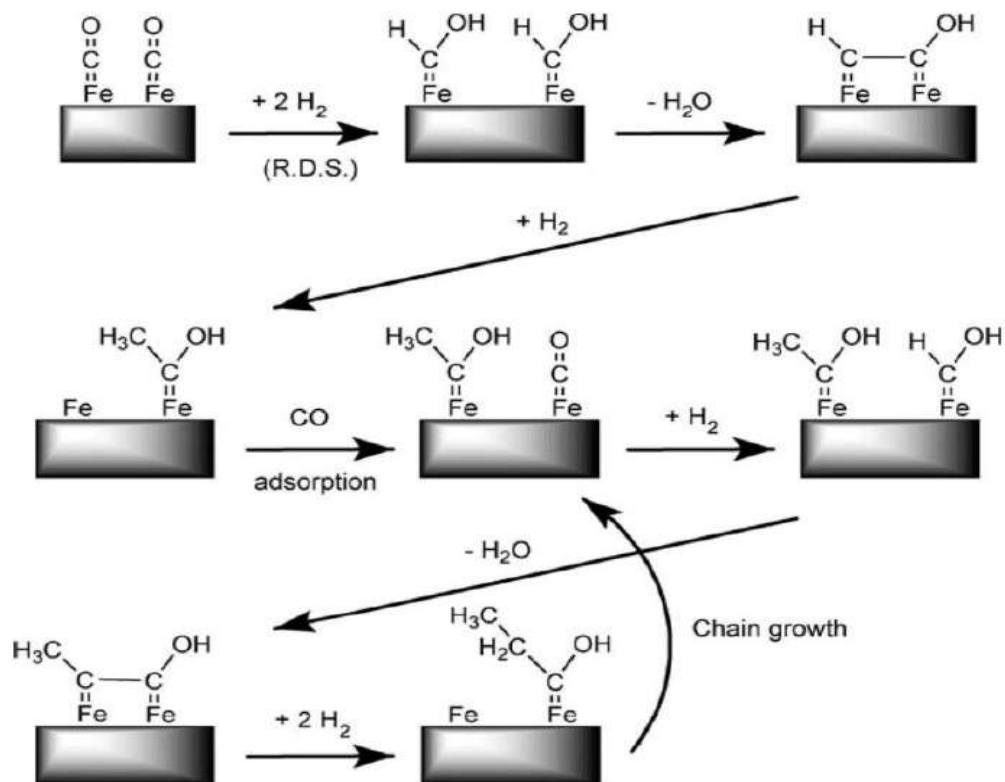


Figure 4. 4: Surface enol mechanism. The rate determining steps (R.D.S.) are indicated in the scheme [194]

In 1958 Wender *et al.* proposed the **CO insertion mechanism** in which the initiation step involves the insertion of a CO molecule into a metal-H bond, the resulting aldehyde is then hydrogenated to CH_3 in a rate determining step; CO insertion then occurs as shown in Figure 4. 5.

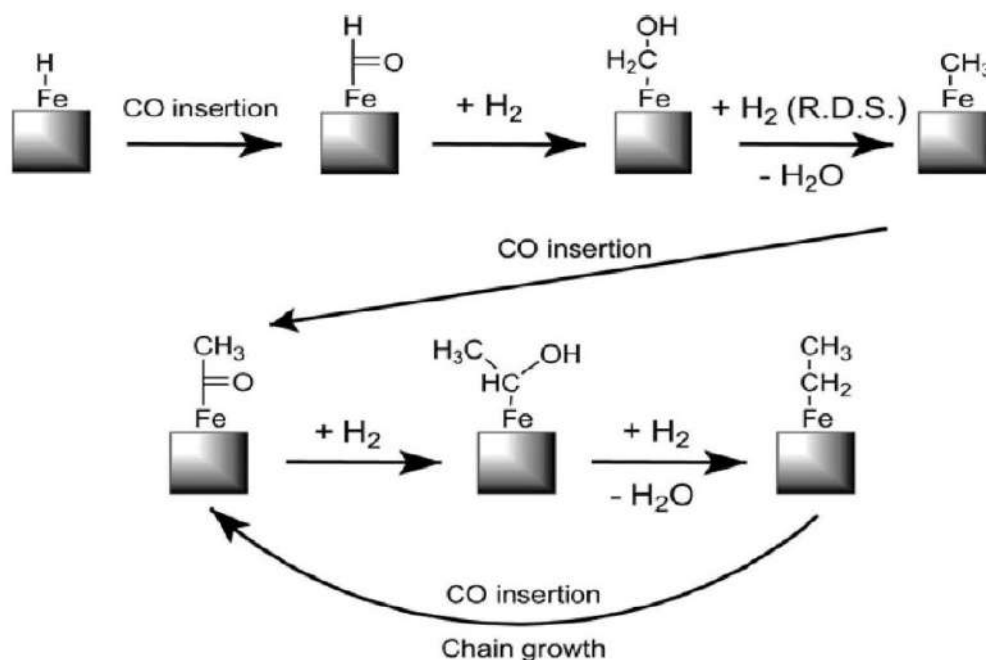


Figure 4. 5: CO insertion mechanism. The rate determining steps (R.D.S.) are indicated in the scheme [194]

Maitlis *et al.* proposed the **alkenyl mechanism** in which surface alkenyl are suggested as polymer chain carriers [197]. Figure 4. 6 shows that the chain starter vinyl species ($-\text{CH}=\text{CH}_2$) is formed by the reaction of a surface methyne ($\equiv\text{CH}$) and surface methylene species ($=\text{CH}_2$); chain growth then occurs by coupling of an alkenyl carbon with a methylene carbon to form an allyl species ($-\text{CH}_2\text{CH}=\text{CH}_2$). The surface allyl species then isomerises to the more reactive propenyl species ($-\text{CH}=\text{CHCH}_3$) with termination occurring by the reaction between surface hydrogen and the surface alkenyl species leading to predominantly α -olefins. This mechanism explains the formation of branched products (by allyl isomerization), the low amount of C_2 products and the release of the 1-alkenes as primary products (by favourable hydrogenation reaction) but it is not able to describe the formation of n-paraffins and oxygenates showing significant limitations considering that n-paraffins are the dominant products in FTS.

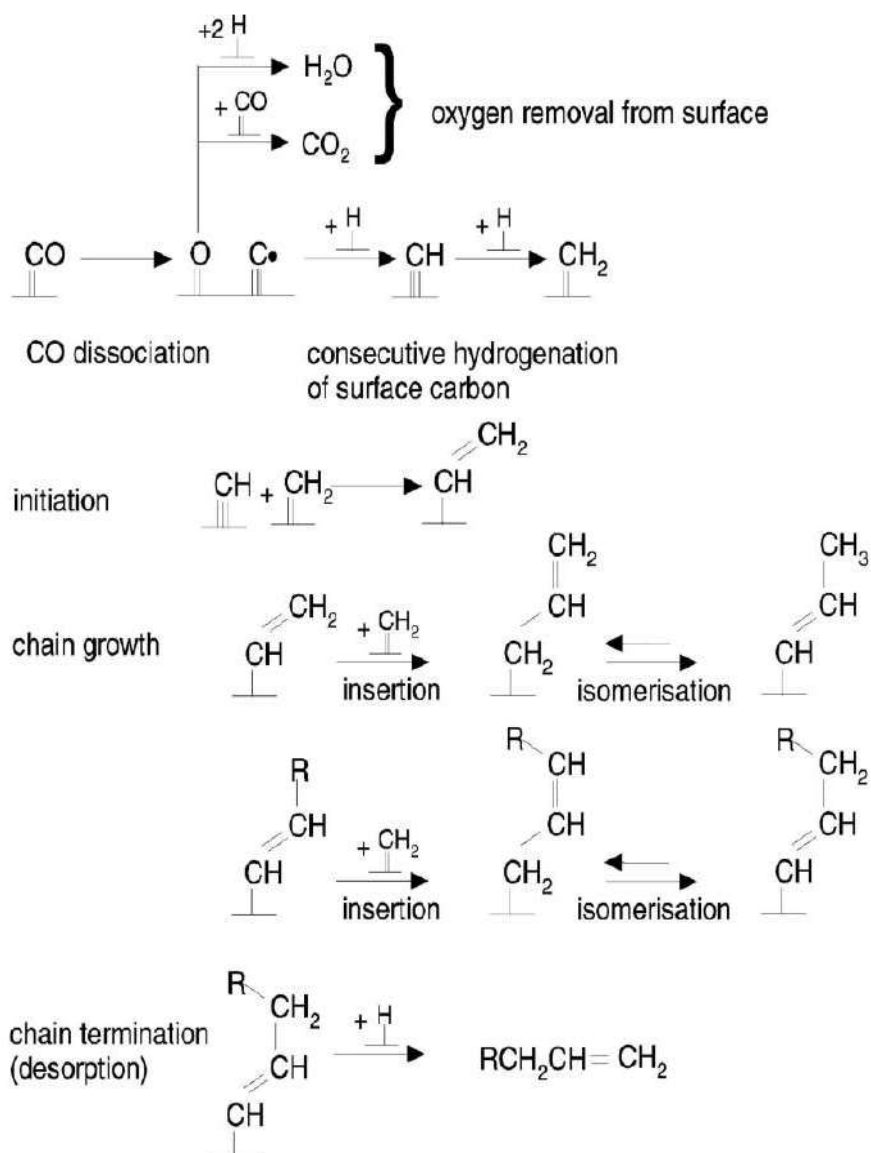


Figure 4. 6: Alkenyl chain growth mechanism [198]

Although different mechanisms have been proposed, it is generally recognised that FT is substantially a polymerisation reaction, kinetically controlled by the addition step of $-\text{CH}_2-$ groups on a catalyst surface. FTS is characterized by relatively high selectivity towards products in the spectrum of a mixture of linear and branched hydrocarbons and α -olefin and oxygenated products.

4.4 Effects of catalyst formulation on FTS

Different active metals can be used in FTS and their choice is critical since it effects the product distribution. The first FTS catalyst used by *Fisher and Tropsch* in 1923 was an iron catalyst but also cobalt, nickel and ruthenium have been shown to be catalytically active in FTS. Nickel presents an undesirable high methane selectivity; it is after all the state of the art catalyst for methanation. Ruthenium, although the most active element for FT, is too expensive making it unsuitable for large-scale industrial use. Iron catalysts find wide application in industry thanks to their relatively low cost and their tolerance to flexible operative conditions [199]. Iron catalysts are usually promoted with alkali (e.g. potassium or sodium) to increase the average molecular weight of the produced hydrocarbons and to promote the water-gas-shift reaction (WGS) [200]. This reaction favours the use of syngas having a low H_2/CO ratio since it in-situ produces additional H_2 by the reaction between feed- CO and the FTS produced H_2O [201]. Some of the problems associated to the use of iron-based catalysts are the high deactivation rates and the relatively short catalyst life time. Co has a higher hydrogenation activity than Fe, resulting in higher yields of high molecular weight paraffins and less oxygenated by-products. Co catalysts are more active than Fe catalysts but the final catalyst formulation is more expensive. For this reason, they are only used industrially as supported catalysts; common supports are SiO_2 [202], TiO_2 [203] and Al_2O_3 [204]. The effects of different catalyst properties such as crystal size, crystallite distribution, type of support and catalyst acidity on the FTS reaction will be discussed below. Since Co was used in the experimental work, further discussions will be referred to this metal.

4.4.1 Effects of crystal size and crystallite distribution on FTS reaction

In the introduction to the thesis a general description of the effect of crystal size, metal surface area etc. on the catalyst performance has been given; in this section the effects of crystal size and crystallite distribution on FTS is given. *Barbier et al.* observed that the turn-over-frequency (TOF) and the polymerization probability were significantly enhanced when the Co crystal size was increased from 4 to 9 nm [205]; a similar behaviour was observed by *Bezemer et al.* and *Borg et al.* for carbon-nano-fibers [206] and alumina supported catalyst respectively [207]. In particular, *Borger et al.* conducted a detailed study of γ -Al₂O₃ with different amounts of Co demonstrating that the C₅₊ selectivity increases with increasing the Co crystal size up to 8-10 nm and then it levels out with a maximum observed at around 8-9 nm; the same maximum value was observed by *Rane et al.* using δ - and θ - Al₂O₃ with different crystal size [208]. *Eggenhuisen et al.* investigated the effects of crystallite distribution on FTS. They used a freeze-drying technique to control the cobalt particle size and its distribution on a silica support. They observed that, while conventional drying gave Co clusters of several hundred nanometers in size, freeze-drying gave an even distribution of equally sized crystallites. The authors reported that, surprisingly, Co clusters favoured C₅₊ selectivity of as much as 6% but no explanation for this observation was given [209]. *Borg et al.* controlled the crystallite distribution in the impregnation method by addition of ethylene glycol to water but no significant effect on the selectivity was found [207]. In contrast, *Marion and Roy* observed a beneficial effect of cluster formation when Co/ γ -Al₂O₃ and Co-Ru/ γ -Al₂O₃ catalysts were used [210]. Although the higher activity as the catalyst crystal size increases may be counterintuitive, a hypothesis reported in the literature is that the CO coordination is favoured on larger particles, thus increasing the CO dissociation rate and the intermediate concentration [211].

4.4.2 Effect of support material and pore structure on FTS reaction

Rytter et al. showed that the selectivity of a Co-Ru/Al₂O₃ catalyst increased by 7-8% by calcining the support to temperature where γ -Al₂O₃ is transformed to α -Al₂O₃ (Figure 4. 7 shows the thermal transformation sequence of the aluminium hydroxides).

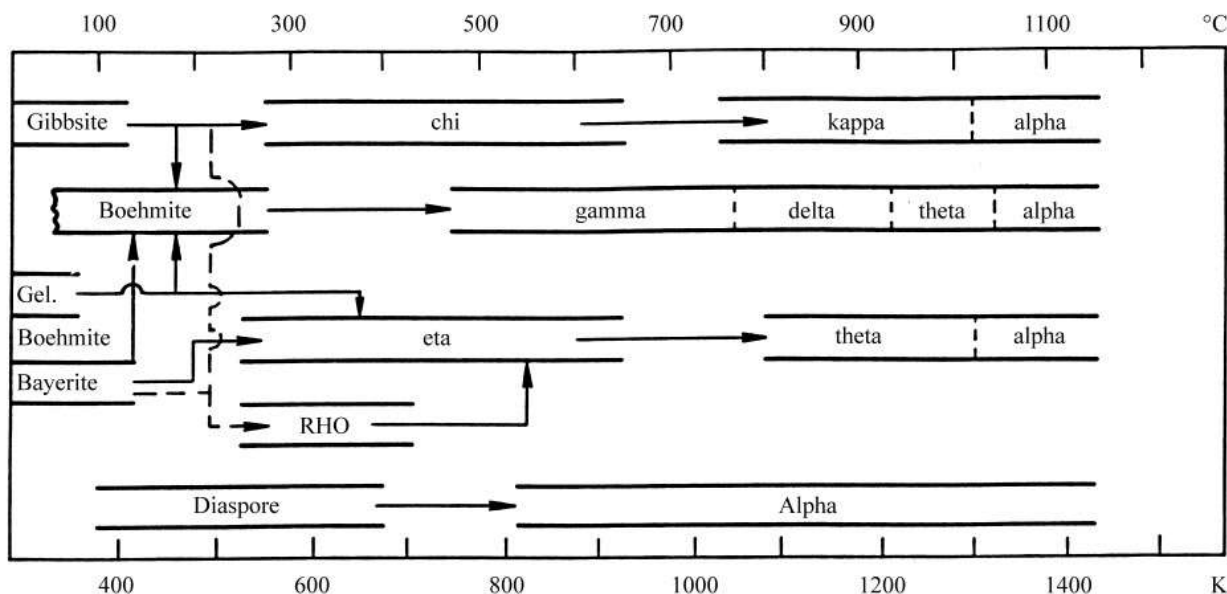


Figure 4. 7: Thermal transformation sequence of the aluminium hydroxides [212]

They observed also an intermediate enhancement of around 3% when a Ni-aluminate was used as support [213]. *Rytter et al.* also reported that titania supported catalysts usually give very high wax (long chain hydrocarbons with carbon number greater than 12) yield indicating that more inert supports are favourable in order to obtain a higher C₅₊ selectivity [214]; this is in agreement with the higher selectivity observed when γ -Al₂O₃ is transformed to α -Al₂O₃. *Rane et al.* found a correlation between C₅₊ selectivity and CH_x coverage on Co [215]; this observation is in agreement with *den Breejen et al.* who proposed that an increased CH_x coverage comes at the expenses of hydrogen coverage enhancing, consequently, chain growth. It is worth noting that the above studies are all characterised by large pore supports. *Rytter et al.* deduced that the pore structure may

influence the selectivity in FTS; they tested γ -aluminas of the Sasol GmbH CCA family having narrow and wide pores. The authors observed that a significantly higher selectivity of around 4% in C_{5+} was obtained when the wide pore aluminas were used [213] [216]. One of the hypotheses proposed by the authors was that wide pores are formed by larger crystallites and, as previously reported, larger crystallites favour C_{5+} selectivity.

4.4.3 Effects of acidity and surface modification of FTS

In the previous section it has been showed that α -alumina and titania are the supports that give the highest wax production, so it could be assumed that low-acidity is beneficial to obtain higher selectivity. This hypothesis seems to be confirmed by Shell's approach to cover the silica surface with zirconia and titania [214]. A similar surface modification approach was used by *Shi et al.* The authors hydrolysed the surface of silica supports to chemically modify it. In particular *Shi et al.* obtained a hydrophobic surface, stable to 400 °C, through methyl *modification* with trimethylchlorosilane. Although the author reported an increase in conversion with silanation, it was surprisingly observed a decrease in the polymerisation probability [217]. *Blekkann et al.* [218] and *Lögdberg et al.* [219] demonstrated that added or in-situ produced water favour the production of higher hydrocarbons; consequently, it can be hypothesized that the conservation of hydroxyl groups has a beneficial effect that is somewhat in conflict with the low acidity requirement. *Rytter et al.* proposed that Brønsted acid sites should be favoured over Lewis sites when Fischer-Tropsch catalysts are prepared [214].

4.4.4 Effects of mass transport on FTS

The effects of external and intra particle diffusion on FTS can be easily tested in fixed bed laboratory experiments. *Rytter et al.* [216] and *Steynberg et al.* [220] proved that the film mass

transport resistance at the film-catalyst interface can be considered negligible by using different superficial gas velocities. On the other hand, *Rytter et al.* showed in their work that catalyst particle size has a significant effect on the selectivity [216]. They observed that the selectivity to C₅₊ is essentially constant up to particle size equal to 350 µm but then drops off for the sample having a particle size of 650 µm. They ascribed this loss in selectivity to the faster diffusion of H₂ than CO that in turn leads to higher H₂/CO ratio in the inner part of the larger particles. The authors also concluded that the pore size characteristics do not have an effect on the selectivity, with the diffusion depending mainly on the transport length. This last observation is in contrast with the observations of *Iglesia et al.* [221] who propose that the C₅₊ selectivity depends on a structural parameter χ defined as:

$$\chi = \frac{R_0^2 \varphi \theta_M}{r_p} \quad (4.3)$$

where R_0 is the radius of the catalyst particle, φ is the porosity, θ_M is the density of the surface Co atoms and r_p is the mean pore radius. The authors found a “volcano-plot” trend when graphing the C₅₊ conversion as a function of the parameter χ ; they ascribed the rising part to the re-adsorption and reinsertion of α -olefins while the reduction part is associated to CO transport limitations. The equation above was further analysed by *de Deugd* who argued that the porosity term should be moved to the bottom; in addition, the author showed that the parameter χ is independent of the particle size [222].

Until now the diffusion limitation of syngas has been discussed, evidently, the products are more prone to diffusion limitation especially when they become longer chained. *Rytter et al.* demonstrated that the product distribution is effected by mass transport; in particular, the olefin/paraffin ratio decreases as the particle size is increased. The authors proposed that the longer

residence time in the pores facilitates the hydrogenation of the olefins suggesting that, in first approximation, the hydrogenation of the olefins is diffusion controlled and takes place independently of chain growth [216]. Although the literature do not always agree on which are the support structural characteristic that effects the catalyst selectivity, it is clear that the different diffusion of the reactant and products have an effect on the final product distribution. For this reason, it is expected that the particular structure of foam supported catalyst may be beneficial in term of C₅₊ selectivity.

4.5 Catalyst Characterization Techniques

The tested catalysts were characterized using a range of techniques to determine the underlying reasons behind the differences in catalyst performances observed. Five main analytical techniques were used: X-Ray Diffraction (XRD), N₂ physisorption, H₂ chemisorption, NH₃ Temperature Program Desorption (TPD), Mercury Intrusion Porosimetry (MIP) and Scanning Electron Microscopy (SEM). A brief description of these techniques will be given in order to introduce the significance of the characterization results that will be presented in the experimental section.

4.5.1 X-Ray Diffraction (XRD)

X-Ray Diffraction uses X-Rays to determine the atomic/molecular structure of a crystal. This technique can be used either on single crystals (X-Ray crystallography) or on powder samples (Powder X-Ray Diffraction). Crystals are formed by regular arrays of atoms which are able to scatter X-Rays producing secondary spherical waves emitted from the electrons; this phenomenon is called elastic scattering. The produced waves cancel each other in most directions due to destructive interference but they add constructively in specific directions described by the Bragg's law [223]:

$$2d\sin\theta = n\lambda \quad (4.4)$$

where d is the spacing between diffracting planes, θ is the incident angle, n is an integer and λ is the beam wavelength. These specific directions appear as spots on the diffraction patterns and they are used to obtain structural information about the investigated sample or to identify unknown samples. The latter is usually achieved by comparison of the unknown diffraction pattern with a known sample or to a database such as the International Centre for Diffraction Data (<http://www.icdd.com/>). The success of X-Rays to investigate the structure of crystals is due to their characteristic wavelengths being the same order of magnitude of the spacing (d) between the crystal planes. In this work however, a Powder X-Ray Diffractometer was used to determine the crystal size of the active metal. The crystal size can be determined using the Scherrer equation which relates the size of sub-micrometer crystallites to the broadening of a peak in a diffraction pattern [224]:

$$\tau = \frac{K\lambda}{\beta\cos\theta} \quad (4.5)$$

where τ is the mean size of the crystalline, K is a dimensionless shape factor with a value close to unity, λ is the X-Ray wavelength, β is the line broadening at half the maximum intensity (FWHM) after subtracting the instrumental line broadening and θ is the Bragg angle. It is important to point out that the Scherrer equation provides the lower bound on the crystallite size since peak broadening can be due to different effects such as inhomogeneous strain and crystal lattice imperfections [225]. A schematic of an X-Ray diffractometer is given in Figure 4. 8.

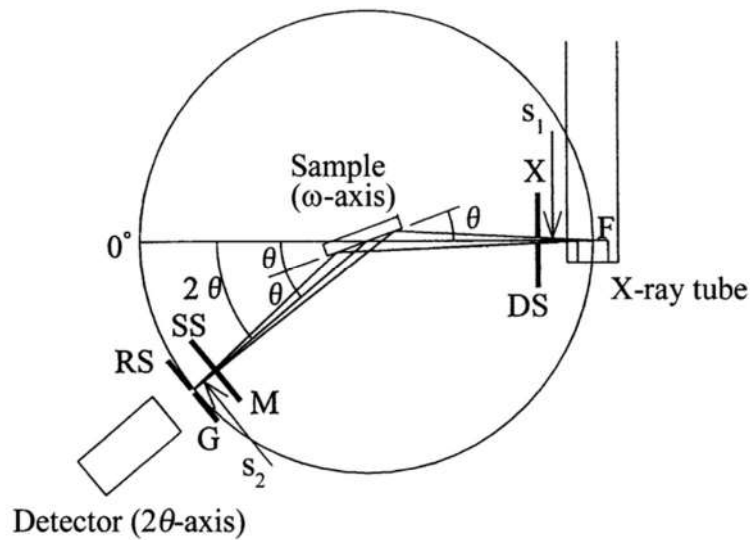


Figure 4. 8: X-Ray diffractometer schematic [226]

The X-Ray diffractometer is composed of two axes (ω and 2θ) of independent rotation. The X-Ray source (F), the sample holder (S) and the detector (G) lie on the circumference of a circle called the focusing circle [226]. The X-Ray source is usually an X-Ray tube in which electrodes are “boiled-off” of a cathode and accelerated through a strong electric potential (around 50 kV). Once the electrons have reached high speed these are collided with a metal plate (usually copper) which in turns emits spectral lines corresponding to the excitation of the inner-shell electrons of the metal. The pattern of diffraction spots can be observed on a screen behind the sample; the relative intensity of these spots provides the structural information about the sample. Typical detectors used to measure the intensity of these reflections are either a photographic film or, more commonly, a Charge Coupled Device (CCD) image sensor. In order to maintain the angle between the plane of the sample and the direction of the incident X-ray beam equal to that of the direction of the diffracted beam, the 2θ axis is rotated two times as much as the ω axis. To minimize the angular dispersion and to improve the spatial resolution for the incident X-Ray beam a series of slits are

inserted into the X-Ray path. The divergent slits (DS) and the scattering slits (SS) are set to restrict each horizontal dispersion of both the incident and diffracted X-Ray beams while the receiving slit (RS) in front of the detector is set to determine the spatial resolution [226].

4.5.2 N₂ Physisorption

N₂ physisorption uses the physisorption of non-reactive species on the surface of a sample to characterise its porous structure. Physisorption forces tend to weakly bind the adsorbate onto the solid surface when a balance is achieved between the intermolecular attractive (e.g. Van der Waals forces) and repulsive forces. The amount of probe-molecule adsorbed on the surface depends on the equilibrium pressure, the temperature and the nature of the gas-solid system [227]; Figure 4. 9 shows the different stages involved in the physisorption process.

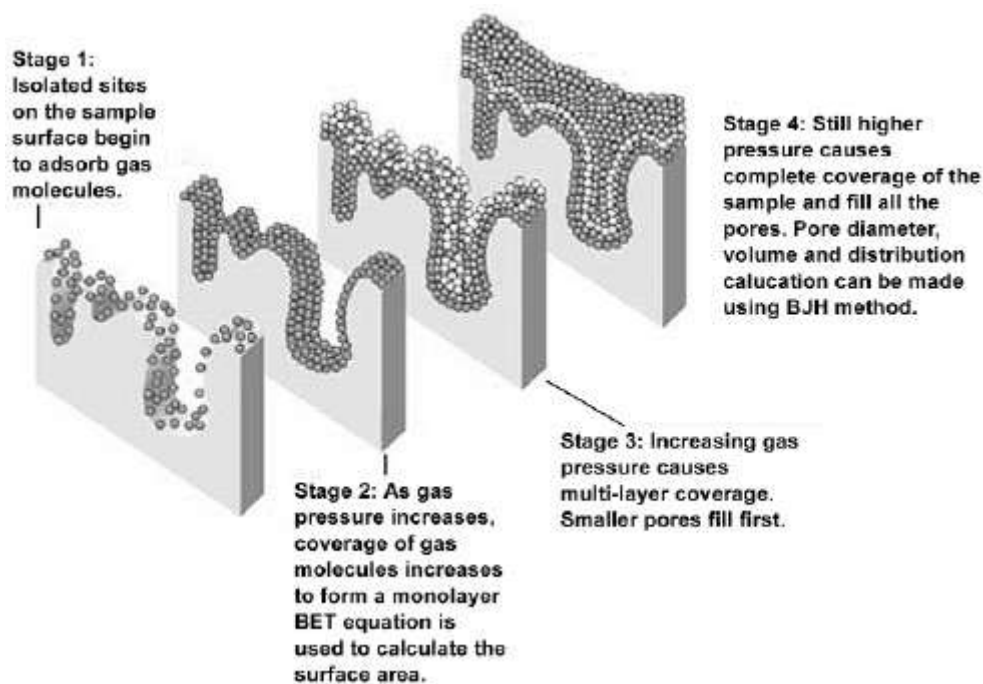


Figure 4. 9: Stages involved in the physisorption process [228]

In the first stage few sites of the samples surface adsorb the gas molecule, increasing the gas pressure the coverage of the surface increases until a monolayer is formed. Further increasing the gas pressure leads to multi-layer coverage until complete coverage of the sample and fill of all the pores is reached.

If the amount of adsorbed gas is plotted against $\frac{p}{p^0}$, where p is the equilibrium pressure and p^0 is the saturation pressure, six different types of isotherms can be obtained; these are shown in Figure 4. 10.

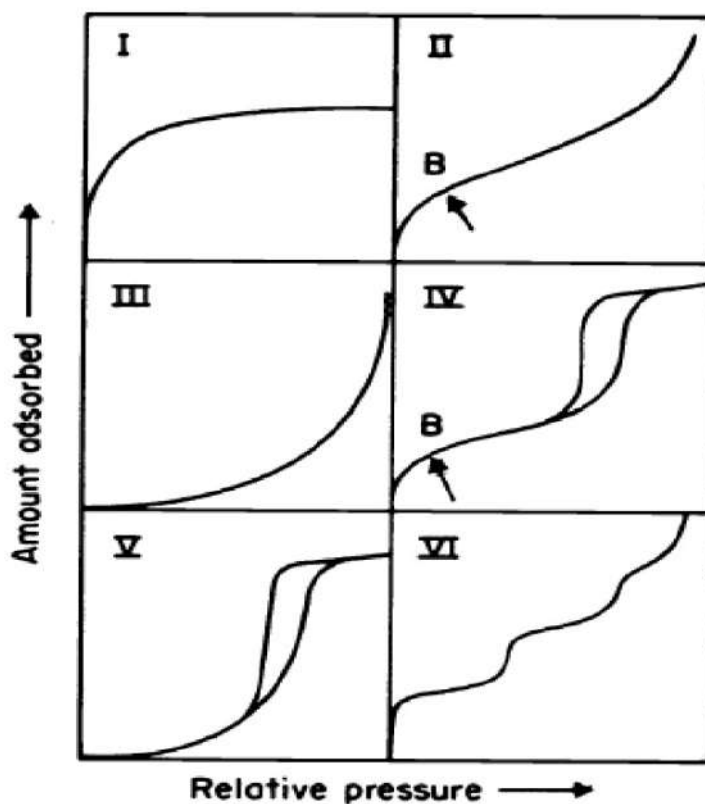


Figure 4. 10: Different types of adsorption isotherms [229]

Type I isotherm usually refers to adsorption on microporous solids where the amount adsorbed approaches a limiting value as the relative pressure is increased, type II isotherm presents an initial intermediate region where monolayer adsorption occurs (point B) followed by multilayer

adsorption; this isotherm is usually characteristic of non-porous or macroporous materials. Type III isotherms are convex to the p/p^0 and consequently does not present a point B; these isotherms are representative of weak attractive forces between the adsorbate and the adsorbent, in addition, the absence of a flat part suggests the absence of the monolayer formation. Type IV isotherm present a point B and multilayer adsorption but the saturation point is reached at a pressure below the saturation pressure indicating capillary condensation of gas in narrow pores. Type V isotherms, as in the case of type IV, present a hysteresis loop but they do not have a point B. Finally, Type VI isotherms represent step-wise multilayer adsorption on the adsorbate surface. The surface area of the investigated samples is commonly determined using the BET theory. This was developed by *Brunauer, Emmet and Teller* and it is based on an over-simplified model for physisorption; the equation proposed by the researchers is:

$$\frac{1}{v[(p^0/p)-1]} = \frac{c-1}{v_m c} \left(\frac{p}{p^0} \right) + \frac{1}{v_m c} \quad (4.6)$$

where v is the adsorbed gas quantity, v_m is the monolayer adsorbed gas quantity and c is the BET constant which is defined as $c = \exp \left(\frac{E_1 - E_L}{RT} \right)$ where E_1 is the heat of adsorption for the first layer and E_L is that for the second and higher layers [230]. $\frac{1}{v[(p^0/p)-1]} = \frac{c-1}{v_m c} \left(\frac{p}{p^0} \right) + \frac{1}{v_m c}$

(4.6) represents an isotherm of adsorption and it can be plotted in the form of a straight line when $1/v[(p^0/p) - 1]$ is plotted as a function of p/p^0 . The values of the slope A and the intercept I are used to calculate the monolayer gas quantity v_m and the BET constant c using the following equations:

$$v_m = \frac{1}{A+I} \quad (4.7)$$

$$c = 1 + \frac{A}{I} \quad (4.8)$$

From these values the total surface area S_t and the specific surface area S_{BET} are given by:

$$S_t = \frac{(v_m N s)}{V} \quad (4.9)$$

$$S_{BET} = \frac{S_t}{a} \quad (4.10)$$

where N is the Avogadro's number, s is the adsorption cross section of the adsorbing species, V is the molar volume of the adsorbate gas and a is the mass of the solid sample.

Barrett, Joyner and Halenda proposed an equation to determine the pore size distribution; this relates the pore volume to the pore size and is commonly referred to as the BJH equation [231].

$$\ln \frac{p}{p^0} = -\frac{2\gamma v^l}{r_k RT} \quad (4.11)$$

where γ is the surface tension, v^l is the molar volume of the liquid and r_k is the Kelvin radius of a cylindrical pore.

The isotherm of adsorption of nitrogen at the temperature of liquid nitrogen (77 K) is usually determined by gas sorption manometry. In this method, the amount of adsorbed gas is evaluated by measuring the change of gas pressure; successive amounts of the adsorbate gas are introduced in the system at each stage and a sufficient time is allowed to attain equilibrium. In this way, a series of single points are obtained which constitute the adsorption isotherm [232].

4.5.3 Chemisorption

Chemisorption analytical techniques uses the formation of surface complexes as a mean to obtain information about the investigated sample. Unlike physisorption, as the name suggests,

chemisorption involves the formation of a chemical bond between the adsorbate and the adsorbent and, consequently, the phenomenon is difficult to reverse. In addition, chemisorption is highly selective and occurs preferentially (depending on the adsorption energy) between certain adsorbate and adsorbent species. Chemisorption is a single layer process since the adsorption only occurs if the adsorbing molecule can make direct contact with the surface. In similar fashion to the physisorption, an adsorption isotherm is obtained during the analysis but this is only representative of the reactive part of the sample surface. This observation remarks the importance of the choice of the suitable probe molecule. Chemisorption tests can be carried out at either isothermal conditions or as temperature programmed test (Temperature Programmed Reaction or Temperature Programmed Desorption). The former is commonly used to determine the active surface area, the crystal size and the metal dispersion while the latter is used to characterize the nature and the strength of the sample's acid/basic sites allowing the reversal of the adsorption [233]. A more detailed description of the two techniques will be given in the next subchapters.

4.5.3.1 Isothermal chemisorption

The isothermal chemisorption experiments can be carried out using two different techniques: static volumetric chemisorption and dynamic chemisorption. In the first one precise dosing steps are required to pursue the equilibration point. This technique is convenient for obtaining high resolution chemisorption isotherms from a very low pressure to atmospheric pressure and at any temperature from ambient to 1000 °C. Dynamic chemisorption is commonly used and consists of the injection of accurately known quantities of the adsorbate. These are introduced in pulses until the sample is saturated. A thermal conductivity detector is used to measure the amount of adsorbate that was not taken up by the active metal; then, by subtracting this quantity to the initial injected

quantity, the amount of adsorbed species is obtained. Chemisorption theory assumes that the active surface of a solid contains a fixed number of adsorption sites N_s and that only one molecule at a time can occupy it. For a specific gas-solid system at certain temperature and pressure, a certain fraction θ of the active sites N_s will be occupied by n_{ads} adsorbed molecules resulting in:

$$\theta = \frac{n_{ads}}{N_s} \quad (4.12)$$

The occupancy of the active sites at different pressures (e.g. concentrations) of the probe molecule can be expressed by the Langmuir isotherm:

$$\theta = \frac{bP}{1+bP} \quad (4.13)$$

where P is the pressure of the probe molecule and b is a constant that includes the concentration-pressure proportionality (adsorption) constant and the ratio between the rate constant of adsorption and the rate constant of desorption. Figure 4. 11 shows an example of chemisorption isotherms for different values of the constant b [233].

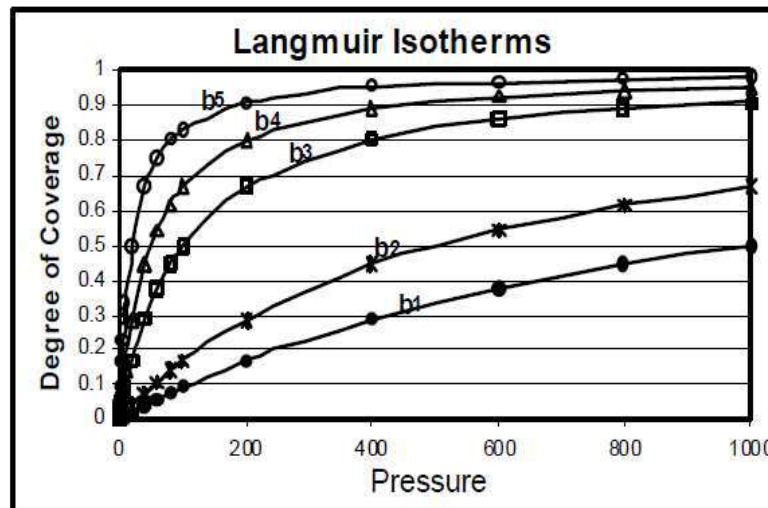


Figure 4. 11: Chemisorption isotherms for different values of the constant b [233].

It can be noted from Figure 4. 11 that the chemisorption isotherm reaches a plateau corresponding to the saturation of the active sites; this values allows to determine the active metal surface area using the following equation [234]:

$$A_m = \left[\left(n \frac{V_{ads}}{V_g} \right) N_A \right] a \quad (4.14)$$

where n is the stoichiometry of the adsorption reaction, V_{ads} is the volume of adsorbed probe molecule, V_g is the molar volume of a gas at standard conditions, N_A is the Avogadro's number and a is the cross-sectional area of the probe molecule. In a similar way, the metal dispersion can be determined by calculating the amount of metal on the surface and the total metal load; this can be achieved using (4.15) and (4.16) respectively [234]:

$$M_{surf} = n \frac{V_{ads}}{V_g} \quad (4.15)$$

$$M_{tot} = \frac{M}{MW * 100} \quad (4.16)$$

where M_{surf} and M_{tot} are the moles of metal on surface and moles of total metals respectively expressed in mol g⁻¹, M is the % metal loading and MW is the molecular weight of the metal. The metal dispersion D is then obtained by:

$$D = \frac{M_{surf}}{M_{tot}} * 100 \quad (4.17)$$

4.5.3.2 Temperature Programmed Desorption (TPD)

Temperature programmed chemisorption involves the effects of temperature on surface reactions. This method is commonly used for the characterisation of active size and for the determination of the thermodynamic and kinetic parameters of the desorption process; this chapter will focus on the

use of TPD for the characterization of active sites. A schematic representation of the TPD instrument is shown in Figure 4. 12.

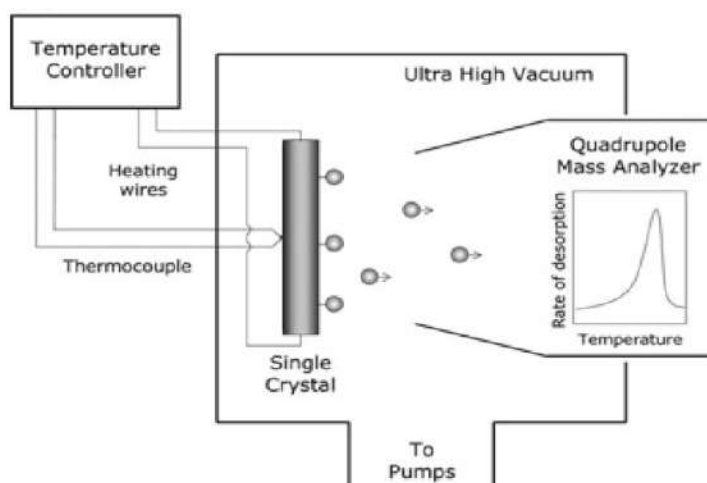


Figure 4. 12: Schematic representation of the Temperature Programmed Desorption instrument [235].

The sample is placed in the sample holder and pre-treated at high temperature and under inert atmosphere to remove adsorbed species, afterwards the sample is exposed to the adsorbate. The selection of the probe species depends on the type of sites that want to be investigated, for example, NH_3 and pyridine are commonly used for the determination of acids sites while CO and CO_2 are generally used for the characterization of basic sites. Subsequently, the physisorbed part of the adsorbed gas is removed by evacuation then, the chemisorbed adsorbate is desorbed by heating the sample in a controlled way. Finally, the evolved gas is quantified using a thermal conductivity detector. It is important to keep in mind that, since different chemical species can desorb from the sample surface, recent TPD instruments have been equipped with a mass spectrometer to discriminate the different desorbed species. The obtained data are usually presented as the variation

of the detector signal as a function of the temperature; Figure 4. 13 shows an example of a TPD curve.

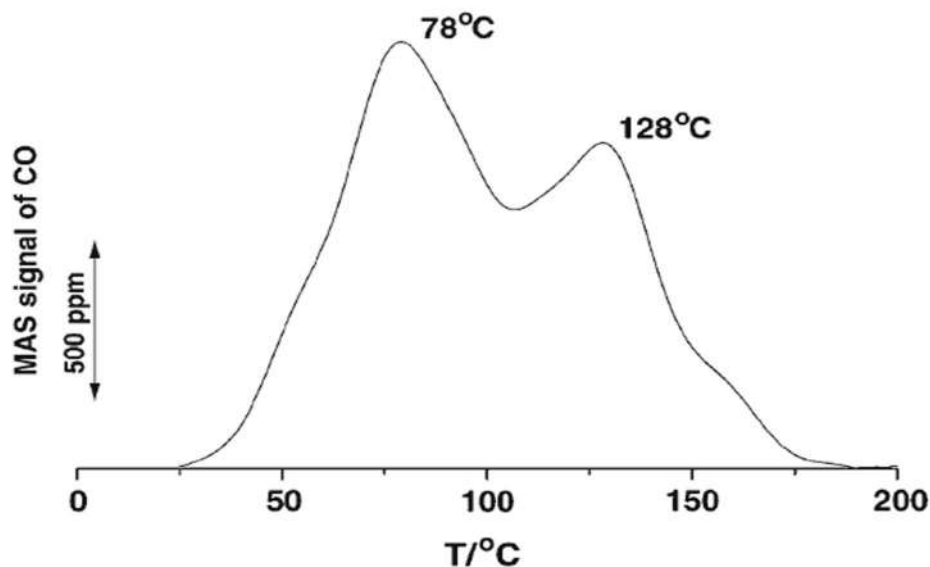


Figure 4. 13: Example of a TPD curve [235]

From a TPD curve different information about the active sites can be obtained. The area under the curve is proportional to the surface coverage θ and consequently TPD can be used to determine the surface coverage. The T_{max} value at which the maximum of a peak occurs is related to the desorption activation energy which in turn is correlated to the bond energy between surface active site and adsorbate. It is important to point out that solid materials have active sites of different strength; this can be due to differences in the nature of the site (e.g. Lewis - Brønsted acids/base) or solid structure heterogeneity (terraces, steps, etc.) [235]. The position of the peak maximum can help to shed lights on the type and strength of the active sites making TPD a powerful technique for the structural characterization of catalysts.

4.5.4 Mercury Intrusion Porosimetry (MIP)

Mercury porosimetry is commonly used for the characterization of porous solids having pores between 500 μm and 3.5 nm [236]; this technique uses the intrusion of mercury into a porous sample to provide a wide range of information such as pore size distribution, total pore volume and the specific surface area of a sample. In mercury porosimetry it is assumed that the pores have a cylindrical geometry and the *Washburn* equation (4.18) is used to correlate the pressure difference across the curved mercury interfaces (r_1 and r_2) to the corresponding pore size r_{pore} through the surface tension of mercury γ and the contact angle σ between the solid and the mercury [237].

$$\Delta P = \gamma \left(\frac{1}{r_1} + \frac{1}{r_2} \right) = \frac{2\gamma \cos \sigma}{r_{pore}} \quad (4.18)$$

From the mercury porosimetry analysis it is also possible to determine the surface area of the sample using the relationship proposed by *Rootare and Prenzlow* (4.19) [238]; this converts the pore volume data into corresponding surface area A .

$$A = - \frac{1}{\gamma_{Hg} \cos \sigma} \int_0^V P dV \quad (4.19)$$

The amount of mercury intruded into the sample is measured using a penetrometer (Figure 4. 14); this is constructed of glass (insulator) and filled with mercury (conductor). The metal planted stem of the penetrometer acts as a reservoir for the analytical volume of mercury. The two conductors (mercury and the metal planting) are separated by glass forming a coaxial capacitor. As the pressure forces the mercury into the pores of the sample, the mercury in the capillary decreases and so is the capacitance. The decrease in capacitance is, therefore, proportional to the volume of mercury leaving the capillary with each change in pressure [239].



Figure 4. 14: Schematic of a Mercury Intrusion Penetrometer [239]

The results of the mercury porosimetry experiments are usually represented in an intrusion/extrusion curve (Figure 4. 15) where the pore diameter is plotted as a function of the cumulative intrusion of mercury.

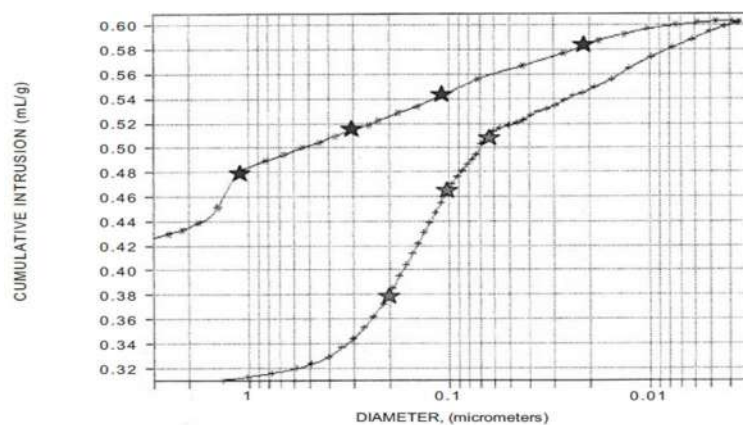


Figure 4. 15: Mercury Intrusion Porosimetry intrusion/extrusion curve [237]

It is important to point out that, mercury porosimetry does not measure the actual internal pore size but it determines the largest connection from the sample surface towards that pore. From Figure 4.15 it can be noted that a hysteresis between the intrusion (increasing pressure) and the extrusion (decreasing pressure) curves exists. Different explanations have been proposed for this phenomenon; one of these attributes it to the contact angle differences in the advancing and receding contact angles but this hypothesis cannot explain, for example, mercury trapping in the sample. The “ink bottle theory” proposes that, since the mercury will enter the cavity at a pressure determined by the entrance size, during the extrusion the mercury network would then break at all the throats between pores, leaving a larger amount of mercury trapped inside the sample. Although this theory explains the mercury entrapment, it does not necessarily explain the hysteresis between the intrusion and the extrusion curve [237]. A drawback of the technique is that the intrusion of Hg at high pressure can damage the porous structure of weaker materials. As it can be deduced from the previous discussion, mercury porosimetry allows to obtain a large set of information from porous samples but data analysis must be conducted carefully in order to take into account the technique limitations.

4.5.5 Scanning Electron Microscope

A Scanning Electron Microscope (SEM) can provide information on surface topography, crystalline structure and chemical composition of the top 1 μm of a specimen; this technique uses a beam of electrons to produce the sample image and magnifications up to 1000000 X with an ultimate resolution of 1 nm [240]. The principle at the basis of a SEM is based on the interaction of accelerated electrons with the sample surface. When the incident electrons are decelerated, due to the interaction with the sample surface, their kinetic energy is dissipated in a variety of signals

such as secondary electrons, backscattered electrons, photons (characteristic X-Rays), Auger electrons, visible light and heat. Secondary electrons and backscattered electrons are commonly used for imaging the samples: secondary electrons for showing morphology and topography on samples and backscattered electrons for illustrating contrast in compositions in multiphase samples. The emission of X-Rays and Auger electrons is the consequence of the interaction of the electrons with the sample's surface atoms. These have a fixed wavelength depending on the elements they were emitted from, so their detection allows to gather valuable information regarding the elemental composition of the sample surface [240].

A Scanning Electron Microscope is composed of an electron gun, condensor lenses and a series of detectors to analyse the different signals; Figure 4. 16 shows a schematic representation of a SEM.

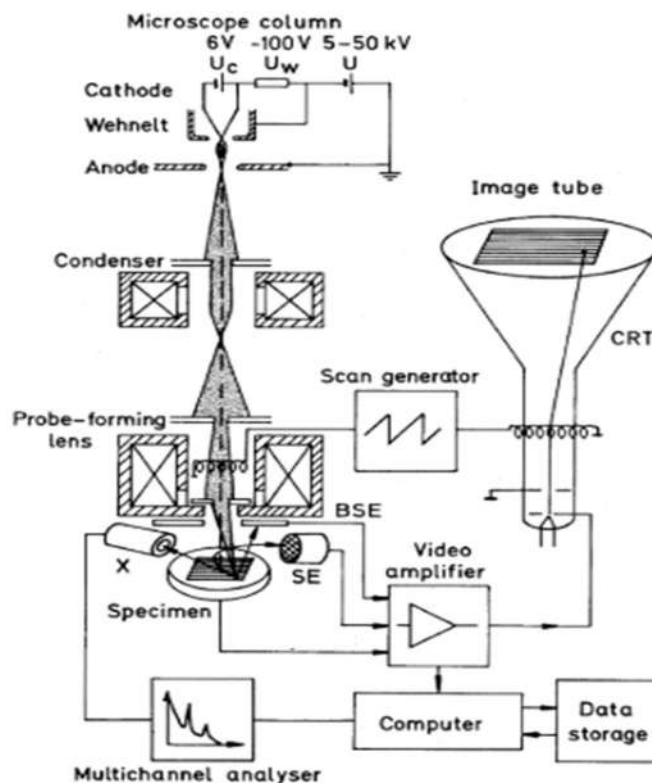


Figure 4. 16: Schematic representation of a SEM (BSE = backscattered electrons, SE = secondary electrons, X = X-Rays, CRT = cathode-ray tube) [241]

The electron gun is fitted with a tungsten filament which is used to thermoionically emit an electron beam having an energy usually comprised between 0.2 and 40 keV. The beam is then focussed by one or two condenser lenses to a spot of about 0.4-5 nm in diameter. The beam is then passed through a pair of scanning coils or deflector plates in the electron column; in this way the beam is deflected in the x and y axes so that it can be scanned over a rectangular area of the sample surface [241]. To avoid electron deflection by the molecules present in the air, high-vacuum is necessary to run the analysis; this is obtained using a high-vacuum pump. A single detector is not capable of registering all the signals emitted by the sample so different detectors are present in the instrument. For example, secondary electrons are detected using a scintillator-photomultiplier detector. The secondary electrons are first collected by attracting them towards an electrically biased grid and then further accelerated towards a scintillator positively biased; this will cause the scintillator to emit flashes of light which are conducted to a photomultiplier outside the SEM. Scintillator detectors are also used to register backscattered electrons but these are positioned above the sample in a “doughnut” type arrangement in order to maximize the solid angle of collection; the detection of these electrons allows to identify areas with different chemical composition since heavy elements backscatter electrons more strongly than light elements. As already said, some instruments are capable of analysing also the emitted X-Rays, this is achieved by energy dispersive X-Ray spectroscopy or wavelength dispersive X-Ray spectroscopy [241].

It is important to point out that sample preparation is a fundamental aspect of the SEM analysis. Non-conductive samples can accumulate electrostatic charge when scanned with an electron beam resulting in scanning faults and image artefacts. For this reason, non-conductive samples are usually coated with a thin layer of conductive material [241]. This is not always the case though,

non-conductive samples can be imaged using a low voltage mode of operation; this was the case for all the SEM images acquired in this work.

4.6 Materials and Methods

4.6.1 Materials

Fumed TiO₂ particles (grade AEROXIDE P25) were obtained from Evonik Industries (Essen, Germany). The supplier technical data sheet states that the primary particles have a mean diameter of approximately 21 nm while their aggregates are several hundred nm in size. Density and surface area are 4 g cm⁻³ and 50 m² g⁻¹ respectively. The AEROXIDE P25 is characterized by an anatase/rutile ratio of 80/20 with both crystal structures having a tetragonal geometry.

The amino acids used to modify the particles surface were DL-valine 99%, DL-leucine 99% and DL-phenylalanine 99% (Alfa Aesar, Heysham, United Kingdom). Other chemical used in the foam preparation were demineralized water, HNO₃ 70%_{v/v} (Alfa Aesar, Heysham, United Kingdom) and KOH 40%_{v/v} prepared by dissolving potassium hydroxide pellets (Alfa Aesar, Heysham, United Kingdom) in demineralized water. A [Co(NH₃)₆]CO₃ solution was used for the support impregnation. This was prepared from a 28% NH₄OH solution (Alfa Aesar, Heysham, United Kingdom), (NH₄)₂CO₃ (Alfa Aesar, Heysham, United Kingdom), 30% H₂O₂ (Alfa Aesar, Heysham, United Kingdom) and 50% CoCO₃ (Shepherd Widnes Ltd).

4.6.2 Slurry preparation and foaming

Titania suspensions were prepared by stepwise addition of the powder to deionised water continuously stirred using an IKA EUROSTAR power control-visc overhead mixer. The pH of all suspensions was adjusted to electrostatically stabilise the particles. Titania particles are stable at pH either below 4 or above 7. To favour the dissolution of amino acids the pH was kept either

below 3 or above 10 through the addition of small aliquots of 70%_{v/v} HNO₃ and 40%_{v/v} KOH respectively. The solid loading of titania suspensions was set to 25%_{w/w}. In a typical formulation, carried out at acid pH, 99.7 g of titania was added to 250 mL of demineralised water containing 50 mL of 5%_{v/v} HNO₃. After powder dispersion, the suspension pH was dropped below 2 through the addition of 5 mL of 70%_{v/v} HNO₃. An amino acid was then added to the titania suspension obtaining the required concentration in the range 0.08 and 0.36 mol L⁻¹. Foaming of 300 mL of titania suspension was carried out using an overhead stirrer equipped with a gas inducing impeller [242]. The vessel diameter and impeller diameter were T = 12 cm and D = 6 cm respectively (D/T = 50%). The vessel was fitted with 4 baffles (B) 1 cm wide (B/T = 8.3%). Mixing was carried out at 2000 rpm for 20 minutes. The foam was dried under ambient conditions and then calcined in a Carbolite Furnace CWF at 600 °C for 4 hours. During the ramping step and for the first 45 minutes the furnace was purged under N₂ followed by air. The heating rate was 2 °C min⁻¹.

4.6.3 Catalyst precursor preparation

A [Co(NH₄)₆]CO₃ solution was prepared as follows. 198 mL of a 28% NH₄OH was added to 20.4 g (NH₄)₂CO₃ in a round bottomed flask and diluted with 193.4 mL demineralised water. The resulting solution was stirred for 20 minutes. Then 23.7 g of CoCO₃ was added over 15 minutes and the solution stirred at 150 rpm for a further 2.5 hr to give a purple solution. 30% H₂O₂ solution was added drop wise while the solution was stirred at 235 rpm until the oxido-reduction potential (Metler Toledo transmitter M700) was near to -100 mV. Stirring was continued for a further 10 minutes and then the solution was filtered. 385 mL of the [Co(NH₄)₆]CO₃ solution (2.6%_{w/w} Co) was added to a 2 L four-necked round bottom flask. A stirrer, temperature probe, lute and condenser were fitted to the flask. 52 g of the ceramic foam, previously ground to a 400-600 µm size fraction,

was added. This mixture was then diluted with 385 mL water and 165 mL NH_4OH before being heated and agitated for 80 minutes to cause evolution of the ammonia and deposition of cobalt oxide in the cells and pores of the ceramic foam. The mixture was filtered and washed with 80 mL demineralised water. The target cobalt content was 13% by weight.

4.6.4 Catalyst test

A schematic of the rig used for the catalyst testing is given in Figure 4. 17.

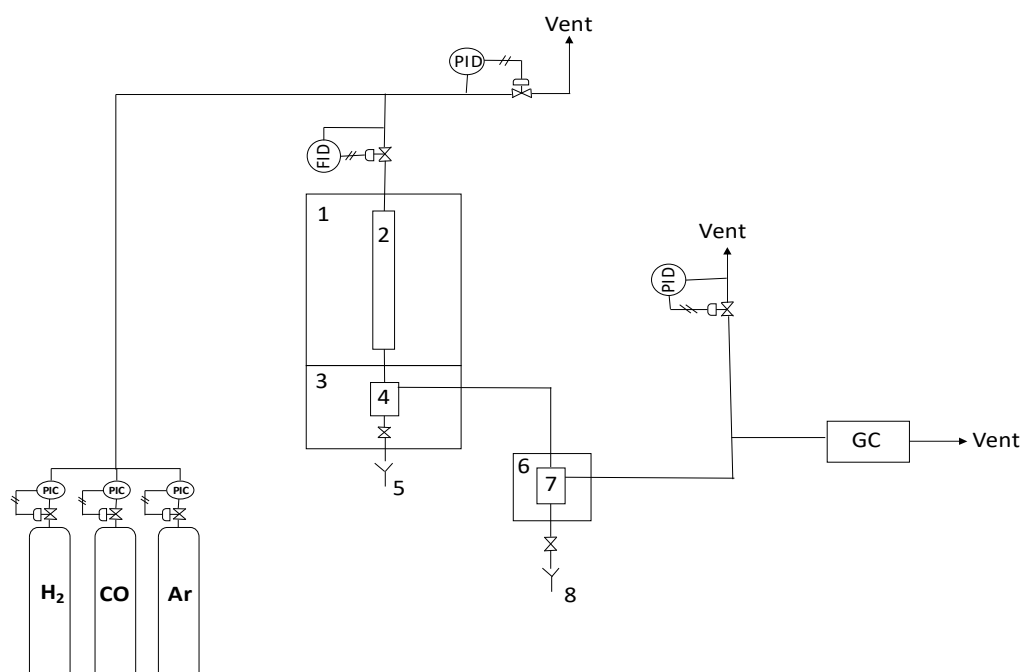


Figure 4. 17: Schematic of the test rig used for the catalyst testing

0.5 g of catalyst were loaded into a fixed bed reactor (2) having an internal diameter of 4 mm; this was placed in an oven (1) to keep the reactor at the pre-treatment/reaction temperature. Before the reaction could be carried out, the catalyst needed to be activated. Catalyst activation was performed in H_2 at 380 °C for 7 hr at a ramp rate of 1 °C min^{-1} , followed by cooling down to 150 °C. The feed was then switched from H_2 to a syngas mixture with a H_2/CO molar ratio of 2 and the reactor was flushed with the syngas at 150 °C for 6 hr (no reaction occurring). The temperature was then

increased to 210 °C (ramp 1 °C min⁻¹) and a syngas flow rate equal to 110 mL min⁻¹ was used. The reactor was kept at these conditions for 24 hr. Finally, the gas flow rate was gradually reduced in order to target a 50% syngas conversion. Under these conditions, the reaction products were passed to a gas-liquid separator (4) which was placed in an oven (3) set at a temperature of approximately 110 °C. The liquid fraction, constituted by waxes, was collected (5) while the gas fraction was passed in a second gas-liquid separator (7); this was placed in a refrigeration chamber (6) at a temperature of approximately 5 °C. The liquid fraction, comprising mainly alcohols and light hydrocarbons, was collected (8) while the residual gas fraction is sent to a gas chromatographer to analyse its composition and to determine the product distribution. The PIC and FID symbols in the schematic represent the pressure controllers and flow rate controllers respectively.

4.6.5 Catalyst Characterization

The basic principles governing the analytical techniques used in the catalyst characterization have already been presented (Section 4.5), only the testing methodology used in this study is described below.

Catalyst crystal size was determined using a Bruker D8 Advance X-Ray Diffractometer, the X-Ray source was a Cu metal plate emitting Ka radiations having a wavelength of 1.5406 Å. 0.5 g of powder sample was pressed into a sample holder and loaded into the instrument. A parallel beam (Gobel mirror) was used as optic. The starting 2θ angle was equal to 10° and the final 2θ angle was equal to 130°; steps of 0.044° were used with a time step of 4 seconds. The Bruker EVA software and the Topas software were used for phase identification and pattern refinement respectively.

The physisorption isotherms were measured using a Micromeritics 2020 ASAP physisorption analyser. The ASTM Method D3663-03 and the ASTM Method D4222-03 were used as the

Standard Test for Surface Area and the Standard Test Method for Isotherm Measurements respectively. Nitrogen was used as the adsorbate and the measurements carried out at liquid nitrogen temperature (77 K). The cross-sectional area of a nitrogen molecule was taken as 16.2 \AA^2 . 0.5 g of the samples was outgassed prior to analysis by purging with dry nitrogen gas for a minimum of 1 hr at 140°C . The adsorption/desorption isotherms consist of approximately 60 adsorption points and 40 desorption points. The BET surface area was calculated using 5 points using the relative pressure region of 0.05 to $0.20 p/p^0$ inclusive. The equilibration time for each point was 10 second. Surface areas are reported based on the weight of the sample post outgassing. The pore size distribution was reported using the BJH method using the adsorption branch of the isotherm.

Co metal area was measured on a Micromeritics 2480 Chemisorb HTP analyser. 0.5 g of sample was charged to a chemisorption tube. The sample was reduced with flowing 100% H_2 at 425°C for 360 minutes. After the reduction stage was finished, all the H_2 was removed by evacuation at 450°C for 120 minutes. Once a vacuum of $<10 \text{ \mu mHg}$ was achieved, the sample temperature was cooled to the analysis temperature of 150°C . At this temperature, the sample was dosed with 100% H_2 over a range of pressures between 100 and 760 mmHg. At each pressure the chemisorbing H_2 was allowed to equilibrate and the volume of H_2 uptake was measure and recorded automatically. Pressure / uptake pairs constitute a chemisorption isotherm. At the end of the analysis the sample was discharged and the reduced weight of sample was recorded. Two isotherms were measured sequentially on the reduced sample. The first was a measure of the “total” H_2 taken up by the sample, which included both chemisorbed and physisorbed hydrogen. The sample was then evacuated to remove the physisorbed (“weak”) component and a second isotherm was measured in

order to quantify the amount of physisorbed H_2 going back on the sample. The instrument software was used to calculate the Co surface area based on the difference between the total uptake and the “weak” uptake; by extrapolating the data back to zero pressure, the Co surface areas based on these values were reported. These are generally referred to as Co area (0_{tot}) and Co area (0_{str}) which refer to the total area (including physisorbed and chemisorbed probe molecule) and to the area due to the active metal respectively. The reduced weight is used to express the Co areas in $m^2 g^{-1}$ of reduced catalyst.

Ammonia Temperature Programmed Desorption was carried out using an Altamira AMI 5200; 0.5 g of sample were loaded into the sample holder. The drying step was carried out using a temperature ramp of $10\text{ }^{\circ}C\text{ min}^{-1}$ until the final temperature of $400\text{ }^{\circ}C$ was reached; drying occurred under a He flow of 10 mL min^{-1} . The sample was kept at $400\text{ }^{\circ}C$ for 100 min. The sample was subsequently cooled down to $40\text{ }^{\circ}C$ in 40 mL min^{-1} He and exposed to 500 ppm of NH_3 in He for 2 hr in order to saturate it. The sample was kept at $40\text{ }^{\circ}C$ for 4 hr and then flushed with a 40 mL min^{-1} He stream and hold at the set temperature for 15 min. The temperature was then ramped at $15\text{ }^{\circ}C\text{ min}^{-1}$ until the set temperature of $1000\text{ }^{\circ}C$ was reached. The desorbed NH_3 was measured by IR.

Mercury intrusion/extrusion data were measured on a Micromeritics AutoPore 9520 mercury porosimeter in accordance with ASTM Method D4284-03. Intrusion curves were measured over the pressure range of $3.4 \cdot 10^{-3}$ to $4.1 \cdot 10^{-8}$ Pa (0.5 to 60000 psia) followed by extrusion down to atmospheric pressure. An equilibration time of 15 seconds was used for each data point on both the intrusion and extrusion curves. Hg contact angle was taken to be 140° and the Hg surface tension taken as 485 dynes cm^{-1} . 1.5 g of samples were dried at $115^{\circ}C$ overnight in an oven prior to analysis. Temperature and glass/mercury compression effects that are manifested during the

porosimetry run were corrected for by running empty penetrometers. The data from these blank runs were subsequently subtracted from the experimental data.

4.7 Catalytic Testing of Foam Supported Catalysts for FTS Applications

A first comparison of a foam supported catalyst against a conventionally supported one was carried out using a foam produced using DL-phenylalanine as amphiphile and commercially available titania spheres respectively. Figure 4. 18 depicts the two supports.



Figure 4. 18: Supports used in FTS test: (a) conventional titania spheres (b) titania foam

The foam sample was produced as described in Section 4.6.2; it is important to point out that the foam was produced at a pH equal to 3.5. Both samples were then impregnated with a Co solution as reported in Section 4.6.3 and tested following the procedure in Section 4.6.4. Table 4. 1 summarises the operating conditions during the test, the product selectivity and the relative activity of the tested catalysts.

Table 4. 1: Comparison of the performances of conventionally supported and foam supported catalysts in FTS

Sample	Particle Size (μm)	Cat. Weight (g)	Temp. ($^{\circ}\text{C}$)	Press. (atm)	Syn. Conv. %	CH_4 Sel. %	C_{5+} Sel. %	Relative Activity
Titania Spheres	250-400	0.2516	209.9	20.4	50.06	7.79	89.87	1.00
Phe-Titania Foam	400-600	0.2538	208.7	20.6	50.68	6.99	91.15	1.17

It can be noted from the table above, that the same catalyst weight, operating conditions (temperature and pressure), and syngas conversion were targeted in the testing of the two samples but the foam supported sample presents a lower (better) selectivity in methane (~0.8% lower) and a higher selectivity in C₅₊ (~1.28% higher). Although these improvement may appear insignificant at small scale they in fact translate to a significant impact on the economics of a commercial scale Fischer-Tropsch plant. To understand the root cause of the observed differences in selectivity, an extensive characterization on the two samples was carried out. Table 4. 2 summarises the characterization results for the two samples.

Table 4. 2: Summary of the characterization undertaken on the two samples

Catalyst	Foam Porosity %	Characterization		
		XRD		
		Anatase Crystal Size (nm)	Rutile Crystal Size (nm)	Co Crystal Size (nm)
Titania Spheres	N/A	21.3	54.1	<3
Phe-Titania Foam	72.79	21.2	48.1	3
		N ₂ -Physisorption		
		BET Area (m ² g ⁻¹)	Pore Volume (cm ³ g ⁻¹)	Ave. Pore Diameter (Å)
Titania Spheres	N/A	87.6	0.270	123
Phe-Titania Foam	72.79	84.3	0.298	141
		Mercury Intrusion Porosimetry		
		Corrected Intrusion Volume (cm ³ g ⁻¹)	Entrapment (% _{v/v})	Median Pore Diameter (Å)
Titania Spheres	N/A	0.384	11	388
Phe-Titania Foam	72.79	0.586	33	474
		H ₂ -Chemisorption		
		Co Metal Area [tot ₀] (m ² g ⁻¹)	Co Metal Area [st ₀] (m ² g ⁻¹)	WLOR %
Titania Spheres	N/A	2.7	0.8	10.8
Phe-Titania Foam	72.79	1.1	0.3	7.1

From the table above, it can be noted that a direct comparison of the two samples Co crystal size is not possible since the crystal size of the sphere supported sample is below the detection limit of the technique. The higher metal area observed for the sphere supported catalyst in the chemisorption analysis confirm that, in the case of the sphere sample, the Co crystal size was smaller than that of the foam sample. Physisorption characterisation showed that the foam, as it may be expected, presents a higher pore volume and pore volume diameter in respect to the conventionally supported one. In the literature it is well documented that both bigger crystal sizes and the presence of macro porosity favour FTS catalyst selectivity towards C_{5+} hydrocarbons [243] [244] [245] [246] [247] [248], for this reason it is not surprising that the foam supported catalyst presented better performances. . Figure 4. 19 shows a direct comparison of the porous structure of the two samples depicting the N_2 physisorption and mercury intrusion porosimetry respectively.

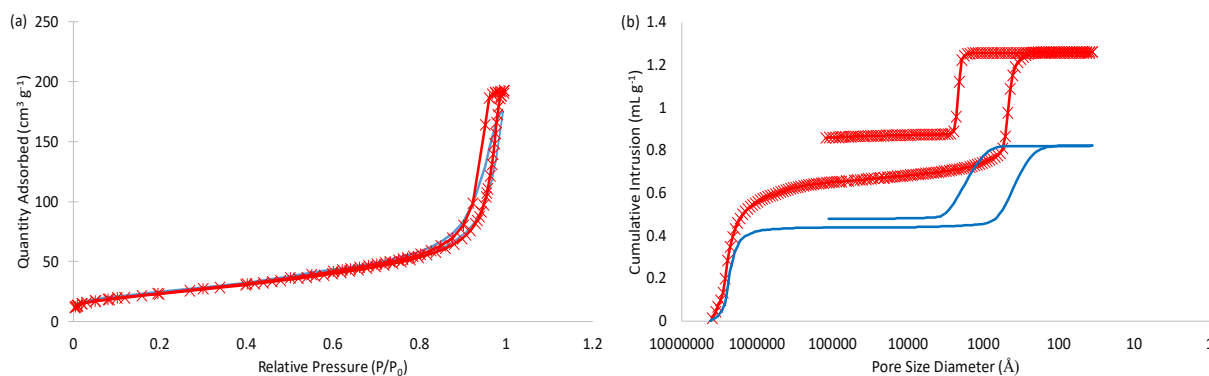


Figure 4. 19: N_2 Physisorption (a) and mercury intrusion porosimetry (b) curves for the spheres (—) and foam (*) supported catalysts respectively

Figure 4. 19 further confirms the difference in the porous structure of the two samples evidencing the higher macro-porosity which characterizes the foam support. The physisorption curves of the two samples overlap in the micropore region indicating that they present the same microporous structure; this is not surprising since the same titania was used for both supports. The curves start to differentiate at higher p/p^0 values where, in particular for the foam supported catalyst, the shape

of the physisorption curve suggests that bigger pores, not detectable by the technique, are present; these are well caught in the mercury intrusion porosimetry curve. The latter curve evidences a significant difference in the macro-porosity of the two samples. This difference is reinforced by the difference in the intrusion volume and the median pore diameter between the two samples which are summarised in Table 4. 2.

The difference in porous structure between the foam support and the sphere support was also evidenced by the SEM images of the samples cross sectional area; Figure 4. 20 shows the SEM images of the two samples.

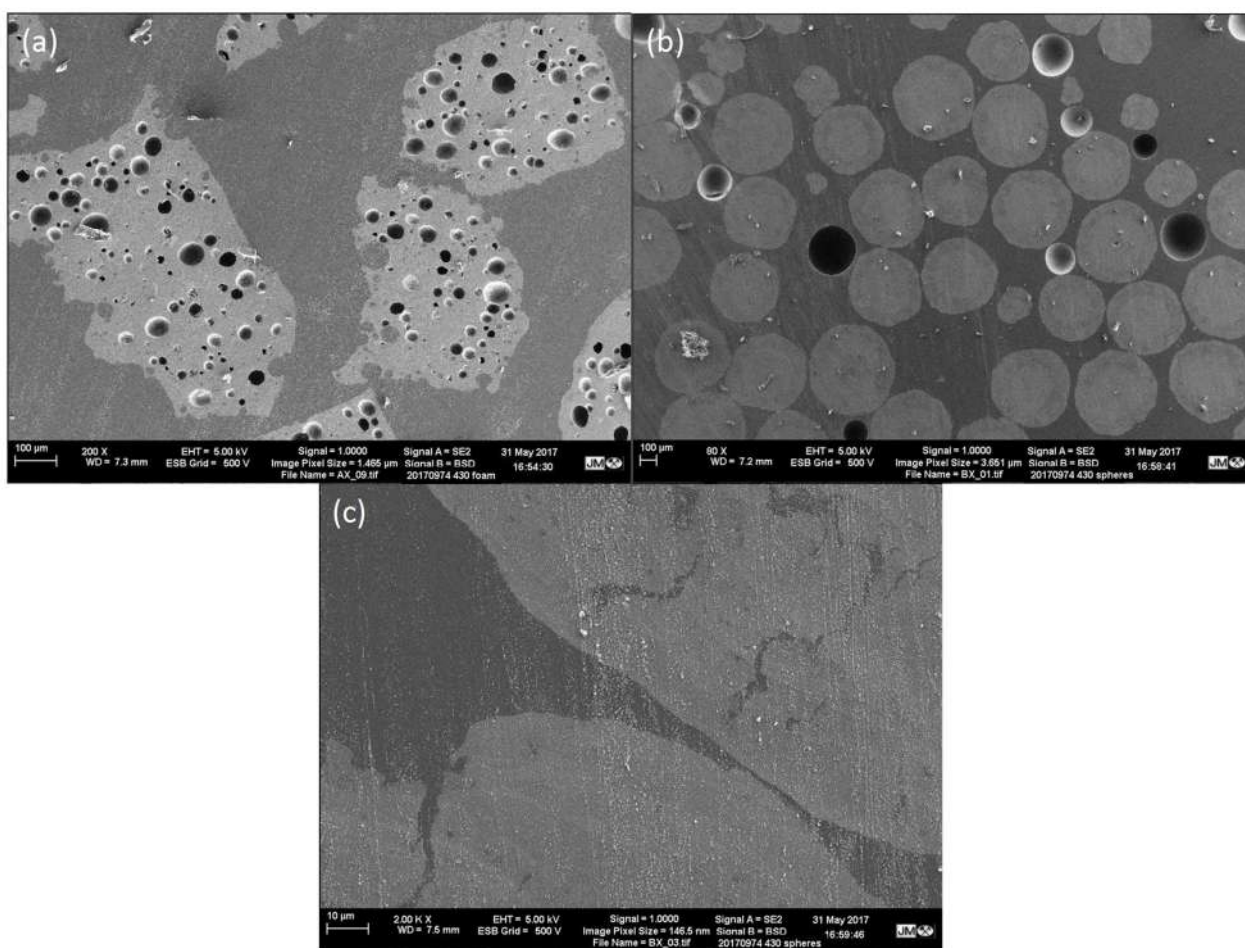


Figure 4. 20: SEM images of the samples cross sectional area: (a) foam support, (b) sphere support, (c) detail of the sphere cross section

The SEM images of the samples' cross sections show that the foam sample is characterized by a significant amount of macro-pores while, in the sphere support, the macro-porosity is limited to a few cracks present in the formed sphere.

Another aspect that could affect the performance of the catalysts is the acidity of the titania support. To determine if the foaming process resulted in a modification of the support acidity, NH_3 -TPD was run on the two samples; the procedure described in Section 4.6.5 was followed for the TPD analysis. Figure 4. 21 shows the comparison between the TPD curves for the two samples.

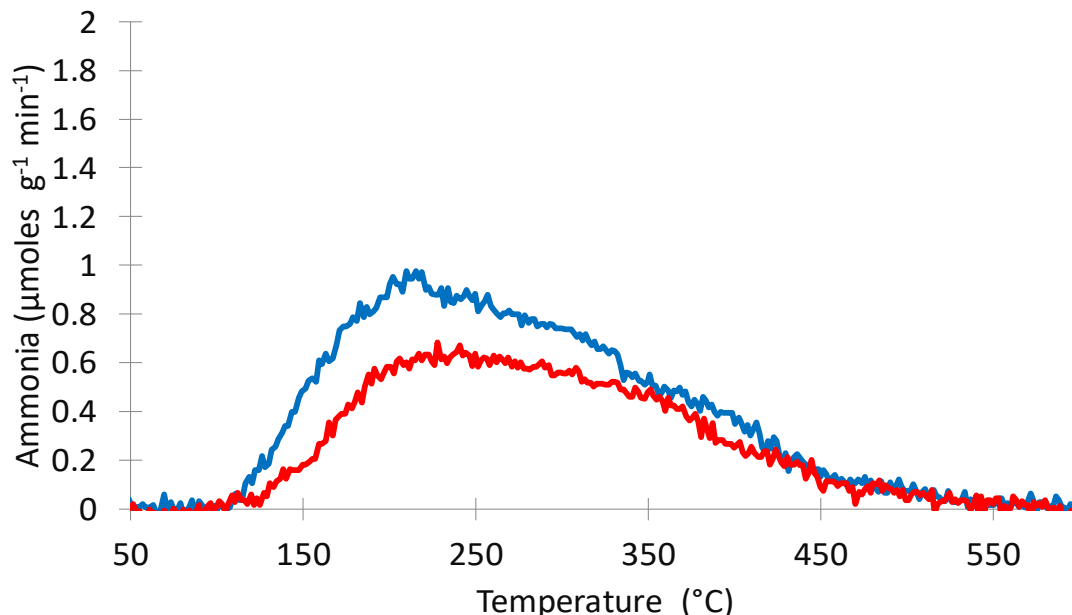


Figure 4. 21: NH_3 -TPD of conventional (—) and foam (—) catalyst supports

The NH_3 -TPD curves for the two titania supports show that the samples have the same type of acid sites characterized by a T_{max} of approximately 200 °C. The low T_{max} values indicates the low strength of the acid sites which is characteristics of low acidity materials such as titania. In addition, the observed difference in the amount of acid sites is not significant enough to result in a different acidity of the two samples.

The encouraging results observed when foam supports were used led to the interest of JM in filing a patent application. For the purpose of further improving patent exemplification, other two foam supported samples were tested for FTS to confirm the effects of the support structure on catalyst selectivity. The foams were produced using DL-leucine and DL-valine as amphiphile respectively; both foams were prepared at a pH equal to 3.5. Table 4. 3 summarises the test operating conditions, the product selectivity and the relative activity of the tested catalysts.

Table 4. 3: Comparison of the performances of conventionally supported and foam supported catalysts in FTS

Sample	Particle Size (μm)	Cat. Weight (g)	Temp. ($^{\circ}\text{C}$)	Press. (atm)	Syn. Conv. %	CH_4 Sel. %	C_{5+} Sel. %	Relative Activity
Titania Spheres	250-400	0.2544	208.8	20.0	48.94	12.16	86.18	0.90
Leu-Titania Foam	400-600	0.2457	210.2	20.4	49.51	9.01	89.51	1.34
Val-Titania Foam	400-600	0.2608	210.0	20.4	50.00	8.41	89.90	0.87

As with the tests presented above, the same catalyst weight, operating conditions (temperature and pressure) and syngas conversion were targeted. It can be noted that, again, the foam supported samples present a higher selectivity in C_{5+} (~3.5% higher) and a desired lower selectivity in methane (~3.5% lower). The characterization of the two foam supported catalysts is summarised in Table 4. 4.

Table 4. 4: Summary of the characterization undertaken on the two samples

Catalyst	Foam Porosity %	Characterization		
		XRD		
		Anatase Crystal Size (nm)	Rutile Crystal Size (nm)	CoO Crystal Size (nm)
Leu-Titania Foam	70.59	22.1	51.8	9.6
Val-Titania Foam	64.39	21.7	50.6	5.2
		N ₂ -Physisorption		
		BET Area (m ² g ⁻¹)	Pore Volume (cm ³ g ⁻¹)	Ave. Pore Diameter (Å)
Leu-Titania Foam	70.59	76.6	0.268	140
Val-Titania Foam	64.39	69.8	0.274	157
		Mercury Intrusion Porosimetry		
		Corrected Intrusion Volume (cm ³ g ⁻¹)	Entrapment (% _{v/v})	Median Pore Diameter (Å)
Leu-Titania Foam	70.59	0.321	100	351
Val-Titania Foam	64.39	0.277	97	313
		H ₂ -Chemisorption		
		Co Metal Area [tot ₀] (m ² g ⁻¹)	Co Metal Area [st ₀] (m ² g ⁻¹)	WLOR %
Leu-Titania Foam	70.59	3.9	1.0	10.1
Val-Titania Foam	64.39	1.6	0.3	9.5

The product selectivity and the characterization data reported in the tables above have been used to have an insight into to reaction mechanism and the effects of the catalyst properties on its performance. In the literature, it is usually assumed that methane is formed on sites separate from chain growth, via a parallel reaction with its own rate determining step [249]. Figure 4. 22 in fact defines this assertion. The linear relationship between CH₄ selectivity and C₅₊ selectivity suggests the existence of a common initial step for C₁ and higher hydrocarbons; and thus both occur on the same or similar active sites. It could be argued that the different samples could have different ratios of independent methanation/chain growth sites but it is extremely unlikely that this would have resulted in such a good correlation between CH₄ and C₅₊ selectivity ($R^2 = 0.98$). In addition, a

similar relationship was observed by *Rane et al.* [208] and *Lögdborg et al.* [250] with the latter proposing a mechanistic link between the formation of methane and higher hydrocarbons, presumably a common precursor pool, and the existence of a “pure methanation” site was therefore ruled out by the authors.

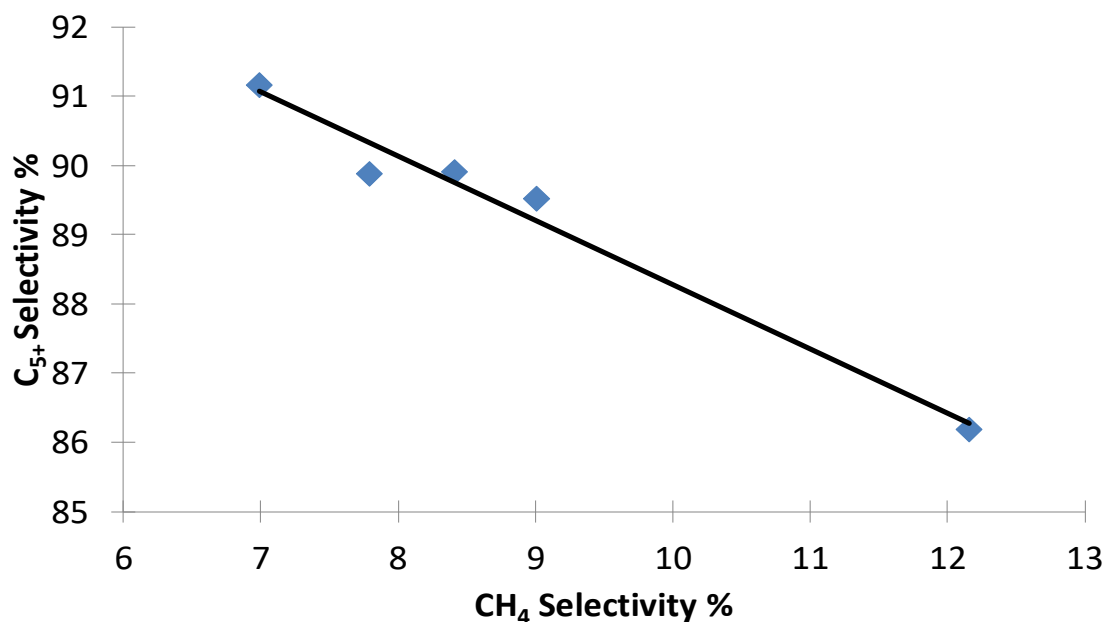
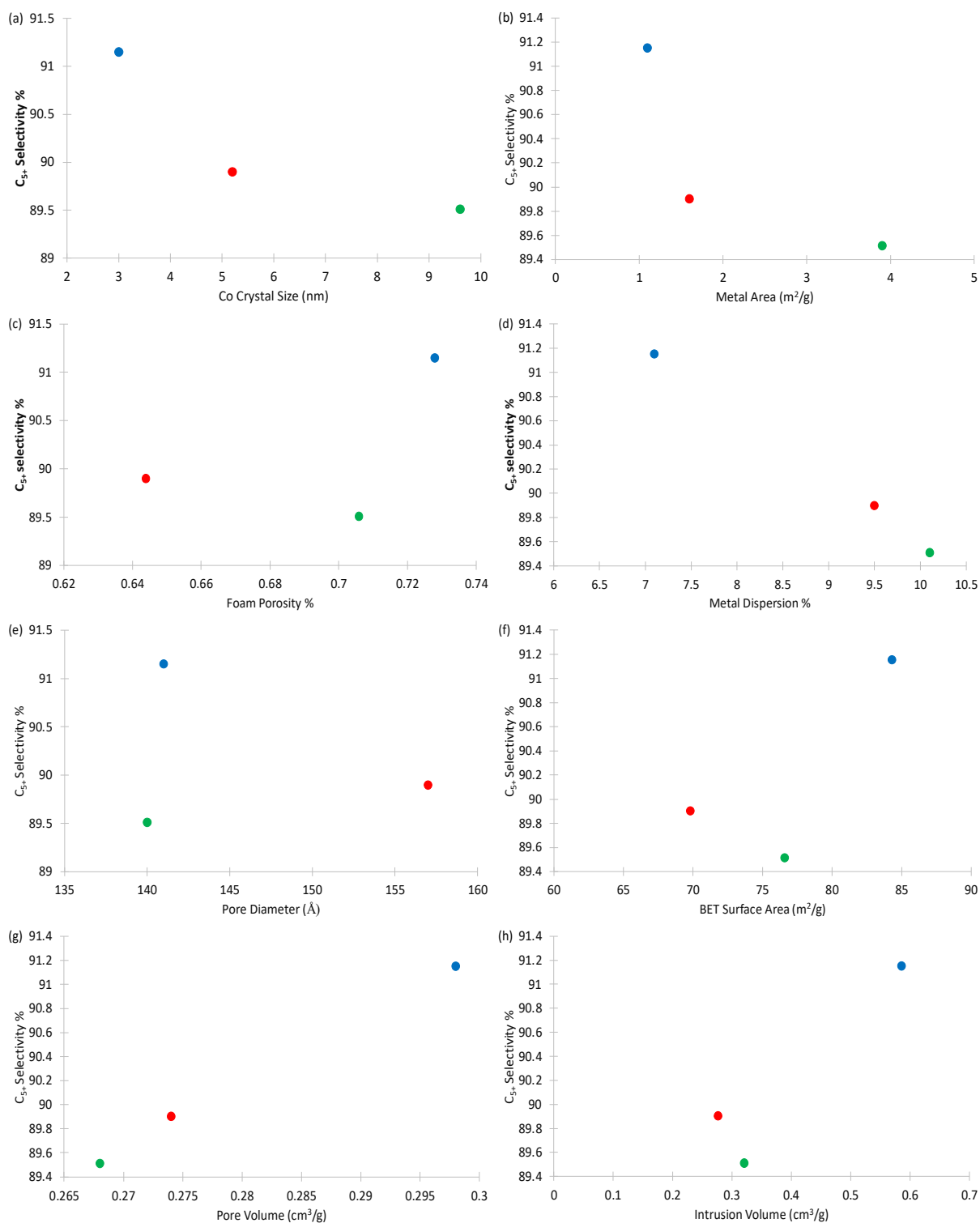


Figure 4. 22: Linear relationship between CH_4 selectivity and C_{5+} selectivity

The C_{5+} selectivity was correlated with the properties of the foam supported catalysts (i.e. crystal size, foam porosity, metal area, metal dispersion, N_2 physisorption pore diameter, BET surface area, N_2 physisorption pore volume, intrusion volume and MIP median pore diameter); Figure 4. 23 shows the plots that report the C_{5+} selectivity as a function of these catalyst properties. It is important to point out that the foam samples reported on the graphs were produced using different amino acids as amphiphiles and that they presented different structural properties (e.g. porosity, pore volume, crystal size, etc.)



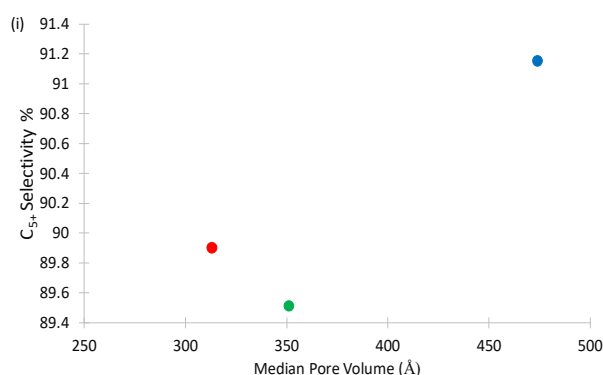


Figure 4. 23: C₅₊ Selectivity as a function of different catalyst properties: (a) Co crystal size (b) Co metal area (c) Foam porosity (d) Metal dispersion (e) N₂ Physisorption pore diameter (f) BET surface area (g) N₂ Physisorption pore volume (h) MIP Intrusion volume (i) MIP Median pore diameter. (●) Phe-Titania Foam (●) Val-Titania Foam (●) Leu-Titania Foam.

From Figure 4. 23 can be noted that the C₅₊ selectivity decreases as the Co crystal size increases (a); this observation is in contrast with what reported in the literature where an increase in selectivity as the Co crystal size increases is usually observed [243] [244] [245] [246] [247] [207]. It is important to point out that the different samples had different porous structure hence a distinction between the effects of crystal size and porous structure on catalyst selectivity is not possible. A similar conclusion can be drawn from graph (b) where catalysts having the same metal area present different C₅₊ selectivity suggesting, again, the concomitant presence of a support structure effect. A clear trend seems to be present when considering the effects of the metal dispersion, with the higher hydrocarbon selectivity monotonically decreasing as the dispersion decreases. Although a clear relationship between the C₅₊ selectivity and both the pore diameter (e) and the BET surface area (f) cannot be identified, the selectivity can be correlated to the N₂ physisorption pore volume (g). The same correlation is not observed when the C₅₊ selectivity is correlated to the pore volume measured by mercury intrusion porosimetry. This suggests that the low end of the macropores (that correspond to the higher detection limit of the physisorption technique) have a major impact on the selectivity. It has been shown in Figure 4. 23 that different

catalyst properties affect the catalyst selectivity; to better summarise these effects a non-dimensional parameter including both the support property and metal catalyst properties that mostly effects selectivity is proposed:

$$\phi = \frac{\text{Physisorption Pore Volume}}{\text{Co Crystal Size} * \text{Metal Dispersion} * \text{Metal Area}} \quad (4.20)$$

The proposed parameter can in some way be seen as the ratio between the physical phenomena (e.g. mass transfer) and chemical ones (e.g. catalyst activity) involved in Fischer-Tropsch. It is important to remark that, either the *Thiele* modulus [251] or the *Weisz-Prater* criteria [252] can be used to determine the influence of pore diffusion on reaction rates in heterogeneous catalysis; in these parameters the ratio between reaction rate and diffusivity is calculated. Since reaction rate data for the studied reaction were not readily available, the parameter ϕ (defined on the basis of the work by *Iglesia et al.* [221]) was used to have an insight into the catalyst structural parameters that effect C_{5+} selectivity; Figure 4. 24 plots the C_{5+} selectivity as a function of the parameter ϕ .

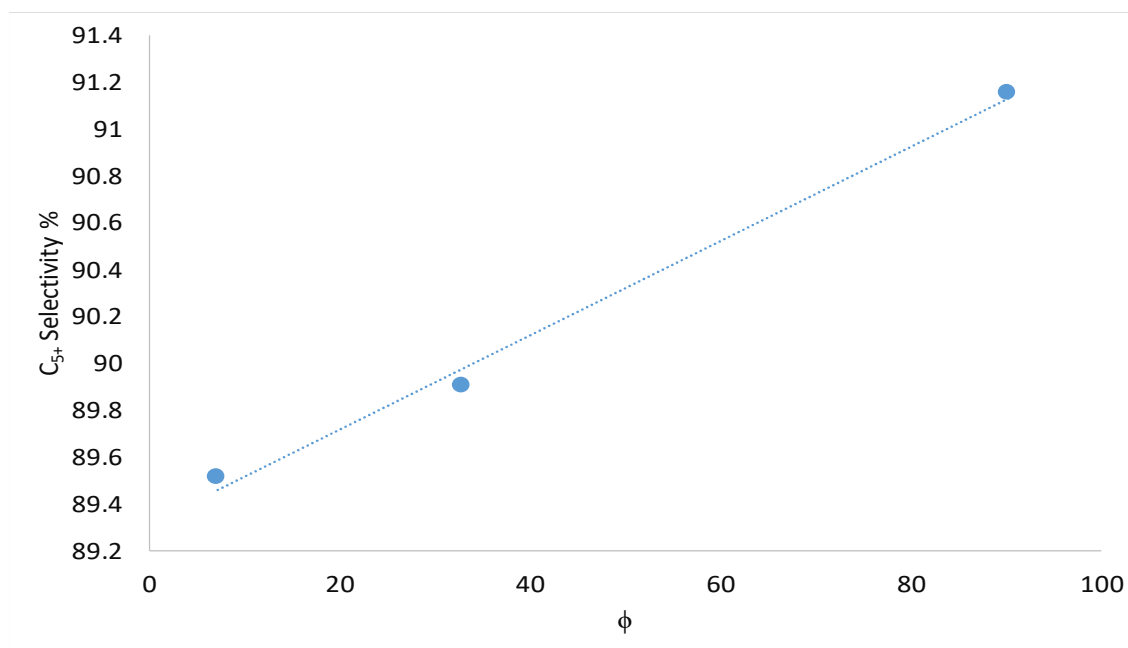


Figure 4. 24: C_{5+} selectivity as a function of the proposed parameter ϕ

From the figure above it can be noted that the proposed parameter well describes the C_{5+} selectivity trend with a directly proportional correlation between ϕ and C_{5+} selectivity. Although the proposed parameter well describes the catalyst performances, the limited number of data points prevents to assume that this parameter is generally applicable to FTS catalyst. Further experiments to generate additional data are recommended to confirm the general applicability of such parameter.

4.8 Conclusions

In this chapter the performance of foam supported catalysts has been compared to that of conventionally supported catalysts for the Fischer Tropsch Synthesis (FTS) reaction. From the testing of two initial samples (phenylalanine-foam and titania spheres), at the same operating conditions, it was found out that the foam supported catalyst gave a higher selectivity in C_{5+} and a reduced selectivity to methane than the conventionally supported one. The characterization of these first samples revealed that they presented different crystal and structural properties. In particular, the foam supported catalyst presented bigger crystal size and higher macroporosity; it is extensively reported in the literature that such characteristics favour C_{5+} selectivity. To further investigate the effects of the catalyst's properties on its performance, two additional foam supported catalysts (leucine-foam and valine-foam) were tested against a conventionally supported one. Catalysts characterization showed differences in the Co crystal size, metal area, surface area, pore volume and metal dispersion. Plots of the C_{5+} selectivity as a function of the different catalyst characteristics were made to determine which factors most affect the catalyst performance. From these graphs, it was noted that the pore volume, Co crystal size, metal dispersion value and Co metal area are the most important variables. A parameter ϕ which specifically includes these catalyst characteristics was proposed; this describes well the variation in C_{5+} selectivity for the

tested foam supported catalysts, evidencing the importance of the support porous structure on the catalysts performances. Although the proposed parameter well describes the variation in selectivity, the limited number of data points prevents its general applicability and further experiments are recommended to validate it.

The improved catalyst performances observed when ceramic foams were used as catalyst supports were considered sufficiently encouraging by Johnson Matthey to file patent applications on both the foam preparation method [253] and their application to Fisher Tropsch Synthesis [254].

Chapter 5

1D + 1D Simulation of CH₄ Oxidation in a Monolith Channel: Intrinsic Kinetic Model Validation against SpaciMS Experimental Results

5.1 Introduction

In this chapter, a Johnson Matthey developed intrinsic kinetic model for methane oxidation was validated against the experimental data results acquired using the SpaciMS technique at Queen's University Belfast. The SpaciMS experimental approach allows the measurement of axially resolved concentration and temperature data through a ceramic monolith coated with a catalyst washcoat. Johnson Matthey's interest in CH₄ oxidation lies in the necessity to develop new and innovative catalysts for methane oxidation. This is a consequence of pressure to reduce the emission of unburned methane from natural gas vehicles (NGVs) and other sources. In fact, although NGVs reduce the emission of CO by 95-97% and of CO₂ by 25% [255], they emit significant amounts of unburned methane which has a greenhouse impact 23 times greater than carbon dioxide [256]. For this reason, CH₄ combustion has been widely studied with a focus on improving the catalytic efficiency of platinum group based catalysts [257]. The validated intrinsic kinetic model, will be used in Chapter 7 to model the CH₄ light-off curve when foams having different structures are used as the catalyst support. In this chapter, the reader will be firstly introduced to the CH₄ kinetic mechanisms and equations proposed in the literature. Then the different diffusion models in porous solids will be discussed followed by a brief description of the SpaciMS technique. The reactor model used for the simulation of CH₄ oxidation will then be described and the validation of the intrinsic kinetic model against experimental results will be finally shown.

5.2 Proposed kinetic equations for catalysed CH₄ oxidation

Supported palladium (Pd) is considered the most active catalyst for the total oxidation of CH₄ at low and moderate temperatures:



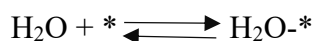
Ling and Wang proposed that C-H bond activation and the interaction with lattice oxygen are the rate determining steps in methane oxidation [258] with *Han et al.* confirming the bulk oxidation of Pd indicating that PdO is the active phase [259]. Although these catalysts present a high initial activity, different phenomenon such as structural collapse of the catalysts support [260], sintering [261], and PdO reduction to Pd [262] have been reported as contributors to catalyst deactivation during methane oxidation. Reaction and feed water also have a significant effect on the catalyst inhibition and it has been shown to be related to the competitive adsorption of water on the active sites. *Shahrestani* summarised the kinetic models for CH₄ oxidation commonly used in the literature [263]; these are reported in Table 5. 1.

Table 5. 1: Summary of the commonly used kinetic expression for CH₄ oxidation [263]

Model	Rate Expression
1	$r_r = k_r P_{CH_4} P_{H_2O}^{-1}$
2a	$r_r = k_r P_{CH_4} P_{H_2O}^a$
2b	$r_r = k_r P_{CH_4} P_{H_2O}^a P_{CO_2}^b$
3	$r_r = \frac{k_r P_{CH_4}}{1 + K_{H_2O} P_{H_2O}}$
4	$r_r = \frac{k_r P_{CH_4}}{(1 + K_{H_2O} P_{H_2O})^2}$
5	$r_r = \frac{k_r P_{CH_4}}{(1 + K_{CH_4} P_{CH_4} + K_{H_2O} P_{H_2O})^2}$
6	$r_r = \frac{k_r P_{CH_4}}{(1 + K_{H_2O} P_{H_2O} + K_{CO_2} P_{CO_2})}$
7	$r_r = \frac{k_r P_{CH_4}}{(1 + K_{H_2O} P_{H_2O} + K_{CO_2} P_{CO_2})^2}$
8	$r_r = \frac{k_r P_{CH_4} k_{O_2} P_{O_2}}{k_{O_2} P_{O_2} + 2k_r P_{CH_4} (1 + K_{H_2O} P_{H_2O}) + (k_r k_{CH_4} / k_3) P_{O_2} P_{CH_4}}$
9	$r_r = \frac{k_r P_{CH_4} k_{O_2} P_{O_2}}{k_{O_2} P_{O_2} (1 + K_{H_2O} P_{H_2O}) + 2k_r P_{CH_4} + (k_r k_{CH_4} / k_3) P_{O_2} P_{CH_4}}$

Models 1, 2a and 2b are simple power law models. Models 2a and 2b include reaction orders with respect to H₂O and CO₂ in order to improve the data fitting. *Zhu et al.* [264] and *Ribeiro et al.* [265] used the power law model to describe the complete oxidation of methane on an 8.5% Pd/Al₂O₃ catalyst. Both groups proposed a reaction order of 1, 0 and -1 for CH₄, O₂ and H₂O respectively and a reaction activation energy of 150 kJ mol⁻¹. The negative order of H₂O implies of course that this has an inhibition effect while the zero order for oxygen indicates that the reactive adsorption of O₂ is not rate influencing. The generally simple 1st order dependency of methane indicates that the rate determining step is an adsorptive or reaction step of methane itself. *Araya et al.* proposed the same reaction order for the before mentioned species but a somewhat higher activation energy of 172 kJ mol⁻¹ when studying the CH₄ oxidation catalysed by a 1% Pd/SiO₂ catalyst [266]. *Fujimoto et al.* proposed values in line with the other research groups when investigating the

complete CH₄ combustion on a 5% Pd/ZrO₂ catalysts; the authors suggested a reaction order of 1.1, 0.1 and -1 for CH₄, O₂ and H₂O respectively and an activation energy of 185 kJ mol⁻¹ [267]. The non-integer reaction order of methane is difficult to reconcile with any mechanistic aspect of the reaction. *Chin and Iglesia* proposed a mechanistic kinetic model in order to incorporate the H₂O effects on the rate of methane combustion; the proposed elementary steps are reported below:



where O^{*} represents PdO sites and * is an O vacancy on the PdO surface. In accordance with the literature, the authors considered the O₂ dissociative adsorption to be kinetically insignificant. This mechanism can be described by a *Langmuir-Hinshelwood* mechanism having the general form:

$$r_r = kP_{\text{CH}_4}\theta_V^n \quad (5.1)$$

where θ_V is the fraction of available adsorption sites with n having a value of 2 when a site pair is kinetically essential for dissociation of CH₄ (e.g. models 4, 5 and 7) or equal to 1 if CH₄ is assumed to be adsorbed on the surface and react with O₂ from the gas phase (e.g. models 3 and 6). *Kikuchi et al.* proposed a mechanistic model in which adsorbed water is assumed to be the most abundant surface intermediate (Models 3 and 4); the authors derived a value of 81 kJ mol⁻¹ and -49 kJ mol⁻¹ for the reaction activation energy and enthalpy of water adsorption respectively for Pd/Al₂O₃ catalysts [268]. *Abbasi et al.* assumed that adsorbed CH₄ and adsorbed H₂O are the most abundant surface intermediates resulting in a kinetic equation expressed by model 5; the authors proposed a reaction activation energy of 72.6 kJ mol⁻¹ and a H₂O adsorption enthalpy of -24.1 kJ mol⁻¹ [269].

It is notable that all the studies using a *Langmuir-Hinshelwood* based kinetic model report activation energies significantly lower than those using a simple order of reaction approach. This indicates that the simple order approach is in fact lumping one or more phenomena into the apparent activation energy value.

Mars van Krevlen models have been used by *Hurtado et al.* [270] to describe the CH₄ combustion over Pd catalysts. In this case, the reaction is assumed to occur through alternative oxidation and reduction of the catalyst surface. The dissociatively chemisorbed O₂ provides the surface O. CH₄ is irreversibly chemisorbed on the oxidized sites and reacts with the surface O leading to the formation of CO₂ and H₂O. This mechanism is described by models 8 and 9 where different assumptions such as the negligible amount of chemisorbed O, the fast desorption of CO₂ and the slow desorption of H₂O are made in order to take into account the inhibition effect of H₂O. The difference between model 8 and 9 lies in the types of catalyst sites affected; in model 8 reduced sites are assumed to be involved in the reaction while in model 9 oxidised sites are taking part in the reaction. The kinetic parameters derived by *Hurtado et al.* are summarised in the table below (Table 5. 2):

Table 5. 2: Kinetic parameters estimated by Hurtado et al. for a Mars van Krevlen CH₄ oxidation mechanism with A_r and A_{O_2} in mol bar⁻¹ min⁻¹ g⁻¹, A_3 in mol min⁻¹ g⁻¹, A_{H_2O} in bar⁻¹ and E_{a_r} , $E_{a_{O_2}}$, E_{a_3} and ΔH_{H_2O} in kJ mol⁻¹

	A_r	E_{a_r}	A_{O_2}	$E_{a_{O_2}}$	A_3	E_{a_3}	A_{H_2O}	ΔH_{H_2O}
Oxidised Sites	4.9×10^{-3}	135.6	3.5×10^{-2}	52.44	1.0×10^{-4}	55.2	974.9	-54.5
Reduced Sites	7.0×10^{-3}	35.9	3.3×10^{-2}	45.3	9.9×10^{-5}	71.4	5082	-66.1

The Johnson Matthey intrinsic kinetic model used in this investigation was developed using catalyst fines (particles size 4-46 µm) to ensure that no transport limitation occurred during the experiment. All the models reported in Table 5. 1 were used to fit the experimental data with model

4 giving the best fit; this suggests that the kinetic mechanism proposed by *Chin and Iglesias* is a good description of the reacting system. The kinetic model parameters were estimated by Dr Sam Wilkinson and Dr Johanna Espach of JM, based on a collaborative work between Johnson Matthey Technology Centres at Chilton and Pretoria using data measured at Sonning Common; these are summarised in Table 5. 3.

Table 5. 3: Kinetic parameters estimated in-house for the kinetic model 4

	Parameter	Parameters Value	Lower conf. as %	Upper conf. as %
1	A_r ($\text{m}^3 \text{s}^{-1} \text{Kg}^{-1}$)	523.5	5.0	5.0
2	E_{a_r} (kJ mol^{-1})	36.49	34.4	34.4
3	A_{H_2O} ($\text{m}^3 \text{mol}^{-1}$)	9.327E-05	13.4	15.4
4	ΔH_{H_2O} (kJ mol^{-1})	-69.74	44.7	44.7

From Table 5. 3 it can be noted that the parameter that presents the highest confidence interval is the enthalpy of water adsorption emphasising the difficulty in estimating this parameter simply from reaction data. As previously mentioned, water adsorption inhibits the rate of reaction; it is expected that the high confidence level of this term will affect the data fitting in systems where water concentration is significant (e.g. wet oxidation of methane). The parameters in Table 5. 3 were used to calculate the rate constant k_r and the water adsorption coefficient K_{H_2O} present in model 4; these are defined as:

$$k_r = A_r e^{-\frac{E_{a_r}}{RT}} \quad (5.2)$$

$$K_{H_2O} = A_{H_2O} e^{-\frac{\Delta H_{H_2O}}{RT}} \quad (5.3)$$

5.3 Diffusion in porous solids

Diffusion can be defined as the movement of molecules or atoms from a region of high concentration to a region of low concentration. The first systematic study of diffusion was performed by *Graham* in 1833 when he studied gas diffusion stating that *gases of different nature, when brought into contact, do not arrange themselves according to their density but they spontaneously diffuse through each other remaining in the intimate state of mixture for any length time* [271]. In 1855, *Fick* proposed his laws of diffusion. *Fick's* first law relates the diffusive flux to the concentration under the assumption of steady state and it is described as follow:

$$J = -D \frac{dc}{dx} \quad (5.4)$$

where J is the diffusion flux expressed in $\text{mol m}^{-2} \text{s}^{-1}$, D is the diffusion coefficient expressed in $\text{m}^2 \text{s}^{-1}$, c is the species concentration in mol m^{-3} and x is the length in m. In his second law *Fick* describes the concentration change in time due to diffusion; this is expressed by the partial differential equation reported below [272]:

$$\frac{\partial c}{\partial t} = D \frac{\partial^2 c}{\partial x^2} \quad (5.5)$$

In 1866 *Maxwell* [273] and *Stefan* [274] independently developed a model for describing diffusion in a multicomponent system. The fundamental assumptions of the model are: the system is in steady state conditions and that two forces, which cancel each other, are exerted on the molecules. These forces are the chemical potential gradient, which is the driving force for diffusion, and the friction with all the other moving species which is proportional to the velocity difference between the two species and their concentration [275]. This model is known with the name of *Stefan-Maxwell* equation and it is described below [276]:

$$\frac{\nabla \mu_i}{RT} = \nabla \ln a_i = \sum_{j=1}^n \frac{\chi_i \chi_j}{D_{ij}} (\vec{v}_j - \vec{v}_i) = \sum_{j=1}^n \frac{c_i c_j}{c^2 D_{ij}} \left(\frac{\vec{J}_j}{c_j} - \frac{\vec{J}_i}{c_i} \right) \quad (5.6)$$

where μ is the chemical potential, R is the gas constant, T is the temperature, a is the activity, χ is the mole fraction, D_{ij} is the *Stefan-Maxwell* diffusion coefficient, c is the molar concentration and J is the component flux. The *Stefan-Maxwell* theory is more comprehensive than the classical *Fick's* diffusion theory and the latter can be derived from the *Stefan-Maxwell* equation (SM). The SM equation is used to describe the diffusion in more complex systems such as the diffusion in microporous systems, and the diffusion of gas and liquids in more extreme conditions such as in the case of high-temperature gas nuclear reactors [277] and in plasma mixtures [278]. The *Stefan-Maxwell* equation can rarely be solved analytically so numerical approaches are usually employed. Due to, both the relative simplicity of the system investigated in this work and the higher computational demand required to solve the *Stefan-Maxwell* equation, the *Fick* classical theory was used for the description of the diffusion phenomena.

Turning now to the different relationships proposed in the literature for the calculation of the binary diffusion coefficient. *Chapman and Cowling* considered molecules as rigid elastic spheres and the binary coefficient of diffusion is described by [279]:

$$D_{AB} = \frac{3}{8n_0\sigma_{12}^2} \sqrt{\frac{k_B T}{2\pi} \left(\frac{1}{m_A} + \frac{1}{m_B} \right)} \quad (5.7)$$

where n_0 is the number density and it is obtained from the ideal gas law ($n_0 = p_0/k_B T$), σ_{12} is the scattering cross section obtained by averaging the molecular radii of each species, k_B is the Boltzmann constant and m_A and m_B are the molecular masses of the considered species. *Mason and Malinauskas* considered intermolecular forces other than a model of rigid elastic spheres and a

temperature dependant pre-factor was introduced via the collision integral Ω_{12} in the diffusion coefficient equation which is reported below [280]:

$$D_{AB} = \frac{3}{8n_0\sigma_{12}^2} \sqrt{\frac{k_B T}{2\pi} \left(\frac{1}{m_A} + \frac{1}{m_B} \right)} \frac{1}{\Omega_{12}(T)} \quad (5.8)$$

It is important to point out that in this latter case the length parameter σ_{12} depends on the intermolecular force law and its value is not the same as in the case of the rigid elastic spherical molecules. *Fuller et al.* proposed a simplified method for predicting the binary gas-phase diffusivities based on the use of special diffusion volumes; the authors compared the proposed method with other widely recognized correlations demonstrating the reliability of their method. The equation proposed by *Fuller, Schettler and Giddings* is [281]:

$$D_{AB} = \frac{1 \cdot 10^{-3} T^{1.75} \left(\frac{1}{MW_A} + \frac{1}{MW_B} \right)^{1/2}}{P [(\sum_A v_i)^{1/3} + (\sum_B v_i)^{1/3}]^2} \quad (5.9)$$

where MW is the molecular weight of the considered species, P is the pressure and v_i is the special diffusion parameters to be summed over atoms, groups, and structural features of the diffusing species. This latter correlation was used in this study to determine the bulk diffusion of the considered gaseous species.

It is important to remark that, when considering diffusion in a porous solid, the porosity ϕ of the medium restricts the cross-sectional area available for transport while the tortuosity τ of the medium accounts for the increased path length that the molecules have to travel. The diffusion coefficient in a Fickian diffusion regime D_F consequently becomes:

$$D_F = \frac{\phi}{\tau} D_{AB} \quad (5.10)$$

where the ratio ϕ/τ takes the name of obstruction factor [280].

In a porous solid, depending on the pores radii and operating conditions, different diffusion regimes can be encountered. At high gas pressure and large pore diameters, molecule-molecule collisions dominate in respect to molecule-walls collisions and the system is said to be in bulk or Fickian diffusion regime. At low pressures and small pore diameters, collisions are predominantly between molecules and the walls and the mean free path (e.g. average distance travelled by a moving particle between successive collisions [282]) is restricted to the geometry of the void space; this regime takes the name of Knudsen regime and the diffusion coefficient is expressed by the following equation:

$$D_K = \frac{2}{3} a \sqrt{\frac{8RT}{\pi MW}} \quad (5.11)$$

where a is the mean radii of the pores.

It is not uncommon in porous systems to have both regimes occurring at the same time, at intermediate pressures, in fact, collisions with pore walls and with other molecules occur with significant frequency. In this case an effective diffusion coefficient can be defined which accounts for the contribution of both the Fickian diffusion coefficient and the Knudsen diffusion coefficient.

Pollard and Present proposed the so called Bosanquet relationship which is shown below [283]:

$$D_{eff} = \frac{1}{1/D_{AB} + 1/D_K} \quad (5.12)$$

Wakao and Smith proposed the Random Pore Model to predict the diffusion rate at constant pressure through bi-disperse porous media. They assumed that the total rate is the sum of separate

contributions for diffusion through macropores, micropores and a series path; the proposed equation is [284]:

$$D_{eff} = \varepsilon_M^2 D_{AB} + \varepsilon_m^2 D_K + \frac{4(\varepsilon_M - \varepsilon_M^2)}{1/D_{AB} + (1 - \varepsilon_M)^2 / (\varepsilon_m^2 D_K)} \quad (5.13)$$

where ε_M is the solid macroporosity and ε_m is the solid microporosity; in order for this relationship to be applied, the characterisation of the solid porous structure is necessary. In this work both the Bosanquet and the *Wakao-Smith* correlations were tested with the latter giving a better matching to the experimental results.

5.4 SpaciMS Technique

The SpaciMS technique was developed by the researchers in the Fuels, Engines, and Emission Research Centre (FEERC) at Oak Ridge National Laboratory (ORNL) as a new measurement technique to study the dynamic chemistry of NO_x storage reduction catalysts [285] [286]. This technique employs fused-silica capillary tubes axially inserted into monolith channels for minimally invasive sampling of reaction mixtures at different locations. Extracted gas samples are analysed with a mass spectrometer to provide highly time-resolved species concentration measurements. The capillary sampling probes can be positioned at multiple axial and/or radial locations to build up detailed spatio-temporal picture of the reaction; Figure 5. 1 shows a schematic of the SpaciMS.

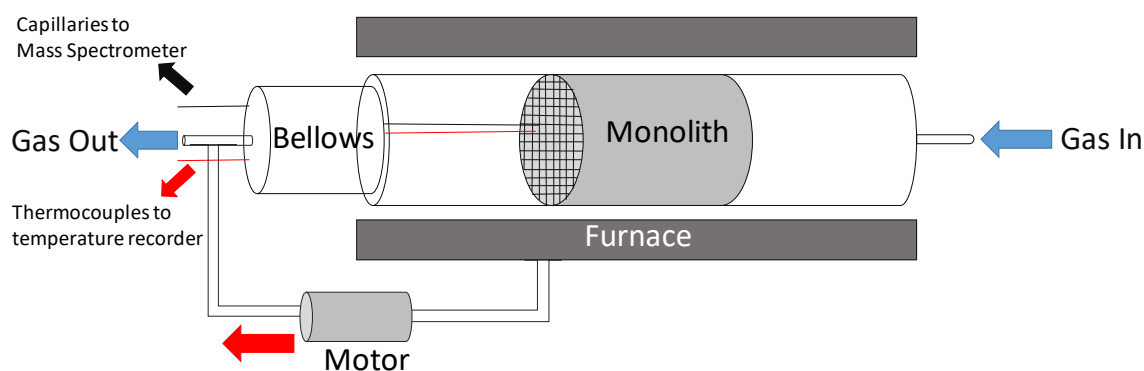


Figure 5. 1: SpaciMS schematic

This technique is an alternative to the conventional approach in which the powdered form of the catalysts are screened for activity and selectivity and thereafter loaded onto a monolith for further evaluation and scale up; the catalyst properties are then measured by analysis of the chemical species at the reactor exit (end-pipe). This conventional approach is limited in the sense that it does not allow to gather information concerning the process within the monolith such as reaction pathways, temperature and formation of intermediates [287]. SpaciMS has become extensively used to gather valuable information especially in fast transient emission associated with the development and operation of Lean NO_x Trap (LNT). *Partridge et al.* used the SpaciMS to study LNT being operated in the exhaust of a diesel engine with in-pipe fuel injection; the authors demonstrated the robust nature of SpaciMS with respect to direct sampling of undiluted diesel exhaust and remarked the need for high temporal resolution in the fundamental research and development of transient LNT [288]. SpaciMS has been extensively employed for general transient exhaust characterisation; *West et al.* used it to assess various in-cylinder fuel management strategies for exhaust hydrogen generation [289] while *Parks et al.* used it to study dynamic rich-lean modulation [290]. SpaciMS has also been applied to elucidate detailed LNT chemistry: *Choi et al.* showed the efficiency of various reducing agents and dynamic Pt poisoning during lean-rich-lean

cycling [291], *Choi et al.* also demonstrated the importance of the water-gas-shift reaction in LNT regeneration with CO [292] and, the same authors, gave an insight into how progressive sulfation uniquely impacts the various LNT chemical functions including NO_x storage and reduction, oxygen-storage capacity and water-gas-shift [293]. More recently, *Sharma and Dearth* used SpaciMS to measure the effective diffusivity of oxygen through the porous washcoat and through the porous walls of a cordierite monolith substrate [294]. In addition to the capability of providing high temporal resolution of reactions transients, the SpaciMS is considered to be non-invasive due to both the small capillary used and the low sampling rate; *Sá et al.* carried out 3D CFD studies to confirm that the impact of both thermocouples and capillary probes within the monolith have no significant effects on the catalytic and dynamic behaviour [287]. *Coney and Goguet* (Queen's University Belfast) used the SpaciMS technique to investigate both the steady state and transient oxidation of methane at different operating conditions such as different temperatures, wet and dry feed (*Coney*, PhD Thesis to be published). In this work, the axial concentrations measured by *Coney*, at steady state and different operating conditions, were used to validate the in-house developed kinetic model. Description of the experimental concentration trends and the effects of feed composition on methane oxidation will be given later on in the chapter.

5.5 Reactor Model

When modelling the performance of a washcoated monolith, the mass and the energy balances have to be carried out on both the solid and the fluid regions of the system. In this section, the reader is introduced to the equations used in the modelling of the reactor performance. It is important to point out that a steady state system was modelled and that, consequently, the time derivative terms of the balances are equal to zero.

Figure 5. 2 shows a schematic of the monolith channel with the grey area representing the catalyst washcoat; the figure also shows the spatial boundary conditions for the washcoat layer.

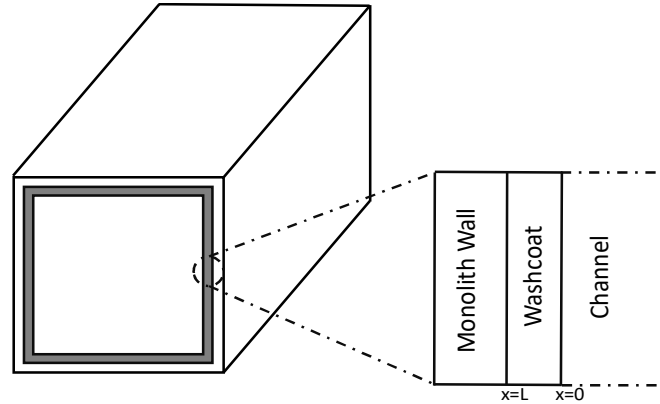


Figure 5. 2: Schematic of a washcoated monolith; grey area represents the catalytic washcoat. Detail of the monolith shows the boundary conditions for the washcoat layer.

The mass and energy balances for the catalysts washcoat are represented by (5.14) and (5.15) respectively [295].

$$\frac{\partial c_i}{\partial t} = D_{eff} \frac{\partial^2 c_i}{\partial x^2} + n_i r_j \quad (5.14)$$

$$\frac{\partial T}{\partial t} = k_{eff} \frac{\partial^2 T}{\partial x^2} - \sum_j r_j (-\Delta H_{r,j}) \quad (5.15)$$

where n_i is the stoichiometric coefficient for the species i , r_j is the reaction rate, k_{eff} is the effective thermal conductivity of the washcoat, h is the thermal convection coefficient, S is the reactor surface area to volume ratio, T_s is the temperature of the solid pellet, T_g is the temperature of the gas phase and $\Delta H_{r,j}$ is the enthalpy of reaction. Considering the boundary condition $x = 0$ the mass and energy balances are represented by (5.16) and (5.17):

$$\frac{\partial c_i}{\partial t} = D_{eff} \frac{\partial c_i}{\partial x} + k_{s,i} (C_{i,b} - C_{i,s}) \quad (5.16)$$

$$\frac{\partial T}{\partial t} = k_{eff} \frac{\partial T}{\partial x} + h (T_s - T_g) \quad (5.17)$$

where k_s is the film mass transfer coefficient. At $x = L$ the mass and energy balances are described by (5.18) and (5.19) respectively [295]:

$$\frac{\partial c_i}{\partial x} = 0 \quad (5.18)$$

$$\frac{\partial T}{\partial x} = 0 \quad (5.19)$$

The mass and energy balances at the reactor scale were determined along the channel axial direction and are represented by (5.20) and (5.21) respectively [295]:

$$u_z \frac{\partial c_i}{\partial z} = a_v k_{s,i} (C_{i,b} - C_{i,s}) \quad (5.20)$$

$$\rho_g C_{p,g} u_z \frac{\partial T_g}{\partial z} = hS (T_s - T_g) \quad (5.21)$$

where u_z is the gas superficial velocity, a_v is the washcoat specific area, defined as $a_v = 4 D_p / D_w$ where D_p is the channel radial length and D_w is the sum of the wall thickness and channel radial length. To determine the film mass transfer coefficient, the following correlations between the Sherwood number and the mass transport Graetz number were used [296]:

$$Sh = 2.997 + 6.874 \left(\frac{1000}{G_{z,m}} \right)^{-0.488} e^{\left(-\frac{57.2}{G_{z,m}} \right)} \quad (5.22)$$

with the Sherwood number defined as $Sh = \frac{k_s d}{D_{AB}}$ and the Graetz number defined as $G_{z,m} = \frac{d Re Sc}{z}$

where z is the reactor length and Sc is the Schmidt number expressed as $Sc = \frac{\mu}{\rho D_{AB}}$.

The analogous correlation between the Nusselt number and the heat transfer Graetz number was used to determine the heat transfer coefficient [296]:

$$Nu = 2.997 + 6.874 \left(\frac{1000}{G_{z,t}} \right)^{-0.488} e^{\left(-\frac{57.2}{G_{z,t}} \right)} \quad (5.23)$$

where the Nusselt number is $Nu = \frac{hd}{k_g}$, whit k_g equal to the thermal conductivity of the gas, and the heat transfer Graetz number is $G_{z,t} = \frac{dRePr}{z}$ where Pr is the Prandtl number expressed as $Pr = \frac{C_p \mu}{k_g}$ whit C_p equal to the gas heat capacity.

5.6 1D + 1D Modelling of CH₄ Oxidation: Comparison of Model and Experimental Results

Athena Visual Studio v14.1 (Neperville, IL 60540; <http://athenavisual.com/>) was used to model the CH₄ oxidation in a monolithic reactor. A 1D + 1D approach was used; a closed subroutine was employed to model radial diffusion and reaction in the washcoat. A Cartesian coordinate system was used and the space domain was integrated between the left boundary $x = 0$ and the right boundary $x = L$ with the global orthogonal collocation used as discretization method; in this method, a finite basis of global interpolating polynomials was used to approximate the state and control at a set of discretisation points. In the global method, collocation is obtained using a global polynomial across the entire interval as the basis for approximation [297]. The subroutine results were then passed to the code describing mass and heat transfer in the monolith channel where the equations were integrated between $x = 0$ and $x = \text{reactor length}$. Table 5. 4 summarises the different operating conditions modelled while Table 5. 5 summarises the model parameters; the kinetic parameters are not shown in the latter table since they have already been summarised in Table 5.

3.

Table 5. 4: Operating conditions of the different CH₄ oxidation reactions simulated and experimentally investigated

Run #	% _{vol} CH ₄	% _{vol} O ₂	% _{vol} Ar	% _{vol} H ₂ O	Temp. (°C)
1	0.4	12	87.6	0	400
2	0.4	12	87.6	0	425
3	0.4	12	87.6	0	450
4	0.4	12	86.6	1	400
5	0.4	12	86.6	1	425
6	0.4	12	86.6	1	450

Table 5. 5: Summary of model parameters

Symbol	Parameter	Value	Derivation
ε_m	Washcoat mesoporosity (fraction)	0.45	Measured by Mercury Intrusion Porsimetry
ε_M	Washcoat macroporosity (fraction)	0.1	SEM image analysis
a	Average washcoat pore diameter	$1.3 \cdot 10^{-10}$ m	Measured by Mercury Intrusion Porosimetry
D_{wash}	Washcoat thickness	$3 \cdot 10^{-5}$ m	SEM image analysis
D_p	Channel radial length	$8.4 \cdot 10^{-4}$ m	SEM image analysis
D_w	Channel radial length + wall thickness	$1.1 \cdot 10^{-3}$ m	SEM image analysis
L_{tube}	Monolith Length	$1 \cdot 10^{-2}$ m	Measured
k_s	Film mass transfer coefficient	0.29 m s^{-1}	Calculated from Sherwood correlation (5.21)
h_t	Heat transfer coefficient	$50.9 \text{ W m}^{-2} \text{ K}^{-1}$	Calculate from Nusselt correlation (5.22)
k_{eff}	Alumina effective thermal conductivity	$26 \text{ W m}^{-1} \text{ K}^{-1}$	From literature [298]
ΔH_r	Enthalpy of reaction	$802.2 \cdot 10^3 \text{ J mol}^{-1}$	Calculated from standard enthalpies of formation
u_z	Superficial velocity	0.27 m s^{-1}	From experimental conditions

In Section 5.3 it has been shown that two different correlations have been proposed for the calculation of the effective diffusivity coefficient, namely the Bosanquet and the *Wakao and Smith* correlations. To select which one better described the diffusion process, the reaction characterised by a dry feed and the highest operating temperature was modelled using both correlations. This reaction was selected because the dry feed and high reaction temperature, give the highest reaction rate, making the effects of diffusion limitation more evident.

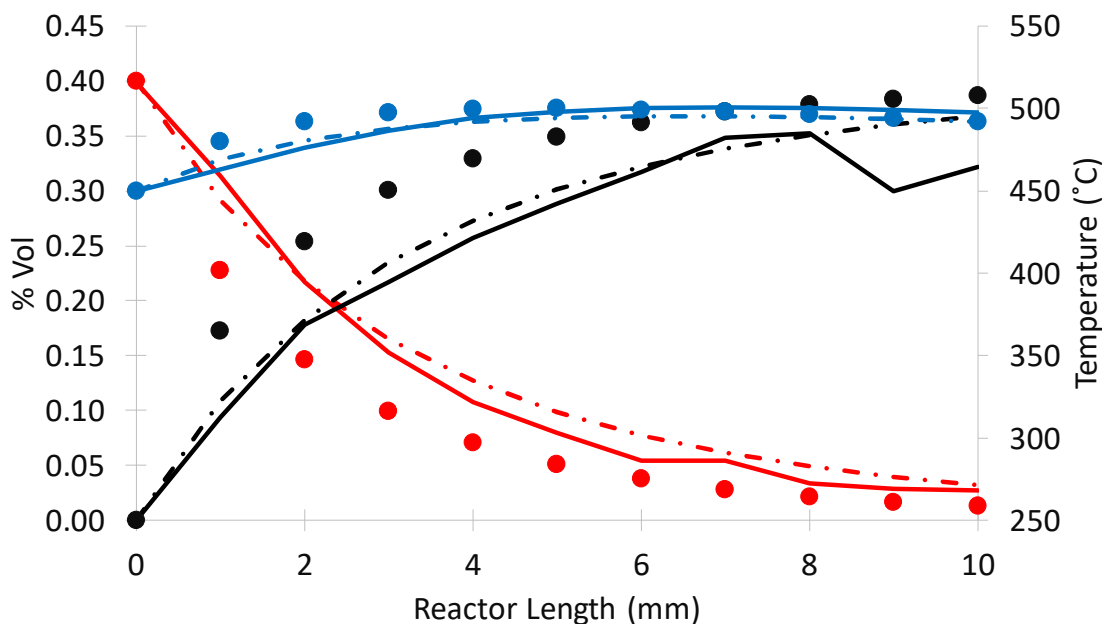


Figure 5. 3: Comparison among model results obtained using both the Bosanquet (Mod-Bos) and the Wakao Smith (Mod-WS) correlation and the experimental results for the CH_4 oxidation reaction conducted at 450 °C and in dry feed. The different species are represented by: (—) CH_4 Exp, (—●) CH_4 Mod-WS, (●) CH_4 Mod-Bos; (—) CO_2 Exp, (—●) CO_2 Mod-WS, (●) CO_2 Mod-Bos; (—) Temp Exp, (—●) Temp Mod-WS, (●) Temp Mod-Bos

Figure 5. 3 shows the comparison between the model results obtained using both correlations and the experimental data. It can be noted from Figure 5. 3 that, when the Bosanquet relationship is used to calculate the effective diffusivity coefficient, the CH_4 conversion is significantly overpredicted in the first part of the reactor. Given the fact that, in both cases, the same experimentally determined parameters (Table 5. 4 and Table 5. 5 above) were used in the intrinsic kinetic model, this indicates that the diffusion itself is over-predicted. For this reason, the *Wakao-Smith* correlation was used in all the following modelling work.

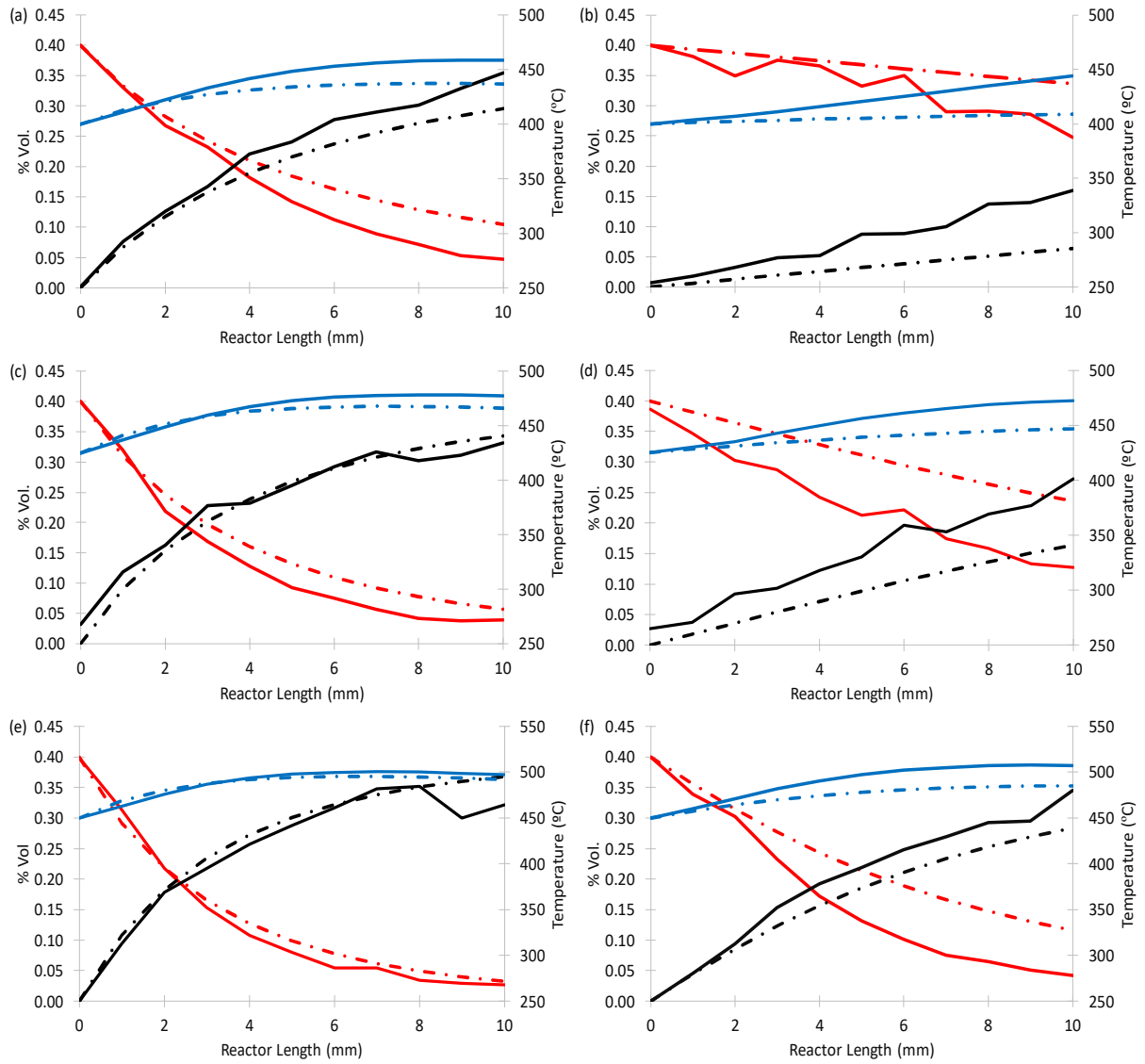


Figure 5. 4: Comparison between model and experimental results for methane oxidation conducted at different operative conditions (a) dry feed, 400 °C (b) wet feed, 400 °C (c) dry feed, 425 °C (d) wet feed, 425 °C (e) dry feed, 450 °C (f) wet feed, 450 °C. The different species are represented by: (—) CH₄ Exp., (—●) CH₄ Mod., (—) CO₂ Exp., (—●) CO₂ Mod., (—) Temp. Exp., (—●) Temp. Mod.

Figure 5. 4 shows the comparison between the model and experimental results for all the investigated operating conditions. It is important to point out the water inhibition effect observed experimentally; in all cases, methane conversion is significantly reduced in the case of wet feed. This observation is in accordance with the kinetic model used for the determination of the intrinsic kinetic parameters. Figure 5. 4 shows that the model well predicts the concentrations and

temperature profile for the dry feed while discrepancies are observed in the case of the wet feed. In addition, it can be noted that, in the case of the dry feed, the model, in every case, well predicts the profiles in the first part of the reactor (up to 3 mm) while the trends' prediction in the second part of the reactor improves as the reaction temperature is increased.

In the kinetic model and reaction mechanism discussed in Section 5.2 it has been shown that water adsorption affects the rate of reaction and consequently methane conversion. Water inhibition effect is more evident in the case of wet feed due to the high initial water concentration. In any case, water inhibition is more pronounced in the second half of the reactor due to the higher water concentration formed as the oxidation reaction proceeds. Temperature also plays an important role; in fact, higher temperatures favour water desorption from the catalyst surface making its inhibition effect less relevant. In Table 5. 3 it was shown that the enthalpy of water adsorption presents the highest confidence interval amongst all the estimated parameters (44.7 %) and, due to the significant impact of this term on the reaction kinetic, the sensitivity of the model to the enthalpy of water adsorption was tested; this allowed to determine if the discrepancy between the model and the experimental results, observed especially for the wet feed, are due to a poor estimation of this parameter. Figure 5. 5 shows the comparison between the model and the experimental results for the CH₄ oxidation carried out at 400 °C and in wet feed condition. In this case the value of the enthalpy of water adsorption was reduced by 5% with respect to the value reported in Table 5. 3; it is important to outline that the new parameters lies inside the confidence interval of the initially estimated parameter. These conditions were selected because at lower temperatures the effect of water inhibition is more marked.

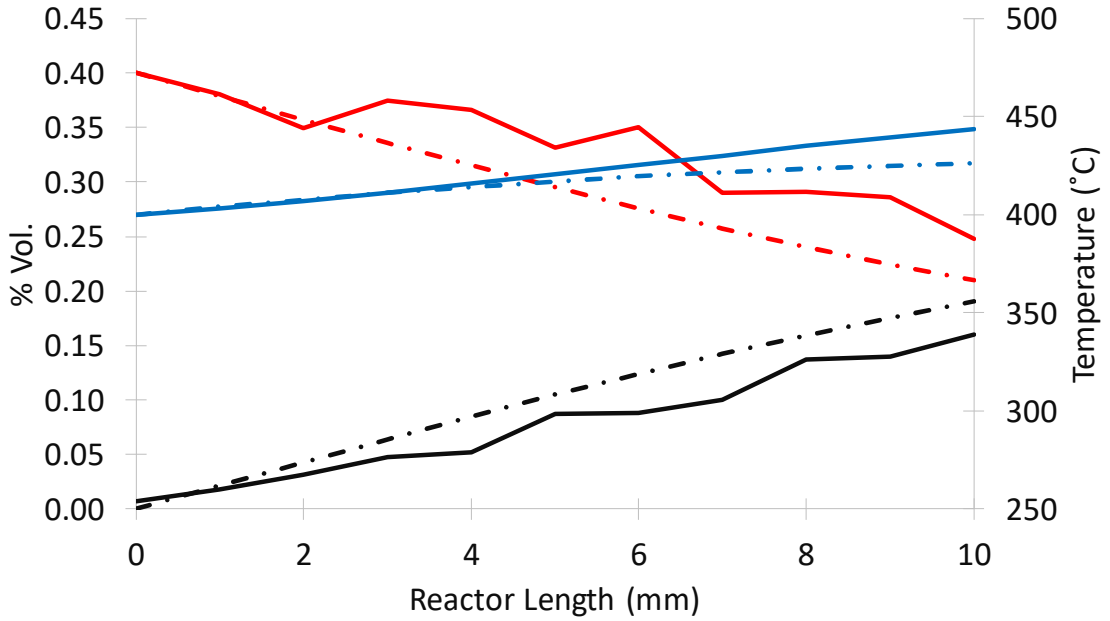


Figure 5. 5: Comparison between model and experimental results for the CH_4 oxidation carried out at 400°C and in wet feed in the case in which the water's enthalpy of adsorption is reduced by 5%. The different species are represented by: (—) CH_4 Exp., (—●) CH_4 Mod., (—) CO_2 Exp., (—●) CO_2 Mod., (—) Temp. Exp., (—●) Temp. Mod.

It can be noted from Figure 5. 5 that the model results agree with the experimental ones when the enthalpy of water adsorption is reduced by 5%. The model sensitivity to the water enthalpy of adsorption also explains the discrepancies observed in the second part of the reactor when the CH_4 oxidation in dry feed is carried out. In the first part of the reactor the amount of produced water is negligible; as the reaction proceeds the amount of formed water, and consequently adsorbed water, increases leading to the observed discrepancies between the model and the experimental results. Water adsorption becomes less significant as the reaction temperature is increased; this explains the better agreement between the model and the experimental results when the reaction temperature is increased. These observations can be explained by the dependence of the water adsorption coefficient on both the enthalpy of adsorption and temperature; such dependence was shown before in equation (5.3).

Once the 1D + 1D model had been validated against the experimental data, this was used to obtain information not readily available experimentally such as the chemical species concentration profile and temperature profile inside the wash-coat. Figure 5. 6 shows the CH₄ concentration profiles, CO₂ concentration profiles and the temperature profiles inside the wash-coat for the CH₄ oxidation reaction carried out at the operating conditions reported in Table 5. 4; it is important to point out that these wash-coat profiles were modelled at a monolith length equal to 5 mm.

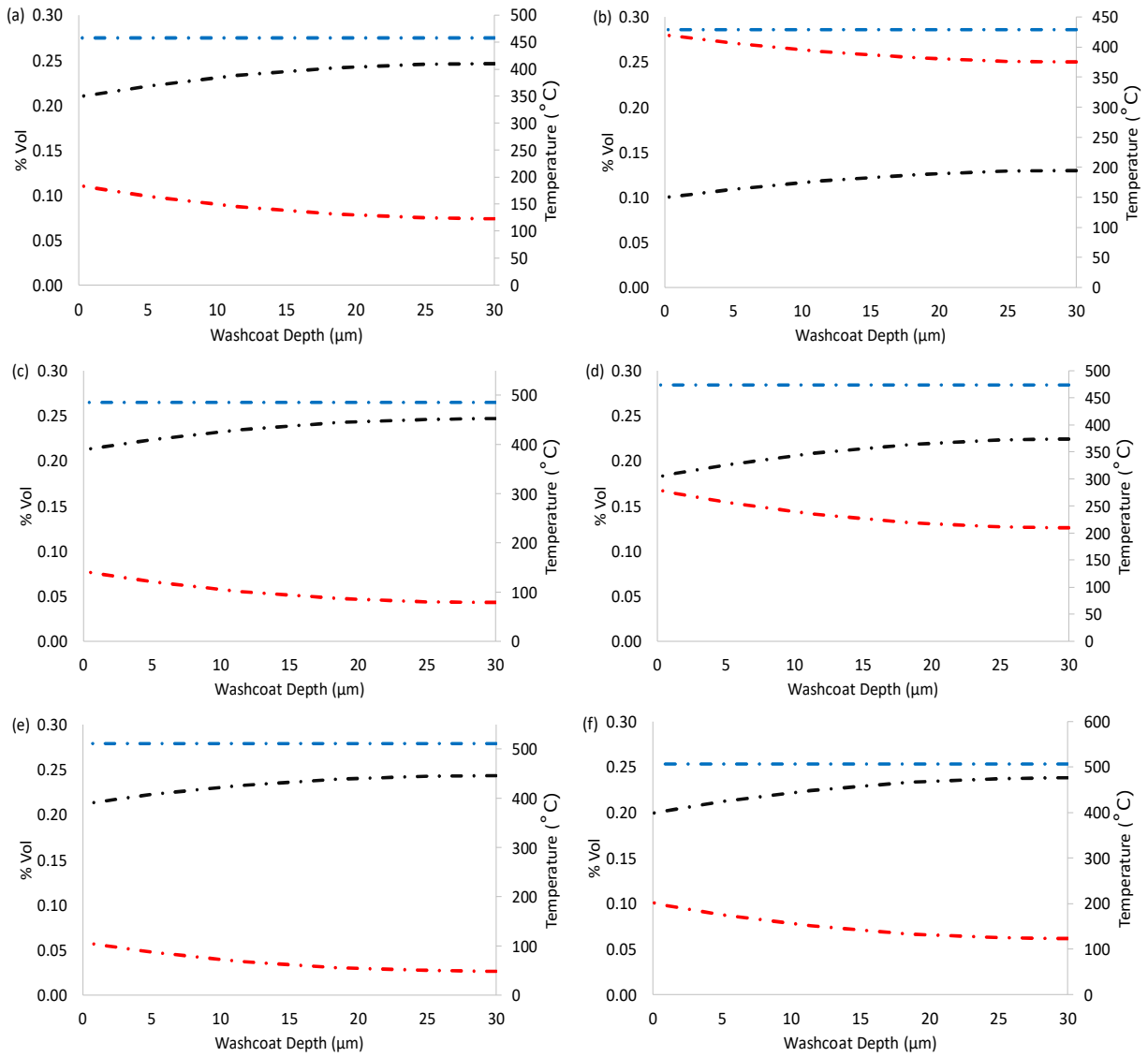


Figure 5. 6: Chemical species concentration profiles and temperature profile inside the wash-coat (model at reactor length of 5 mm) for methane oxidation conducted at different operative conditions (a) dry feed, 400 $^{\circ}\text{C}$ (b) wet feed, 400 $^{\circ}\text{C}$ (c) dry feed, 425 $^{\circ}\text{C}$ (d) wet feed, 425 $^{\circ}\text{C}$ (e) dry feed, 450 $^{\circ}\text{C}$ (f) wet feed, 450 $^{\circ}\text{C}$. The different species are represented by: (—●) CH_4 , (—●) CO_2 , (—●) Temp. Mod.

From Figure 5. 6 it can be noted that the wash-coat is isothermal; this was expected due to its small depth (30 μm). In addition, also in these graphs, it can be observed the water inhibition effect with a lower CH_4 conversion observed in the case of the wet feeds. The model can also be used to determine the 2D concentration profiles inside the wash-coat. For simplicity, Figure 5. 7 shows only the 2D concentration profile for CH_4 ; the graphs depict the change in CH_4 concentration within

the wash-coat and along the reactor channel. The different colours of the surface plot help the reader to visualise areas at which different concentrations occur.

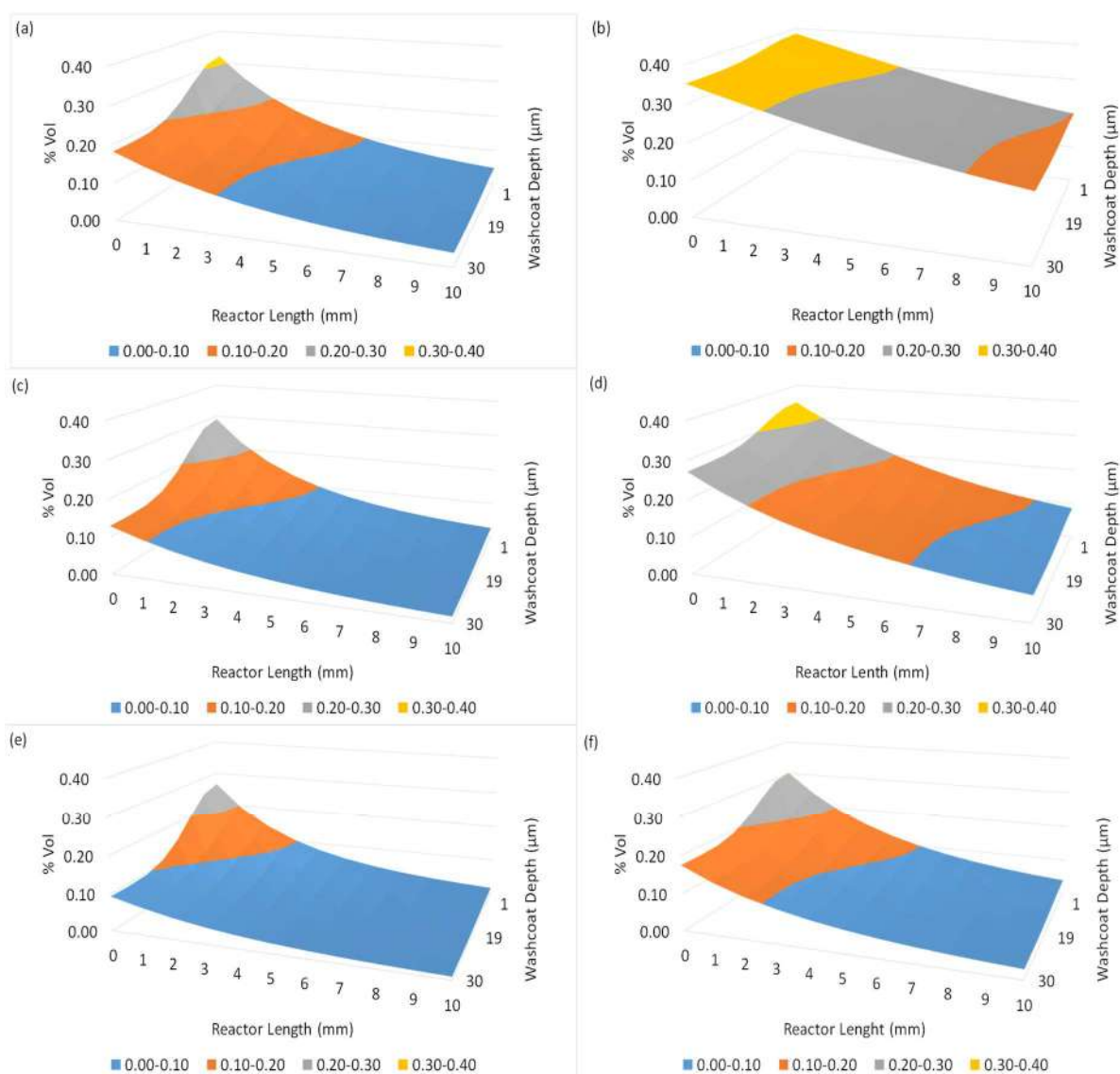


Figure 5. 7: 2D CH₄ concentration profile within the washcoat and along the reactor channel for methane oxidation conducted at different operating conditions (a) dry feed, 400 °C (b) wet feed, 400 °C (c) dry feed, 425 °C (d) wet feed, 425 °C (e) dry feed, 450 °C (f) wet feed, 450 °C. The different colours of the surface plot indicates areas at different CH₄ concentration: ■ 0-0.1 % vol., ■ 0.1-0.2 % vol., ■ 0.2-0.3 % vol., ■ 0.3-0.4 % vol.,

5.7 Conclusions

In this chapter, a Johnson Matthey intrinsic kinetic model was validated against the experimental results acquired using the SpaciMS technique at Queen's Belfast University. Athena Visual Studio was employed to generate the 1D + 1D code which was used to simulate CH₄ oxidation at different operating conditions. At first, two different effective diffusivity models (e.g. Bosanquet and *Wakao-Smith*) were tested to determine which one is the most appropriate to describe the diffusion phenomena. The Bosanquet model was shown to significantly over predict diffusion, and consequently CH₄ conversion, in the first part of the reactor making the *Wakao-Smith* correlation the most suitable to describe the mass transport phenomena. The comparison of the model and experimental results for CH₄ oxidation carried out at different operating conditions showed that the model satisfactorily predicts the reaction progression in the case of dry feed. Discrepancies are however observed in the case of the wet feed. This discrepancy was explained by the sensitivity of the model to the enthalpy of water adsorption term, in fact, a reduction by 5% of the mentioned term led to a good agreement between model and experimental results. The significant percentage error on the estimated enthalpy of adsorption term during kinetic model parameterisation (44.7%) suggests that this value could be significantly different from the actual value. The model was also used to have an insight into the concentration and temperature profiles inside the wash-coat. In addition, a 2D concentration profile for CH₄ was obtained showing the change in concentration within the wash-coat and along the reactor length. In conclusion, this study showed that the proposed model is capable of well predicting the course of the CH₄ oxidation reaction in dry feed conditions while the same is not true in the case of wet feed conditions. The significant percentage

error on the water enthalpy of adsorption term suggests that direct measurement of this value could be a valuable alternative to have a better insight into the energetic associated with water adsorption.

Chapter 6

Validation of a new OpenFOAM CFD reactor model using SpaciMS experimental data and 1D + 1D simulations

6.1 Introduction

One of the current challenges in catalysis is not only to develop new catalysts formulations but also to understand the interaction of the catalyst with the surrounding reactive flow field. For this reason, the understanding of gas-solid flows in chemical reactors is of paramount importance, calling for the development of reliable simulation tools. These simulation packages have to integrate detailed models of reaction chemistry and computational fluid dynamic (CFD) modelling of macro-scale flow structures. The use of CFD to model diffusion and reaction has historically found significant application in the modelling of packed bed reactors. *Xu and Froment* investigated methane steam reforming reaction using a modified collocation method to obtain parallel pressure profiles of the reacting components in the catalyst pellet [299]. *Salmi and Warna* investigated both the water-gas shift reaction and the methanol synthesis in fixed bed reactors; the authors used an algorithm which combined the orthogonal collocation for the pellet equations and a backward difference method for the bulk phase equations [300]. *Dixon et al.* used CFD to simulate the flow, diffusion, reaction and heat transfer in a 120° segment of a $N = 4$ packed tube for the endothermic methane steam reforming reaction [301]. Recently, a greater interest is arisen in the study of monolithic reactors. *Canu and Vecchi* used CH_4 oxidation experimental data (present in the literature) to compare different 2D and 3D approximations of the square monolith channel; the authors showed that 3D models predict different ignition behaviour with respect to 2D approximations because of the faster heating of the corners [302]. *Canu and Vecchi* also proved that the decrease in the combustion rate at a higher conversion is mostly a chemical effect rather

than a diffusion limitation effect hence the authors recommended that detailed surface and gas-phase reaction mechanisms must be included in the simulation study [302]. *Mazumder and Sengupta* used CFD to investigate the heterogeneous chemical reactions and transport in full-scale catalytic converters [303]. *Kumar and Mazumder* compared various diffusion models for the prediction of heterogeneous combustion in monolith tubes; the authors demonstrated that the dilute approximation model (Fick's law used in this model), is accurate within 2% of the rigorous multi-component diffusion model (Stefan-Maxwell equation used in this model) hence, it can be used with confidence in catalytic combustion applications [304]. *Maffei et al.* studied the effects of different monolith channel shapes (circular and square) in the partial CH₄ oxidation on Rh; the authors showed that the outlet composition and temperature are not considerably affected by the different geometries but, on the other hand, different geometries can lead to different local transport properties resulting in consistent variations within the reactor [305]. In a similar way, *Sadeghi et al.* used CFD to investigate the effect of channel geometry on selective catalytic reduction of NO_x in monoliths [306] while *Allouche et al.* used CFD to develop a non-isothermal model for diesel particulate filters including exothermic and competing chemical reactions [307].

Johnson Matthey Technology Centre, in collaboration with Tridiagonal Solutions, has developed an in-house CFD package capability for modelling reaction and diffusion in porous zones. . This is an OpenFOAM based solver that can be used to model diffusion and reaction. In this chapter the reader is introduced to the CFD package. Then the in-house developed software will be validated against both, the experimental and the 1D + 1D model results, presented in the previous chapter.

6.2 Computational Fluid Dynamic (CFD)

In recent years, the use of CFD has been enlarged to the field of chemical engineering with the option to solve for fluid mixing and chemical reactions [308]. CFD numerically solves the continuity equations over a large number of control volumes; the solution is obtained by supplying boundary conditions to the model boundaries and iteration of the initially guessed solution. The fluid flow balance is described by the *Navier Stokes* equations for the conservation of mass and momentum; these are expressed by (6.1) and (6.2) respectively [309].

$$\frac{\partial \rho}{\partial t} + \frac{\partial(\rho u_i)}{\partial x_i} = S_m \quad (6.1)$$

$$\frac{\partial(\rho u_i)}{\partial t} + \frac{\partial(\rho u_i u_j)}{\partial x_j} = -\frac{\partial P}{\partial x_i} + \frac{\partial \tau_{ij}}{\partial x_j} + \rho g_i + F_i \quad (6.2)$$

where u_i is the fluid velocity and x_i is the considered coordinate, P is the static pressure, ρg_i is the gravitational body force, F_i is an external body force and τ_{ij} is the stress tensor defined as:

$$\tau_{ij} = \left[\mu \left(\frac{\partial u_i}{\partial x_j} + \frac{\partial u_j}{\partial x_i} \right) \right] - \frac{2}{3} \mu \frac{\partial u_1}{\partial x_1} \delta_{ij} \quad (6.3)$$

where μ is the molecular viscosity and the second term on the right-hand side of the equation is the effect of volume dilation. All the simulations in this work were carried out using a laminar flow model which can be solved resolving the *Navier Stokes* equation.

The conservation equation for chemical species was solved using the following equation [309]:

$$\frac{\partial(\rho Y_i)}{\partial t} + \nabla \cdot (\rho \vec{v} Y_i) = -\nabla \cdot \vec{J}_i + R_i + S_i \quad (6.4)$$

where \vec{J}_i is the diffusion flux of species i , R_i is the rate of production of species i by chemical reaction and S_i is the rate of creation by addition from the dispersed phase plus any user defined sources; in OpenFOAM the rate of reaction R_i is expressed as [310]:

$$R_i = \frac{(k_1 [\prod_{i=1}^u K_{1,i}] [\prod_{i=1}^m C_i^{n_{1,i}}]) (1 - K_{eq} \prod_{i=1}^m C_i^{n_{2,i}})}{(a + \sum_{i=1}^u [K_{2,i} \prod_{i=1}^m C_i^{n_{3,i}}])^{q_1} (b + \sum_{i=1}^u [K_{3,i} \prod_{i=1}^m C_i^{n_{4,i}}])^{q_2}} \quad (6.5)$$

In the equation above each k is of the form:

$$k = AT^\beta e^{(-E_a/T)} \quad (6.6)$$

where A is the pre-exponential factor, T is the temperature and E_a is the activation energy. As specified in Chapter 5, the Fickian diffusion model was used to model diffusion with the bulk diffusivity and effective diffusivity calculated using the *Fuller et al.* and *Wakao-Smith* correlations respectively.

In a monolith reactor, heat transfer is generally due to conduction and convection which take place between the flowing fluid, the solid washcoat and the monolith wall; the generalized energy balance equation in the direction of I is:

$$\frac{\partial((\rho E))}{\partial t} + \frac{\partial}{\partial x_i} (u_i (\rho E + p)) = \frac{\partial}{\partial x_i} \left(k_{eff} \frac{\partial T}{\partial x_i} - \sum_j h_j \vec{J}_j + (\overline{\tau_{eff}} u_i) \right) + S_h \quad (6.7)$$

where k_{eff} is the effective conductivity, \vec{J}_j is the diffusion flux of species j and the term E is defined as:

$$E = h - \frac{p}{\rho} + \frac{u_i^2}{2} \quad (6.8)$$

with the sensible enthalpy h defined as the addition of all the terms of multiplied mass fractions and enthalpies for each species. The energy balance equation for the solid section is similar to (6.7):

$$\frac{\partial(\rho h)}{\partial t} + \frac{\partial}{\partial x_i}(u_i \rho h) = \frac{\partial}{\partial x_i} \left(k \frac{\partial T}{\partial x_i} \right) + S_h \quad (6.9)$$

where k is the thermal conductivity of the solid media.

The partial differential equations for the conservation of mass, momentum and energy shown above are solved in the integral form using a finite-volume based technique. This consist of, first of all, dividing the domain into discrete control volumes then, the governing equations on the control volumes are integrated to create an algebraic equation for unknowns and finally the governing equations are solved sequentially. Since these equations are coupled, an implicit and iterative approach to their solution is required.

To conduct CFD simulations, the in-house developed code was used; the package consists of two modules in which different part of the process take place.

The first step is the mesh creation and it is carried out in SnappyHex which, as the name suggests, uses hexahedral mesh structure. The mesh size controls the accuracy of the simulation with a too coarse a mesh resulting in an oversimplified flow profile and a too fine a mesh requiring a long iteration time. When an optimal mesh density is found, refining the mesh will increase the model size without displaying more flow details. The mesh creation consists of three major steps. In the first one a CAD program is used to generate the desired geometry, the second step is the creation of the surface mesh and finally, the surface mesh is interpolated to the fully three-dimensional volume mesh. If local refinement of the mesh is required (e.g. point of contacts), different mesh densities can be defined to surfaces or edges specifically.

The generated mesh is then imported into the OpenFOAM solver and the CFD simulation can be started. In order to perform the simulation, several steps have to be performed:

1. Definition of the turbulence model. At the investigated conditions, Reynolds number in the channel was comprised between 80 and 300 hence the laminar model was used.
2. Definition of the number of species and their properties. 5 species were defined in this study (CH_4 , O_2 , N_2 , CO_2 and H_2O); the required properties for each species were: molecular weight, viscosity, specific heat and enthalpy of formation.
3. Reaction setting. The reaction parameters reported in Section 5.2 were inputted; reaction was set to occur only in the porous zone.
4. Diffusion model setting. Wakao-Smith model was used to calculate diffusion in the porous zone (monolith washcoat) with the equations showed in Section 5.3 used to calculate both molecular and Knudsen diffusivity. Only molecular diffusivity was assumed to occur in the fluid zone (monolith channel).
5. Definition of the boundary conditions. The classification of the boundaries and the selected type of boundary are listed below:
 - Inlet: velocity inlet
 - Wall: wall with stationary velocity specification
 - Outlet: pressure outlet
 - Fluid zones: fluid, with porous zone selected for the solid body
 - Periodic boundary conditions mid-wall (zero mass or heat flux and zero pressure gradient) allowing the assumption that simulation of a single channel is representative of the whole monolith assembly.

6. Solver settings. Here the matrix solver and the solver settings for flow, species and energy are selected:

- PCG-PBiCG (Preconditioned (Bi-) Conjugate Gradient) was selected as matrix solver algorithm. This is an iterative method for solving large systems of linear equations; this is effective for systems of the form:

$$Ax = b$$

where x is the unknown vector, b is a known vector and A is a known, square, symmetric, positive-definite matrix [311].

- For the flow, species and energy iteration parameters are set in order to determine how the solution will be established. The two main iteration parameters that have to be set are the under-relaxation factor, which determines the solution adjustment after each iteration step, and the residual cut off value which determines when the iteration process can be terminated. The relaxation factor is the factor with which the iteration step change is multiplied before it is applied to the result for the next iteration step. In this study, this was set to 1 since a local time stepping approach was used; in this method the time step is manipulated for each individual cell in the mesh, making it as high as possible to enable the simulation to reach steady-state quickly [312]. The relaxation factor can also be larger than 1 (over-relaxed process) resulting in large step changes and faster convergence but it could lead to process divergence. On the contrary, when the relaxation step is less than 1 the process is called under-relaxed resulting in a slower iteration process but with a lower likelihood of process divergence. The residual value (difference between the current

and the former iteration value) determines when a solution is converged. Ideally, the residuals will go to zero as the process converges but in practice, with digital simulations, the residuals decay to a certain small value (round-off) and then stop changing; this decay may be up to six order of magnitude for single precision computations. When the set upper limit of the residual is reached, typically set at 10^{-4} , the process is considered to have reached its round-off value and the iteration process is stopped.

7. Initiation. The number of iterations and the number of processors to be used are selected and the simulation is then initiated.

Once the simulation has converged, the data are post-processed in Paraview. This software allows to display the data in different ways, for example, contour plots will give a plot in a defined collection of control volumes or plane showing the selected variable contour in the defined plane or volume. Numerical data can also be exported in different formats allowing the external manipulation of the data set.

6.3 CFD Model Validation

To validate the CFD model, methane oxidation conducted at different operative conditions (Section 5.6) was simulated. The system was considered to be at steady state and a laminar model was used to describe the flow field inside the monolith channel. The reaction was described by the kinetic equation and kinetic parameters estimated by Dr Sam Wilkinson and Johanna Espach [313]. The mass transport phenomena were described using Fick's law with the diffusivity in the monolith channel assumed to be molecular diffusivity and the one in the washcoat to be a mixture of molecular and Knudsen diffusivity; in the latter, the effective diffusivity was determined using the

Wakao-Smith correlation. The used boundary conditions were illustrated in Section 6.2 while the relaxation and the convergence criteria were set to 1 and 10^{-6} respectively. The first aspect that was investigated was the effect of mesh size on the simulation results in order to establish mesh independence. Figure 6. 1 summarises the steps followed to generate the mesh. The geometry of a single monolith's channel was reproduced using a CAD software (SolidWorks, Simulia Inc.) and the mesh was then generate using SnappyHex.

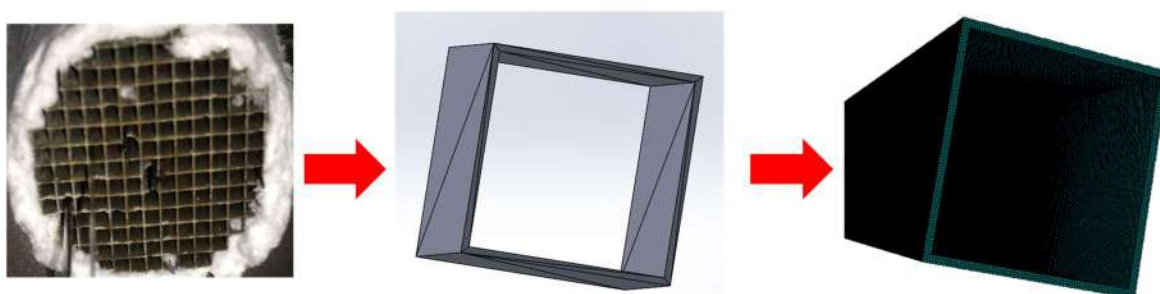


Figure 6. 1: Sequence followed to generate the mesh

Since the reactants have to diffuse and react through the washcoat thickness, it was important to investigate the effects of different cell numbers along the washcoat thickness; meshes with 1 (total cells number = 542136), 3 (total cells number = 2522876) and 6 cells (total cells number = 14881222) were made. Figure 6. 2 shows the CH_4 trend obtained when the different meshes were used to simulate the methane oxidation at 400 °C and in dry feed.

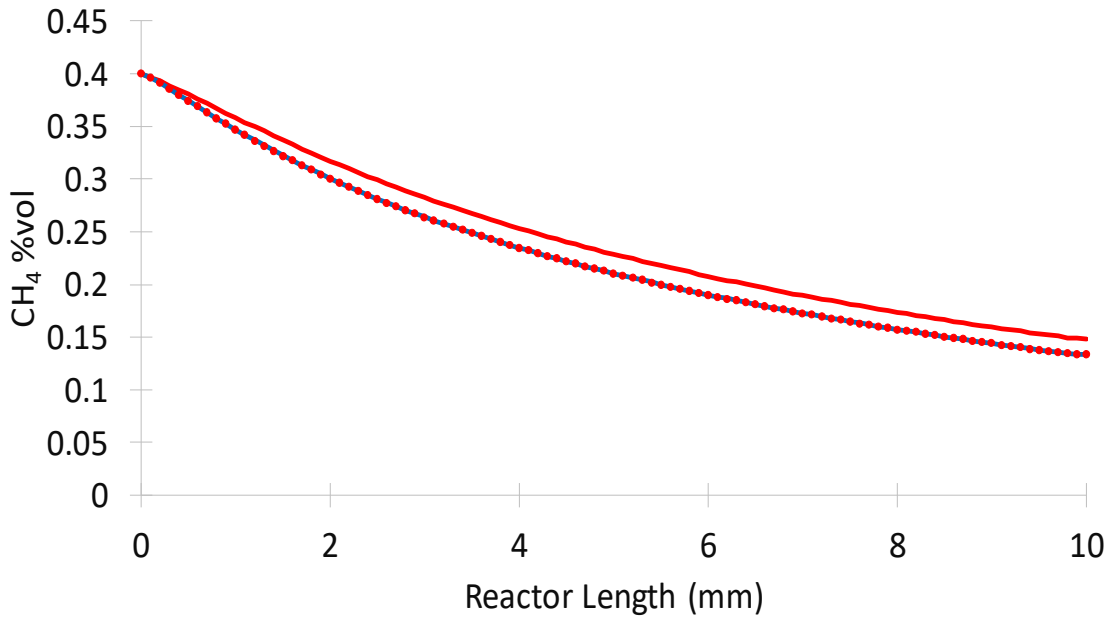


Figure 6. 2: CH_4 trend comparison when different mesh sizes were used to model CH_4 oxidation: (—) 1 Cell, (—) 2 Cells, (●) 6 Cells.

Figure 6. 2 shows that the CH_4 trend perfectly overlaps when 3 and 6 cells were present along the monolith thickness; this indicates that mesh independence was already reached when 3 cells were used. All further simulations were carried out using the 3 cells mesh.

At this point, methane oxidation, carried out at the different operative conditions reported in Section 5.6, was simulated; Figure 6. 3 shows the comparison among the methane concentration along the monolith channel for the different cases.

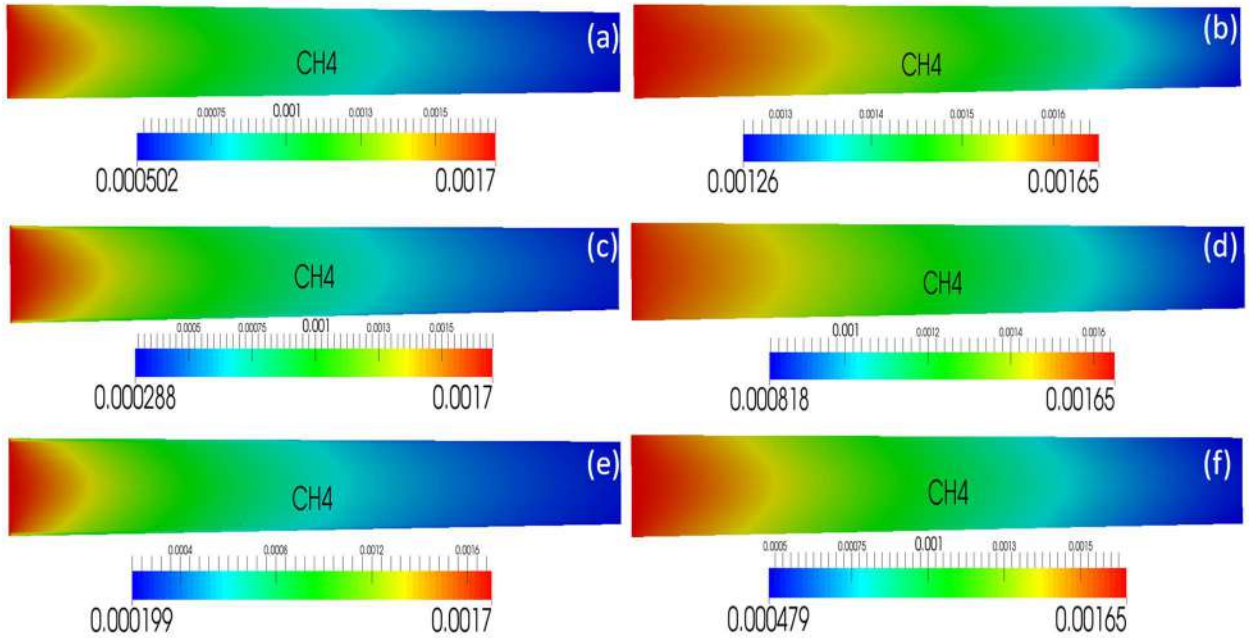


Figure 6. 3: CH_4 concentration profile along the monolith channel for CH_4 oxidation carried out at different operative conditions: (a) 400 °C and dry feed, (b) 400 °C and wet feed, (c) 425 °C and dry feed, (d) 425 °C and wet feed, (e) 450 °C and dry feed, (f) 450 °C and wet feed

In Figure 6. 3, the left side of the monolith channel represents the methane inlet, in addition, in all cases it can be noted the flow parabolic profile characteristic of a laminar flow. The figure also shows the water inhibition effect previously noted in Section 5.6, in the case of the wet feed, which results in a later CH_4 light-off in respect to the reaction conducted in dry feed. In addition, as it would be expected, methane combustion occurs earlier in the monolith channel as the reaction temperature is increased. The OpenFOAM simulation results were compared to those obtained experimentally and by 1D + 1D simulation; this is shown in Figure 6. 4.

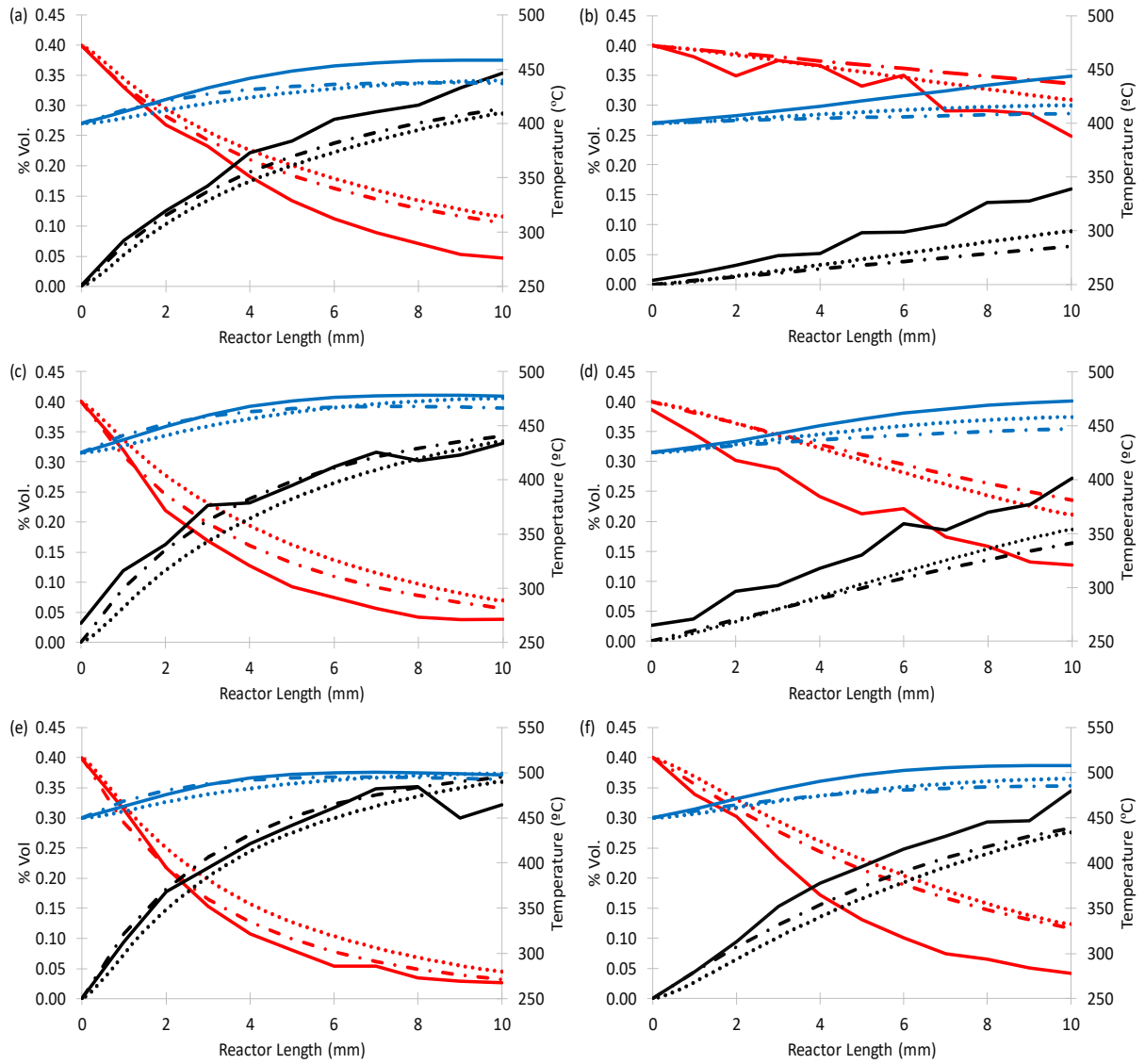


Figure 6. 4: Comparison among CH_4 concentration profile along the monolith channel for CH_4 oxidation carried out at different operative conditions: (a) 400 °C and dry feed, (b) 400 °C and wet feed, (c) 425 °C and dry feed, (d) 425 °C and wet feed, (e) 450 °C and dry feed, (f) 450 °C and wet feed. The different species are represented by: (—) CH_4 Exp., (---) CH_4 1D + 1D, (...) CH_4 OpenFOAM, (—) CO_2 Exp., (---) CO_2 1D + 1D, (...) CO_2 OpenFOAM, (—) Temp. Exp., (---) Temp. 1D + 1D, (...) Temp. OpenFOAM

From Figure 6. 4, it can be noted that the 1D + 1D and OpenFOAM simulations results, except for some discrepancies in the case of wet feed and low temperature, are essentially in agreement. OpenFOAM, in the case of dry feed, slightly under predicts CH_4 conversion in the central part of the reactor with the difference between the two approaches never greater than 10%. In the case of

wet feed, CFD gives a better prediction of the CH₄ trend with the difference between the CH₄ concentrations at the reactor exit determined by the 1D + 1D and CFD approaches as high as 20%. A similar difference between a 2D and a 3D approach was reported by *Canu and Vecchi*; the authors showed that the surface temperature in the 3D model is higher than in the case of the 2D model, with this difference more pronounced in the corners. This is due to a stagnation zone in the corners that reduces the heat transfer and increases the residence time resulting in higher conversion [302]. Although the observations of *Canu and Vecchi* potentially explain the differences observed for the wet feed, they do not rationalise the discrepancies observed for the dry feed. At this stage of the study, a simple comparison between the two modelling approaches was in scope and further investigations to explain the observed discrepancies are recommended. From Figure 6. 4 it can be noted that, also in the case of the CFD results, discrepancies between the model and the experimental results are observed in the case of wet feed. These, as explained in the previous chapter, are associated to the uncertainty in the estimated value of the enthalpy of adsorption of water.

6.4 Conclusions

In this chapter, the implemented simulation package OpenFOAM developed by Johnson Matthey in collaboration with Tridiagonal Solutions has been compared against the experimental results acquired at the SpaciMS by Ciaran Coney and the 1D + 1D simulation results presented in the previous chapter. The comparison showed that, although OpenFOAM and the 1D + 1D model results present some discrepancies (especially for the wet feed case), the predicted trends are comparable. The higher conversions predicted by the 3D model can be explained, as suggested by *Canu and Vecchi* by the formation of a stagnation zone in proximity of the channel corners that

result in higher temperatures and residence time hence in higher conversions. The slightly lower conversions predicted by the 3D model in the case of the dry feed cannot be explained by the previously presented reasoning. It is important to remark that, at this preliminary stage, a simple comparison of the two modelling approach was in scope and further studies are recommended to investigate the differences between the two approaches.

Chapter 7

Effects of Foam Structure on the CH₄ Oxidation Reaction: Experimental and Computational Determination of CH₄ Light-Off Curve

7.1 Introduction

In this chapter, catalyst supports having different porous structures were impregnated with Pd and tested in the methane oxidation reaction. The selected supports were an alumina foam having a total porosity of 95%, an alumina foam having a total porosity of 77%, alumina pellets having a density of 1.33 g cm⁻³ and alumina pellets made crushing the 77% foam and pelletising it; the density of the latter was 1.39 g cm⁻³. The impregnated supports were tested in a micro-reactor where the CH₄ light-off curve was determined. The light-off curve is the conversion-temperature plot of a catalytic reaction and it is commonly used in catalyst development; this set of data in addition, allows the determination of kinetic parameters such as the apparent reaction order and the activation energy [314]. These types of experiments are usually designed in order to avoid external and internal mass transport limitation so that intrinsic kinetic data can be obtained. In this study, pellets' sizes at which internal mass transport limitation was present were selected; this allowed to study the effects of the different porous structures on diffusion and consequently on the catalyst performances. The light-off curve was then computationally determined using a 1D + 1D model to simulate the packed bed reactor. Two different approaches were used to determine the effective diffusivity. The first used the *Wakao-Smith* correlation where the percentage of macro and mesopores was determined by mercury intrusion porosimetry with the mercury intrusion below 50 nm considered to be exclusively in mesopores and the intrusion above 50 nm to be exclusively in macropores. The second method used a pore resolved approach [315] where the effective

diffusivity was computationally determined upon input of the percentage of mesopores, the percentage of macropores and their size distribution. One of the aims of this study is also to explore the advantages and limitations of these two different approaches. The reader is firstly introduced to the reactor model used to simulate the light-off curve, then a more detailed description of the pore resolved model is given, finally the experimental and computational determination of the light-off curve is described.

7.2 Packed Bed Reactor Model

Similarly to what discussed in Section 5.5, when studying a packed bed reactor, the mass and the energy balances have to be carried out on both the porous pellet and the fluid regions of the system. In this section the reader is introduced to the equations used in modelling the reactor performance. The determination of the light-off curve is a transient process, in fact, the temperature of the reactor is typically ramped at $15\text{ }^{\circ}\text{C min}^{-1}$. The experiment is designed in a way that pseudo-steady state conditions are reached during each temperature ramp; viz. that transient thermal and surface effects are not significant. For this reason, the system was described using a series of steady state models at different reaction temperatures; the sequential steady state approach to modelling dynamic systems. It is important to remark that in a steady state system the time derivative terms of the balances are equal to zero. Figure 7. 1 shows a schematic of the packed bed reactor; the figure also shows the spatial boundaries for the pellet.

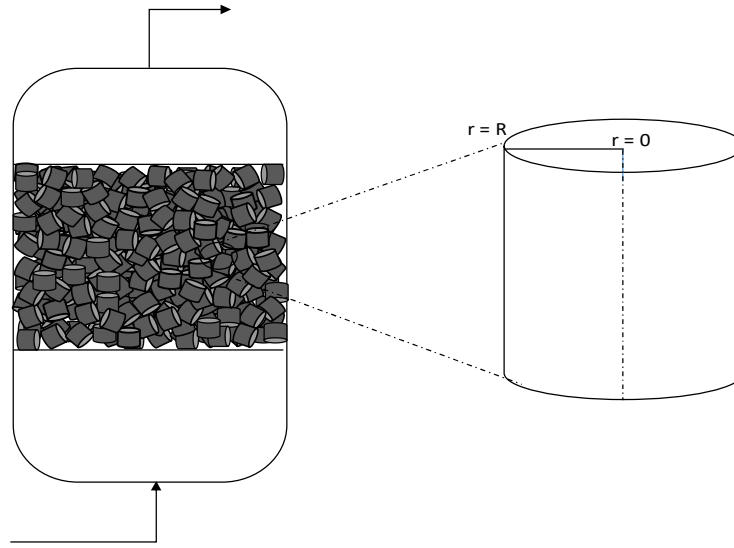


Figure 7. 1: Schematic of a packed bed reactor with detailed representation of the pellet boundaries

The mass and energy balances for the catalysts pellets are represented by (7.1) and (7.2) respectively [316].

$$\frac{\partial c_i}{\partial t} = D_{eff} \frac{\partial^2 c_i}{\partial x^2} + n_i r_j \quad (7.1)$$

$$\rho_s C_{p,s} \frac{\partial T}{\partial t} = k_{eff} \frac{\partial^2 T}{\partial x^2} - \sum_j r_j (-\Delta H_{r,j}) \quad (7.2)$$

where n_i is the stoichiometric coefficient for the species i , r_j is the reaction rate, k_{eff} is the effective thermal conductivity of the pellet, h is the thermal convection coefficient, S is the reactor surface area to volume ratio, T_s is the temperature of the solid pellet, T_g is the temperature of the gas phase and $\Delta H_{r,j}$ is the enthalpy of reaction. Considering the boundary condition $r = 0$ the mass and energy balances are represented by:

$$\frac{\partial c_i}{\partial x} = 0 \quad (7.3)$$

$$\frac{\partial T}{\partial x} = 0 \quad (7.4)$$

while at $r = R$ the balances are described by:

$$\frac{\partial C_i}{\partial t} = D_{ef} \frac{\partial C_i}{\partial x} + k_{s,i}(C_{i,b} - C_{i,s}) \quad (7.5)$$

$$\frac{\partial T}{\partial t} = k_{eff} \frac{\partial T}{\partial x} + h(T_s - T_g) \quad (7.6)$$

where k_s is the film mass transfer coefficient. The mass and energy balances at the reactor scale were determined along the reactor axial direction and are represented by (7.7) and (7.8) respectively.

$$u_z \frac{\partial C_i}{\partial z} = a_v k_{s,i}(C_{i,b} - C_{i,s}) \quad (7.7)$$

$$\rho_g C_{p,g} u_z \frac{\partial T_g}{\partial z} = hS(T_s - T_g) \quad (7.8)$$

where u_z is the gas superficial velocity, a_v is the pellet specific area defined as $a_v = 6(1 - \varepsilon)/d_p$ where ε is the bed porosity and d_p is the pellet diameter. The bed porosity was determined using the correlation proposed by *Dixon* [317]; this correlation, reported below, is valid when the ratio between the reactor diameter d_r and the particles diameter d_p is bigger than 2:

$$\varepsilon = 0.4 + 0.05 \left(\frac{d_r}{d_p} \right)^{-1} + 0.412 \left(\frac{d_r}{d_p} \right)^{-2} \quad (7.9)$$

The film mass transfer coefficient was determined using the correlation proposed by *McCune and Wilhelm* [318] where the mass j-factor is related to the Re number of the system. The j-factor is expressed as $j_m = \frac{Sh}{Re Sc^{1/3}}$ where Sh is the Sherwood number $\left(Sh = \frac{k_s d_p}{D_{AB}} \right)$, Re is the Reynolds number expressed as $Re = \frac{G d_p}{\mu}$ where G is the mass superficial velocity and Sc is the Schmidt number $\left(Sc = \frac{\mu}{\rho D_{AB}} \right)$; the *McCune and Wilhelm* correlation is reported below:

$$j_m = 1.625Re^{-0.507} \quad (7.10)$$

In a similar way, the film heat transfer coefficient h was determined using the *Pfeffer* [319] correlation:

$$j_h = 1.26 \left\{ \frac{1}{Re} \sqrt{\frac{1-(1-\varepsilon)^{5/3}}{2-3\gamma+3\gamma^5-2\gamma^6}} \right\}^{2/3} \quad (7.11)$$

where j_h is the heat j-factor expressed as $j_h = \frac{Nu}{RePr^{1/3}}$ where Nu is the Nusselt number $\left(Nu = \frac{hd}{k_{eff}}\right)$ and Pr is the Prandtl number $\left(Pr = \frac{\mu C_p}{k_{eff}}\right)$; the Re number is expressed, as previously said, in terms of mass superficial velocity while γ is given by $\gamma = (1 - \varepsilon)^{1/3}$.

7.3 Computational determination of D_{eff} coefficient in porous solids: Pore Resolved Method

The computational method used in this work was developed at the Institute of Chemistry and Technology (ICT) in Prague and it uses a spatially resolved approach to model diffusion in porous solids. *Kočí et al.* used this method to carry out multi-scale modelling of CO oxidation in porous Pt/ γ -Al₂O₃ catalyst. In particular, the authors used the pore resolved method to generate, at the nano level, a spatial 3D model of a single meso-porous γ -Al₂O₃ particle and to deposit individual Pt crystallites on the particle; at the micro level, the authors used the pore resolved method to generate a 3D spatial model of porous catalytic washcoat. The authors also compared the multi-scale results with those obtained by standard models showing good agreement [315]. Similarly, *Novák et al.*, used the pore resolved method in a multi-scale modelling study of CO oxidation over a Pt/ γ -Al₂O₃ catalyst. The authors compared the light-off curve obtained experimentally with the one obtained by modelling showing good agreement [320].

This method uses an *in silico* generated pore structure which acts as a statistically representative sample of the real experimental sample. The first step of this method is the characterization of the porous structure of the sample (e.g. pore size distribution and porosity) by different analytical techniques such as SEM, XRT, TEM and MIP to name a few. The experimentally determined particle size distribution is generated *in silico* and shrunk down to the experimentally determined porosity using the Discrete Element Model code developed by ICT Prague. This leads to a statistically representative structure of the original sample; an example of this procedure is shown in Figure 7. 2.

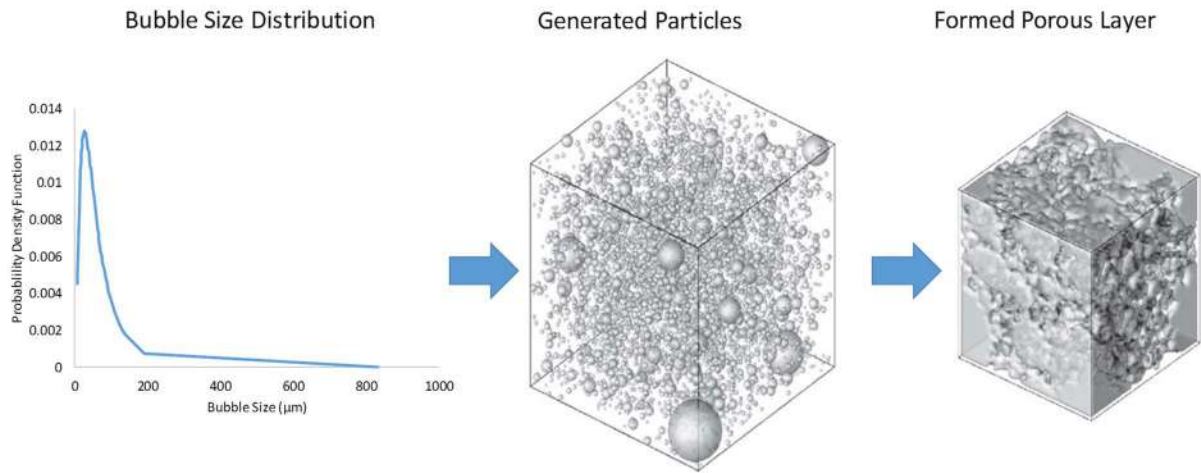


Figure 7. 2: Example of the method used for the generation of the porous structure using the ICT Prague DEM code [321]

The reconstructed porous structure is then used to carry out diffusion simulations. In this method, the desired effective diffusivity through the reconstructed porous medium is calculated from the mass fluxes obtained by the simulation of the system with an imposed concentration gradient and no reactions. Two different boundary concentrations of the diffusing component i are set at z_0 and z_l :

$$Y_i|_{z=z_0} = Y_i^{bnd,z_0} \quad (7.12)$$

$$Y_i|_{z=z_1} = Y_i^{bnd,z_1} \quad (7.13)$$

The difference between Y_i^{bnd,z_1} and Y_i^{bnd,z_0} acts as a driving force for diffusion in the z -direction; the effective diffusivity of gas component i is then calculated:

$$D_{eff,i} = -\frac{J_i}{A_z} \frac{L_z}{c(Y_i^{bnd,z_1} - Y_i^{bnd,z_0})} \quad (7.14)$$

where $L_z = (z_1 - z_0)$ is the thickness of the reconstructed medium in the direction z and J_i is the overall molar flux through the medium; this is obtained by integrating the fluxes across the cross-section area A_z perpendicular to the z -direction [321]:

$$J_i = \int_A -D_i \frac{\partial c_i}{\partial z} dx dy \quad (7.15)$$

To solve the large systems of linear equations, the Aggregation based Multigrid Method (AGMG) solver, developed at Université Libre de Bruxelles by Prof. Yvan Notay was used [322]. The coarsening is obtained by aggregation of the unknowns. The aggregation scheme uses two passes of a pairwise matching algorithm applied to the matrix graph, resulting in most cases in a decrease of the number of variables by a factor slightly less than four. The matching algorithm favours the strongest negative coupling, inducing a problem dependent coarsening. This aggregation is combined with piecewise constant prolongation, ensuring low setup cost and memory requirements [323]. Figure 7. 3 shows an example of the simulation output.

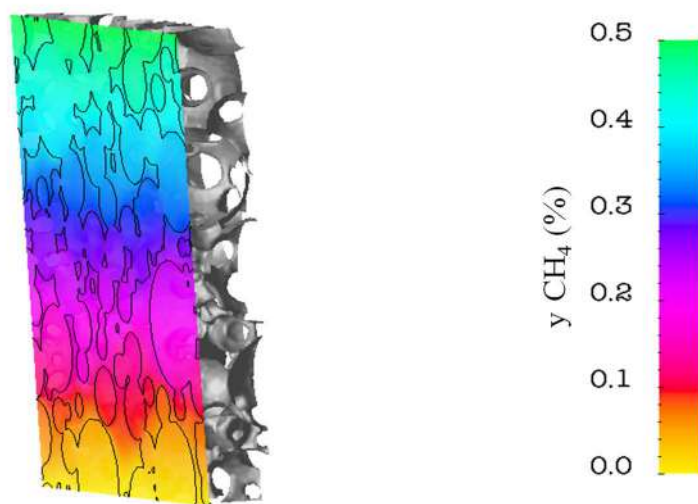


Figure 7. 3: Example of diffusion simulation output

From Figure 7. 3, it can be noted a portion of the 3D reconstructed structure of the foam sample; the simulation also provides a concentration map of the diffusing species along the axial direction of the sample and the value of the effective diffusivity in the solid sample.

7.4 Materials and Method

7.4.1 Materials

The fumed Al_2O_3 particles (AEROXIDE AluC) used in this study were obtained from Evonik Industries (Essen, Germany). The alumina is crystalline with a γ/δ - structure. Density and surface area are 50 g L^{-1} and $85\text{-}115 \text{ m}^2 \text{ g}^{-1}$ respectively.

Butyric acid was obtained from Alfa Aesar (Heysham, United Kingdom) and it was used to modify the particles' surface properties. 40%_{v/v} KOH solution, prepared dissolving KOH pellets (Alfa Aesar, Heysham, United Kingdom) in demineralized water, and 70%_{v/v} HNO_3 (Alfa Aesar, Heysham, United Kingdom), were used to adjust the suspension's pH. A 15.18% $\text{Pd}(\text{NO}_3)_2$ metal solution (Johnson Matthey, Batch No. DA0325) was used to prepare the dilute Pd solution

employed for the impregnation of the catalyst support. Graphite fine powder 99% (Alfa Aesar, Heysham, United Kingdom) was used as lubricant during pelleting.

7.4.2 Foam and Alumina Pelletting

Foam samples characterized by a porosity (determined by water pick-up) of 95% and 77%, prepared using the methods described in Section 3.5.3, were ground to a size range 250-750 μm . To obtain the foam derived pellets, the 77% foam granules were densified by compaction in an Enerpac press; an 8 cm die was used and the powder was compressed up to $1.4 \cdot 10^7$ Pa (2000 psi). The compacted disk was then grounded to 250-750 μm . 10 %_{w/w} graphite was added to the granules and a single pin pellets machine (Model: CPR6, Serial Number: 73), equipped with a 3.3 mm die, was used to pelletize the powder. The same procedure, for the exception of the initial grounding, was repeated for the pelleting of the as received alumina powder.

7.4.3 Catalyst Support Impregnation and Characterization

The four catalyst supports (e.g. foam 95%, foam 77%, foam pellet and alumina pellet) were grounded between 710 μm and 1000 μm . The supports' pore volumes were determined by water pick-up. 2 g of exactly weighed support were put in a glass vial, water was then added drop-wise. After each addition the vial was tumbled to homogeneously distribute the water among the support particles. Water addition was stopped when support granules started to adhere to each other; the support pore volume was obtained by dividing the volume of added water by the dry weight of the catalyst support. The volume of diluted Pd solution to be used for the support impregnation was obtained by multiplying the weight of the support by the previously determined pore volume. The mass of 15.18% $\text{Pd}(\text{NO}_3)_2$ solution that has to be present in the impregnation solution, in order to obtain a 3% $\text{Pd}/\text{Al}_2\text{O}_3$ catalyst, was determined using the following formula:

$$\text{mass of 15.18\% Pd sol.} = \frac{\text{Desired \% of Pd on catalyst} * \text{weigh of the support} * 100}{(100 - \text{desired \% of Pd on catalyst}) * 15.18} \quad (7.16)$$

4 g of support were then put in a glass vial and the diluted solution was added drop wise. The vial was hand-rolled to facilitate the impregnation. At the end, some additional demineralised water was added to capture the final residue of the Pd(NO₃)₂ solution. The sample was then placed in a dish and left in a drying oven at 110 °C for two hours. Periodically during this time, the sample was removed from the oven and the powder turned, so that the drying was relatively even throughout the sample. The catalyst precursor formation was calcined in an oven at 800 °C for 5 h in an inert atmosphere; this procedure was repeated for all the samples.

X-Ray Diffraction, N₂-Physisorption, Chemisorption and Mercury Intrusion Porosimetry were run on the samples as described in Section 4.6.5. In addition, X-Ray Tomography was carried out on the samples using a Bruker Skyscan 1172 instrument; the source voltage was set at 54 kV and the object to source distance was 71.74 mm giving an image pixel size of 2.98 µm. The rotation step was equal to 0.2° and no filters were used during the image acquisition.

7.4.4 Catalyst Testing: CH₄ Light-Off curve

The use of micro-reactors for catalyst testing is a standard test methodology in Johnson Matthey [324]. The catalyst sample (0.2 g and 0.4 g for the foam and pellet sample respectively) was placed in a stainless steel reactor (diameter 8 mm). The flows of reactant gases and diluent (N₂) were controlled by mass flow controllers; the total gas flow was 2 L min⁻¹. The flow of liquid H₂O into the reactor was controlled by a peristaltic pump. The reactor was heated in an oven and the experiments were run with a temperature ramp of 5 °C min⁻¹. The catalyst gas inlet temperature was measured by a thermocouple placed approximately 15 mm in front of the catalyst bed. Gas

from the reactor outlet was led to analysers by heated lines; separate analyser units were used to measure the concentration of CO (infra-red), CO₂ (infra-red) and O₂ (electrochemical cell). A schematic of the test rig used for the determination of the CH₄ light-off is given in Figure 7. 4.

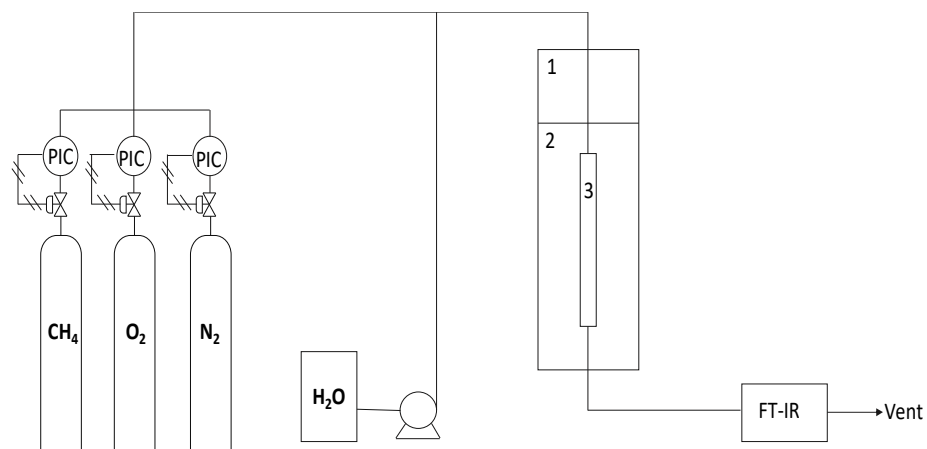


Figure 7. 4: Schematic of the test rig used for the determination of the CH₄ light-off curve

The gases, at the desired concentration, and water (if required in the experiment) are fed into the packed bed reactor (3). The reactor inlet is enclosed in an oven (1) at a temperature of 150 °C in order to evaporate the water before it enters the reactor. The actual reactor is enclosed in an oven whose temperature is ramped at 5 °C min⁻¹ from 150 °C to 530 °C. The products are then analysed via FT-IR. A typical testing protocol for the catalyst is summarised in Table 7. 1.

Table 7. 1: Example test protocol used for testing 3% Pd/Al₂O₃ catalysts

Step No	Gas	Start temp (°C)	Ramp rate (°C min ⁻¹)	Set Point (°C)	Hold Time (min)
1	500 ppm CH ₄ /10% O ₂ / bal. N ₂	150	5	530	15
2	10% O ₂ / bal. N ₂	530	15	150	15
3	500 ppm CH ₄ /10% O ₂ / bal. N ₂	150	5	530	15
4	10% O ₂ / bal. N ₂	530	15	150	15
5	500 ppm CH ₄ /10% O ₂ / 12% H ₂ O / bal. N ₂	150	5	530	15
6	10% O ₂ / bal. N ₂	530	15	150	15
7	500 ppm CH ₄ /10% O ₂ / 12% H ₂ O / bal. N ₂	150	5	530	15
8	10% O ₂ / bal. N ₂	530	15	150	then end

7.5 Catalysts characterization results

Different analytical techniques were carried out on the four supports (e.g. XRT, N₂-Physisorption, Mercury Intrusion Porosimetry, CO chemisorption); Figure 7. 5 shows the four supports before size reduction.

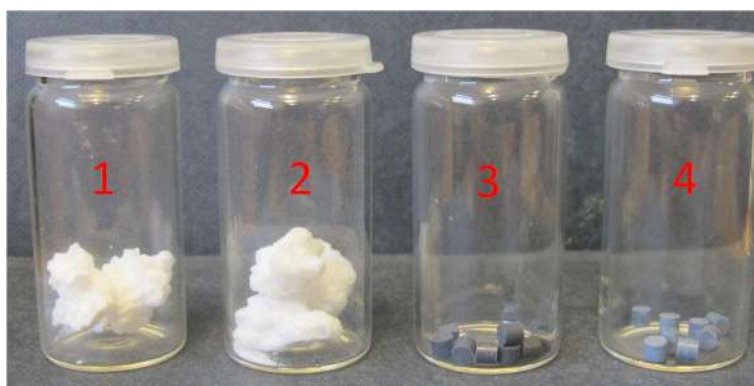


Figure 7. 5: Catalyst supports before grinding: 1-77% Al₂O₃ foam, 2-95% Al₂O₃ foam, 3-Al₂O₃ pellet, 4-Al₂O₃ foam pellet

N₂-physorption and Mercury Porosimetry were carried out to investigate the pore structure of the samples. Figure 7. 6 shows the isotherm of adsorption and the pore size distribution obtained by

physisorption while Figure 7. 7 shows the intrusion/extrusion curves and the pore size distributions obtained by mercury porosimetry.

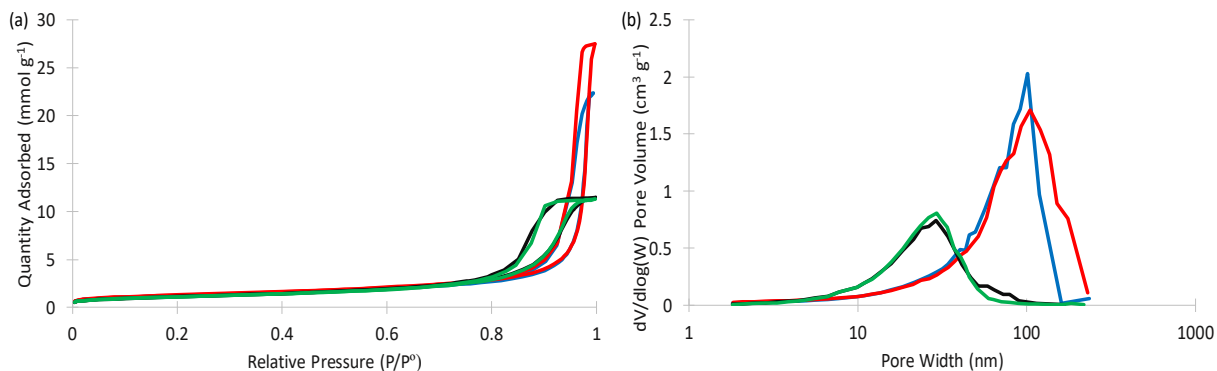


Figure 7. 6: (a) N_2 -Isotherm of adsorption, (b) pore size distribution for the different samples: (—) Foam 77%, (—) Foam 95%, (—) Foam Pellet, (—) Alumina Pellet.

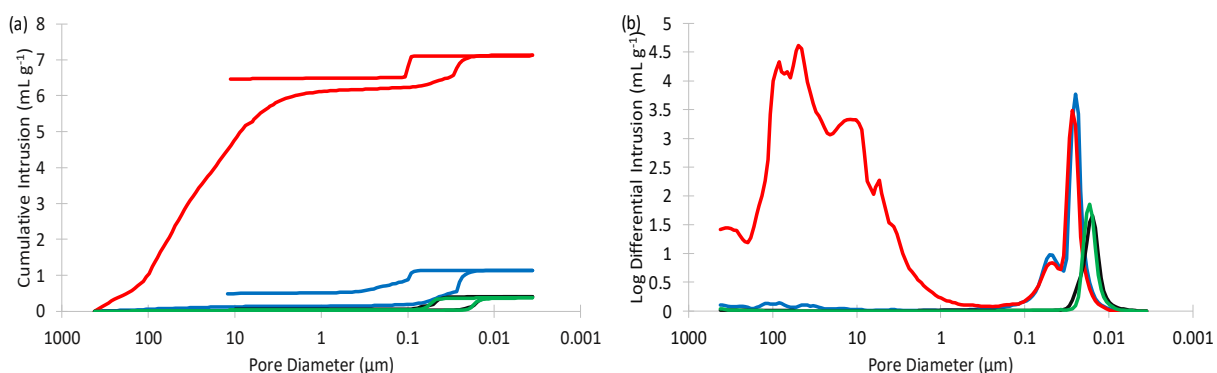


Figure 7. 7: (a) Mercury intrusion/extrusion curve, (b) Pore size distribution for the different samples: (—) Foam 77%, (—) Foam 95%, (—) Foam Pellet, (—) Alumina Pellet

From the N_2 -isotherm of adsorption it can be noted that all samples present a type IV isotherm with the hysteresis loop indicating capillary condensation in narrow pores. The fact that in the two foam samples the plateau of the isotherm is not present, indicates that the porosity of the samples extends beyond the upper limit of the technique and, consequently, the pore size distribution (PSD) will be incomplete with an underestimation of both the pore volume and the average pore diameter. This observation is confirmed by the analysis of the pore size distribution obtained by mercury intrusion

porosimetry; it can be observed, in fact, that the PSD obtained by physisorption and mercury intrusion agree in the case of the pellet samples while additional pores are observable in the foam samples when considering the PSD obtained by MIP. The difference in PSD between the two techniques is also evident when comparing the estimated mean pore diameter. In particular, the mean pore diameter of the 95% porosity foam is significantly higher when determined by MIP. Table 7. 2 summarises the BET surface area, the pore volume and average pore diameter, obtained by N₂-physisorption and compare them with intrusion volume, % of entrapment and mean pore diameter obtained by MIP.

Table 7. 2: Summary of the N₂-physisorption and Mercury Intrusion Porosimetry results

N₂-Physisorption			
Sample	BET Area (m ² g ⁻¹)	Pore Volume (cm ³ g ⁻¹)	Mean Pore Diameter (nm)
Foam 77%	99.0	0.775	31.3
Foam 95%	103.4	0.952	36.8
Foam Pellet	92.2	0.397	17.2
Alumina Pellet	89.6	0.392	17.5
Mercury Intrusion Porosimetry			
Sample	Intrus. Volume (cm ³ g ⁻¹)	% Entrapment	Mean Pore Diameter (nm)
Foam 77%	1.145	43	27
Foam 95%	7.125	91	23790
Foam Pellet	0.398	11	16
Alumina Pellet	0.363	8	17

From the mercury porosimetry data, it can also be noted that, contrary to expectation, a significant difference in porosity between the foam pellet and the alumina pellet was not present. This is almost certainly due to the destruction of the microporous foam structure during the pelleting process. This was confirmed by SEM where, although the foam pellet sample appears to have a slightly higher porosity in respect to the conventional pellet, a significant difference between the two samples is not notable. Figure 7. 8 shows the SEM images for the four supports.

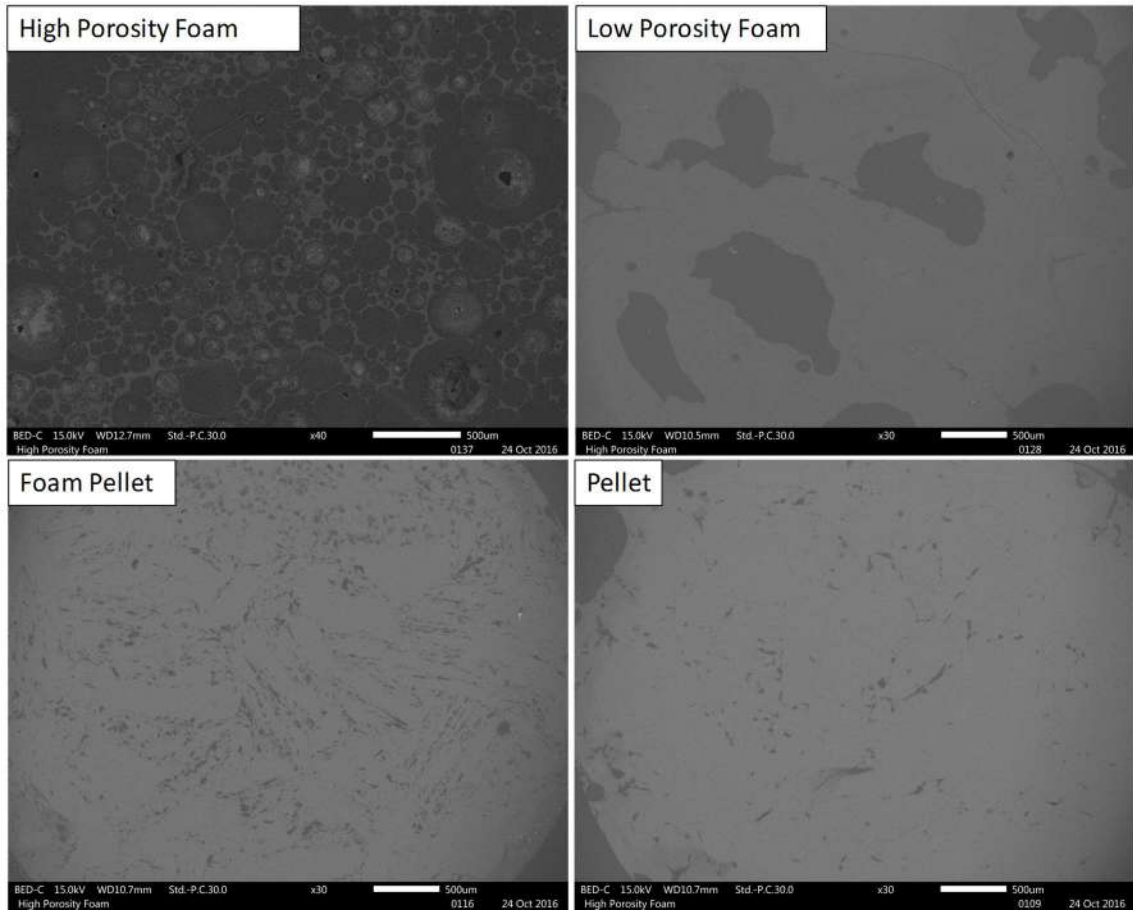


Figure 7. 8: SEM images of the cross section of the four samples

From the SEM images, it can also be observed that the low porosity foam is characterized by big macropores. This is in contrast to the observations from the mercury porosimetry analysis. A possible explanation is the shielding effects in MIP. This phenomenon is due to the fact that mercury porosimetry does not measure the actual internal pore size but it determines the largest connection from the sample surface towards that pore. This results in the underestimation of the pore size when big pores are connected to smaller pores.

The sample pore structure was also investigated by X-Ray tomography; in particular, the reconstruction of the samples 3D structure could be employed in running Computational Fluid

Dynamic simulations. The analysis of the pellet samples by XRT was particularly challenging so only the 2D and 3D reconstructed images of the foam samples are presented in Figure 7. 9.

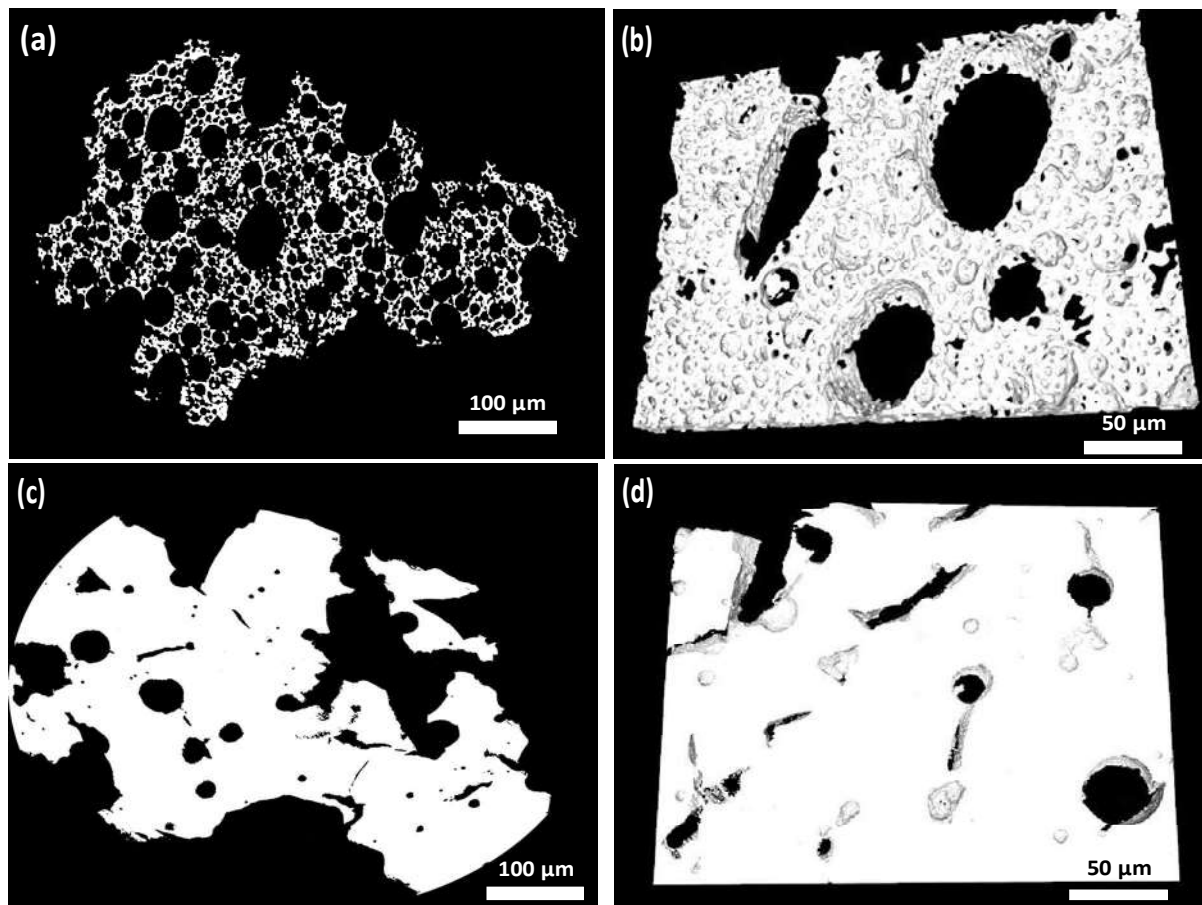


Figure 7. 9: CD-XRD images of the foam samples: (a) 2D image of the 95% foam, (b) 3D reconstructed image of a 95% foam Region of Interest (ROI), (c) 2D image of the 77% foam, (d) 3D reconstructed image of a 77% foam ROI

To characterise the impregnated supports, CO-chemisorption was carried out in order to determine the metal area and the metal dispersion while XRD was used to measure the catalyst crystal size; the determination of the percentage of Pd by XRD was prevented by the transitional nature of the alumina support. Table 7. 3 summarises the results obtained using the mentioned analytical techniques.

Table 7. 3: Summary of the CO-Chemisorption and XRD analysis for the four samples

CO-Chemisorption		
Sample	Metal Area ($\text{m}^2 \text{g}^{-1}$)	Dispersion %
Foam 77%	1.24	3.7
Foam 95%	1.35	11.9
Foam Pellet	1.03	3.1
Alumina Pellet	0.95	4.6
XRD		
Sample	PdO Crystal Size (nm)	
Foam 77%	5.4	
Foam 95%	5.4	
Foam Pellet	6.9	
Alumina Pellet	7.4	

With the exception of the metal dispersion, which is slightly higher in the 95% foam, the samples present similar properties in terms of metal area and crystal size.

7.6 Catalytic test of Pd/Al₂O₃ catalysts for CH₄ oxidation

The granules of the four samples were tested at the micro-reactor rig using the protocol reported in Section 7.4.4. As discussed in the experimental methodologies section, the light-off experiment provides performance data over the 150-530 °C temperature range; each light-off test result was produced twice to show repeatability and stability of the testing data. In all the experiments, inlet CH₄ and O₂ compositions were fixed at 500 ppm and 12% respectively. Figure 7. 10 shows the light-off curve for the foam and pellet supported samples respectively for both dry and wet feed.

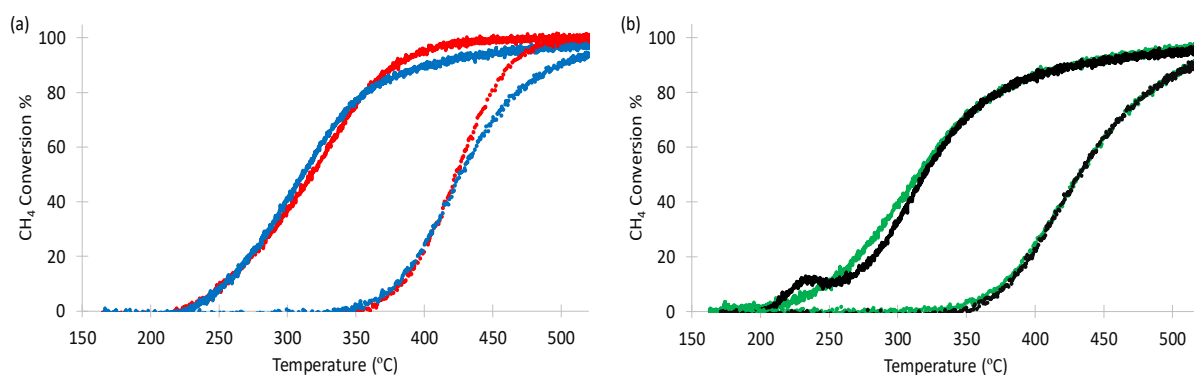


Figure 7. 10: Light-off curve for (a) foam supported and (b) pellet supported catalyst for both dry and wet feed: (—) 95% Foam-Dry, (—) 77% Foam-Dry, (•) 95% Foam-Wet, (•) 77% Foam-Wet, (—) 77% Al_2O_3 pellet-Dry, (—) Foam pellet-Dry, (•) 77% Al_2O_3 pellet-Wet, (•) Foam pellet-Wet

The light-off curve of the foam supported catalysts confirms, in both cases (e.g. dry and wet feed), that the porous structure of the supports impacts the catalyst performances. The curves for the 95% foam and 77% foam are superimposed for the temperature region in which the system is expected to be kinetically limited while they start to diverge above temperatures at which the system becomes diffusion limited (e.g. $T > 300^\circ\text{C}$ for the dry feed and $T > 400^\circ\text{C}$ for the wet feed). The light-off curves for both the foam supported and pellet supported samples also confirm the inhibition effects of H_2O with the 0% H_2O data showing CH_4 conversion at least 100°C earlier than that of 12% H_2O data. The beneficial effect of the original support structure are not observed in the pellet supported samples where the Al_2O_3 pellets sample and the foam pellet sample present similar trends of the light-off curves. This can be attributed to the similar porosity presented by the two sample that, as presented in in the characterization results section, it is due to the destruction of part of the foam structure during pelleting. Figure 7. 11 shows the comparison of the light-off curves for both the foam supported and pellet supported samples.

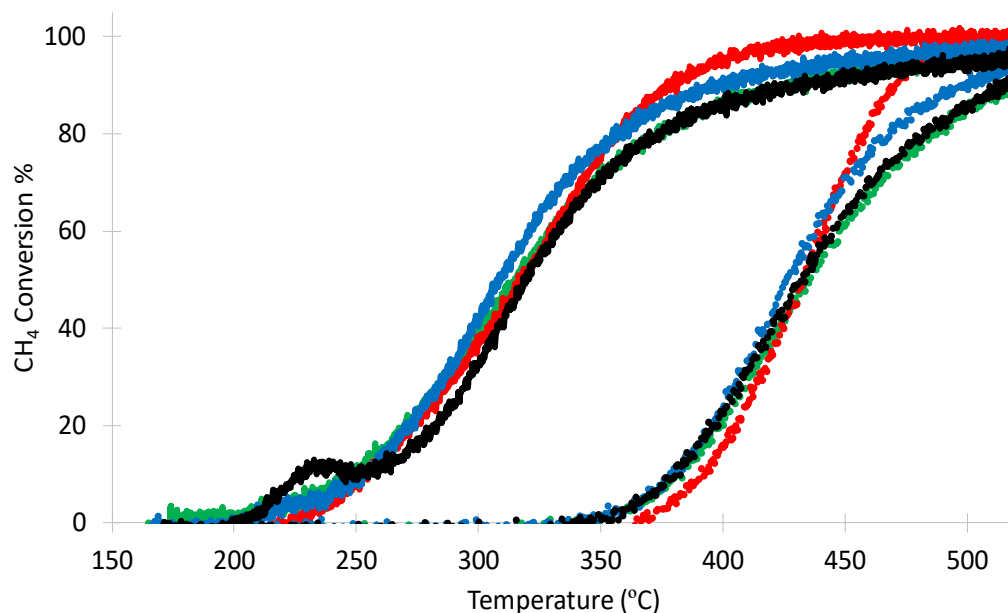


Figure 7. 11: Foam supported and pelleted supported samples, light off curves comparison: (—) 95% Foam-Dry, (—) 77% Foam-Dry, (●) 95% Foam-Wet, (●) 77% Foam-Wet, (—) 77% Al_2O_3 pellet-Dry, (—) Foam pellet-Dry, (●) 77% Al_2O_3 pellet-Wet, (●) Foam pellet-Wet

From the light-off curves comparison, it can be observed that the foam supported catalysts, in both dry and wet feed, perform better than the pellet supported ones. In addition, it is important to point out that the foam supported samples had half the weight of catalyst in respect to the pellet supported catalysts making the difference in performances even more outstanding.

7.7 Light-Off Curve Modelling

The light-off curves for the high and low porosity foams were modelled using the 1D + 1D code described in Section 7.2. The two different approaches used for the determination of the effective diffusivity coefficient D_{eff} were compared. In one case this was calculated using the *Wakao-Smith* correlation and in the other the value obtained in the PMS simulation was directly inputted into the code. In both cases, it was necessary to know the percentage of macro and meso pores in the samples, the corresponding reactor density (which accounts for both the catalyst density and the bed voidage), and the catalyst bed length. Table 7. 4 summarises the total mercury intrusion, the

intrusion above and below 50 nm, the percentage of macro and meso pores, the reactor density and the bed length for the two samples.

Table 7. 4: Foam samples characteristics

Sample	Tot Intr. (mL g ⁻¹)	Intr. above 50 nm (mL g ⁻¹)	Intr. below 50 nm (mL g ⁻¹)	Tot Porosity %	Macro-porosity %	Meso-porosity %	React. Dens. (Kg m ⁻³)	Cat. Weight (g)	Bed Length (mm)
77% Foam	1.1452	0.8224	0.3228	0.7741	0.5559	0.2182	405.6	0.2	9.8
95% Foam	7.1249	6.3685	0.7564	0.9556	0.8541	0.1015	80.5	0.2	49.4

Figure 7. 12 shows the comparison among the experimental light-off curve and the model light-off curve, obtained using the two different approaches, for the high and low porosity foam supported catalysts.

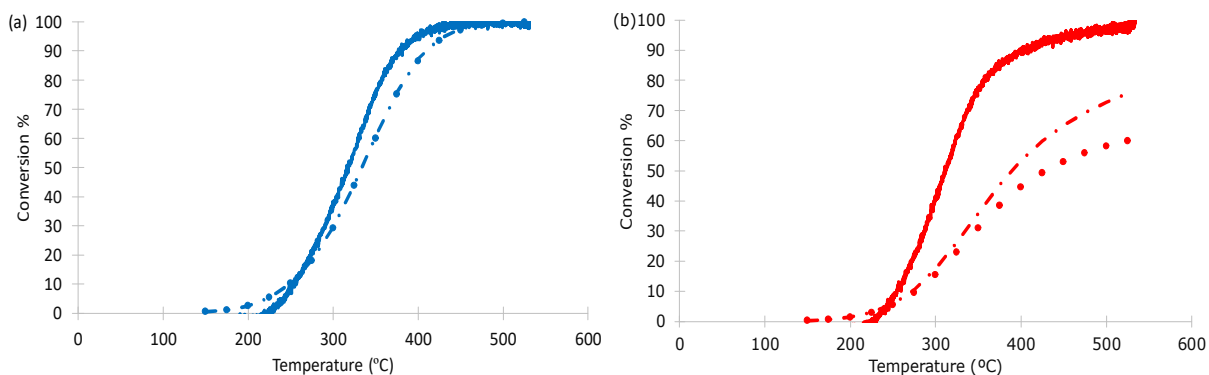


Figure 7. 12: Comparison among experimental and model results. (a) 95% foam: (—) Exp., (—●) Mod. Wakao-Smith, (●) Mod. PMS. (b) 77% foam: (—) Exp., (—●) Mod. Wakao-Smith, (●) Mod. PMS.

From Figure 7. 12 it can be noted that, in the case of the 95% foam, the model results satisfactorily describe the experimental light-off curves. In addition, it is notable that the model results obtained using the *Wakao-Smith* correlation and the PMS method are in agreement. The observed differences are due, first of all, to the uncertainty introduced by the fact that a series of steady state simulations were used to model a transient system.

The other source of error is due to the location of the thermocouple in the experimental set-up. Figure 7. 13 shows the position of the thermocouple which was located at the inlet of the reactor and not inside the catalyst bed. Although the reactor was considered to be isothermal, differences between the temperature of the thermocouple and the actual temperature of the catalyst bed were expected.

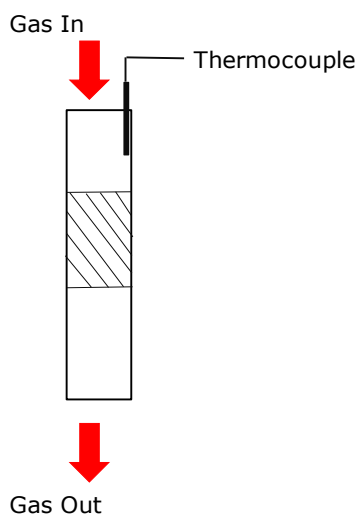


Figure 7. 13: Thermocouple position inside the micro-reactor

The position of the thermocouple can, in part, explain the differences observed between the experimental and the model light-off curve. At the beginning of the experiment, the catalyst bed will be at a lower temperature in respect to that measured by the thermocouple due to the thermal lag required to heat the catalyst pellets up. As the reaction kicks-in the heat of reaction will heat up the catalyst bed and its temperature will be higher than that measured by the thermocouple. Although the temperature of the bed before the reaction starts is difficult to estimate, its temperature during the reaction was estimated by adding to the temperature measured by the thermocouple the adiabatic temperature rise due to the reaction; the latter was calculated using the following equation [325]:

$$\Delta T = \frac{\Delta H_{\text{reaz}} [CH_4]_{\text{react}} V_{\text{bed}}}{\sum_i (C_{p,i} [C_i]_{\text{out}} V_{\text{bed}})} \quad (7.17)$$

where ΔH_{reaz} , is the heat of reaction, $[CH_4]_{\text{react}}$ is the concentration of reacted methane, V_{bed} is the volume of the bed, $C_{p,i}$ is the heat capacity of the different species and $[C_i]_{\text{out}}$ is the concentration of the different species exiting the reactor. Figure 7. 14 shows the comparison between the model light-off curve and both the experimental curves with the uncorrected and corrected bed temperature.

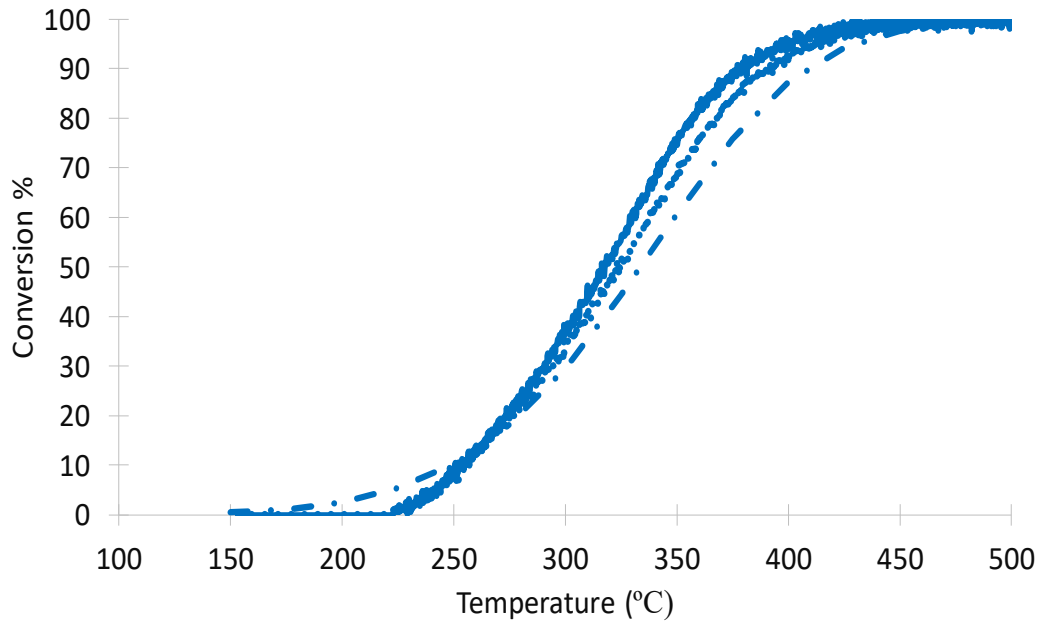


Figure 7. 14: Comparison among model light-off curve and both experimental curves with corrected and uncorrected bed temperature: (—) Exp., (—●) Mod., (●) Exp.-Corrected temperature.

It can be noted from Figure 7. 14 that, after temperature correction, the experimental curve get closer to the model one. In addition, it is important to remark that, as shown in Section 5.6, the used kinetic model presents a significant error on the value of the estimated enthalpy of water adsorption. This has a significant impact on the reaction rate, and consequently on conversion, as the reaction progresses (higher temperatures in the light-off curve) leading to a probable under

estimation of methane conversion. Despite the described differences, the model satisfactorily predicts the light-off curve trend; the same is not true when comparing the experiment and model results for the 77% porosity foam (Figure 7. 12). Furthermore, in the case of the low porosity foam, the model light-off curves obtained using the *Wakao-Smith* and the PMS methods are not in agreement. This is due to a limitation of the PMS method that is not capable of generating a representative reconstruction of the low porosity sample. In fact, the presence of few pores and their wide size distribution prevents the construction of a representative sample. This underlines a limitation of the pore resolved method showing its difficulty in generating a representative sample in the case of few and widely distributed macro-pores. The discrepancies between the experimental results and those obtained using the *Wakao-Smith* correlation was attributed to an underestimation of the amount of macro pores during the analysis of the mercury intrusion porosimetry curve. It was already mentioned in Section 7.5 that shielding effect in the porosimetry analysis of the lower porosity foam could lead to an underestimation of the amount of macro pores. Some of them, in fact, could be included in the characteristic region of the meso pores. Different macro-meso pores threshold values were used to determine the percentage of macro and meso pores from the Mercury Intrusion Porosimetry curve; these were then used to assess the sensitivity of the model to different values of meso and macro porosities.

Table 7. 5 summarises the total intrusion, the intrusion in macro and meso pores, the total percentage, the macro porosity and the meso porosity for different threshold selections.

Table 7. 5: Comparison among the different macro and meso porosities values obtained when different macro/meso pore thresholds were selected

Threshold (nm)	Total Intrusion (mL g ⁻¹)	Intrusion in Macro Pores (mL g ⁻¹)	Intrusion in Meso Pores (mL g ⁻¹)	Total Porosity %	Macro Porosity %	Meso Porosity %
50	1.1452	0.3358	0.8094	77.42	22.70	54.72
30	1.1452	0.5252	0.6200	77.42	35.50	41.92
25	1.1452	0.8224	0.3228	77.42	55.59	21.83

Figure 7. 15 shows the model light-off curves obtained when the macro and meso porosities values obtained at the different thresholds were used. The model curves were also compared to both the corrected and uncorrected experimental ones.

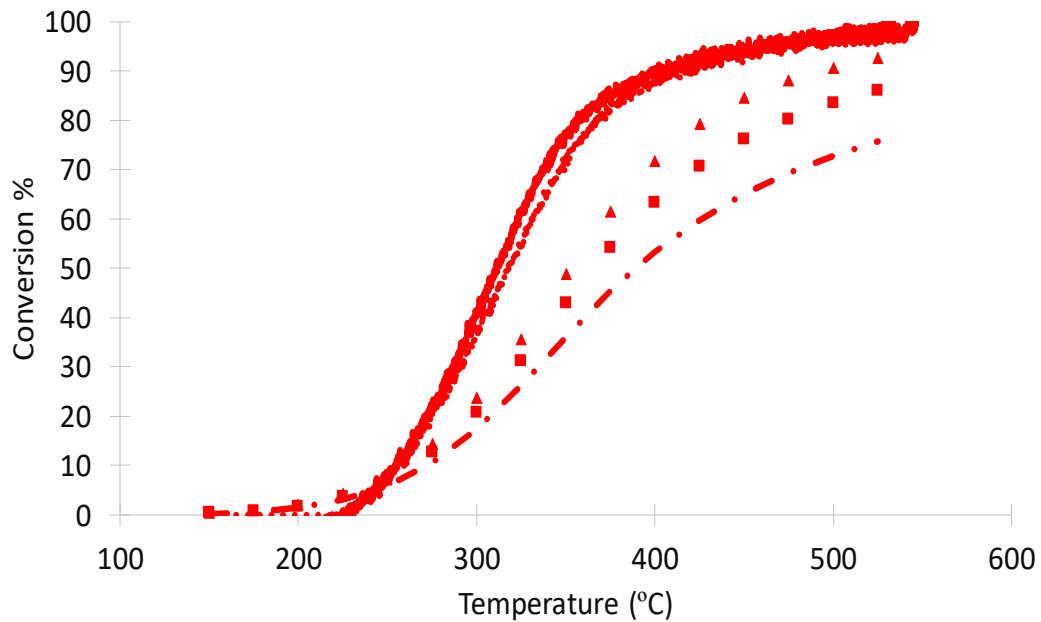


Figure 7. 15: Comparison among model light off curves obtained using different macro-meso pores thresholds and both the corrected and uncorrected experimental ones: (—) Exp., (●) Exp.-Corrected temperature, (—●) Mod.-TS50, (■) Mod.-TS30, (▲) Mod.-TS25

It can be noted from Figure 7. 15 that, varying macro-meso pores threshold from 50 nm to 30-25 nm, the model curves get closer to the corrected experimental light-off curve. This suggests that the percentage of macro pores was underestimated due to shielding effect. It is obviously not possible, in the case to the 77% foam, to exactly determine the amount of macro pores using

mercury intrusion porosimetry experiments, but this last investigation shows that the discrepancy between model and experimental results was due to a limitation of the used characterization technique and not to the inadequacy of the model.

7.8 Conclusions

In this chapter, supports having different porous structures have been impregnated with Pd and their performances in the methane oxidation reaction have been compared. The light-off experiment was designed in order to remark the mass transport differences among the samples. The experimental work showed that foam supported catalyst gave better performances in respect to conventionally supported ones. In particular, the 95% foam supported catalyst presented higher conversion in respect to the 77% foam sample in the light-off curve region where diffusion limitation was expected. The light-off curve was then computationally determined through the use of a 1D + 1D steady state model. Two different approaches (e.g. *Wakao-Smith* and PMS) were used and compared for the determination of the samples effective diffusivity. In the *Wakao-Smith* correlation the percentage of macro and meso pores was determined by analysing the mercury intrusion porosimetry curve. Although this approach was suitable in the case of the high porosity foam, underestimation of the macro porosity in the 77% foam was observed due to macro pores shielding during the analysis. This underlined the necessity of selecting the right analytical technique for the determination of the sample's porous structure. The PMS approach gave comparable results with the *Wakao-Smith* correlation in the case of the higher porosity foam while discrepancies were observed in the case of the lower porosity sample; this is due to the impossibility of obtaining a representative sample for the low porosity foam. This observation shows the limitation of the PMS method at the macro scale, where the dimension of the pores and their wide size distribution could

prevent the construction of a representative samples. In addition, the observed accordance between the *Wakao-Smith* and the PMS, in the case of the high porosity foam, rules out the necessity of using a computationally intense method, such as PMS, at the macro scale. It is also important to remark that the differences observed between the model and experimental curves are due to three other factors. Firstly, a series of steady state simulations were used to represent a transient system and, although the light-off experiment was design to have a series of pseudo steady state system at each temperature ramp, a certain error was introduced by this model assumption. Secondly, in Chapter 5 it has been shown that the used kinetic model does not well represent the reaction when water is present; this is particularly relevant at the higher temperatures of the light-off curve where more water is present in the system leading to an underestimation of methane conversion. Finally, the thermocouple in the micro-reactor was not positioned exactly in the catalyst bed leading to uncertainty about the exact bed temperature; the bed temperature was corrected accounting for the heat of reaction bringing the experimental curve closer to the model one. In conclusion, the benefit of the foam porous structure on the catalyst performances was proved. A 1D + 1D model was developed and the importance of sample characterization to satisfactorily represent the experimental results was shown. In fact, in the case of the higher porosity foam, for which it was possible to obtain a representative characterization of its porous structure, the model was capable of representing the experimental results. This highlights the possibility of using the developed model to quickly screen the performances of catalysts having different porous structures.

Chapter 8

Conclusions and Future Work

8.1 Conclusions

In this thesis, the importance of catalyst formulation was underlined and the cross-linking of different disciplines was shown to be fundamental for the successful development and manufacturing of newly formulated products. Chemistry, analytical chemistry, chemical engineering and computational techniques played a key role in the development, characterisation and manufacturing of new macroporous catalysts supports. Referring to the aims presented in Chapter 1, a brief conclusion on each point is given below:

- **Developing new, more flexible and more sustainable ceramic foams formulations.**

Amino acids have been identified as flexible and environmentally friendly amphiphiles. The presence of both the (basic) amino and the (acidic) carboxylic group on the same molecules allows the amphiphile-particle interactions at both acidic and basic pHs. Correlations between amino acids hydrophobicity and foam structure (porosity and bubble size) have been proposed, giving an insight on how to control the initial formulation depending on the desired final structure. Amphiphile adsorption at different interfaces has been studied (solid-liquid and liquid-gas) and the minimum concentration of amphiphile that has to be added in order to obtain a stable foam was identified leading to optimization of amphiphile usage and reduction of gas emission during the foam after-treatment (calcination) [326]. This resulted in a patent application by JM on the use of these novel amphiphiles for ceramic foam production [327].

- **Establishing the basis for a fundamental understanding of foam manufacturing.** An aerated stirred vessel was used to produce ceramic foams and to provide an insight into the parameters that affect the resultant foam structure. Correlations between global mixing parameters and both gas hold-up and bubble size were applied to ceramic foams. Although discrepancies between the exponents of the different parameters were observed, the correlations present in the literature were capable of correlating mixing conditions to foam properties. Determination of the mixing regime inside the vessel and the comparison with the structure of the produced foams gave a clear idea of the mixing conditions necessary to have the desired foam structures. Foam rheology was measured and the comparison of characteristic rheology curve features (inflection point or “kink”) were compared to foam bubble size and bubble size distribution, resulting in a correlation between them. This opens to the possibility of developing an at-line measurement to qualitatively control the foam structure [328].
- **Testing of foam supported catalysts in different reaction systems.** Foam supported catalyst were tested in different reaction such as Fischer Tropsch Synthesis and methane oxidation. In both cases, better performances were observed when foam supported catalyst were used; in the first case an increase of around 2% in C_{5+} selectivity was observed while in the second one lower light-off temperatures and better performances at high temperatures (diffusion limited region) were observed. In FTS, although it was hypothesised that the better performances were due to the improved diffusion in the catalyst, a clear dependence on foam structure was not identified due to differences in the other properties of the catalyst (e.g. crystal size, metal area, etc.). In the case of methane oxidation, the tested catalysts

presented comparable crystal size and metal area so the improved performances could be attributed to the higher macro-porosity presented by foams. This resulted in a patent application by JM on the use of foam supported catalysts for FTS [329].

- **Developing reactor models to screen the performances of porous catalysts in different reactor configurations.** 1D + 1D models to simulate the performance of porous catalysts in both coated monolith and packed bed reactors were developed and their results compared to experimental data. The model results for the monolith were compared to those experimentally acquired at the SpaciMS at Queen's University Belfast. Chemical species trends along the monolith channel obtained from the model were generally in agreement with the experimental ones. The quantitative difference observed in term of methane conversion, especially at lower temperatures, was attributed to the uncertainty in the value of the enthalpy of adsorption of water which led to an underestimation of methane conversion when water was present in either the feed or reacting mixture. The developed model was also used to collect non-experimentally accessible information such as the chemical species concentrations profiles and the temperature profile inside the wash-coat layer.

Methane light-off curve were modelled and compared to those obtained experimentally for both high and low porosity foams. While quantitative differences in the light-off temperature were found, good agreement was observed for the trend of the high porosity foam light-off curve. Major discrepancies, in both the trend and the light-off temperature, were observed in the case of the low porosity foam. The quantitative difference was attributed to three main reasons: the use of a series of sequential steady state approach to the simulation of a transient system that could introduce lag errors, the position of the

thermocouple outside the catalyst bed in the experimental set up that leads to uncertainty about the actual bed temperature and the underestimation of methane conversion (especially at higher temperatures) due to the poor estimation of the enthalpy of adsorption of water in the used kinetic model. In the case of the low porosity foam the discrepancies in the observed trend were attributed to the difficulty in determining the percentage of meso and macro pores from the mercury intrusion curve due to shielding effects; an underestimation of the amounts of macropores significantly effects the trend of the light-off curve.

In conclusions, this part of the work, led to the development of reactor models suitable to describe the catalyst performances in different reactors configurations and underlined the importance of selecting the right kinetic model and analytical techniques to describe and characterize the reacting system.

- **Comparing different modelling approaches to understand the level of complexity necessary to effectively screen catalysts performances.** Two main comparisons were carried out:
 - Comparison between model results obtained from 1D + 1D simulations and those obtained using a CFD (OpenFOAM) with porous media representation of the catalyst and including diffusion and kinetic models.
 - Comparison between the use of *Wakao-Smith* correlation and the Pore Resolved Model to determine the effective diffusivity in macro-porous materials.

Although the comparison between the OpenFOAM and the 1D + 1D model results presented some discrepancies (especially for the wet feed case), the predicted trends were comparable. The higher conversions predicted by the 3D model were explained by the formation of a stagnation zone in proximity of the channel corners that results in higher

temperatures and residence time hence in higher conversions. The slightly lower conversions predicted by the 3D model in the case of the dry feed cannot be explained by the previously presented reasoning and further studies are recommended to investigate the differences between the two approaches.

Effective diffusivity coefficients determined by *Wakao-Smith* and PMS agreed in the case of the high porosity foam while discrepancies were observed in the case of the low porosity one. In the latter case, the methods were not able to generate a representative sample of the support. That used was characterised by few bubble with a wide bubble size distribution. This comparison showed that, although PMS can be satisfactory used at the nano and micro scale, it presents limitations when it is used to represent macroporous samples with a low porosity and wide bubble size distribution.

8.2 Future Work

This work showed the beneficial effects of using ceramic foams as catalysts supports; although a good understanding of foam formulation and manufacturability impact on foam properties was obtained, different aspects needs to be considered in order to produce technical catalysts.

Amino acids were mostly used as amphiphiles to modify the surface properties of titania particles and, although this class of molecules effectively stabilized titania foams, it is fundamental to test their performances when different powders are used. This will allow broadening and optimisation of their use with different inorganic supports and hence different applications. One of the limit of amino acids is their low solubility and the necessity to work at extremely low or high pH to have a sufficient amount of amphiphile dissolved. Mixtures of different amino acids or mixtures of amino acids and conventional amphiphiles could be used to modify the surface particles. The second

option, in particular, could help to reduce the price of the amphiphilic mixture since less amino acids would be used which are usually more expensive than conventional ones.

The manufacturing study using an aerated stirred vessel gave a valuable insight into the manufacturing of these materials but it also showed some of the limitation of using this system at industrial scale. The dependence of foam structure on power consumption would result in high energy consumption at industrial scale, especially when foams with smaller bubbles want to be obtained. In addition, vessel having a significant volume are necessary to accommodate the foam expansion resulting in higher costs (e.g. bigger vessel, longer impeller shafts) and longer operational times. Alternatives could be the design of continuous process using, for examples, membranes to entrain the gas in a ceramic slurry flowing inside a static mixer. On-demand foam systems could be realized by dissolving the gas in the ceramic slurry and generating, upon pressure release, the desired amount the foam. Finally, another system to generate gas in-situ could be chemical decomposition such as the evolution of CO₂ from carbonates, evolution of O₂/H₂ from peroxides or N₂ from ammonium nitrite.

Although the effects of formulation and manufacturing have been widely investigated, other aspects of the catalysts manufacturing could affect its performances such as thermal treatment and forming. Drying and calcination could have a significant impact on the structural and mechanical properties of the support; different drying techniques such as freeze drying, drying in a controlled atmosphere could be used to reduce the amounts of cracks in the support and in turn to improve its mechanical properties. Pelleting it has been shown to have a detrimental effect on the structure of the foam, in fact, some of the foam porosity is lost during pelleting; alternatives to shape the support such as extrusion or granulation could be investigated.

Ceramic foams have been successfully tested in Fisher Tropsch Synthesis and methane oxidation; due to the potential benefit of using these novel supports, ceramic foam supported catalysts should be tested in other reaction systems, especially those characterized by strong diffusion limitation, either due to inherently fast kinetics or slow (liquid phase or large molecule) diffusion.

Reactor models for the study of the performances of supported catalysts have been developed and they have been used for the study of methane oxidation. These models could now be used to screen the effect of the support structure on the reaction performances in order to accelerate the development of new structured supports. In addition, kinetic models for reaction system of particular interest could be developed and the effects of the support structure on these reactions could be quickly assessed using the aforementioned models.

References

- [1] S. Green, *Industrial Catalysis*, New York: Macmillan Company, 1928.
- [2] A. J. B. Robertson, "The early history of catalysis," *Platinum Metals Rev.*, vol. 19, no. 2, pp. 64-69, 1975.
- [3] O. Levenspiel, *Chemical Reactino Engineering 3rd Edition*, New York: John Wiley & Son Inc., 1999.
- [4] "World Catalysts: Industry study with forecasts for 2018 & 2023," The Freedonia Group, 2014.
- [5] A. J. B. Robertson, *Catalysis of gas reactions by Metals*, London: Logos Press, 1970.
- [6] J. Kirchnerova and D. Klavana, "Synthesis and characterization of perovskite catalysts," *Solid State Ionics*, vol. 123, pp. 307-317, 1999.
- [7] E. Fontes, "<https://www.comsol.com/blogs/modeling-approaches-in-heterogeneous-catalysis/>," Comsol, 3 February 2015. [Online]. [Accessed 18 October 2017].
- [8] E. W. Thiele, "Relation between catalytic activity and size of particles," *Industrial and Engineering Chemistry*, vol. 31, pp. 916-920, 1939.
- [9] C. H. Bartholomew and R. J. Farrauto, *Fundamentals of Industrial Catalytic Processes 2nd Edition*, Hoboken, New Jersey: John Wiley & Sons Inc., 2006.
- [10] J. Song and D. Li, "Effect of catalyst pore size on the catalytic performance of silica supported cobalt Fischer-Tropsch catalyst," *Journal of Molecular Catalysis A: Chemical*, vol. 247, pp. 206-212, 2006.
- [11] H. Li, J. Wang, C. Chen, L. Jia, B. Hou and D. Li, "Effects of macropores on reducing internal diffusion limitations in Fischer-Tropsch synthesis using a hierarchical cobal catalyst," *RSC Adv.*, vol. 7, p. 9436, 2017.
- [12] V. Rao, P. A. Simonov, E. R. Savinova, J. V. Plaksin, S. V. Cherepanova, G. N. Kryukova and U. Stimming, "The influence of carbon support porosity on the activity of PtRu/Sibunit anode catalyst for methanol oxidation," *Journal of Power Sources*, vol. 145, pp. 178-187, 2005.
- [13] S. Vadja, M. J. Pellin, J. P. Greeley, C. L. Marshall, L. A. Curtiss, G. A. Ballentine, J. W. Elam, S. Catillon-Mucherie, P. C. Redfern, F. Mehmood and P. Zapol, "Subnanometre platinum clusters as highly active and selective catalysts for the oxidative dehydrogenation of propane," *Nat Mater*, vol. 8, pp. 213-216, 2009.
- [14] J. M. Thomas, *Design and Applications of single-site heterogeneous catalyst-Contribution to green chemistry*, London: London Imperial College Press, 2012.

- [15] F. Yang, D. Deng, X. Pan, Q. Fu and X. Bao, "Understanding nano effects in catalysis," *Nat Sci Rev*, vol. 2, no. 2, pp. 183-201, 2015.
- [16] S. Cao, F. Tao, Y. Tang, Y. Li and J. Yu, "Size- and shape-dependent catalytic performances of oxidation and reduction reactions on nanocatalysts," *Chem Soc Rev*, vol. 45, p. 4747, 2016.
- [17] X. Bokhimi and R. Zanella, "Crystallite size and morphology of the phases in Au/TiO₂ and Au/Ce-TiO₂ catalysts," *J Phys Chem C*, vol. 111, no. 6, pp. 2525-2532, 2007.
- [18] G. S. Zafiris and R. J. Gorte, "CO oxidation on Pt Alpha-Al₂O₃(0001)- Evidence for structure sensitivity," *Journal of Catalysis*, vol. 140, no. 2, pp. 418-423, 1993.
- [19] R. Zanella, C. Louis, S. Giorgio and R. Touroude, "Crisinaldehyde hydrogenation by gold supported in TiO₂: structure sensitivity and mechanism," *Journal of Catalysis*, vol. 223, no. 2, pp. 328-339, 2004.
- [20] S. W. Cao, J. Fang, M. M. Shahjamali, Z. Wang, Z. Yin, Y. H. Yang, F. Y. C. Boey, J. Barber, S. C. J. Loo and C. Xue, "Insitu growth of Au nanoparticles on Fe₂O₃ nanocrystals for catalytic applications," *CrystEngComm*, vol. 14, no. 21, pp. 7229-7235, 2012.
- [21] W. Kossel, "Extending the Law of Bravais," *Nachr. Ges. Wiss. Gottingen*, p. 143, 1927.
- [22] I. N. Stranki, "On the theory of crystal accretion," *Zeitschrift fur physikalische chemie-stoichiometrie und verwandtschaftslehre*, vol. 136, no. 3-4, pp. 259-278, 1928.
- [23] L. Bahrig, S. G. Hickey and A. Eychnuller, "Mesocrystalline materials and the involvement of oriented attachment- a review," *CrystEngComm*, vol. 16, p. 9408, 2014.
- [24] D. W. Blakely and G. A. Somorjai, "Dehydrogenation and hydrogenolysis of cyclohexane and cyclohexene on stepped (high Miller index) platinum surfaces," *J. Catal.*, vol. 42, no. 2, pp. 181-196, 1976.
- [25] L. P. Ford, P. Blowers and R. I. Masel, "Role of steps and kinks in catalytic activity," *Journal of Vacuum Science & Technology*, vol. 17, p. 1705, 1999.
- [26] J. S. Spendelow, Q. Xu, J. D. Goodpaster, P. J. A. Kenis and A. Wieckowski, "The role of surface defects in CO oxidation, methanol oxidation and oxygen reduction on Pt (111)," *Journal of the Electrochemical Society*, vol. 154, no. 12, pp. F238-F242, 2007.
- [27] Z. T. Wang, Y. Xu, M. El-Soda, F. R. Lucci, R. J. Madix, C. M. Friend and C. H. Sykes, "Surfacestructure dependence of the dry dehydrogenation of alcohols on Cu(111) and Cu(110)," *J. Phys. Chem. C*, vol. 121, pp. 12800-12806, 2017.
- [28] X. G. Zhang, M. A. Van Hove, G. A. Somorjai, P. J. Rous, D. Tobin, A. Gonis, J. M. MacLaren, K. Heinz, M. Michl, H. Lindner, K. Muller, M. Ehsasi and J. H. Block, "Efficient determination of

multilayer relaxation in the Pt(210) stepped and densely kinked surface," *Phys. Rev. Lett.*, vol. 67, p. 1298, 1991.

- [29] G. J. Hutchings, "Promotion in heterogeneous catalysis: a topic requiring a new approach?," *Catalysis Letters*, vol. 75, no. 1-2, pp. 1-11, 2001.
- [30] C. Peters, K. Schaefer and R. Krabetz, "The importance of aluminium oxide on the structure of ammonia catalysts," *Electrochem.*, vol. 64, p. 1194, 1960.
- [31] G. Ertl, S. B. Lee and M. Weiss, "Kinetics of nitrogen adsorption on Fe (111)," *Surface Science*, vol. 114, no. 2-3, pp. 515-526, 1982.
- [32] Z. Paal, G. Ertl and S. B. Lee, "Interactions of potassium, oxygen and nitrogen with polycrystalline iron surfaces," *Appl. Surf. Sci.*, vol. 8, no. 3, pp. 231-249, 1981.
- [33] C. T. Campbell, "Coadsorption, Promoters and Poisons," in *The chemical physics of solid surfaces*, Amsterdam, Elsevier, 1993, p. 287.
- [34] J. Nakamura, J. M. Campbell and C. T. Campbell, "Kinetics and mechanism of the water-gas shift reaction catalysed by the clean and Cs-promoted Cu (110) surface- A comparison with Cu (111)," *J. Chem. Soc. Faraday Trans.*, vol. 86, no. 15, pp. 2725-2734, 1990.
- [35] C. T. Campbell and B. E. Koel, "A model study of alkali promotion of water gas shift catalyst Cs-Cu (111)," *Surf. Sci.*, vol. 186, no. 3, pp. 393-411, 1987.
- [36] A. Palermo, A. Husain and R. M. Lambert, "Triply-promoted ethene epoxidation: NO_x promotion of the Ag-catalysed reaction in the presence of alkali and chlorine under electrochemical control," *Cat. Lett.*, vol. 69, no. 3-4, pp. 175-179, 2000.
- [37] S. Ahmed, S. Kasztelan and J. B. Moffat, "Mechanistic relationship in the activation of methane and the conversion of methanol on heteropoly oxometallates," *Faraday Discuss. Chem. Soc.*, vol. 87, pp. 23-32, 1989.
- [38] P. Fordham, R. Garcia, M. Besson and P. Gallezot, "Selective catalytic oxidation with air of glycerol and oxygenated derivatives on platinum metals," *Stud. Surf. Sci. Catal.*, vol. 101, pp. 161-170, 1996.
- [39] S. Mitchell, N. L. Micheals and J. Perez-Ramirez, "From powder to technical body: the undervalued science of catalyst scale up," *Chem. Soc. Rev.*, vol. 42, pp. 6094-6112, 2013.
- [40] D. J. Birdsall, E. H. Stitt, M. Nijemeisland, M. P. U. Carlsson, M. Bobovic, S. A. French and W. M. Sengelow, "Shaped Heterogeneous Catalysts". Worldwide Patent WO2010029324, 12 September 2008.
- [41] "Annual Report & Accounts," Johnson Matthey, 2017.

- [42] L. J. Gauckler, M. M. Waeber, C. Contand and M. Jacobduliere, "Ceramic Foam for Molten-Metal Filtration," *J. Metals*, 37 [9], pp. 47-50, 1985.
- [43] M. Colombo and P. Sheffled, *Cellular Ceramics: structure, Manufacturing, Porperties and Applications*, Weihheim: Wiley-VCH, 2005.
- [44] A. R. Studart, U. T. Gonzenbach, E. Tervoort and L. J. Gauckler, "Processing Routes to Macroporous Ceramics: A Review," *J. Am. Ceram. Soc.* 89 [6], pp. 1771-1789, 2006.
- [45] T. Ota, M. Imaeda, H. Takase, M. Kobayashi, N. Kinoshita, T. Hirashita, H. Miyazaki and Y. Hikichi, "Porous Titania Ceramic Prepared by Mimicking Silicified Wood," *J. Am. Ceram. Soc.*, 83 [6], pp. 1521-3, 2000.
- [46] R. A. White, E. W. White and J. N. Weber, "Replamineform-New Process for Preparing Porous Ceramic, Metal and Polymer Prosthetic Materials," *Science* 176 [4037], p. 922, 1972.
- [47] J. Saggio-Woyansky, S. C. E and W. P. Minnear, "Processing of Porous Ceramics," *Am. Ceram. Soc. Bull.*, 71 [11], pp. 1674-82, 1992.
- [48] J. Luyten, S. Mullens, J. Cooymans, A. M. De Wilde and I. Thijs, "New Processing Techniques if Ceramic Foams," *Adv. Eng. Mater.*, 5 [10], pp. 715-8, 2008.
- [49] R. A. Segadaes and A. M. Lopes, "Microstructure, Permeability and Mechanical Behaviour of ceramic Foams," *Mater. Sci. Eng. A-Struct. Mater. Prop. microstruct. Process.*, 209 [1-2], pp. 149-55, 1996.
- [50] H. Kim, C. da Rosa, M. Boaro, V. J. M and R. J. Gorte, "Fabrication of Highly Porous Yttria-Stabilised Zirconia by Acid Leaching Nickel from a Nickel-Yttria-Stabilized Zirconia Cement," *J. Am. Ceram. Soc.* 85 [6], pp. 1473-6, 2002.
- [51] A. Pine and D. J. Imhof, "Ordered macroporous Materials by Emulsaion Templating," *Nature*, 389 [6654], pp. 948-51, 1997.
- [52] U. T. Gonzenbach, A. R. Studart, E. Tervoort and L. J. Gauckler, "Stabilization of Foams with Inorganic Colloidal Particles," *Langmuir* 22, pp. 109383-88, 2006.
- [53] J. F. A. Plateau, "Statique Experimentale et Theorique del Liquides Soumis aux Seules Forces Moleculaires," *Gauthier-Villard*, 1873.
- [54] F. J. Almgren and J. E. Taylor, *Scient. Amer.*, vol. 235, p. 82, 1976.
- [55] M. F. Vaz, "Liquid Foams: an Introduction," *Philosophical Magazine Letters*, vol. 88, no. 9, pp. 627-636, 2008.
- [56] W. Thomson, *Phil. Mag.*, vol. 24, p. 503, 1887.

- [57] D. Weaire and R. Phelan, "A counter-example to Kelvin's conjecture on minimal surfaces," *Phil. Mag. Lett.*, vol. 69, pp. 107-110, 1994.
- [58] G. Verbis, D. Weaire and A. M. Kraynik, "The foam drainage equation," *J. Phys. Condens. Matter*, vol. 8, no. 21, pp. 3715-3731, 1996.
- [59] M. A. Fortes and S. Coughlan, "Simple-Model of Foam Drainage," *J. App. Phys.*, vol. 76, no. 7, pp. 4029*-4035, 1994.
- [60] P. C. Hiemenz and R. Rayagopalan, *Principles of Colloids and Surface Chemistry*, New York: Marcel Dekker Inc., 1997.
- [61] W. C. Griffin, "Calculation of HLB values of Non-Ionic surfactants," *Journal of the Society of Cosmetic Chemists*, vol. 5, no. 4, p. 249.256, 1954.
- [62] J. T. Davies, "A quantitative kinetic theory of emulsion type, I. Physical chemistry of the emulsifying agent," *Gas/Liquid and Liquid/Liquid Interface, Proceedings of the International COngress of Surface Activity*, pp. 426-438, 1957.
- [63] W. C. Griffin, "Clasifcation of Surface-Active Agents by "HLB"," *Journal of the Society of Cosmetic Chemists*, vol. 1, no. 5, pp. 311-326, 1949.
- [64] R. Aveyard, B. P. Binks and J. Mead, "Interfacial tension minima in oil-water surfactant systems," *J. Chem. Soc. Faraday Trans 1*, vol. 82, pp. 1755-1770, 1986.
- [65] L. A. Pugnaloni, E. Dickinson, R. Ettelaie, A. R. Mackie and P. J. Wilde, "Competitive Adsorption of Proteins and Low-Molecular-Weight Surfactants: Computer Simulation and Microscopic Imaging," *Adv. Colloid Interf. Sci.*, vol. 107, pp. 27-49, 2004.
- [66] L. L. Wood, P. Messina and K. Frisch, "Method of Preparing Porous Ceramic Structures by Firing a Polyurethane Foam that is Impregnated with Organic Materia". U.S. Patent USRE32603, 1974.
- [67] T. Tomita, S. Kawasaki and K. Okada, "A Novel Preparation Method for Foamed Solica Ceramics by Sol-Gel Reaction and Mechanical Foaming," *J. Porous Mater.*, vol. 11, no. 2, pp. 107-115, 2004.
- [68] J. G. P. Binner, "Production and Properties of Low Density Engineering Ceramic Foams," *Br. Ceram. Trans.*, vol. 96, no. 6, pp. 247-249, 1997.
- [69] F. S. Ortega, P. Sepulveda and V. C. Pandolfelli, "Monomer Systems for the Gelcasting of Foams," *J. Eur. Ceram. Soc.*, vol. 22, no. 9-10, pp. 1395-1401, 2002.
- [70] F. S. Ortega, F. A. O. Valenzuela, C. H. Scuracchio and V. C. Pandolfelli, "Alternative Gelling Agents for the Gelcasting of Ceramic Foams," *J. Eur. Ceram. Soc.*, vol. 23, no. 1, pp. 75-80, 2003.
- [71] S. U. Pickering, "Emulsions," *J. Chem. Soc. Trans.*, vol. 91, pp. 2001-2021, 1907.

- [72] Z. P. Du, M. P. Bilbao-Montoya, B. P. Binks, E. Dickinson, R. Ettelaie and B. S. Murray, "Outstanding Stability of Particle-Stabilized Bubbles," *Langmuir*, vol. 19, no. 8, pp. 3106-3108, 2003.
- [73] B. P. Binks, "Particles as Surfactants-Similarities and Differences," *Curr. Opin. Colloid Interf. Sci.*, vol. 7, no. 1-2, pp. 21-41, 2002.
- [74] A. R. Studart, R. Libanori, A. Moreno, U. T. Gonzenbach, E. Tervoort and L. G. Gauckler, "Unifying Model for the Electrokinetic and Phase Behavior of Aqueous Suspensions Containing Short and Long Amphiphiles," *Langmuir* 27, pp. 11835-11844, 2011.
- [75] U. T. Gonzenbach, A. R. Studart, E. Tervoort and L. J. Gauckler, "Tailoring the Microstructure of Particle-Stabilized Wet Foams," *Langmuir* 23, pp. 1025-1032, 2007.
- [76] S. E. Forrester, C. D. Rielly and K. J. Carpenter, "Gas-inducing impeller design and performance characteristics," *Chemical Engineering Science*, 53, pp. 603-615, 1998.
- [77] J. Schindelin, I. Arganda-Carreras and E. Frise, "Fiji: an open-source platform for biological-image analysis," *Nature Methods*, vol. 9, no. 7, pp. 676-682, 2012.
- [78] A. Williams, C. P. Garner and J. G. P. Binner, "Measuring Pore Diameter Distribution of Gelcast Ceramic Foams from Two-Dimensional Cross Sections," *Loughborough's Institutional Repository*.
- [79] S. M. I. Saad, Z. Policova and A. W. Neumann, "Design and Accuracy of Pendant Drop Methods for Surface Tension Measurement," *Colloids and Surfaces A: Physiochem. Eng. Aspects*, 384, pp. 442-452, 2011.
- [80] H. Wagner and I. Musso, "New naturally Occurring Amino Acids," *Angew. Chem. Int. Ed. Engl.*, 22, pp. 816-828, 1983.
- [81] J. Hans-Dieter and S. Norbert, "Amino Acids," in *Peptides form A to Z: A Concise Encyclopedia*, Wiley-VCH, 2008, p. 20.
- [82] R. H. Garrett and C. M. Grisham, *Biochemistry*, Boston: CENGAGE Learning, 2016.
- [83] K. Bourikas, C. Kordulis and A. Lycourghiotis, "Titanium Dioxide (Anatase and Rutile): Surface Chemistry, Liquid-Solid Interface Chemistry, and Scientific Synthesis of Supported Catalysts," *Chem. Rev.*, pp. 9754-9823, 2014.
- [84] H. C. Tseng, C. Y. Lee, W. L. Weng and I. M. Shiah, "Solubilities of amino acids in water at various pH value under 298.15 K," *Fluid Phase Equilibria*, 285, pp. 90-95, 2009.
- [85] R. M. Silverstein, F. X. Webster and D. J. Kiemle, *Spectrometric Identification of Organic Compounds* (th Edition), John Wiley & Sons, 2005.

- [86] D. Megias-Alguacil, E. Tervoort, C. Cattin and L. J. Gauckler, "Contact Angle and Adsorption Behaviour of Carboxylic Acids on α -Al₂O₃," *Journal of Colloid and Interface Science* 353, pp. 512-518, 2011.
- [87] V. B. Fainerman, E. H. Lucassen-Reynders and R. Miller, "Adsorption of Surfactant and Proteins at Fluid Interfaces," *Colloids Surfaces A: Physicochem. Eng. Aspects*, 143, pp. 141-165, 1998.
- [88] I. Langmuir, "The constitution and Fundamental Properties of Solids and Liquids. II. Liquids," *J. Am. Chem. Soc.*, 39, pp. 1848-1906, 1917.
- [89] A. V. Makievski, V. B. Fainerman, R. Miller, M. Bree, L. Liggieri and F. Ravera, "Determination of Equilibrium Surface tension Values by Extrapolation Via Long Time Extrapolations," *Colloids Surf. A*, 122, pp. 269-273, 1997.
- [90] J. Eastoe and J. S. Dalton, "Dynamic Surface Tension and Adsorption Mechanisms of Surfactants at the Air-Water Interface," *Adv. Colloid Interface Sci.*, 85, pp. 103-144, 2000.
- [91] S. S. Dukhin, G. Kretschmar and R. Miller, *Dynamics of Adsorption at Liquid Interfaces*, Elsevier Science, 1995.
- [92] C. Chothia, "The Nature of the Accessible and Buried Surfaces in Proteins," *J. Mol. Biol.*, 105, pp. 1-14, 1976.
- [93] J. Kyte and R. F. Doolittle, "A Simple Method for Displaying the Hydrophobic Character of a Protein," *J. Mol. Biol.*, 157, pp. 105-32, 1982.
- [94] H. B. Bull and K. Breese, "Surface tension of Amino Acids Solutions: A Hydrophobicity Scale of the Amino Acid Residues," *Archives of Biochemistry and Biophysics*, 161, pp. 665-670, 1974.
- [95] G. Jones and W. A. Ray, "The Surface Tension of Solutions of Electrolytes as a Function of the Concentration I A Differential Method for Measuring Relative Surface Tension," *J. Amer. Chem. Soc.*, vol. 59, pp. 187-198, 1937.
- [96] A guidebook to particle size analysis, Irvine, USA: Horiba Instruments Inc.
- [97] H. G. Merkus, *Particles Size Measurements: Fundamentals, Practice, Quality*, Springer, 2009.
- [98] T. E. Needham, "The solubility of Amino Acids in Various Solvent Systems," *PhD Thesis*, 1970.
- [99] U. T. Gonzenbach, A. R. Studart, E. Tervoort and L. J. Gauckler, "Ultrastable Particle-Stabilized Foams," *Angew. Chem. int. Ed.*, 45, pp. 3526-3530, 2006.
- [100] B. L. Welch, "The generalization of "Student's" problem when several different population variances are involved," *Biometrika*, 34 (1-2), pp. 28-35, 1947.

- [101] U. T. Gonzenbach, A. R. Studart, D. Steinlin, E. Tervoort and L. J. Gauckler, "Processing of Particle-Stabilized Wet Foams Into Porous Ceramics," *J. Am. Ceram. Soc.*, vol. 90, no. 11, pp. 3407-3414, 2007.
- [102] L. J. Gauckler, A. R. Studart, E. Tervoort, U. T. Gonzenbach and I. Akartuna, "Ultrastable Particle-Stabilized Foams and Emulsions". Patent EP1960097, 04 July 2012.
- [103] V. R. Salvini, B. A. Sandurkov, R. F. K. Gunnewiek, D. S. Rosa and V. C. Pandolfelli, "Porous Ceramics with Tailored Properties," *American Ceramic Society Bulletin*, vol. 86, no. 3, pp. 9401-9405.
- [104] A. J. Worthen, S. L. Bryant, C. Huh and K. P. Johnston, "Carbon Dioxide-in-Water Foams Stabilized with Nanoparticles and Surfactant Acting in Synergy," *AIChE Journal*, vol. 59, no. 9, pp. 3490-3501, 2013.
- [105] E. L. Paul, V. A. Atiemo-Obeng and S. M. Kresta, *Handbook of Industrial Mixing: Science and Practice*, Hoboken, NJ: Wiley-Interscience, 2004.
- [106] A. H. P. Skelland, *Non-Newtonian Flow and Heat Transfer*, Wiley, 1967.
- [107] S. Nagata, *Mixing: Principles and Applications*, Wiley, 1975.
- [108] V. W. Uhl and J. B. Gray, *Mixing: Theory and Practice*, Vol. I, Academic Press, 1966.
- [109] F. A. Holland and F. S. Chapman, *Liquid Mixing and Processing in Stirred Tanks*, Reinhold, 1966.
- [110] N. Harnby, M. F. Edwards and A. W. Nienow, *Mixing in the Process Industries*, 2nd Edition, Oxford: Reed Educational and Professional Publishing Ltd., 1992.
- [111] B. N. Murthy and J. B. Joshi, "Assessment of Standard k-eps, RMS and LES turbulence models in a baffled stirred vessel agitated by various impeller designs," *Chemical Engineering Science*, vol. 63, pp. 5468-5495, 2008.
- [112] V. V. Renade and J. B. Joshi, "Flow Generated by Pitched Blade Turbines I. Measurements using laser doppler anemometer," *Chemical Engineering Communication*, vol. 81, pp. 197-224, 1989.
- [113] Z. Jaworski, A. W. Nienow, E. Koutsakos, E. Dyster and W. Bujalski, "A LDA Study of Turbulent Flow in a Baffled Vessel Agitated by a Pitched Blade Turbine," *Chemical Engineering Research and Design*, vol. 64, no. A4, pp. 313-320, 1991.
- [114] S. M. Kresta and P. E. Wood, "The Flow Field Produced by a Pitched Blade turbine: Characterization of the Turbulence and Estimation of the Dissipation Rate," *Chemical Engineering Science*, vol. 48, no. 10, pp. 1761-1774, 1993.

- [115] A. Amanullah, S. A. Hjorth and A. W. Nienow, "Cavern Sizes Generated in Highly Shear Thinning Viscous Fluids by SCABA 3 SHP1 Impeller," *transactions IChemE*, vol. 75, no. C, pp. 232-238, 1997.
- [116] A. W. Nienow, "Suspension of Solid Particles in Turbine Agitated Baffled Vessels," *Chemical Engineering Science*, vol. 23, pp. 1453-1459, 1968`.
- [117] P. M. Armenante and E. U. Nagamine, "Effect of Low Off-Bottom Impeller Clearance on the Minimum Agitation Speed for Complete Suspension of Solid in Stirred Tanks," *Chemical Engineering Science*, vol. 53, pp. 1757-1775, 1998.
- [118] G. Montante, K. C. Lee, A. Brucato and M. Yinneskis, "Double to Single Loop Flow Pattern transition in Stirred Vessels," *The Canadian Journal of Chemical Engineering*, vol. 77, pp. 649-659, 1999.
- [119] K. Rutherford, S. M. S. Mahmoudi, K. C. Lee and M. Yianneskis, "the Influence of Rushton Impeller Blade and Disk Thickness on the Mixing Characteristics of Stirred Vessels," *Chemical Engineering Research and Design*, vol. 74, no. A, pp. 369-378, 1996.
- [120] H. Ameer, M. Bouzit and M. Helmaoui, "Numerical Study of Fluid Flow and Power Consumption in a Stirred Vessel with a SCABA 6SRGT Impeller," *Chemical Process Engineering*, vol. 32, no. 4, pp. 351-366, 2011.
- [121] N. Harnby, M. F. Edwards and A. W. Nienow, *Mixing in the process industries* 2nd Edition, Oxford: Butterworth-Heinemann, 2001.
- [122] A. B. Metzner and R. E. Otto, "Agitation of Non-Newtonian Fluids," *A.I.Ch.E. Journal*, vol. 3, no. 1, pp. 3-10, 1957.
- [123] W. Tauscher and P. Mathys, "Proc. 1st Eur. Conf. in Mixing and Centrifugal Separation," in *BHRA Fluid Engineering*, Bedford, 1975, pp. D3-25 to D3-32.
- [124] S. J. Chen, "Proc. 1st Eur. Conf. on Mixing and Centrifugal Separation," in *BHRA Fluid Engineering*, Bedford, 1975, pp. D2-13 to D2-24.
- [125] J. A. C. van der Donk, R. G. J. M. Lans and J. M. Smith, "Proc. 3rd European Mixing Conf.," in *BHRA*, Cranfield, 1979, pp. 289-297.
- [126] W. Bruijn, K. Van't Riet and J. M. Smith, "Power-Consumption with Aerated Rushton Turbines," *Trans. Instn Chem. Engrs*, vol. 52, pp. 88-104, 1974.
- [127] K. van't Riet, *Turbine Agitator Hydrodynamics and Dispersion Performances*, T.H. Delft: PhD Thesis, 1975.
- [128] A. W. Nienow, "gas Dispersion Performances in Fermenter Operation," *Chem. Eng. Prog.*, vol. 86, no. 2, pp. 61-71, 1990.

- [129] Y. Zundeleovich, "Power-Consumption and Gas Capacity of Self-Inducting Turbo Aerators," *A.I.Ch.E.J.*, vol. 25, no. 5, pp. 763-773, 1979.
- [130] P. H. Calderbank, *Trans.I.Chem.E.*, vol. 36, p. 443, 1958.
- [131] B. J. Michel and S. A. Miller, "Power Requirements of Gas-Liquid Agitated Systems," *A.I.Ch.E.J.*, vol. 8, no. 2, pp. 262-266, 1962.
- [132] J. C. Pharamond, M. Roustan and H. Roques, "Determination of Consumed Power in an Aerated and Agitated Tank," *Chem. Eng. Sci.*, vol. 30, no. 8, pp. 907-912, 1975.
- [133] M. Greaves and K. H. Kobbacy, *I.Chem.E.Symp.Ser.*, vol. 64, p. J1, 1981.
- [134] A. W. Nienow, D. J. Wisdom and J. C. Middleton, "Proceedings of 2nd European Conference on Mixing," *BHRA Fluid Engineering, Cranfield*, pp. pp. F1-1-F1-16 and X54, 1978.
- [135] J. M. Smith, *Proc. 5th Eur. Conf. Mixing*, p. 13, 1985.
- [136] M. C. G. Warmoeskerken and J. M. Smith, "The Hollow Blade Agitator for Dispersion and Mass-Transfer," *Chem. Eng. Res. Des.*, vol. 67, no. 2, pp. 193-198, 1989.
- [137] J. M. Smith, "Simple performance Correlations for Agitated Vessels," *Proc. 7th Euro. Congress on Mixing, Brugge*, pp. 233-241, 1991.
- [138] M. Greaves and M. Barigou, "Estimation of Gas Hold-Up and Impeller Power in a Stirred Vessel Reactor," *Fluid Mixing III*, vol. 108, pp. 235-255, 1990.
- [139] J. M. Smith, "Simple Performance Correlations for Agitated Vessels," *Proc. 7th Euro. Congress on Mixing*, pp. 233-241, 1991.
- [140] V. B. Rewatkar, A. B. Deshpande, A. B. Pandit and J. B. Joshi, "gas Hold-Up Behaviour of Mechanically Agitated Gas-Liquid Reactors using Pitched Blade Downflow Turbines," *Can. J. Chem. Eng.*, vol. 71, pp. 226-237, 1993.
- [141] M. J. Whitton and A. W. Nienow, "Scale-up Correlations for Gas Hold-up and Mass transfer Coefficients in Stirred Tank Reactors," *Proc. 3rd Int. Conference on Bioreactor and Bioprocess Fluid Dynamics*, pp. 135-149, 1993.
- [142] A. A. Yawalkar, V. G. Pangarkar and A. A. C. M. Beenackers, "Gas Hold-Up in Stirred Tank Reactors," *The Canadian Journal of Chemical Engineering*, vol. 80, pp. 158-166, 2002.
- [143] D. Pinelli, M. Nocentini and F. Magelli, "Solids Distribution in Stirred Slurry Reactors: Influence of Some Mixer Configurations and Limits to the Applicability of a Simple Model for Predictions," *Chemical Engineering Communications*, vol. 00, pp. 1-18, 2001.

- [144] G. Montante and F. Magelli, "Modelling of Solids Distribution in Stirred Tanks: Analysis of Simulation Strategies and Comparison with Experimental Data:," *International Journal of Computational Fluid Dynamics*, vol. 19, no. 3, pp. 253-262, 2005.
- [145] A. R. Khopkar, G. R. Kasat, A. B. Pandit and V. V. Ranade, "Computational Fluid Dynamics Simulation of the Solid Suspension in a Stirred Slurry Reactor," *Industrial & Engineering Chemistry Research*, vol. 45, pp. 4416-4428, 2006.
- [146] A. N. Kolmogoroff, *Dokl. Akad. Nauk. S.S.S.R. (N.S.)*, vol. 66, p. 825, 1949.
- [147] A. Frohn and N. Roth, *Dynamics of Droplets*, Springer Science & Business Media, 2000.
- [148] J. O. Hinze, "Fundamentals of the hydrodynamic mechanism of splitting in dispersion processes," *A.I.Ch.E. Journal*, vol. 1, pp. 289-295, 1955.
- [149] V. Machon, A. W. Pacek and A. W. Nienow, "Bubble sizes in electrolyte and alcohol solutions in a turbulent stirred vessel," *TransIChemE*, vol. 75 (A), pp. 339-348, 1997.
- [150] F. B. Sprow, "Drop Size Distributions in Strongly Coalescing Agitated Liquid-Liquid Systems," *AIChE Journal*, vol. 13, no. 5, pp. 995-998, 1967.
- [151] V. Machon, A. W. Pacek and A. W. Nienow, "Bubble Sizes in Electrolyte and Alcohol Solutions in a Turbulent Stirred Vessel," *TransIChemE*, vol. 75, no. A, pp. 339-348, 1997.
- [152] B. Hu, A. W. Nienow and A. W. Pacek, "The effect of sodium caseinate concentration and processing conditions on bubble sizes and their break-up and coalescence in turbulent, batch air/aqueous dispersions at atmospheric and elevated pressures.," *Colloids and Surfaces B: Biointerfaces*, vol. 31, pp. 3-11, 2003.
- [153] B. Hu, A. W. Pacek, E. H. Stitt and A. W. Nienow, "Bubble sizes in agitated air-alcohol systems with and without particles: turbulent and transitional flow," *Chemical Engineering Science*, vol. 60, pp. 6371-6377, 2005.
- [154] A. W. Nienow, B. Hu and A. W. Pacek, "Bubble Sizes in Stirred Reactors: What can We Predict?," *Annual Meeting*, p. Paper 361a, 2003.
- [155] H. A. Barnes, *A Handbook of Elementary Rheology*, Penglais, Wales: The University of Wales Institute of Non-Newtonian Fluid, 2000.
- [156] G. Schramm, *A Practical Approach to Rheology and Rheometry* 2nd Edition, Karlsruhe: Gebrueder HAAKE, 2000.
- [157] "<http://www.tainstruments.com/wp-content/uploads/CA-2016-Rheology.pdf>," [Online].

- [158] B. Kasprzyk-Hordern, "Chemistry of alumina, reactions in aqueous solution and its application in water treatment," *Advances in Colloid and Interface Science*, vol. 110, pp. 19-48, 2004.
- [159] R. V. Lenth, "Quick and Easy Analysis of Unreplicated Factorials," *Technometrics*, vol. 31, pp. 469-473, 1989.
- [160] JMP 10 Modeling and Multivariate Method, Cary: SAS Institute, 2012.
- [161] K. Q. Ye and M. Hamada, "Critical Values of the Lenth Method for Unreplicated Factorial Designs," *Journal of Quality technology*, vol. 32, no. 1, pp. 57-66, 2000.
- [162] T. H. McCulloh, "Mass properties of sedimentary rocks and gravimetric effects of petroleum and natural-gas reservoirs," *USGS Professional Paper*, vol. 528, 1967.
- [163] S. Tamari, "Optimum design of the constant-volume gas pycnometer for determining the volume of solid particles," *Meas. Sci. Technol.*, vol. 15, pp. 549-558, 2004.
- [164] S. Lowell, J. E. Shields, M. A. Thomas and M. Thommes, *Characterisation of Porous Solids and Powders: Surface Area, Pore Size and Density*, Springer, 2004.
- [165] L. F. Albright, *Albright's Chemical Engineering Handbook*, Taylor & Francis Group LLC, 2009.
- [166] B. Hu, A. W. Nienow, E. H. Stitt and A. W. Pacek, "Bubble size in agitated solvent/reactant mixtures used in heterogeneous catalytic hydrogenation of 2-butyne-1,4-diol," *Chemical Engineering Science*, vol. 61, pp. 6765-6774, 2006.
- [167] A. Fernandez-Neives, H. Wyss, J. Mattson and D. A. Weitz, *Microgel Suspensions: Fundamentals and Applications*, Wiley-VCH Verlag, 2011.
- [168] H. A. Barnes, "A review of the slip (wall depletion) of polymer solutions, emulsions and particulates suspensions in viscometers: its cause, character, and cure.," *Journal of non-Newtonian Fluid Mechanics*, vol. 56, pp. 221-251, 1995.
- [169] S. P. Meeker, R. T. Bonnecaze and M. Cloitre, "Slip and flow in pastes of soft particles: Direct observation and rheology," *Journal of Rheology*, vol. 48, pp. 1295-1320, 2004.
- [170] S. P. Meeker, R. T. Bonnecaze and M. Cloitre, "Slip and flow in soft particles pastes," *Physical Review Letters*, vol. 92, no. 19, p. 4, 2004.
- [171] H. Bianco and A. Marmur, "Gibbs elasticity of a soap bubble," *Journal of colloid and interface science*, vol. 158, pp. 295-302, 1993.
- [172] H. F. Xiong, Y. H. Zhang, S. G. Wang and J. L. Li, "Fischer-Tropsch synthesis: the effect of Al₂O₃ porosity on the performances of Co/Al₂O₃," *Catal. Commun.*, vol. 6, no. 8, pp. 512-516, 2005.

- [173] B. H. Davis, "Fischer-Tropsch synthesis: relationship between iron catalyst composition and process variables," *Catal. today*, vol. 84, no. 1-2, pp. 83-98, 2003.
- [174] "GGFR Partners Unlock Value of Wasted Gas," World Bank, 2009.
- [175] A. N. Stranges, "A history of the Fischer-Tropsch synthesis in Germany 1926-1945," in *Fischer Tropsch synthesis, catalyst and catalysis*, 2006, pp. 1-27.
- [176] M. E. Dry, "Sasol routes to fuels," *Chem. Tech.*, vol. 12, no. 12, pp. 744-750, 1982.
- [177] D. O. Uner, "A sensible mechanism of alkali promotion in Fischer-Tropsch synthesis: Adsorbate mobilities," *Ind. Eng. Chem. Res.*, vol. 37, no. 6, pp. 2239-2245, 1998.
- [178] B. H. Weil and J. L. Lane, *The technology of the Fischer-Tropsch process*, London: Constable & Co. LTD, 1949.
- [179] W. S. Ning, N. Koizumi, H. Chang, T. Mochizuki, T. Itoh and M. Yamada, "Phase transformation of unpromoted and promoted Fe catalysts and the formation of carbonaceous compounds during Fischer-Tropsch synthesis reaction," *Appl. Catal. A: Gen.*, vol. 312, pp. 35-44, 2006.
- [180] A. K. Dalai and B. H. Davis, "Fischer-Tropsch synthesis: A review of water effects on the performance of unsupported and supported Co catalysts," *Appl. Catal. A: Gen.*, vol. 348, no. 1, pp. 1-15, 2008.
- [181] M. E. Dry, "The Fischer-Tropsch process: 1950-2000," *Catal. Today*, vol. 71, no. 3-4, pp. 227-241, 2002.
- [182] P. L. Spath and D. C. Dayton, "Preliminary screening - Technical and economic assessment of synthesis gas to fuels and chemicals with emphasis on the potential for biomass derived syngas," National Renewable Energy Laboratory, Golden, 2003.
- [183] G. Henrici-Olive and S. Olive, *Angew. Chem. Int. Ed. Engl.*, vol. 15, p. 136, 1976.
- [184] G. P. van der Laan and A. A. C. M. Beenackers, "alpha-Olefin readsorption product distribution model for the gas-solid Fischer-Tropsch," *Stud. Surf. Sci. Catal.*, vol. 119, pp. 179-184, 1998.
- [185] M. E. Dry, *The Fischer-Tropsch synthesis*, New York: Springer-Verlag, 1981.
- [186] B. H. Davis, "Overview of reactors for liquid phase Fischer-Tropsch synthesis," *Catal. Today*, vol. 71, no. 3-4, pp. 249-300, 2002.
- [187] M. E. Dry, "Practical and theoretical aspects of the catalytic Fischer-Tropsch process," *Appl. Catal. A: Gen.*, vol. 138, no. 2, pp. 319-344, 1996.

- [188] S. T. Sie, "Process development and scale up: IV. Case history of the development of a Fischer-Tropsch synthesis process," *Rev. Chem. Eng.*, vol. 14, no. 2, pp. 109-157, 1998.
- [189] B. Jager, R. C. Kelfkens and A. P. Steynberg, *A slurry bed reactor for low temperature Fischer-Tropsch*, Elsevier Science, 1994.
- [190] F. Fischer and H. Tropsch, "The direct synthesis of petroleum hydrocarbons with standard pressure," *Brennst.-Chem.*, vol. 59, pp. 830-831, 1926.
- [191] S. R. Craxford and E. K. Rideal, "The mechanism of the synthesis of hydrocarbons from water gas," *J. Chem. Soc.*, pp. 1604-1614, 1939.
- [192] L. C. Browning and P. H. Emmett, "Equilibrium measurements in the Ni₃C-Ni-CH₄-H₂ and CO₂-Co-CH₄-H₂ systems," *J. Am. Chem. Soc.*, vol. 74, no. 7, pp. 1680-1682, 1952.
- [193] O. Evans and A. Nash, *Nature*, vol. 118, p. 1926, 1954.
- [194] E. de Smith and B. M. Weckhuysen, "The renaissance of iron-based Fischer-Tropsch synthesis: on the multifaceted catalyst deactivation behaviour," *Chem. Soc. Rev.*, vol. 37, no. 12, pp. 2758-2781, 2008.
- [195] J. T. Kummer and P. H. Emmett, "Fischer-Tropsch synthesis mechanism studies: the addition of radioactive alcohols to the synthesis gas," *J. Am. Chem. Soc.*, vol. 75, no. 21, pp. 5177-5183, 1953.
- [196] W. K. Hall, R. J. Kokes and P. H. Emmett, "Mechanism studies of the Fischer-Tropsch synthesis: the incorporation of radiocative ethylene, propionaldehyde and propanol," *J. Am. Chem. Soc.*, vol. 82, no. 5, pp. 1027-1037, 1960.
- [197] M. L. Turner, H. C. Long, A. Shenton, P. K. Byers and P. M. Maitlis, "The alkenyl mechanism for Fischer-Tropsch surface methylene polymerization: the reactions of vinylic probes with CO/H₂ over Rhodium catalysts," *Chem. Eur. J.*, vol. 1, no. 8, pp. 549-556, 1995.
- [198] S. B. Ndlovu, N. S. Phala, M. Hearshaw-Timme, P. Beagly, J. R. Moss, M. Claeys and E. van Steen, "Some evidence refuting the alkenyl mechanism for chain growth in iron-based Fischer-Tropsch," *Catal. Today*, vol. 71, no. 3-4, pp. 343-349, 2002.
- [199] W. Ngantsoue-Hoc, Y. Q. Zhang, R. G. O'Brien, M. S. Luo and B. H. Davies, "Fischer-Tropsch synthesis: activity and selectivity for group I alkali promoted iron-based catalysts," *Appl. Catal. A: Gen.*, vol. 236, no. 1-2, pp. 77-89, 2002.
- [200] D. B. Bukur, D. Mukesh and S. A. Patel, "Promoter effects on precipitated iron catalysts for Fischer-Tropsch synthesis," *Ind. Eng. Chem. Res.*, vol. 29, no. 2, pp. 194-204, 1990.
- [201] M. S. Luo, H. Hamdeh and B. H. Davis, "Fischer-Tropsch synthesis catalysts activation of low alpha iron catalyst," *Catal. Today*, vol. 140, no. 3-4, pp. 127-134, 2009.

- [202] A. Y. Khodakov, A. Griboval-Constant, R. Bechara and V. L. Zholobenko, "Pore size effects in Fischer-Tropsch synthesis over cobalt-supported mesoporous silicas," *J. Catal.*, vol. 206, no. 2, pp. 230-241, 2002.
- [203] D. Schanke, A. M. Hilmen, E. Bergene, K. Kinnari, E. Rytter, E. Adnanes and A. Holmen, "Reoxidation and deactivation of supported cobalt Fischer-Tropsch catalysts," *Energy and Fuels*, vol. 10, no. 4, pp. 867-872, 1996.
- [204] M. Kraum and M. Baerns, "Fischer-Tropsch synthesis: the influence of various cobalt compounds applied in the preparation of supported cobalt catalysts on their performance," *Appl. Catal. A: Gen.*, vol. 186, no. 1-2, pp. 189-200, 1999.
- [205] A. Barbier, A. Tuel, I. Arcon, A. Kodre and G. A. Martin, "Characterization and catalytic behaviour of Co/SiO₂ catalysts: Influence of dispersion in the Fischer-Tropsch reaction," *J. Catal.*, vol. 200, no. 1, pp. 106-116, 2001.
- [206] G. L. Bezemer, J. H. Bitter, H. P. C. E. Kuipers, H. Oosterbeek, J. E. Holewijn, X. D. Xu, F. Kapteijn, A. J. van Dillen and K. P. de Jong, "Cobalt particle size effects in the Fischer-Tropsch reaction with carbon nanofiber supported catalysts," *J. Am. Chem. Soc.*, vol. 128, no. 12, pp. 3956-3964, 2006.
- [207] O. Borg, P. D. C. Dietzel, A. I. Spjelkavik, E. Z. Tveten, J. C. Walmsley, S. Diplas, S. Eri, A. Holmen and E. Ryttera, "Fischer-Tropsch synthesis: Cobalt particle size and support effects on intrinsic activity and product distribution," *J. Catal.*, vol. 259, no. 2, pp. 161-164, 2008.
- [208] S. P. Rane, O. Borg, E. Rytter and A. Holmen, "Relation between hydrocarbons selectivity and cobalt particle size for alumina supported cobalt Fischer-tropsch catalysts," *Appl. Catal. A: Gen.*, vol. 437, pp. 10-17, 2012.
- [209] T. M. Eggenhuisen, P. Munnik, H. Talsma, P. E. de Jongh and K. P. de Jong, "Freeze-drying for controlled nanoparticle distribution in Co/SiO₂ Fischer-Tropsch catalysts," *J. Catal.*, vol. 297, pp. 306-313, 2013.
- [210] M. C. Marion and M. Roy, "Process for the conversion of synthesis gas in presence of a catalyst comprising a metal of group VIII, its particles being spread as aggregates". US Patent US6235798, 2000.
- [211] R. C. Reuel and C. H. Bartholomew, "Effects of support and dispersion on the CO hydrogenation activity selectivity properties of cobalt," *J. Catal.*, vol. 85, no. 1, pp. 78-88, 1984.
- [212] P. Souza Santos, H. Souza Santos and S. P. Toledo, "Standard transition aluminas. Electron microscopy studies," *Material Research*, vol. 3, no. 4, pp. 104-114, 2000.

- [213] E. Rytter, S. Eri, D. Schanke, H. Wigum, T. H. Skagseth, O. Borg and E. Bergene, "Development of an attrition resistant Fischer-Tropsch catalyst for slurry operation," *Top. Catal.*, vol. 54, no. 13-15, pp. 801-810, 2011.
- [214] E. Rytter, N. E. Tsakoumis and A. Holmen, "On the selectivity to higher hydrocarbons in Co-based Fischer-tropsch synthesis," *Catalysis Today*, vol. 261, pp. 3-16, 2016.
- [215] S. Rane, O. Borg, J. Yang, E. Rytter and A. Holmen, "Effect of alumina phases on hydrocarbon selectivity in Fischer-Tropsch synthesis," *Appl. Catal. A:Gen.*, vol. 388, no. 1-2, pp. 160-167, 2010.
- [216] E. Rytter, S. Eri, T. H. Skagseth, D. Schanke, E. Bergene, R. Myrstad and A. Lindvag, "Catalyst partacle size of cobalt/rhenium on porous alumina and the effect of Fischer-Tropsch catalytic performance," *Ind. Eng. Chem. Res.*, vol. 46, no. 26, pp. 9032-9036, 2007.
- [217] L. H. Shi, J. G. Chen, K. G. Fang and Y. H. Sun, "CH₃-modified Co/Ru/SiO₂ catalysts and the performances for Fisher-Tropsch synthesis," *Fuel*, vol. 87, no. 4-5, pp. 521-526, 2008.
- [218] E. A. Blekkan, O. Borg and A. Holmen, *Catal.: R. Soc. Chem.*, vol. 20, p. 13, 2007.
- [219] S. Logdberg, M. Boutonnet, J. C. Walmsley, S. Jaras, A. Holmen and E. A. Blekkan, "Effect of water on the space-time yield of different supported cobalt catalysts during Fischer-Tropsch synthesis," *Appl. Catal. A.: Gen.*, vol. 393, no. 1-2, pp. 109-121, 2011.
- [220] A. P. Steynberg, M. E. Dry, B. H. Davis and B. B. Breman, "Fischer-Tropsch reactors," *Fischer-Tropsch Technol.*, vol. 152, pp. 64-195, 2004.
- [221] E. Iglesia, S. C. Reyes, R. J. Madon and S. L. Soled, "Selectivity control and catalyst design in the Fischer-Tropsch synthesis-sites, pellets and reactors," *Adv. Catal.*, vol. 39, pp. 221-302, 1993.
- [222] D. E. Deugd, "Fischer-Tropsch synthesis revisited; efficiency and selectivity benefits from imposing temporal and/or spatial structure in the reactor," 2004.
- [223] W. H. Bragg and W. L. Bragg, "The reflexion of X-ray by crystals," *Proc. R. Soc. lond. A.*, vol. 88, no. 605, pp. 428-438, 1913.
- [224] A. Patterson, "The Scherrer formula for X-ray particle size determination," *Phys. Rev.*, vol. 56, no. 10, pp. 978-982, 1939.
- [225] A. K. Singh, *Advanced X-ray techniques in research and industries*, Ios Pr Inc, 2005.
- [226] Y. Waseda and K. S. Matsubara, *X-Ray diffraction crystallography: Introduction, examples and solved problems*, London ,New York: Springer Heidelberg Dordrecht, 2011.
- [227] F. Rouquerol, J. Rouquerol and K. Sing, *Adsorption by powders and porous solids: Principles, methodology and applications*, Milton Keynes: Academic Press, 1999.

- [228] M. F. Orellana, A. E. Nelson, J. R. P. Carey, G. Heo, D. G. Boychuk and P. W. Major, "Surface Analysis of Etched Molar Enamel by Gas Adsorption," *Journal of Dental Research*, vol. 87, no. 6, pp. 532-536, 2008.
- [229] K. S. W. Sing, D. H. Everett, R. A. W. Haul and L. Moscou, "Reporting physisorption data for gas/solid systems with special reference to surface area and porosity," *Pure and Applied Chemistry*, vol. 47, pp. 603-619, 1985.
- [230] S. Brunauer, P. H. Emmett and E. Teller, "Adsorption of gases in multimolecular layers," *J. Am. Chem. Soc.*, vol. 60, no. 2, pp. 309-319, 1938.
- [231] E. P. Barrett, L. G. Joyner and P. P. Halenda, "The Determination of Pore Volume and Area Distributions in Porous Substances. 1. Computations from Nitrogen Isotherms," *J. of Am. Chem. Soc.*, vol. 73, no. 1, pp. 373-380, 1951.
- [232] K. Sing, "The use of nitrogen adsorption for the characterisation of porous materials," *Colloids and Surfaces A: Physicochem. Eng. Aspects*, Vols. 187-188, pp. 3-9, 2001.
- [233] P. A. Webb, "introduction to chemical adsorption analytical techniques and their applications to catalysis," *MIC Technical Publications*, pp. 1-12, 2003.
- [234] G. Ertl, H. Knozinger and J. Weitkamp, *Handbook of heterogeneous catalysis*, WileyVCH, 1997.
- [235] V. Rakic and L. Damjanovic, "Temperature programmed Desorption methods," in *Calorimetry and Thermal Methods in Catalysis*, Springer-Verlag Berlin Heidelberg, 2013, pp. 131-174.
- [236] G. Herbert, "Mercury Porosimetry: A General (Practical) Overview," *Part. Part. Syst. Charact.*, vol. 23, pp. 9-19, 2006.
- [237] H. Giesche, "Mercury Porosimetry: A General (Practical) Overview," *Part. Part. Syst. Charact.*, vol. 23, pp. 9-19, 2006.
- [238] H. M. Rootare and C. F. Prezlow, "Surface Area from Mercury Porosimetry Measurements," *J. Phys. Chem.*, pp. 2733-2736, 1967.
- [239] "http://www.micromeritics.com/Repository/Files/Mercury_Porosemity_Theory_poster_.pdf," Micromeritics Instrument Corporation. [Online]. [Accessed 25 04 2017].
- [240] K. D. Vernon-Parry, "Scanning Electron Microscopy: an Introduction," *Analysis*, vol. 13, no. 4, pp. 40-44, 2000.
- [241] L. Reimer, *Scanning Electron Microscopy: Physics of Image Formation and Microanalysis*, Springer, 2013.

- [242] S. E. Forrester, C. D. Rielly and K. J. Carpenter, "Gas-inducing impeller design and performance characteristics," *Chemical Engineering Science*, 53, pp. 603-615, 1998.
- [243] J. X. Liu, P. Wang, W. Xu and E. J. M. Hensen, "Particle Size and Crystal Phase Effects in Fischer-Tropsch Catalysts," *Engineering*, vol. 3, pp. 467-476, 2017.
- [244] J. P. Den Breejen, P. B. Radstake, G. L. Bezemer, J. H. Bitter, V. Froseth and A. Holmen, "On the origin of the cobalt particle size effects in Fischer-Tropsch catalysis," *J Am Chem Soc*, vol. 131, no. 20, pp. 7197-7203, 2009.
- [245] E. Iglesia, "Design, synthesis, and use of cobalt-based Fischer-Tropsch synthesis catalysts," *Appl Catal A Gen*, vol. 161, no. 1-2, pp. 59-78, 1997.
- [246] Z. Wang, S. Skiles, F. Yang, Z. Yang and D. W. Goodman, "Particle size effects in Fischer-Tropsch synthesis by cobalt," *Catal Today*, vol. 181, no. 1, pp. 75-81, 2012.
- [247] G. Prieto, A. Martinez, P. Concepcion and R. Moreno-Tost, "Cobalt particle size effects in Fischer-Tropsch synthesis: Structural and in-situ spectroscopy characterisation on reverse micelle-synthesised Co/ITQ-2 model catalysts," *J Catal*, vol. 26, no. 6, pp. 129-144, 2009.
- [248] H. Li, J. Wang, C. Chen, L. Jia, B. Hou and D. Li, "Effects of macropores on reducing internal diffusion limitations in Fischer-Tropsch synthesis using a hierarchical cobalt catalyst," *RSC Adv.*, vol. 7, p. 9436, 2017.
- [249] H. Schulz, Z. Q. Nie and F. Ousmanov, "Construction of the Fischer-Tropsch regime with cobalt catalysts," *Catal. Today*, vol. 71, no. 3-4, pp. 351-360, 2002.
- [250] S. Logdberg, M. Lualdi, S. Jaras, J. C. Walmsley, E. A. Blekkan, E. Rytter and A. Holmen, "On the selectivity of cobalt-based Fischer-Tropsch catalysts: Evidence for a common precursor for the methane and long-chain hydrocarbons," *J. Catal.*, vol. 274, no. 1, pp. 84-98, 2010.
- [251] E. W. Thiele, "Relation between catalytic activity and size of particle," *Industrial and Engineering Chemistry*, vol. 31, pp. 916-920, 1939.
- [252] P. B. Weisz and C. D. Prater, "Interpretation of Measurements in Experimental Catalysis," *Advances in Catalysis*, vol. 6, p. 143, 1954.
- [253] A. Celani and E. M. Holt, "Method for preparing particle-stabilized foams comprising amino acids". Patent WO 2016/156790 A1, 15 March 2016.
- [254] A. Celani, L. H. Davies, E. M. Holt and G. J. Kelly, "Catalyst precursor, method of preparation and use thereof". Patent WO 2016/156789 A1, 15 March 2016.
- [255] "Clean Alternative Fuels: Compressed Natural Gas," U.S. Environmental Protection Agency report, 2012.

- [256] P. Gelin and M. Primet, "Complete Oxidation of Methane at Low Temperature Over Noble Metal Based Catalysts: a Review," *Appl. Catal. B*, vol. 1, p. B39, 2002.
- [257] T. V. Choudhary, S. Banerjee and V. R. Choudhary, "Catalysts for Combustion of Methane and lower Alkanes," *Appl. Catal. A*, vol. 234, no. 1, 2002.
- [258] K. Ling and G. Wang, "Methane Combustion on Pd-based Model Catalysts: Structure Sensitive or Insensitive?," *J. Chem. Phys.*, vol. 131, 2009.
- [259] J. Han, D. Y. Zemlyanov and F. H. Ribeiro, "Catalytic Combustion of Methane on Palladium Single Crystals," *Catal. today*, vol. 117, no. 537, 2006.
- [260] D. Ciuparu, M. R. Lyubovsky, E. Altman, L. D. Pfefferle and A. Datye, "Catalytic Combustion of Methane over Palladium-based Catalysts," *catal. Rev.*, vol. 44, p. 593, 2002.
- [261] T. W. Hansen, A. T. De la Riva, S. R. Challa and A. K. Datye, "Sintering of Catalytic Nanoparticles: Particle Migration or Ostwald Ripening?," *Acc. Chem. Res.*, vol. 46, p. 1720, 2013.
- [262] R. F. Hicks, H. Qi, M. L. Young and R. G. Lee, "Structure Sensitivity of Methane Oxidation over Platinum and Palladium," *J. Catal.*, vol. 122, p. 280, 1990.
- [263] R. G. Shahrestani, PhD Thesis, Kinetic and Deactivation Studies of Methane Oxidation over Palladium Catalysts, Vancouver, Canada, 2015.
- [264] G. Zhu, J. Han, D. Y. Zemlyanov and F. H. Ribeiro, "The Turnover Rate for the Catalytic Combustion of Methane Over Palladium is not Sensitive to the Structure of the Catalyst," *J. Am. Chem. Soc.*, vol. 126, p. 9896, 2004.
- [265] F. H. Ribeiro, M. Chow and R. A. Dallabetta, "Kinetics of the Complete Oxidation of Methane Over Supported Palladium Catalysts," *J. Catal.*, vol. 146, p. 537, 1994.
- [266] P. Araya, S. Guerrero, J. Robertson and F. J. Gracia, "Methane Combustion over Pd/SiO₂ Catalysts with Different Degrees of Hydrophobicity," *Appl. Catal. A*, vol. 283, p. 225, 2005.
- [267] K. Fujimoto, F. H. Ribeiro, M. Avalos-Borja and E. Iglesia, "Structure and Reactivity of PdO_x/ZrO₂ Catalysts for methane Oxidation at Low Temperature," *J. Catal.*, vol. 179, p. 431, 1998.
- [268] R. Kikuchi, S. Maeda, K. Sasaki, S. Wennerstrom and K. Eguchi, "Low-Temperature Methane Oxidation over Oxide-Supported Pd Catalysts: Inhibitory Effect of Water Vapour," *Appl. Catal. A*, vol. 232, p. 23, 2002.
- [269] R. Abbasi, L. Wu, S. E. Wanke and R. E. Hayes, "kinetics of Methane Combustion over Pt and Pt-Pd Catalysts," *Chem. Eng. Res. Design*, vol. 90, pp. 1930-1942, 2012.

- [270] P. Hurtado, S. Ordonez, H. Sastre and F. V. Diez, "Development of a kinetic Model for the Oxidation of Methane over Pd/Al₂O₃ at Dry and Wet Conditions," *Appl. Catal. B*, vol. 51, p. 229, 2004.
- [271] J. N. Sherwood, A. V. Chadwick, W. M. Muir and F. L. Swinton, *Diffusion Processes*, Thomas Graham Symposium, London: Gordon and Breach, 1971.
- [272] A. Fick, "On liquid diffusion (reprinted)," *Journal of Membrane Science*, vol. 100, pp. 22-38, (1855) 1995.
- [273] J. C. Maxwell, "On the Dynamic Theory of Gases," *The Scientific Paper of J.C. Maxwell*, vol. 2, pp. 26-78, 1965.
- [274] J. Stefan, "Über das Gleichgewicht und Bewegung, insbesondere die Diffusion von Gemischen," *Sitzungsberichte der Kaiserlichen Akademie der Wissenschaften Wien*, vol. 63, pp. 63-124, 1871.
- [275] E. Leonardi and C. Angeli, "On the Maxwell-Stefan Approach to Diffusion: A General Resolution in the Transient Regime for One-Dimensional Systems," *J. Phys. Chem. B*, vol. 114, pp. 151-164, 2010.
- [276] R. B. Bird, W. E. Stewart and E. N. Lightfoot, *Transport Phenomena*, Wiley, 2007.
- [277] H. C. No, H. S. Lim, J. Kim, C. Oh, L. Siefken and C. Davis, "multi-component diffusion analysis and assessment of GAMMA code and improved RELAP5 code," *Nucl. Eng. Des.*, vol. 237, no. 10, pp. 997-1008, 2007.
- [278] T. E. Magin and G. Degrez, "Transport algorithms for partially and unmagnetized plasmas," *J. Comput. Phys.*, vol. 198, no. 2, pp. 424-449, 2004.
- [279] S. Chapman and T. G. Cowling, *The Mathematical Theory of Non-Uniform Gases*, Cambridge: Cambridge University Press, 1970.
- [280] E. A. Mason and A. P. Malinauskas, *Gas transport in Porous Media: The Dusty-Gas Model*, New York: Elsevier, 1983.
- [281] E. N. Fuller, P. D. Schettler and J. C. Giddings, "A New Method for Prediction of Binary Gas-Phase Diffusion Coefficients," *Industrial and Engineering Chemistry*, vol. 58, no. 5, pp. 18-27, 1966.
- [282] S. Jennings, "The Mean Free Path in Air," *Journal of Aerosol Science*, vol. 19, no. 2, p. 159, 1988.
- [283] W. G. Pollard and R. D. Present, "On Gaseous Self-Diffusion in Long Capillary Tubes," *Phys. rev.*, vol. 73, no. 7, pp. 762-774, 1948.
- [284] N. Wakao and J. M. Smith, "Diffusion in Catalysts Pellets," *Chem. Eng. Sc.*, vol. 17, pp. 825-834, 1962.

- [285] B. H. West, S. P. Huff, J. E. Parks, S. A. Lewis, J. S. Choi, W. P. Partridge and J. M. Storey, "SAE Technical Paper," Vols. 2004-01, p. 3023, 2004.
- [286] W. P. Partridge, J. M. E. Storey, S. A. Lewis, R. W. Smithwick, G. L. DeVault, M. J. Cunningham, N. W. Currier and T. M. Yonushonis, "SAE Technical Paper," Vols. 2000-01, p. 2952, 2000.
- [287] J. Sa, D. L. A. Fernandes, F. Aiouache, A. Goguet, C. Hardacre, D. Lundie, W. Naeem, W. P. Partridge and C. Stere, "SpaciMS: spatial and temperature operando resolution of reactions within catalytic monoliths," *Analyst*, vol. 135, pp. 2260-2272, 2010.
- [288] W. P. Partridge, J. M. E. Storey, S. A. Lewis, R. W. Smithwick, G. L. DeVault, M. J. Cunningham, N. V. Currier and T. M. Yonushonis, *SAE Int. J. Fuels Lubr.*, vol. 109, p. 2992, 2000.
- [289] B. H. West, S. P. Huff, J. E. Parks, S. A. Lewis, J. S. Choi, W. P. Partridge and J. M. Storey, *SAE Int. J. Fuels Lubr.*, vol. 4, p. 1975, 2004.
- [290] J. Parks, S. Huff, J. A. Pihl, J. S. Choi and B. West, *SAE [Tech. Pap.]*, p. 3876, 2005.
- [291] J. S. Choi, W. P. Partridge and C. S. Daw, "Spatially resolved in situ measurements of transient species breakthrough during cyclic, low-temperature regeneration of a monolithic Pt/K/Al₂O₃NO_x storage-reduction catalyst," *Appl. Catal. A*, vol. 293, pp. 24-40, 2005.
- [292] J. S. Choi, W. P. Partridge, W. S. Epling, N. W. Currier and T. M. Yonushonis, "Intra-channel evolution of carbon monoxide and its implication on the regeneration of a monolithic Pt/K/Al₂O₃ NO_x storage-reduction catalyst," *Catal. Today*, vol. 114, no. 1, pp. 102-111, 2006.
- [293] J. S. Choi, W. P. Partridge and C. S. Daw, "Sulfur impact on NO_x storage, oxygen storage, and ammonia breakthrough during cyclic lean/rich operation of a commercial lean NO_x trap," *Appl. Catal. B*, vol. 77, no. 1-2, pp. 145-156, 2007.
- [294] M. Sharma and M. Dearth, "Effective Diffusivity Measurement on a Monolithic Reactor using SPACI-MS Technique," *Applied Catalysis B: Environmental*, vol. 188, pp. 177-188, 2016.
- [295] J. Chen, H. Yang, N. Wang, Z. Ring and T. Dabros, "Mathematical modeling of monolith catalysts and reactors for gas phase reactions," *Appl. Catal. A*, vol. 345, pp. 1-11, 2008.
- [296] M. Maestri, E. Tronconi, R. L. Berger, F. Kapteijn and J. A. Moulijn, "Monolithic reactors," Eurokin Consortium internal report, 2014.
- [297] G. T. Huntington and A. V. Rao, "A Comparison between Global and Local Orthogonal Collocation Methods for Solving Optimal Control Problems," *Proceedings of the 2007 American Control Conference*, pp. 1950-1957, 2007.
- [298] R. H. Perry and D. W. Green, *Perry's Chemical Engineers' Handbook* 8th edition, McGraw-Hill, 2007.

- [299] J. G. Xu and G. F. Froment, "Methane Steam Reforming .2. Diffusionla Limitations and Reactor Simulation," *AIChE Journal*, vol. 35, no. 1, pp. 97-103, 1989.
- [300] T. Salmi and J. Warna, "Modelling of Catalytic Packed-Bed Reactors: Comparison of Different Diffusion-Models," *Computers & Chemical Engineering*, vol. 15, no. 10, pp. 715-727, 1991.
- [301] A. G. Dixon, M. E. Taskin, E. H. Stitt and M. Nijemeisland, "3D CFD simulations of steam reforming with resolved intraparticle reaction and gradients," *CHemical Engineering Science*, vol. 62, pp. 4963-4966, 2007.
- [302] P. Canu and S. Vecchi, "CFD Simulation of Reactive Flows: Catalytic Combustion in a Monolith," *AIChE Journal*, vol. 48, no. 12, pp. 2921-2935, 2002.
- [303] S. Mazumder and D. Sengupta, "Sub-Grid Scale Modelling of Heterogeneous CHemical Reactions and Transport in FULL-Scale Catalytic Converters," *Combustion and Flame*, vol. 131, pp. 85-97, 2002.
- [304] A. Kumar and S. Mazumder, "Assessment of various diffusion models for the prediction of heterogeneous combustion in monolith tubes," *Computers and Chemical Engineering*, vol. 32, pp. 1482-1493, 2008.
- [305] T. Maffei, S. Rebughini, G. Gentile, S. Lipp, A. Cuoci and M. Maestri, "CFD Analysis of the Channel Shape Effect in Monolith Catalysts for the CH₄ Partial Oxidation on Rh," *Chem. Ing. Tech.*, vol. 86, no. 7, pp. 1099-1106, 2014.
- [306] F. Sadeghi, B. Tirandazi, A. Khalili-Garakani, S. Masseri, R. N. Nodehi and N. Mostoufi, "Investigating the effect of channel geometry on selective catalytic reduction of NO_x in monolith reactors," *Chemical Engineering Research and Design*, vol. 118, pp. 21-30, 2017.
- [307] M. H. Allouche, R. Enjalbert, F. Alberini, M. Ariane, A. Alexiadis, S. Wilkinson and L. Liu, "Development of a combined solver to model transport and chemical reactions in catalytic wall-flow filters," *Chemical Engineering Research and Design*, vol. 117, pp. 681-687, 2017.
- [308] J. Bode, "Applications of Computational Fluid-Dynamic in the Chemical Industry," *Chem. Eng. Technol.*, vol. 17, no. 3, pp. 145-148, 1994.
- [309] V. M. Janardhanan and O. Deutschmann, "Computational Fluid Dynamic of Catalytic Reactors," in *Modelling of Heterogeneous Catalytic Reactions: From the molecular process to the technical system*, Weinheim, Germany, Wiley-VCH & Co. KGaA, 2012.
- [310] Y. Bapat, "User Guide for Reactions: Johnson Matthey Internal Report," Tridiagonal Solutions, 2016.
- [311] A. Shewchuk, "An Introduction to the Conjugate Gradient Method without the Agonizing Pain," School of Computer Science, Carnegie Mellon Univeristy, Pittsburgh, 1994.

- [312] C. Greenshields, "OpenFOAM 2.0.0: Steady-State VoF," The OpenFOAM Foundation Ltd, 16th June 2011. [Online]. Available: <https://openfoam.org/release/2-0-0/steady-state-vof/>. [Accessed 27 August 2018].
- [313] J. Espach, "Pore structure modelling: Methane oxidation kinetic," Johnson Matthey Internal Report, 2017.
- [314] F. Duprat, "Light-off curve of catalytic reaction kinetics," *Chemical Engineering Science*, vol. 57, pp. 901-911, 2002.
- [315] P. Koci, V. Novak, F. Stepanek, M. Marek and M. Kubicek, "Multi-scale modelling of reaction and transport in porous catalysts," *Chemical Engineering Science*, vol. 65, pp. 412-419, 2010.
- [316] Y. Dong, F. J. Keil, O. Korup, F. Rosowski and R. Horn, "Effect of the catalyst pore structure on fixed-bed reactor performance of partial oxidation of n-butane: A simulation study," *Chemical Engineering Science*, vol. 142, pp. 299-309, 2016.
- [317] A. G. Dixon, "Correlations for Wall and Particle-Shape Effects on Fixed Bed Bulk Voidage," *Can. J. Chem. Eng.*, vol. 66, no. 5, pp. 705-708, 1988.
- [318] L. K. McCune and R. H. Wilhelm, "Mass and Momentum Transfer in Solid-Liquid System-Fixed and Fluidized Beds," *Ind. Eng. Chem.*, vol. 41, no. 6, pp. 1124-1134, 1949.
- [319] R. Pfeffer, "Heat and Mass Transport in Multiparticle Systems," *Ind. Eng. Chem. Fund.*, vol. 3, no. 4, p. 380, 1964.
- [320] V. Novak, P. Koci, M. Marek, F. Stepanek, P. Blanco-Garcia and G. Jones, "Multi-scale modelling and measurements of diffusion through porous catalytic coatings: An application to exhaust gas oxidation," *Catalysis Today*, vol. 188, pp. 62-69, 2012.
- [321] M. Dudak, V. Novak, P. Koci, M. Marek, P. Blanco-Garcia and G. Jones, "Prediction of Diffusivity and Conversion of n-decane and CO in Coated Pt/-Al₂O₃ Catalyst Depending on porous Layer Morphology," *Applied Catalysis B: Environmental*, Vols. 150-151, pp. 446-458, 2014.
- [322] "AGMG website," [Online]. Available: <http://agmg.eu/>. [Accessed 2018 08 29].
- [323] Y. Notay, "An Aggregation-Based Algebraic Multigrid Method," *Electronic Transactions and Numerical Analysis*, vol. 37, pp. 123-146, 2010.
- [324] J. E. Etheridge and T. C. Watling, "Is reactor light-off data sufficiently discriminating between kinetic parameters to be used for developing kinetic models of automotive exhaust aftertreatment catalysts? The effect of hysteresis induced by strong self inhibition," *Chemical Engineering Journal*, vol. 264, pp. 376-388, 2015.
- [325] O. Levenspiel, *Chemical Reaction Engineering*, John Wiley & Sons, 1999.

- [326] A. Celani, S. Blackburn, M. J. Simmons, L. M. Holt and E. H. Stitt, "Formulation of ceramic foams: a new class of amphiphiles," *Colloids and Surface A*, vol. 536, pp. 104-112, 2018.
- [327] A. Celani and E. M. Holt, "Method for preparing particle-stabilized foams comprising amino acids". Patent WO 2016/156790, 6 October 2016.
- [328] A. Celani, S. Blackburn, M. J. H. Simmons and E. H. Stitt, "Effect of mixing conditions on the wet preparation of ceramic foams," *Chemical Engineering Research and Design*, vol. 34, no. 1, pp. 1-14, 2018.
- [329] A. Celani, L. H. Davies, E. M. Holt and G. J. Kelly, "Catalyst precursor, method of preparation and use thereof". Patent WO 2016/156789, 6 October 2016.
- [330] A. Buffo and V. Alopaeus, "Experimental determination of size distribution: analyzing proper sample size," *Meas. Sci. Technol.*, vol. 27, pp. 1-6, 2016.

Appendix I

Comparison between foam porosity values obtained by water pick-up and Mercury Intrusion Porosimetry

The porosity of two foams having different structures was determined and compared by water pick-up and Mercury Intrusion Porosimetry. The water pick up and MIP methodologies have already been described; the calculations used to determine the porosity in the two methods are reported below:

- **Water Pick-Up**

The amount of water picked up is obtained by difference between the weight of the wet sample and the initial weight of the dry sample; then the volume of water picked up is calculated by dividing the mass of water by its density. The pore volume of the sample is obtained by dividing the volume of water picked up by the initial sample weight; finally, foam porosity is calculated by:

$$Porosity \% = \frac{V_{H_2O}}{V_{H_2O} + \frac{W_0}{\rho_s}} * 100$$

where V_{H_2O} is the volume of water picked up, W_0 is the initial weight of the sample and ρ_s is the solid density.

- **Mercury Porosimetry**

The porosity of the sample was determined by mercury porosimetry using the following formula:

$$Porosity \% = \frac{W_s * I_{tot}}{V_{por} + \frac{W_s}{\rho_{sk}}}$$

where W_s is the sample weight, I_{tot} is the total intrusion, V_{por} is the pore volume and ρ_{sk} is the skeletal density of the solid sample.

Table I.1 summarises the porosities calculated, using the two different techniques, for two different samples and the percentage error between them.

Table I.1 Comparison between sample porosity obtained by water pick-up and mercury porosimetry.

Sample #	Porosity % Water Pick-Up	Porosity % Mercury Intrusion Porosimetry	% Error
1	83.42	77.41	7.20
2	96.71	95.56	1.19

Table I.1 shows that the water pick-up method gives comparable results to those obtained by mercury intrusion porosimetry. Water pick-up tends to over-estimate the sample porosity, especially for lower porosity samples, but considering the small percentage error and the time saving in using this technique instead of MIP it is convenient to use this technique when a large number of sample has to be analysed.

Appendix II

Confidence Interval of Mean Bubble Size Determined by Image Analysis

The confidence interval of bubble size determined by image analysis was determined following the procedure proposed by *Buffo and Alopaeus* [330]. Considering that the result of the bubble size measurement is an array of N values of particle size, $\mathbf{L} = \{L_1, L_2, \dots, L_N\}$ the mean value of this sample is equal to:

$$\bar{L} = \frac{1}{N} \sum_{i=1}^N L_i$$

while the variance of the sample is defined as:

$$S^2 = \frac{1}{N-1} \sum_{i=1}^N (L_i - \bar{L})^2$$

Mean and standard deviation could also be written as a function of the sample raw moment M_k which is defined as:

$$M_k = \sum_{i=1}^N L_i^k$$

with $k = 0, 1, 2, \dots, N_k$. Mean and standard deviation expressed as function of the sample raw momentum are reported below:

$$\bar{L} = \frac{M_1}{M_0}$$

$$S^2 = \frac{M_0 M_2 - M_1^2}{M_0(M_0 - 1)}$$

The confidence interval can then be calculated using the following equation:

$$\Delta \bar{L} = 2t_{N-1, \alpha/2} \frac{S}{\sqrt{N}}$$

Table II.1 summarises the mean and the confidence interval for the bubble size of the foam produced during the DoE study described in Chapter 3. It has to be borne in mind that the mean value reported in this Appendix is different from the Sauter mean diameter presented in the chapter; the latter is commonly used to correlate bubble size to different process parameters and for this reason it was selected. Here an estimation of the error encountered in the image analysis is desired and the arithmetic mean is used for this study. The table shows the experiment number, the number of the bubbles analysed, mean, standard deviation and confidence interval for the different foams. A 90% confidence level was selected to determine the confidence interval.

Table II.1 Summary of number of bubbles analysed, mean, standard deviation, t-student value and confidence interval for the foams produced in the DoE experiment reported in Chapter 2

Exp #	# of Bubbles	Mean	Standard Deviation	t_{N-1, α/2}	Confidence Interval
1	65	265.19	239.56	1.6706	99.28
2	54	77.75	112.12	1.6759	51.14
3	75	91.78	54.54	1.6669	20.99
4	123	172.45	143.76	1.6602	43.04
5	100	235.70	240.57	1.6602	79.88
6	80	66.65	51.97	1.6641	19.34
7	90	174.36	242.24	1.6620	53.23
8	126	218.81	194.51	1.6551	57.36
9	86	89.29	63.58	1.6620	22.79
10	129	263.13	269.48	1.6602	78.77
11	76	154.07	103.73	1.6641	39.60
12	97	125.67	86.00	1.6602	18.09
13	120	88.02	79.48	1.6602	15.03
14	103	120.65	110.11	1.6602	36.02
15	105	91.96	104.65	1.6602	33.91
16	66	288.45	344.20	1.6669	141.24

It can be noted that the confidence interval is quite wide especially for the samples where a lower number of bubbles were analysed; this, as said in Chapter 3, was due to the limited amount of sample available.

Appendix III

Publications and Presentations

Publications

Colloids and Surfaces A 536 (2018) 104–112



Contents lists available at ScienceDirect

Colloids and Surfaces A

journal homepage: www.elsevier.com/locate/colsurfa



Formulation of Ceramic Foams: a New Class of Amphiphiles

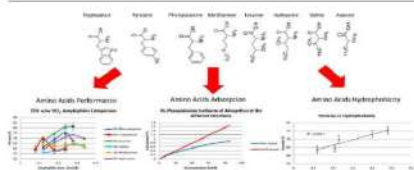
Andrea Celani^{a,b,*}, Stuart Blackburn^a, Mark J. Simmons^a, Liz M. Holt^b, E. Hugh Stitt^b

^a School of Chemical Engineering, University of Birmingham, B15 2TT, United Kingdom

^b Johnson Matthey Technology Centre, Billingham, TS23 1LB, United Kingdom



GRAPHICAL ABSTRACT



ARTICLE INFO

Keywords:

Ceramic Foams
Amino Acids
Hydrophobicity
Isotherm of Adsorption

ABSTRACT

In this work, amino acids are proposed and assessed as a new class of amphiphiles that is more environmentally benign and present a wider operational window than those reported in the literature. The effects of the amphiphile concentration and structure on the foam properties were investigated (e.g. porosity, bubble size distribution). These were classified depending on their different hydrophobicity by establishing a hydrophobicity index. Monotonic relationships between the hydrophobicity index and the foam structural properties (e.g. porosity, bubble size) were found. In addition, the more suitable amino acid to be used at larger scales was identified and it was used as a model amphiphile to have a deeper insight into the foaming process. In particular, the repartition of the amino acids among the different interfaces and the minimum amphiphile concentration to obtain stable foams were identified.

1. Introduction

In recent years ceramic foams have been receiving an increasing interest thanks to their applicability in several technology fields. Among others, ceramic porous materials are used as refractory insulators, catalyst supports and filters for molten metals [1,2]. Several techniques have been developed for the production of ceramic foams; these include replica technique, sacrificial templating and direct foaming [3]. The replica technique consists in the impregnation of a natural (e.g. wood [4], coral [5]) or a synthetic template (e.g. polymer foam [6]) with a ceramic suspension. In order to obtain a thin ceramic coating on the template surface, the suspension in excess is removed by passing the template through rollers. After drying and calcination a

ceramic positive replica of the template is obtained. Sacrificial templating uses a biphasic mixture of a template and ceramic slurry to generate the porous structure inside the ceramic body. The sacrificial material can be natural [7] or synthetic [8] and either in solid [9] or liquid form [10]. These are then either extracted or decomposed to form a negative replica of the sacrificial template in the ceramic material. Direct foaming is an ostensibly straightforward method for the production of ceramic foams. In this process, air is directly entrained into the ceramic suspension causing the attachment of the previously modified particles at the air/water interface, leading to stable foams [11]. Particles surface properties are modified in order to reduce their hydrophilicity. This is realized through the addition of an amphiphile; namely a chemical that has a polar head which electrostatically

* Corresponding author at: School of Chemical Engineering, University of Birmingham, B15 2TT, United Kingdom.
E-mail address: andrea.celani@matthey.com (A. Celani).

<http://dx.doi.org/10.1016/j.colsurfa.2017.07.031>

Received 29 September 2016; Received in revised form 16 June 2017; Accepted 8 July 2017

Available online 11 July 2017

0927-7757/ © 2017 The Authors. Published by Elsevier B.V. This is an open access article under the CC BY license (<http://creativecommons.org/licenses/by/4.0/>).

interacts with the particles surface and a hydrophobic tail that is directed toward the aqueous phase. Several classes of chemicals have been proposed as amphiphiles, these include among others carboxylic acids, amines and gallates [11]. The selection of the suitable amphiphile is largely governed by the particle's surface charge where carboxylic acids are used with positively charged particles, amines with negatively charged particles and gallates with either positively charged or neutral particles. It has been demonstrated that both the structural characteristics of the amphiphile and its concentration strongly affect foam properties such as porosity, stability and bubble size distribution [12,13].

Although the use of the previously mentioned amphiphiles is widely reported in the literature, the use of these amphiphiles is limited to a certain pH range dictated by the particle surface charge. In addition, many of these amphiphiles present acute toxicity limiting their usage at production scale. The aim of this work is to investigate the possibility of using amino acids as amphiphiles. Amino acids are organic compounds containing an amine group ($-\text{NH}_2$), a carboxylic group ($-\text{COOH}$) and a side chain specific to each amino acid. There are about 500 natural occurring amino acids [14]; these can be classified according to the position of the functional groups in α - (alpha), β - (beta), γ - (gamma) or δ - (delta). In this work attention was posed on the α - amino acids; in these molecules the carboxylic and the amino groups are attached to the first carbon or α - (alpha) carbon. The selection of this class of amino acids was based on their lower cost relative to hydrophobic β -, γ - and δ -amino acids making them more economically suitable for the scale up of the process in the future. This class of molecules is environmentally friendly and allows a wider pH operational window courtesy of the presence of both the carboxylic and the amino group on the same molecule. In the present study the amino acids are classified according to their different hydrophobicity. This is then shown to influence both the porosity and the bubble size distribution of the obtained foams. Among the tested amino acids the best amphiphile in term of operability is identified; then its adsorption at the different interfaces and the minimum amphiphile concentration necessary to obtain stable foams is identified.

2. Materials and Methods

2.1. Materials

Fumed TiO_2 particles (grade AEROXIDE P25) were obtained from Evonik Industries (Essen, Germany). The supplier technical data sheet states that the primary particles have a mean diameter of approximately 21 nm while their aggregates are several hundred nm in size. Density and surface area are 4 g/cm^3 and $50 \text{ m}^2/\text{g}$ respectively. The AEROXIDE P25 is characterised by an anatase/rutile ratio of 80/20 with both crystal structures having a tetragonal geometry.

The amino acids used to modify the particles surface were DL-Alanine 99%, DL-Valine 99%, DL-Isoleucine 99%, DL-Leucine 99%, DL-Methionine 99%, DL-Phenylalanine 99%, DL-Tyrosine 98% and DL-Tryptophan 99% (Alfa Aesar, Heysham, United Kingdom). Other chemical used in the experiments were demineralised water, nitric acid 70% v/v (Alfa Aesar, Heysham, United Kingdom) and potassium hydroxide solution 40% v/v prepared by dissolving potassium hydroxide pellets (Alfa Aesar, Heysham, United Kingdom) in demineralised water.

2.2. Suspension Preparation

Titania suspensions were prepared by stepwise addition of the powder to deionised water continuously stirred using an IKA EUROSTAR power control-visc overhead mixer. The pH of all suspensions was adjusted to electrostatically stabilise the particles. Titania particles are stable at pH either below 4 or above 7. To favour the dissolution of amino acids the pH was kept either below 2 or above 10 through the addition of small aliquots of 70% v/v HNO_3 and 40% v/v

KOH respectively. The solid loading of titania suspensions was set to 25% w/w. In a typical formulation, carried out at acid pH, 99.7 g of titania was added to 250 ml of demineralised water containing 50 ml of 5% v/v HNO_3 . After powder dispersion the suspension pH was dropped below 2 through the addition of 5 ml of 70% v/v HNO_3 . Then an amino acid was added to the titania suspension to obtain the required concentration in the range 0.08 and 0.36 mol/L.

2.3. Foaming and Foam Characterisation

Foaming of 300 mL suspension was carried out using an overhead stirrer equipped with a gas inducing impeller [15]. The vessel diameter and impeller diameter were $T = 12 \text{ cm}$ and $D = 6 \text{ cm}$ respectively ($D/T = 50\%$). The vessel was fitted with 4 baffles 1 cm wide ($B/T = 8.3\%$). Mixing was carried out at 2000 rpm for 20 minutes. The foam was dried under ambient conditions and then calcined in a Carbolite Furnace CWF at 600°C for 4 hours. During the ramping step and for the first 45 minutes the furnace was purged under N_2 followed by air. The heating rate was $2^\circ\text{C}/\text{min}$.

The porosity of the calcined foam was initially evaluated by both mercury intrusion porosimetry and water pick-up. The average difference between the two techniques was 4% so the quicker water pick-up experiment was used for further analysis; for this reason, only the porosity values determined by water pick-up are reported herein. In this technique, the initial weight of four foam samples was recorded then these were immersed in water and the weight of the wetted samples was recorded over a four days period. The average amount of water picked up was determined by difference between the weight of the wet foam and the initial weight. From this value the foam porosity and pore volume were calculated.

Foam bubble size distribution was determined by acquiring optical microscope (Nikon Eclipse E200) images of the foam cross section. Bubble's diameters were obtained by analysing the acquired images with Fiji ImageJ 1.50a (Wayne Rasband, National Institute of Health, USA) [16]. The obtained diameters were corrected by dividing them by 0.79 in order to take into account the random position of the bubbles during sample sectioning. The correction factor was determined by Williams et al.; they identified that the mean pore diameter determined from 2D images is 79% of the actual pore diameter. This factor was derived from numerical methods that they developed and described in order to correct the underestimated pore size obtained from 2-D cross section [17].

2.4. SS-NMR

Titania suspensions having pH of 1, 4 and 10 were prepared using the procedure described in Section 2.2. Titania particles were modified by the addition of 0.2 mol/L of DL-Phenylalanine. The suspensions were dried at ambient condition and then ground using mortar and pestle. The SS-NMR spectrum was acquired at a static magnetic field strength of 9.4 T ($\nu_0(^1\text{H}) = 400.16 \text{ MHz}$) on a Bruker Avance III console using a widebore Bruker 4 mm BB/1H WVT MAS probe and TopSpin 3.1 software. For ^{13}C , the probe was turned to 100.63 MHz and the spectrum referenced to the alanine CH_3 signal at 20.5 ppm. The powdered sample was packed into a zirconia MAS rotor with a Kel-F cap, with weighing before and after packing to obtain the sample mass. The rotor was spun using room-temperature purified compressed air. The total experiment time to acquire the spectrum was 18 hours. The spectrum was acquired using the cross polarisation (CP) method, in which magnetisation on ^1H nuclei is transferred to nearby ^{13}C nuclei via the dipolar coupling. Magnetisation was transferred in a contact time of 1 ms. High power (100 W) SPINAL-64 decoupling was applied to the ^1H channel during acquisition.

2.5. Surface Tension Measurements

The surface tension of both suspensions and amino acid solutions was measured using the pendant drop method (Krüss Drop Shape Analyser, Hamburg, Germany). In this method, a drop of the solution under analysis is suspended from a needle. The shape of the drop results from the relationship between the surface tension and gravity. Using the drop shape analysis software, the solution surface tension can be determined using the following formula [18] (Eq. (1)):

$$\gamma = \frac{\Delta \rho g R^2}{\beta} \quad (1)$$

where γ is the surface tension in mN/m, $\Delta \rho$ is the density difference between the two phases in kg/m³, g is the gravitational acceleration (9.81 m/s²), R is the maximum drop radius (m) and β is the shape factor. Suspensions were prepared using the procedure mentioned in Section 2.2 while amino acid solutions were prepared dissolving different amount of amino acids in 45 ml of demineralised water containing 5 ml of 70% v/v of HNO₃. The drop volumes were in the range 20 μ L–25 μ L, depending on the surface tension of the sample. At least 5 drops for each sample were analysed in order to obtain an average value of the surface tension.

2.6. Suspension Filtration and Supernatant UV–Vis Analysis

To determine the amount of amino acid adsorbed at the particles surface, titania suspensions having different amino acid concentration were prepared. 99.6 g of titania were stepwise dispersed in 300 ml of demineralised water. Amphiphile concentrations between 0.01 M and 0.125 M were dissolved in the suspension. To favour the amphiphile–particles interaction the modified suspensions were stirred at 200 rpm for 20 minutes using an overhead stirrer. The suspensions were then centrifuged at 3000 rpm for 90 minutes using a Falcon 6/300 centrifuge (MSE, London, United Kingdom). The supernatant was then separated from the solid residue. To remove finer particles still in suspension, the supernatant was filtrated using 0.1 μ m PTFE membrane syringe filters (Whatman GE Healthcare, Amersham, United Kingdom). The filtrate was diluted ten times and the amino acid concentration was determined by UV–Vis. The UV–Vis spectra were recorded using a UV-1 ThermoSpectronic (Thermo Scientific, USA).

3. Results and Discussion

3.1. Amino Acids Screening

To assess the performance of the different amino acids, titania suspensions, prepared as described in Section 2.2, were foamed using different amino acids and amino acid concentrations; the hydrophobic amino acids used in this work are shown in Fig. 1. At pH < 2 the titania surface is positively charged due to the presence of $-\text{OH}_2^+$

groups [19]. At this conditions the dissociated fraction of $-\text{COO}^-$ groups present on the amino acids electrostatically interacts with the titania surface. The pK_a of the carboxylic group of the tested amino acids ranges between 1.8 and 2.4 and, at pH < 2, less than 20% of the carboxylic groups are dissociated but the low solubility of some of the amino acids made it necessary to work at such a low pH. The amino acid solubility is strongly dependent on the pH; Tseng et al. showed, for example, that the solubility of DL-Isoleucine is around 40 g/L at pH comprised between 3 and 8 while it is greater than 150 g/L for pH < 1.5 and pH > 10.5 [20].

Fig. 2 shows the difference in the foam structure when different amino acids are used as amphiphiles (e.g. Phenylalanine and Tryptophan respectively) while Fig. 3 reports the porosity trend of foams obtained using different amino acids and amino acid concentrations.

The lines connecting the experimental points in Fig. 3, are meant to guide the reader eyes and not to fit them. With the exception of DL-Methionine, an increase in porosity was observed increasing the amphiphile concentration till it reached a maximum value, beyond which the porosity decreased. The initial increase in porosity is due to the higher concentration of amphiphile adsorbed on the particles surface resulting in a higher particle hydrophobicity giving in turn more stable foams. A further increase in the amino acid concentration in solution however leads to saturation of the particles surface by the amphiphile. This causes a reduction in electrostatic stabilisation, that in turn increases the suspension viscosity hindering air entrainment. This trend was also observed by Gonzenbach et al. when producing ceramic foams using different concentration of amphiphiles [11]. The fact that DL-Methionine does not follow this trend suggests that the amino acid was either slightly adsorbed on the particles surface or that the particles saturation by the amphiphile was already been reached and, consequently, a further increase in the amino acid concentration did not result in an increase in particles hydrophobicity. In addition, it can be noted that different amino acids gave different values of the maximum porosity obtainable while the use of DL-Alanine and DL-Tyrosine as amphiphiles did not lead to the formation of stable foams.

3.2. SS-NMR Analysis

It was theorised that amino acids would be capable of acting as amphiphiles even in basic conditions thanks to the presence of the amino group; the protonated fraction of $-\text{NH}_3^+$ groups could, in fact, electrostatically interact with the $-\text{O}^-$ groups present on the titania surface at basic pH [19]. To confirm this hypothesis dried samples of functionalised titania were analysed by SS-NMR following the methodology reported in section 2.4. Fig. 4 shows the spectra for the samples prepared at pH = 1 (red line), at pH = 4 (green line) and at pH = 10 (blue line).

At pH = 1 less than 5% of the amino acid carboxylic group was dissociated so the particles–amphiphile interaction was assumed to be negligible. The chemical shift values relative to DL-Phenylalanine

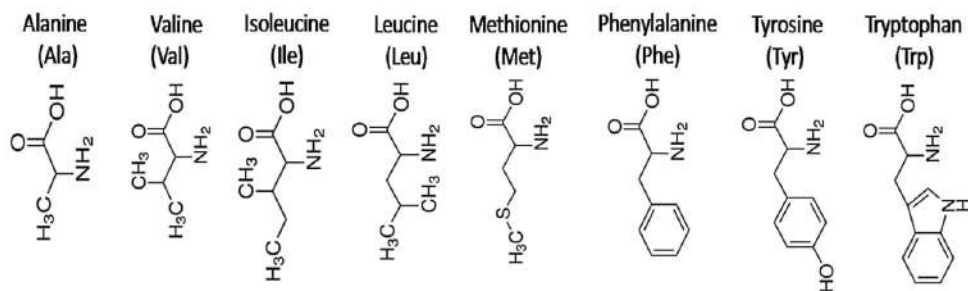


Fig. 1. Hydrophobic α -amino acids tested in this work.

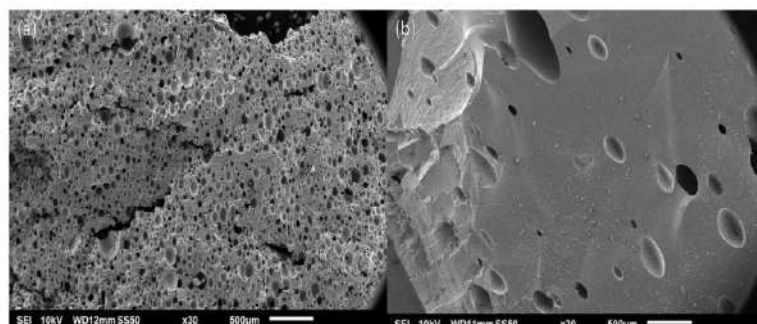


Fig. 2. SEM images of foam cross section produced using: (a) Phenylalanine and (b) Tryptophan as amphiphiles.

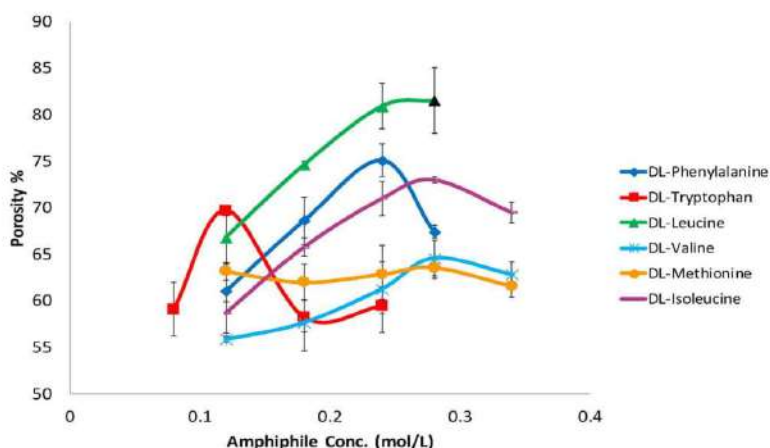


Fig. 3. Foam porosity as a function of amphiphile concentration for foams obtained using different amino acid concentrations. The black triangle in the Leucine curve indicates the solubility limit point. α -Alanine and α -Tyrosine are not present in the graph since they did not give stable foams.

carbons are reported next to each of them in the amino acid structure shown in Fig. 4; these were obtained from a database search and were relative to Phenylalanine in solution. It should be noted that the chemical shifts observed for the solid sample were very close to the solution data. In addition, the fact that the peaks were sharp suggested that no particle-amphiphile interaction was present. The spectrum for the solid sample prepared at pH 4 (green line) shows that the sharp peaks seen for the pH 1 solution derived sample, and attributed to crystalline Phenylalanine, are no longer present. The broadening of the carbonyl and α -carbon peaks indicates that the Phenylalanine has a more amorphous structure. The spectrum of the basic solution derived sample (blue line) shows sharp peaks for the aromatic and carbonyl sites, but peaks of the α - and β -carbons are broader. This implies a difference in the local environment of these sites, possibly a disordered distribution of environments or hindered mobility that could be an indication of an interaction between the titania and the Phenylalanine amino group. Although titania is weakly paramagnetic ($\chi_{\text{mol}} = 74 \text{ m}^3/\text{mol}$), this is probably too weak an effect to cause the observed broadening. The changes in the α - and β -carbon peaks in basic conditions and the changes in the carbonyl and α -carbon peaks in acidic conditions confirm the interaction of the amino acid through the amino and the carboxylic group in basic and acid conditions respectively. This confirms the initially suggested capability of the amino acids of interacting with both positively and negatively charged particles extending, as a consequence, the pH operating range with respect to the amphiphiles commonly reported in the literature.

3.3. Amphiphile Adsorption at the Different Interfaces

The presence of three phases (e.g. solid, liquid and gas) in the system leads to three interfaces: solid-liquid, solid-gas and liquid-gas. The relative adsorption of the amphiphile on these interfaces affects the hydrophobic character of the modified particles [21]. It will be shown later that, for several reasons, Phenylalanine presents the best choice of amphiphile from those studied in this work. It was therefore used as a representative example for the determination of the amphiphile adsorption at the different interfaces. In this work attention was posed on firstly identifying the amount of amphiphile adsorbed at the particles surface (e.g. solid-liquid interface) and consequently to determine the concentration of amino acid present as a free amphiphile in solution. Then, the amount of free amphiphile adsorbed at the liquid-gas interface was evaluated. The amount of amphiphile adsorbed at an interface can be described by an isotherm of adsorption which relates the amount of amphiphile adsorbed at the interface Γ to its bulk concentration c [22]. One of the most commonly used non-linear isotherms is that of Langmuir (Eq. (2)) [23].

$$\Gamma = \Gamma_{\text{max}} \frac{c}{c + a} \quad (2)$$

where a is the Langmuir constant [24] and Γ_{max} the maximum concentration of adsorbed amphiphile. The Langmuir isotherm is based on a lattice-type model with the assumptions that every adsorption site is equivalent (same energy of adsorption) and that the probability for adsorption at an empty site is independent of the occupancy of

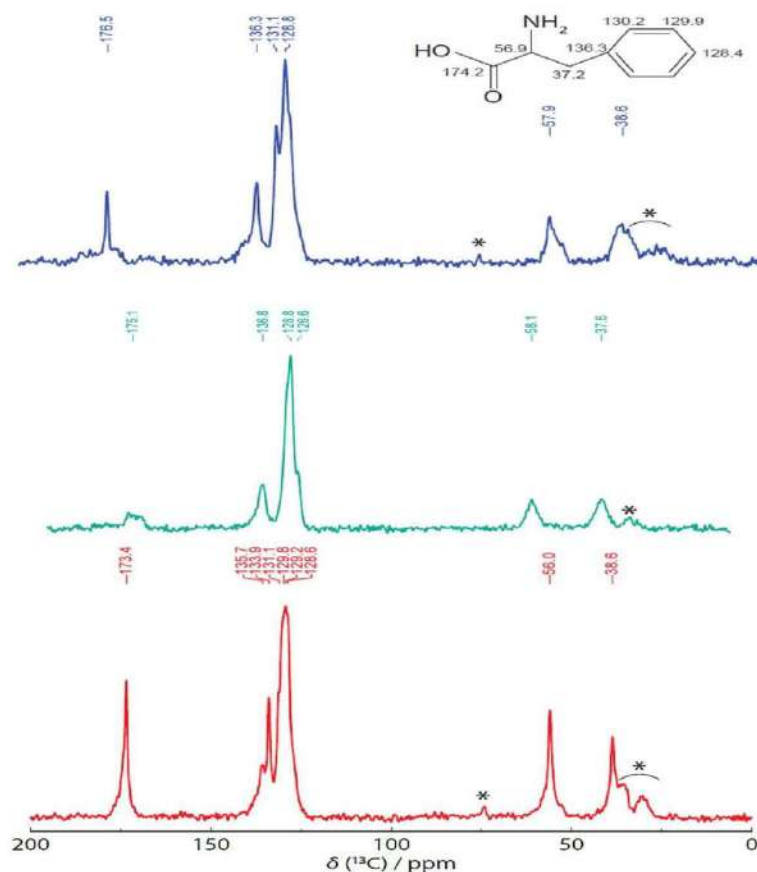


Fig. 4. ^{13}C -NMR spectra for the samples prepared at pH = 1 (red line), pH = 4 (green line) and pH = 10 (blue line).

neighbouring sites, that there are no interactions between the monomers and that no intermolecular forces act between the latter [25]. The adsorbed amount of amphiphile at the solid-liquid Γ_{SL} and gas-liquid Γ_{GL} interfaces could not be directly measured. Firstly, the adsorption of amphiphile at the particles surface Γ_{SL} was determined by differential concentration determination of the amino acid in the supernatant of particulate suspensions, before and after some equilibrating time as described in section 2.6. The adsorption at the gas-liquid interface Γ_{LG} was obtained from the surface tension γ of Phenylalanine solutions, having different concentrations, using the Langmuir-Szyszkowski's state equation [26] (Eq. (3)), which relates the equilibrium interfacial tension to the bulk amphiphile concentration c .

$$\gamma = \gamma_0 - RT\Gamma_{\text{max}} \ln \left(1 + \frac{c}{a} \right) \quad (3)$$

where γ_0 is the interfacial tension corresponding to the amino acid free interface and R and T are the gas constant and temperature respectively. The result, in Fig. 5, confirms that there is a progressive decrease in the surface tension with rising concentration of the amino acid. This indicates the effective adsorption at the air liquid interface. From Fig. 5 it can be noted the absence of the plateau indicative of the critical micelle concentration (C.M.C.); this is due to the low solubility of phenylalanine at pH 4.

Fitting these data with the Langmuir-Szyszkowski equation allowed the values of Γ_{max} and a to be determined. Table 1 summarises the Γ_{max}

and a values for both the solid-liquid and the gas-liquid interfaces.

These values were then substituted into the Langmuir isotherm equation for each amphiphile concentration giving the amount of amino acid adsorbed at the liquid-gas interface. Fig. 6 shows both the isotherm of adsorption at the solid-liquid and gas-liquid interfaces.

Comparing the isotherms at the two different interfaces (Fig. 6) it is possible to observe the preferential adsorption of the amphiphile on one interface or the other. At Phenylalanine concentrations below 10 mM the amphiphile is equally distributed between the two interfaces while at higher concentrations the amino acid preferentially adsorbs at the solid-liquid interface with this trend more and more pronounced as the concentration increases. In Fig. 6 it can be observed that the gas-liquid isotherm starts to reach a plateau corresponding to the saturation of the considered interface. The same trend cannot be observed for the solid-liquid isotherm since the solubility limit for the amino acid was reached before particles surface saturation.

3.4. Amino Acids Hydrophobicity

The measurement of surface tension of amino acid solutions has been employed to rank them based on their hydrophobicity [27]; Bull et al. [25] showed that the gradient of the surface tension curve constitutes a hydrophobicity scale for the amino acids. Specifically, it was noted that the higher the gradient the higher the hydrophobicity. Although it was commented that expressing the hydrophobicity index in

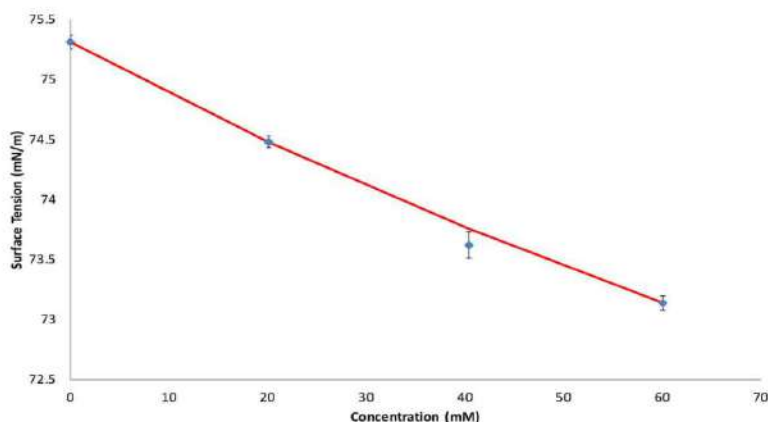


Fig. 5. Experimental (symbols) equilibrium values of the interfacial tension as a function of the amphiphile bulk concentration. Solid line represents the Langmuir-Szyszkowski equation.

Table 1

Values of maximum surface concentration Γ_{\max} and parameter a for the different interfaces.

Solid-Liquid Interface		Gas-Liquid Interface	
Γ_{\max} ($\mu\text{mol}/\text{m}^2$)	a (mol/L)	Γ_{\max} ($\mu\text{mol}/\text{m}^2$)	a (mol/L)
4628	238	2.11	0.12

mN L/m mmol is not an easy interpretation, this is not a concern for this study since the aim is to simply rank the amino acids based on their different hydrophobicity index (H.I.).

Surface tension measurements were carried out by pendant drop method as described in Section 2.5. The surface tension of amino acid solutions with concentration ranging from 0 to 1 M was measured; the results are presented in Fig. 7.

The hydrophobicity index was established from the gradient of the linear section of the surface tension curve, below the critical micelle concentration. Table 2 lists the amino acids and the corresponding hydrophobicity index (expressed in mN L/m mmol); the table also compares the hydrophobicity scale determined in this work with that presented by Bull et al. [27].

With the sole exception of Tyrosine, the two scales are in complete agreement. Bull et al. [27] reported that great difficulty was

encountered during the Tyrosine surface tension measurement and that the slope value was subject to significant error. This could explain the observed difference in Tyrosine position in the hydrophobicity scales.

3.5. Influence of Amino Acids Hydrophobicity on Foam Properties

The amino acids Hydrophobicity Indexes were compared with the maximum foam porosities and the corresponding mean Sauter diameter of foams obtained when the different amino acids were used as amphiphiles. The foam Sauter diameter (d_{32}) was determined using the following equation [28] (Eq. (4)):

$$d_{32} = \frac{\sum (n_i d_i^3)}{\sum (n_i d_i^2)} \quad (4)$$

while the distribution width was expressed by the span value defined as (Eq. (5)) [29]:

$$Span = \frac{D_{90.9} - D_{10.1}}{D_{50.5}} \quad (5)$$

It has been previously shown that foaming was not observed, under these conditions, when Tyrosine and Alanine were used as amphiphiles. Their low position in the hydrophobicity scale suggests that the low hydrophobicity of the amino acids side chain is not capable of sufficiently reducing the hydrophilicity of titania particles. In addition, since the solubility limit of DL-Leucine was reached before the maximum

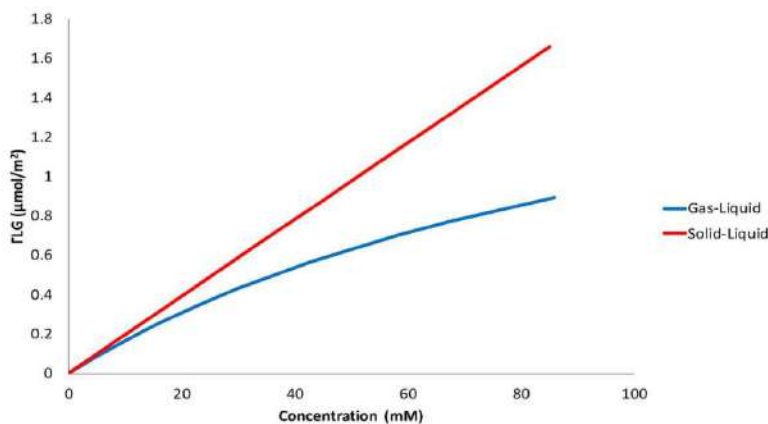


Fig. 6. Comparison of the DL-Phenylalanine isotherms at the Gas-Liquid and Solid-Liquid interfaces.

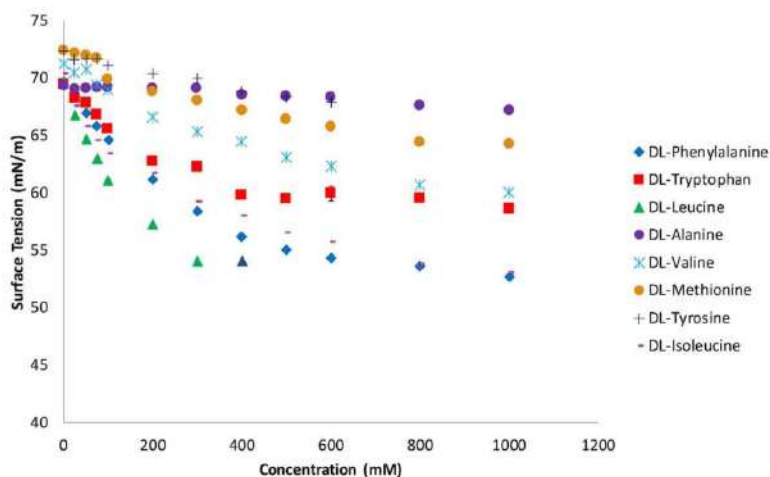


Fig. 7. Surface tension curves for amino acids solutions having different concentrations. The black point in the Leucine curve indicates that the solubility limit for the amino acid was reached.

Table 2
Comparison between the amino acids hydrophobicity scale determined in this work and that proposed by Bull et al.

	Current Work	Bull et al.
Hydrophobicity ↑	Leucine (H.I. = 0.84)	Leucine
	Phenylalanine (H.I. = 0.48)	Phenylalanine
	Isoleucine (H.I. = 0.40)	Isoleucine
	Tryptophan (H.I. = 0.23)	Tyrosine
	Valine (H.I. = 0.21)	Tryptophan
	Methionine (H.I. = 0.12)	Valine
	Tyrosine (H.I. = 0.072)	Methionine
	Alanine (H.I. = 0.020)	Alanine

porosity was observed (Fig. 3), this amino acid is not included in Fig. 8 which shows the porosity and the d_{32} as a function of the amino acids hydrophobicity index.

From Fig. 8 it can be noted that both, the foam porosity and the Sauter diameter, present a monotonic relationship with the amino acid hydrophobicity. The foam porosity increases as the amino acid hydrophobicity increases; the effect of amino acids hydrophobicity on the foam porosity explains the trend observed in Fig. 3 with the maximum foam porosity depending on the type of amino acid used. The opposite trend is observed for the d_{32} where a reduction in bubble size is observed increasing the amino acid hydrophobicity; the distribution span was equal to 1.36, 3.15, 1.56, 2.48 and 2.36 for foams made using Phenylalanine, Isoleucine, Tryptophan, Valine and Methionine respectively as amphiphiles. The effect of particle hydrophobicity on bubble size and foam porosity is extensively reported in the literature. Gonzenbach et al. showed that increasing the amphiphile concentration, and consequently the particle hydrophobicity, leads to a reduction in bubble size [13]. In their case the particles hydrophobicity was increased by incrementing the concentration of a given amphiphile with the same effect expected when the particles hydrophobicity is changed varying the nature of the amphiphile. The latter observation is supported by the relationships between foam properties and amino acids hydrophobicity confirming the role of particle hydrophobicity on foam properties and allowing *a priori* selection of the amino acid depending on the desired foam structure.

3.6. Determination of Minimum Amphiphile Concentration

It has been shown in section 3.1 that for the exception of DL-Tyrosine and DL-Alanine all the hydrophobic amino acids gave stable foams. The selection of the ideal amino acid to be used as amphiphile depends on its performances (e.g. possibility of obtaining a good range of porosities), solubility and price. In terms of performances the amino acids that allow to get a wide porosity range are DL-Leucine, DL-Phenylalanine, DL-Isoleucine and DL-Tryptophan. The solubility and the cost of the mentioned amino acids are summarised in Table 3 allowing a direct comparison among them.

Both solubility and prices were obtained from the Sigma-Aldrich website (consulted on September 2016). The solubility values refer to solubility in water; this values were selected because, at industrial scale, foam production is unlikely to be carried out at such an acidic pH. In addition, the solubility rank is not expected to change with pH [30]. From Table 3, it can be seen that Phenylalanine is the amino acids that presents the lower cost and an acceptable solubility; for this reasons Phenylalanine was selected as a model amphiphile to be used in order to have a deeper insight into the foaming process. In particular, it was quantified the minimum amphiphile concentration necessary to observe the attachment of the modified particles at the air-water interface. This value was determined by surface tension measurement of 25% w/w titania suspensions having different amino acid concentrations [31]. Fig. 9 shows the surface tension trend as a function of the DL-Phenylalanine concentration.

The surface tension value is constant below a Phenylalanine concentration somewhere in the range 0.045–0.055 M. After this point the surface tension drops indicating that the modified particles start to attach at the air-water interface. The measurement of the surface tension of titania suspensions having Phenylalanine concentrations higher than 0.065 M was not possible due to the formation of foams that prevented the formation of a drop. The equality of the surface tension values below 0.065 M was assessed by statistical analysis. The *t*-test for unequal variances populations was run on each pair of values [32]. The *t*-test was used to test the null hypothesis that the means of the two populations were equal. In order for the null hypothesis to be true the t_{Stat} value has to be comprised between $-t_{Crit}$ and t_{Crit} ($-t_{Crit} < t_{Stat} < t_{Crit}$); Table 4 summarises the t_{Crit} and the t_{Stat} values for the tested surface tension pairs.

From Table 4 it should be noted that pair N° 5 is the first one to present inequality between the two surface tension values but, from Fig. 9, it can be seen that the error bars for the surface tension values

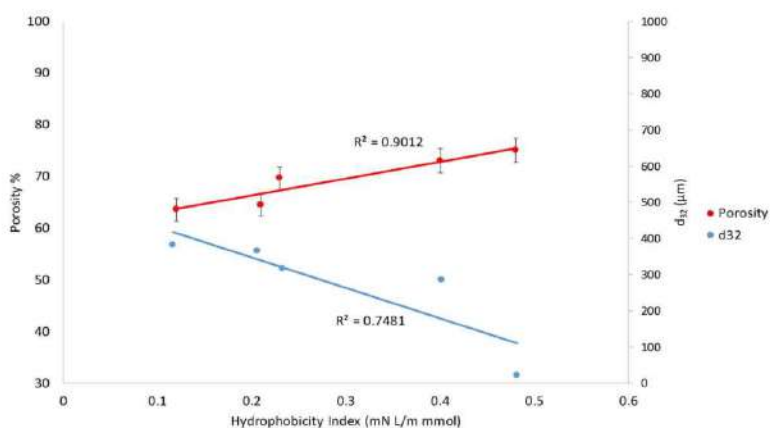


Fig. 8. Maximum foam porosity and d_{32} as a function of the amino acid hydrophobicity index.

Table 3
Comparison of amino acids solubility and cost.

Amino Acid	Solubility (g/L)	Cost (£/100 g)
Leucine	24.3	138.50
Phenylalanine	29.6	39.80
Isoleucine	41.2	154.50
Tryptophan	11.4	171.20

relative to a Phenylalanine concentration of 0.02 M and 0.055 M overlaps. For this reason, the t-test on these two values was carried out and from Table 4 it can be observed that the difference between them is not significant. The surface tension for the 0.065 M suspension was compared to the surface tension values of both the 0.055 M and 0.02 M suspensions. In both cases the difference between the two values was statistically significant indicating that a Phenylalanine concentration of (0.060 ± 0.005) M is the minimum amount that has to be added in order to have the attachment of the modified particles at the air-water interface. It has to be borne in mind that this concentration value is specific for the tested amino acid and the operating conditions. This value is, in fact, affected by the pH of the ceramic suspension, due to the different pK_a values of the amino acids, and by the different

hydrophobicity of the amino acids side chains.

4. Conclusion

Hydrophobic α -amino acids were used as amphiphiles for the production of ceramic foams using the direct foaming technique. This class of amphiphile is more environmentally benign in respect to conventional ones and allows a wider pH operational window. It has been demonstrated that the amino acids adsorb on the particles surface by either the carboxylic or amino group in acidic and basic conditions respectively. In addition, the partition of a model amino acid (e.g. Phenylalanine) between the solid-liquid and gas-liquid interfaces has been determined giving an insight into the distribution of the amino acid among the different interfaces. The tested amino acids have been classified accordingly to the hydrophobicity of their side chain. The amphiphile hydrophobicity index has been related to both the maximum porosity and the bubble size distribution of foams obtained when they are used as amphiphiles. Monotonic relationships have been observed in both cases with the possibility of a linear relationship in the case of porosity. These give a deeper insight into the role of amphiphile structure on the foam properties offering the possibility of tailoring them. Among the tested amino acids α -Phenylalanine has been identified as the most suitable to be used thanks to its acceptable solubility

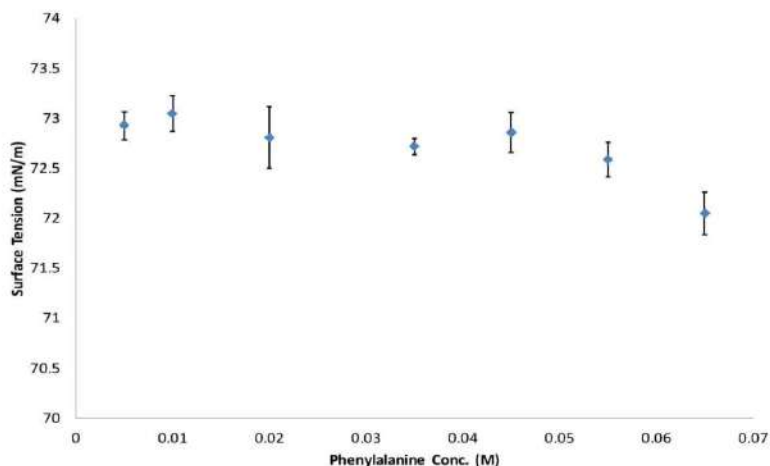


Fig. 9. Surface tension measurement of 25% w/w titania suspension having different phenylalanine concentrations.

Table 4
 γ_{crit} and γ_{stat} values for surface tension pairs.

Pair N°	Surface Tension Pairs (mN/m)	γ_{crit}	γ_{stat}	Response
1	72.93 \pm 0.14 (0.005 M)–73.05 \pm 0.18 (0.010 M)	2.31	–1.15	Equal
2	73.05 \pm 0.18 (0.010 M)–72.81 \pm 0.31 (0.020 M)	2.45	1.49	Equal
3	72.81 \pm 0.31 (0.020 M)–72.72 \pm 0.08 (0.035 M)	2.77	2.13	Equal
4	72.72 \pm 0.08 (0.035 M)–72.86 \pm 0.20 (0.045 M)	2.57	–1.49	Equal
5	72.86 \pm 0.20 (0.045 M)–72.59 \pm 0.17 (0.055 M)	2.31	2.35	Not Equal
6	72.59 \pm 0.17 (0.055 M)–72.05 \pm 0.21 (0.065 M)	2.31	4.46	Not Equal
7	72.81 \pm 0.31 (0.020 M)–72.59 \pm 0.17 (0.055 M)	2.45	1.41	Equal
8	72.81 \pm 0.31 (0.020 M)–72.05 \pm 0.21 (0.065 M)	2.36	4.51	Not Equal

and relatively low cost. For this amino acid the minimum amphiphile concentration necessary to have stable foams has been identified, however this value is specific to the tested amino acid since it depends on both pH and amino acid hydrophobicity.

Acknowledgements

We thank Dr Jonathan Bradley for NMR analysis. Acknowledgments to EPSRC and Johnson Matthey PLC for funding.

References

- [1] L.J. Gauckler, M.M. Waerber, C. Contad, M. Jacobdelliere, Ceramic Foam for Molten-Metal Filtration, *J. Met.* 37 (9) (1985) 47–50.
- [2] P. Colombo, M. Sheffield, Cellular ceramics: structure, Manufacturing, Properties and Applications, Wiley-VCH, Weinheim, 2005.
- [3] A.R. Studart, U.T. Gonzenbach, E. Tervoort, L.J. Gauckler, Processing Routes to Macroporous Ceramics: a Review, *J. Am. Ceram. Soc.* 89 (6) (2006) 1771–1789.
- [4] T. Ota, M. Imaeda, H. Takase, M. Kabayashi, N. Kinoshita, T. Hirashita, H. Miyazaki, Y. Hikichi, Porous Titania Ceramic Prepared by Mimicking Silicified Wood, *J. Am. Ceram. Soc.* 83 (6) (2000) 1521–1523.
- [5] R.A. White, E.W. White, J.V. Weber, Replamineform-New Process for Preparing Porous Ceramic, Metal and Polymer Prosthetic Materials, *Science* 176 (4037) (1972) 922.
- [6] J. Saggio-Woyansky, C.E. Scott, W.P. Minnear, Processing of Porous Ceramics, *Am. Ceram. Soc. Bull.* 71 (11) (1992) 1674–1682.
- [7] J. Layten, S. Mullens, J. Coymans, A.M. De Wilde, I. Thijs, New Processing Techniques of Ceramic Foams, *Adv. Eng. Mater.* 5 (10) (2008) 715–718.
- [8] R.A. Lopes, A.M. Segadas, Microstructure, Permeability and Mechanical Behaviour of ceramic Foams, *Mater. Sci. Eng. A-Struct. Mater. Prop. Microstruct. Process.* 209 (1–2) (1996) 149–155.
- [9] H. Kim, C. De Rosa, M. Boaro, J.M. Vohs, R.J. Gorte, Fabrication of Highly Porous Yttria-Stabilized Zirconia by Acid Leaching Nickel from a Nickel-Yttria-Stabilized Zirconia Cement, *J. Am. Ceram. Soc.* 85 (6) (2002) 1473–1476.
- [10] A. Imhof, D.J. Pine, Ordered macroporous Materials by Emulsion Templating, *Nature* 389 (6654) (1997) 948–951.
- [11] U.T. Gonzenbach, A.R. Studart, E. Tervoort, L.J. Gauckler, Stabilization of Foams with Inorganic Colloidal Particles, *Langmuir* 22 (2006) 109383–109388.
- [12] A.R. Studart, R. Libanori, A. Moreno, U.T. Gonzenbach, E. Tervoort, L.J. Gauckler, Unifying Model for the Electrokinetic and Phase Behavior of Aqueous Suspensions Containing Short and Long Amphiphiles, *Langmuir* 27 (2011) 11835–11844.
- [13] U.T. Gonzenbach, A.R. Studart, E. Tervoort, L.J. Gauckler, Tailoring the Microstructure of Particle-Stabilized Wet Foams, *Langmuir* 23 (2007) 1025–1032.
- [14] I. Wagner, H. Musso, New naturally Occurring Amino Acids, *Angew. Chem. Int. Ed. Engl.* 22 (1983) 816–828.
- [15] S.E. Forrester, C.D. Rielly, K.J. Carpenter, Gas-inducing Impeller design and performance characteristics, *Chem. Eng. Sci.* 53 (1998) 603–615.
- [16] J. Schindelin, I. Arganda-Carreras, E. Frise, Fiji: an open-source platform for biological-image analysis, *Nature Methods* 9 (7) (2012) 676–682.
- [17] A. Williams, C.P. Garner, J.C.P. Binner, Measuring Pore Diameter Distribution of Gelcast Ceramic Foams from Two-Dimensional Cross Sections, Loughborough's Institutional Repository.
- [18] S.M.I. Saad, Z. poliova, A.W. Neumann, Design and Accuracy of Pendant Drop Methods for Surface Tension Measurement, *Colloids and Surfaces A: Physicochem. Eng. Aspects* 384 (2011) 442–452.
- [19] K. Bourikas, C. Kordulis, A. Lycourghiotis, Titanium Dioxide (Anatase and Rutile): Surface Chemistry, Liquid-Solid Interface Chemistry, and Scientific Synthesis of Supported Catalysts, *Chem. Rev.* (2014) 9754–9823.
- [20] H.G. Tseng, C.Y. Lee, W.L. Weng, I.M. Shiah, Solubilities of amino acids in water at various pH values under 298.15 K, *Fluid Phase Equilibria* 285 (2009) 90–95.
- [21] D. Megias-Alguacil, E. Tervoort, C. Cattin, L.J. Gauckler, Contact Angle and Adsorption Behaviour of Carboxylic Acids on α -Al₂O₃, *Journal of Colloid and Interface Science* 353 (2011) 512–518.
- [22] V.B. Fainerman, E.H. Lucassen-Reynders, R. Miller, Adsorption of Surfactant and Proteins at Fluid Interfaces, *Colloids Surfaces A: Physicochem. Eng. Aspects* 143 (1998) 141–165.
- [23] I. Langmuir, The constitution and Fundamental Properties of Solids and Liquids. II. Liquids, *J. Am. Chem. Soc.* 39 (1917) 1848–1906.
- [24] A.V. Makievski, V.B. Fainerman, R. Miller, M. Bree, L. Liggieri, F. Ravera, Determination of Equilibrium Surface tension Values by Extrapolation Via Long Time Extrapolations, *Colloids Surf. A* 122 (1997) 269–273.
- [25] J. Eastoe, J.S. Dalton, Dynamic Surface Tension and Adsorption Mechanisms of Surfactants at the Air-Water Interface, *Adv. Colloid Interface Sci.* 85 (2000) 103–144.
- [26] S.S. Dukhin, G. Kretzschmar, R. Miller, Dynamics of Adsorption at Liquid Interfaces, Elsevier Science, 1995.
- [27] H.B. Bull, K. Breese, Surface tension of Amino Acids Solutions: a Hydrophobicity Scale of the Amino Acid Residues, *Archives of Biochemistry and Biophysics* 161 (1974) 665–670.
- [28] H.G. Merkus, Particles Size Measurements: Fundamentals, Practice, Quality, Springer, 2009, 2017.
- [29] A guidebook to particle size analysis, Hariba Instruments Inc., Irvine, USA.
- [30] T.E. Needham, The solubility of Amino Acids in Various Solvent Systems, (1970) PhD Thesis.
- [31] U.T. Gonzenbach, A.R. Studart, E. Tervoort, L.J. Gauckler, Ultrastable Particle-Stabilized Foams, *Angew. Chem. Int. Ed.* 45 (2006) 3526–3530.
- [32] B.L. Welch, The generalization of Student's problem when several different population variances are involved, *Biometrika* 34 (1–2) (1947) 28–35.



Contents lists available at ScienceDirect

Chemical Engineering Research and Design

journal homepage: www.elsevier.com/locate/cherd


Effect of mixing conditions on the wet preparation of ceramic foams

A. Celani^{a,b}, S. Blackburn^a, M.J.H. Simmons^{a,*}, E.H. Stitt^b^a School of Chemical Engineering, University of Birmingham, B15 2TT, United Kingdom^b Johnson Matthey Technology Centre, Billingham, TS23 1LB, United Kingdom

ARTICLE INFO

Article history:

Received 30 October 2017

Received in revised form 26 March 2018

Accepted 26 March 2018

Available online 4 April 2018

Keywords:

Ceramic foams

Mixing

Aerated stirred vessel

Design of Experiment

Rheology

ABSTRACT

Ceramic foams are a promising alternative to conventional catalyst supports due to their macro-porosity, which should enhance mass transport properties during reactions. Whilst direct foaming is a straightforward production method, the use of kitchen mixers commonly reported in the literature to initially froth the ceramic slurry limits understanding of scale-up. This study reports a systematic experimental investigation of the impact of mixing parameters on the properties of the foams produced in an agitated baffled vessel of diameter, $T = 175$ mm, equipped with an up-pumping pitch blade turbine with diameter of either $D = 0.23 T$ or $0.51 T$ and a bottom round sparger with a diameter of 45 mm. The flow conditions in the present study were in the low to mid transitional regime ($50 < Re < 1000$). Design of Experiments (DoE) was employed to generate a series of screening experiments by variation of sparging time, air flow rate, impeller speed and impeller diameter. The mixing behaviour was described as a function of relevant dimensionless groups (Re , Fr , Fl_g , etc.) whilst the gas-liquid flow regime was estimated by examination of a ceramic particles free system. The properties of the foams obtained were correlated with key dimensionless numbers, though the exponents obtained deviated from values in the published literature. In addition, the rheology of the foam was correlated to the bubble size distribution showing that rheology measurements have potential for at-line measurement to control the structure of the produced material.

© 2018 The Authors. Published by Elsevier B.V. on behalf of Institution of Chemical Engineers. This is an open access article under the CC BY license (<http://creativecommons.org/licenses/by/4.0/>).

1. Introduction

The direct foaming of a ceramic slurry is a simple and versatile method to generate macroporous ceramic materials. These can be used as refractory insulators, filters for molten metals filtration and catalyst supports (Gauckler et al., 1985; Colombo and Sheffield, 2005). The structural properties of these materials are influenced by the formulation of the initial ceramic slurry: in particular, the amphiphile structure and concentration, the solid percentage and the operational pH play a significant role. Gonzenbach et al. (2007) reported an increase in foam porosity as the amphiphile concentration was increased due to the higher particle hydrophobicity as the amount of amphiphile adsorbed at the particle surface increases. Amphiphile concentration also has

an effect on bubble size with a reduction in bubble dimensions as the concentration of the amphiphile is increased (Gonzenbach et al., 2006). The percentage of solid in the initial slurry influences both the foam porosity and bubble size. Gonzenbach et al. (2007) observed a reduction in bubble size and porosity as the solid percentage was increased; they suggested that the decrease in porosity was due to the higher viscosity of the suspension that in turn hindered the air entrainment within the suspension. Finally, pH affects both the particle stabilization in the initial slurry and the dissociation of the functional group of the amphiphile, with the ideal pH reported to be equal to the pKa of the functional group (Gonzenbach et al., 2007; Studart et al., 2006).

Although the formulation of the initial ceramic slurry and its relationship with the structural properties of the foam has been widely

* Corresponding author.

E-mail address: m.j.simmons@bham.ac.uk (M.J.H. Simmons).

<https://doi.org/10.1016/j.cherd.2018.03.044>

0263-8762/© 2018 The Authors. Published by Elsevier B.V. on behalf of Institution of Chemical Engineers. This is an open access article under the CC BY license (<http://creativecommons.org/licenses/by/4.0/>).

investigated, little attention has been given to the manufacturing process. In the literature, the usage of a kitchen mixer is normally reported to mechanically froth the ceramic slurry (Gonzenbach et al., 2007; Gonzenbach et al., 2006; Wong et al., 2011) which presents limitations in term of process scale-up since key mixing parameters such as power input and flow field cannot be easily correlated or extrapolated to industrial scale equipment.

The objective of this study is to gain an understanding of how mixing parameters impact the structure of a ceramic foam slurry produced in a sparged vessel which is more representative of an industrially used process. In order to determine which parameters were statistically significant in affecting the properties of the forms formed, a Design of Experiments (DoE) approach was employed. The investigated parameters were impeller diameter (D), impeller speed (N), gas flow rate (G), sparging time (t) and mean pore size of the sparging disks (\bar{d}). These factors were changed between two different values to develop a wide range of foam properties. The significant parameters, once identified, were related to the foam properties (e.g. porosity, bubble size distribution) using global mixing parameters. The correlation of system properties to dimensionless groups is well-established in chemical engineering, for example the relationship between the Sauter mean diameter of drops and the Weber number in emulsions (Shinnar, 1961; Calabrese et al., 2000) and the correlation between gas hold-up and superficial gas velocity in slurry bubble columns (Bach and Pilhofer, 1978; Hikita et al., 1980; Hughmark, 1967). These correlations were applied to wet foams to give deeper insight into the effects of mixing and process variables on the preparation of the foam precursors. Foam rheology was correlated to the structure of the foams produced under different mixing conditions, suggesting the possibility of using this technique as an at-line measurement to control the structure of the produced foams.

2. Materials and methods

2.1. Materials

Fumed Al_2O_3 particles (AEROXIDE AluC) were obtained from Evonik Industries (Essen, Germany). The alumina was crystalline with a γ/δ -structure. Density and surface area were 50 g L^{-1} and $85\text{--}115\text{ m}^2\text{ g}^{-1}$ respectively. Butyric acid obtained from Alfa Aesar (Heysham, United Kingdom) was used to modify the particle surface properties. Potassium hydroxide solution 40% $_{\text{w/v}}$, prepared by dissolving potassium hydroxide pellets (Alfa Aesar, Heysham, United Kingdom) in demineralized water, and nitric acid 70% $_{\text{w/v}}$ (Alfa Aesar, Heysham, United Kingdom) were used to adjust the suspension pH.

2.2. Suspension preparation

Alumina suspensions were prepared by stepwise addition of the powder to an acidic solution while being continuously stirred using an overhead mixer. The pH of all suspensions was adjusted to electrostatically stabilise the particles. The isoelectric point of alumina occurs between pH 7–10 depending on the type of alumina (Kasprzyk-Hordern, 2004). The suspension solid loading and pH were set to 20% $_{\text{w/w}}$ (83% $_{\text{v/v}}$) and 4.70 respectively. In a typical formulation, 1.1 kg of alumina was added to 4.425 L of demineralized water containing 75 mL of 70% $_{\text{v/v}}$ HNO_3 . 155 mL of butyric acid was added to the suspension to modify the surface properties of the ceramic precursor. After amphiphile addition, the suspension pH was adjusted to 3.50 through the addition of 40% $_{\text{v/v}}$ KOH.

2.3. Suspension foaming

Foaming of 4.5 L suspension was carried out in a 5 L stainless-steel vessel having a diameter, $T=175\text{ mm}$. The vessel was

fitted with four vertical baffles of width $T/10$ and with a circular gas sparger having a diameter of 45 mm fitted 20 mm from the bottom of the vessel whilst the disk-impeller clearance was 30 mm. Two different metal sintered sparging disks (ASCO Filtri s.r.l., Binasco, Italy) were used with an average pore size of 40 μm and 100 μm respectively. During foaming, depending on the experiment being carried out, the slurry was agitated with an up-pumping pitch blade turbine having a diameter, D, of either 40 mm or 90 mm. A gas flow rate equal to 2 L min^{-1} and 20 L min^{-1} and a sparging time of 1 min and 20 min were used. The impeller Reynolds number varied between 50 and 1000 depending upon the operating conditions; the values were calculated using the viscosity of the initial alumina suspension. The shaft torque was recorded by attaching a Binsfeld Engineering Inc. Torque Trak 10 K strain gauge to the impeller shaft. The density of the foam was determined by weighing a known volume of foam. Some of the wet foam was stored in a sealed graduated container to assess its stability; the foam was left for two weeks and the change in volume was noted. The rest of the foam was dried at 80 °C for 2 h in a Carbolite Furnace CWF. The dry foam was calcined at 600 °C for 4 h. During the ramping step and for the first 45 min the furnace was purged under N_2 while after the furnace was run under air. The heating rate was 2 °C min^{-1} .

2.4. Determination of foam porosity

To determine the porosity of the calcined foam, a water pick-up experiment was carried out. The initial weight of four foam lumps was recorded then these were submerged in water and the weight of the wet lumps was recorded for four days. The average amount of water picked up was determined by difference between the weight of the wet foam and its initial weight. From this value the foam porosity and pore volume were calculated.

2.5. Foam bubble size measurement

The mean bubble size was expressed in terms of Sauter mean diameter (Merkus, 2009). Direct imaging of the bubbles in the wet three phase foam was not possible; consequently, the bubble size was determined by image analysis of cross sections cut from the dried and calcined foams. The drying, sectioning and processing led to uncertainties in the accuracy of the bubble size present in the foam during mixing. However, all measurements were made in the same way and thus the error would be systematic in nature allowing comparison between foams. Foam bubble size distribution was determined by acquiring optical microscope images (Nikon Eclipse E200) of cross sections of the foams under investigation. Bubble diameters were obtained by analysing the acquired images with Fiji ImageJ 1.50a (Wayne Rasband, National Institute of Health, USA). Fig. 1(a) shows an example of the cross-sectional image of one of the produced foam while Fig. 1(b) shows a binary image of the same image as Fig. 1(a). The binary images were used to determine the bubble size; it should be noted that only the bubbles that were in focus were analysed. The distributions were corrected by dividing the cross sectional diameter by 0.79 to account for the random position of the bubbles during sample sectioning. The correction factor was determined by Williams et al. (2008). Typically, due to the rate of data acquisition, 100 bubbles were measured per sample. Although this ultimately limited the accuracy and precision of the data it did allow comparisons to be made; the bubble size confi-

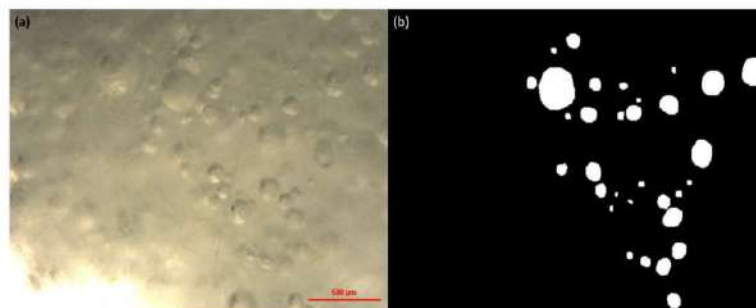


Fig. 1 – Example of cross-sectional image for one of the produced foam: (a) optical microscope image, (b) thresholded image.

dence interval was determined using the procedure of Buffo and Alopaus (2016).

2.6. Foam rheology measurement

Foam rheology was measured using an AR2000 rheometer (TA Instruments, Brusselsesteenweg, Belgium). The rheological measurements were carried out using a 40 mm acrylic hatched parallel plate (geometry inertia = $1.56 \mu\text{N m s}^2$) with the geometry gap set to $500 \mu\text{m}$. To check for the occurrence of slip, two further geometries were employed: a 40 mm steel parallel plate (geometry inertia = $8.30 \mu\text{N m s}^2$) and a standard size vane-rotor with stator inner radius 15 mm and rotor outer radius 14 mm (geometry inertia = $2.44 \mu\text{N m s}^2$). The gap was set to $500 \mu\text{m}$ and $4000 \mu\text{m}$ when the parallel plate and the standard vane geometry were employed respectively. Flow curves and viscoelasticity were measured with all the experiments conducted at 20°C . The sample was firstly equilibrated for 2 min and then pre-sheared at 900 s^{-1} for 30 s. In the upward ramp, the shear rate was increased from 10^{-3} s^{-1} to 1000 s^{-1} , a log ramp mode was used with 10 points per decade acquired every 20 s. The same procedure was followed in the downward ramp where the shear rate was varied from 1000 s^{-1} to 10^{-3} s^{-1} . The selected shear rate range includes the shear rate at which the foam is usually subjected during the foaming experiment; this ranges between 30 and 180 s^{-1} depending upon the operating conditions. To assess the viscoelasticity of the sample an oscillation experiment was carried out. The typical procedure included equilibration of the sample for 2 min followed by a stress sweep step where the oscillation stress was varied from 0.1 Pa to 1000 Pa. The oscillation frequency was equal to 1 Hz and a log ramp mode was used to increase the stress value with 10 points per decade being acquired.

2.7. Design of Experiments (DoE)

A half factorial design with five factors and two levels was employed to screen the significance of the different parameters. Parameter levels were selected through scoping experiments where the parameters were set to their lower and higher values to ensure that an appropriate range of foam properties could be obtained. The screening design generated 16 runs to investigate the effect of independent factors, including impeller diameter D (40–90 mm), impeller speed N (200–1000 rpm), gas flow rate G ($2\text{--}20 \text{ L min}^{-1}$), sparging time t (1–20 min) and sparging disk mean pore size \bar{d} (40 and $100 \mu\text{m}$). Foam porosity, foam density, foam stability and foam bubble size distribution were selected as responses; Table 1 shows the

16 runs with the factors levels and the measured responses. Foam stability is not included in the table since it was observed that it was not affected by the manufacturing process.

3. Theory

It is important to remark that the flow conditions in the present study are low to mid transitional ($50 < \text{Re} < 1000$). Since correlations in this regime cannot be found in the literature, in this work only the correlations from other regimes that gave the best fit are presented. Correlations developed in the turbulent regime were found to give the best fit for the gas hold-up and bubble size correlations whilst, in the absence of a superior approach, the Metzner–Otto correlation was used to determine the impeller mean shear rate.

3.1. Gas hold-up correlations

In the literature, it has been reported that the gas hold-up is affected by gas/liquid/solid physical properties (Ozturk et al., 1987; Bhaga et al., 1971; Sada et al., 1983), operating variables (e.g. pressure, temperature, superficial gas velocity) (Zou et al., 1988; Benkhish et al., 2007; Lau et al., 2004), reactor size (Kastanek et al., 1984; Sarrafi et al., 1999) and type of gas distributor (Wilkinson et al., 1992; Heijnen and Van't Riet, 1984) and several correlations based on these parameters have been proposed. Greaves and Barigou (1990), who studied gas hold-up in large vessels (1–2.7 m) equipped with six blade disc turbines proposed the following:

$$\varepsilon_g = 4.07(N)^{0.62}(Q_g)^{0.64}(D/T)^{1.39} \quad (1)$$

where N is the impeller speed, Q_g is the gas flow rate, D is the impeller diameter and T is the tank diameter. They observed that there is a wide divergence in prediction for different system configurations and operating conditions; they attributed this lack of agreement to the exclusion of the dependence of the gas hold-up on the different flow regimes that could occur under different operating or geometric conditions. These flow regimes were originally proposed by Nienow et al. (1978): at low N the gas passes through the agitator without dispersion and the liquid flows around the outer part of the blades; in this case the impeller is said to be flooded. As the impeller speed is increased beyond the flooding speed N_f the gas is captured by the vortex behind the blades and the impeller is said to be loaded; in this situation, the gas is dispersed and P_g (power consumption of the gassed system) decreases due to the formation of larger cavities. A further increase in N causes the

Table 1 – Half factorial design runs with factors levels and response values.

Run #	Air flow rate (L min ⁻¹)	Impeller speed (RPM)	Sparging time (min)	Impeller diameter (cm)	Sintered disk mean pore size (μm)	Density (g mL ⁻¹)	Porosity %	d ₃₂ (μm)
1	2	200	1	4	100	1.17	82.18	367
2	2	200	20	9	100	0.55	88.68	150
3	20	1000	1	9	40	0.8	88.65	96
4	20	1000	20	4	40	0.36	95.71	189
5	2	1000	1	4	40	0.91	83.42	236
6	2	1000	20	9	40	0.56	95.13	59
7	20	200	1	9	100	1.02	84.63	169
8	20	200	20	4	100	0.56	89.75	240
9	2	1000	20	4	100	0.86	89.71	91
10	20	200	1	4	40	1.02	83.24	331
11	20	200	20	9	40	0.58	91.32	175
12	2	1000	1	9	100	0.92	86.64	129
13	20	1000	20	9	100	0.3	96.71	86
14	20	1000	1	4	100	0.73	86.39	114
15	2	200	1	9	40	1.09	83.43	93
16	2	200	20	4	40	0.96	85.84	384

cavities to change into “vortex” cavities. N_{CD} is the impeller speed at which the gas becomes completely dispersed in the whole vessel while at N_R gross recirculation of gas into the agitator commences.

Smith (1991) used a similar approach to Greaves and Barigou (1990) to predict the gas hold-up correlation; but in this case the extent of gas dispersion was attributed to the different flow regimes. The correlation suggested by Smith (1991) is illustrated below:

$$\varepsilon_g = 0.85(ReFrFl_g)^{0.35}(D/T)^{1.39} \quad (2)$$

where Re is the impeller Reynolds number ($Re = \frac{ND^2\rho}{\mu}$), Fr is the Froude number ($Fr = \frac{N^2D}{g}$) and Fl_g is the gas flow number ($Fl_g = \frac{Q_g}{ND^3}$). Smith (1991) proposed that, except for small tanks ($T < 0.44$ m), gas hold-up can be predicted using dimensionless numbers. Rewatkar et al. (1993) investigated the effects of different sparger types and positions on the gas hold-up proposing the following correlation:

$$\varepsilon_g = 3.54(D/T)^{2.08}(Fr)^{0.51}(Fl_g)^{0.43} \quad (3)$$

Despite the number of available correlations, one of the most frequently used is that based upon the power dissipated in the system:

$$\varepsilon_g \propto (P_g/V)^A v_s^B \quad (4)$$

where P_g is the power consumption of the gassed system, V is the liquid volume and v_s is the superficial gas velocity. Values of A and B range from 0.2 to 0.7 with the tendency for A to be higher for non-coalescing systems (e.g. solutions of electrolytes) compared to coalescing (e.g. pure liquids). Whitton and Nienow (1993) proposed A and B values of 0.26 and 0.66 respectively while Yawalkar et al. (2002) proposed values of 0.25 and 0.41 respectively. It is important to consider that the gas hold-up can be very different in real systems with compared to pure liquids. In addition, bubble diameter may change due to adsorption, desorption and evaporation meaning that these correlations are not universally applicable. However, since ε_g is controlled by bubble size and the amount of recirculating gas, which are functions of both (P_g/V) and v_s , the basic form of (4) appears reasonable (Harnby et al., 2001).

3.2. Bubble size correlations

Different models to correlate the drop size to the process variables have been suggested in the literature; these correlations were commonly derived for emulsions but they can be applied to gas–liquid systems. Kolmogoroff proposed that the eddies in the turbulent flow give rise to different stresses depending on their size relative to the Kolmogoroff scale, λ_k , which is expressed by:

$$\lambda_k = \left(\frac{\nu^3}{\varepsilon}\right)^{1/4} \quad (5)$$

where ν is the kinematic viscosity of the continuous phase and ε is the average dissipation usually expressed as $\varepsilon = \frac{P}{V}$ (Pinelli et al., 2001; Montante and Magelli, 2005; Khopkar et al., 2006). The turbulent eddies will give rise to different stresses depending on their size relative to the Kolmogoroff scale. Drop breakage will occur if the pressure across the drop exceeds the pressure due to surface tension holding the drop together (Kolmogoroff, 1949) (turbulent inertial break-up) and, for eddy sizes, where $\lambda \gg \lambda_k$, the following relationship is valid:

$$(d_d)_{max} = c \left(\frac{\sigma}{\rho_c}\right)^{0.6} \varepsilon^{-0.4} \quad (6)$$

where c is a constant, σ is the interfacial tension, ρ_c is the density of the continuous phase and ε is the mean energy dissipation rate. Eq. (6) can also be expressed in the form of dimensionless groups:

$$d_{32}/\delta = AWe^{-0.6} \quad (7)$$

where A in this case A is equal to $CP_0^{-0.4}$. The Weber number (We) is used for analysing the fluid flow when there is an interface between two different fluids with strongly curved surfaces and it is a measure of the relative importance of the fluid inertia compared to its surface tension (Frohn and Roth, 2000); the Weber number in agitated vessels is expressed as:

$$We = \frac{\rho_c N^2 D^3}{\sigma} \quad (8)$$

This theory was originally employed by Hinze (1955) for dilute liquid/liquid systems and was later adopted for

gas/liquid systems (Machon et al., 1997a). It is important to note that, for bubbles smaller than λ_k , viscosity also affects the fluctuating eddy velocity and the following relationship for the turbulent viscous break-up has been proposed by Sprow (1967):

$$\frac{d_{max}(\mu_c \varepsilon / \rho_c)^{1/2}}{\sigma_f(\frac{\mu_d}{\mu_c})} = \text{const.} \quad (9)$$

Eqs. (6) and (7) satisfactorily correlate the effect of surface tension and agitation conditions on bubble/drop size in the case of liquid–liquid systems while discrepancies are observed in the case of gas–liquid systems (Machon et al., 1997b). Acceptable correlations were obtained in gas–liquid systems where bubble coalescence was reduced (e.g. protein solutions) but, in every case, very different values of both the correlating coefficient and the exponent were required to predict the correct value of the mean bubble size (Hu et al., 2003; Hu et al., 2005). Machon et al. (1997a) and Nienow et al. (2003) suggest that the proposed relationships differ because the Weber number only relates to bubble breakage while, in gas–liquid systems, bubble size is determined by a balance between breakage and coalescence. It is evident that, reducing the contribution of coalescence in the gas–liquid systems, leads to better predictions of the bubble size when relationships (6) and (7) are used.

3.3. Rheology models

The rheology of the produced foams will be investigated and correlated to its structural properties. In this section the rheology models used to describe the foam rheological behaviour are introduced. Fluids can be classified as either Newtonian or non-Newtonian, depending on whether they obey Newton's law of viscosity, expressed as:

$$\tau = \mu \dot{\gamma} \quad (10)$$

where τ is the shear stress, μ is the viscosity and $\dot{\gamma}$ is the shear rate. Non-Newtonian fluids may be classified as either time independent, including shear-thinning (pseudoplastic) and shear-thickening (dilatant) fluids or time dependent, which include thixotropic and rheopectic liquids as well as viscoelastic materials (Paul et al., 2004).

Ceramic foams may be considered as viscoelastic fluids with both a time dependent and shear dependent thinning behaviour and only a description of the relationships describing this class of fluids will be given. Shear thinning fluids present a decrease in viscosity when the shear rate is increased from low to high levels; their behaviour can be described by different constitutive laws but power law is commonly used:

$$\tau = k \dot{\gamma}^n \quad (11)$$

where k is the fluid consistency index and n is the flow behaviour index; this assumes values less than 1 for shear thinning fluids. However, for ceramic foams, a yield stress exists; below this value the interfacial and inter-particle forces prevent fluid motion ("infinite" viscosity). For shear stresses above the yield stress, the external forces are strong enough

to overcome these and the foam flows. These materials can be described by the Herschel–Bulkley constitutive law:

$$\tau = \tau_y + k \dot{\gamma}^n \quad (12)$$

where τ_y is the yield stress. Ceramic foams present a viscoelastic behaviour so a brief description on how to measure this property will be given. Purely elastic materials, can be described by a Hookean spring and their response to an oscillating strain can be expressed by the following stress function:

$$\tau = G \gamma_0 \sin(\omega t) \quad (13)$$

where G is the elastic modulus, γ_0 is the maximum strain exerted on the spring, ω is the angular velocity and t is the time. In the case of elastic fluids, strain and stress are in-phase with each other with the strain and stress presenting their maximum at the same time. Purely viscous materials, can be described by a dashpot and their response to an oscillating strain can be described by:

$$\tau = \eta \omega \gamma_0 \cos(\omega t) \quad (14)$$

Visco-elastic fluids can be described by the Kelvin–Voigt model which combines a dashpot and a spring in parallel; the equation of state to describe this model is:

$$\tau = G \gamma_0 \sin(\omega t) + \eta \omega \gamma_0 \cos(\omega t) \quad (15)$$

Real visco-elastic fluids are obviously more complex than the Kelvin–Voigt model and it is common to use the term complex modulus G^* to describe them which represents the total resistance of the substance against the applied strain; this is defined as:

$$G^* = G' + iG'' = \tau_0(t)/\gamma_E(t) \quad (16)$$

where G' and G'' are the storage modulus and the loss modulus respectively. The storage modulus indicates that the stress energy is temporarily stored during the test but that it can be recovered afterwards while the loss modulus indicates that the energy which has been used to initiate the flow is irreversibly lost.

4. Results

4.1. Determination of process parameters affecting foam structure

The DoE responses summarized in Table 1 were analysed using JMP 10 software (SAS Institute Inc.) to determine the process factors that affect the foam properties.

Table 2 lists the parameters affecting the different foam properties. Five columns are presented. In the first column, the factors and the factor interactions are listed, the second column shows the contrast value that, in the case of an orthogonal design, is the same as the regression parameter estimates. The third column lists the Lenth t -ratio which is used for the calculation of the individual and simultaneous p -values; this is obtained by the ratio between the contrast value (second column) and the Lenth's Pseudo-Standard Error (PSE). The latter is calculated by Lenth's method which identifies inactive effects from which it constructs an estimate of the residuals standard errors (PSE) (Lenth, 1989). The last

Table 2 – Process parameters affecting foam properties.

Parameter	Contrast	Lenth t-ratio	Individual p-value	Simultaneous p-value
Density				
Sparging time	−0.183	−3.91	0.0074	0.0682
Air flow rate	−0.103	−2.20	0.0489	0.3726
Impeller speed	−0.094	−2.01	0.0624	0.4768
Porosity				
Sparging time	3.159	4.07	0.0063	0.0581
Impeller speed	1.848	2.38	0.0367	0.2910
Air flow rate	1.568	2.02	0.0617	0.4712
Impeller diameter	1.416	1.83	0.0830	0.5917
Bubble size				
Impeller speed	−209.491	−9.49	0.0004	0.0080
Impeller diameter	−87.032	−3.94	0.0072	0.0660
Sparging time & air flow rate	−82.409	−3.73	0.0088	0.0792
Impeller diameter & sintered disk	178.843	8.10	0.0004	0.0041

two columns list the individual and simultaneous p-values respectively. The individual p-value is an indication of the significance of the considered factor; if the factor's individual p-value has a value lower than 0.05 it can be considered a significant factor. The p-values are generated via a Monte Carlo simulation of 10,000 runs of $n-1$ purely random values and Lenth's t-ratios are produced for each set. The p-value is the interpolated fractional position among these values in descending order. The simultaneous p-value is the interpolation along the $\max(|t|)$ of the $n-1$ values across the runs (Anon, 2012; Ye and Hamada, 2000).

Sparging time, impeller speed and air flow rate were the factors affecting foam density and foam porosity while foam bubble size was governed by impeller speed, impeller diameter and a series of factor interactions between sparging time and air flow rate and between impeller diameter and sintered disk porosity. This study shows the significance of all the considered factors in developing the structure of ceramic foams. Based on this study, the foam properties were correlated to different global mixing parameters.

4.2. Gas hold-up correlations applied to ceramic foams

A parallelism can be drawn between the porosity of the wet foam and the gas hold-up in bubble columns. A similar approach has been applied in the case of wet foams, where their porosities were correlated to a series of mixing parameters such as energy dissipation (P_g/V), Reynolds number (Re), Froude number (Fr) and gas flow number (Fl_g); in particular, Eq. (2) was used to correlate foam porosity to the dimensionless group. It is important to note that this correlation was obtained for pure gas–liquid systems under steady state conditions while, in the current study, a three-phase unsteady system (e.g. solid–gas–liquid) was present and divergences from the aforementioned relationship are to be expected. Fig. 2 shows the foam porosity as a function of the dimensionless group ($ReFrFl_g$) for foams produced using different entrainment times. Due to the transient nature of the system and the consequent change in the slurry physical properties (e.g. density and viscosity), dimensionless numbers such as the Reynolds number were calculated using the initial physical properties of the ceramic slurry. The Reynolds number, in particular, is expected to decrease in value during the foaming due to a decrease in density and increase in viscosity. In addition, the impeller speed was varied subjecting the slurry to different shear rates; this resulted in different alumina slurry viscosities due to its non-Newtonian nature.

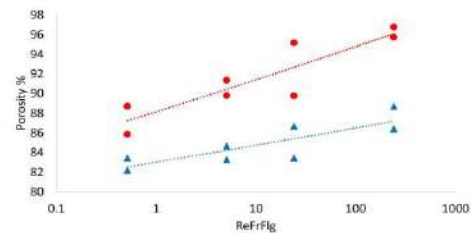


Fig. 2 – Foam porosity as a function of the dimensionless group ($ReFrFl_g$) for foams produced using different sparging times and impeller diameters. $T = 1'$ (●) and $T = 20'$ (▲).

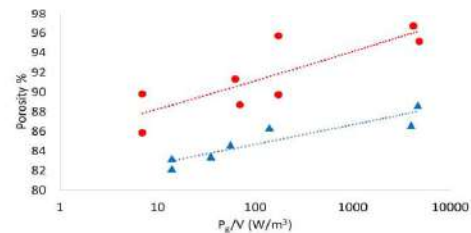


Fig. 3 – Foam porosity as a function of mean energy dissipation for foams produced using different air entrainment times. $T = 1'$ (●) and $T = 20'$ (▲).

The average impeller shear rate was determined using the Metzner–Otto correlation ($\dot{\gamma}_A = k_s N$); with the impeller used characterized by a mixer shear constant k_s of 12 (Albright, 2009). Since the viscosity of the ceramic slurry is shear rate dependent, these average shear rates were used to interpolate the viscosity curve of the starting alumina suspension and determine its viscosity at the different operating conditions.

As a result of foam porosity being strongly affected by sparging time, different correlations were derived for foams produced using different entrainment times. Fig. 2 shows a monotonic correlation in all cases (R^2 equal to 0.80 and 0.69 for foam produced a $1'$ and $20'$ air entrainment time respectively) but, as expected, the exponent of the dimensionless group significantly differed from that proposed by Smith (1991). It has been previously shown that the gas hold-up is more usefully expressed as a function of the mean power dissipation; Fig. 3 shows foam porosity as a function of the mean power dissipation for foams produced using different air entrainment times.

Table 3 – Comparison between exponent values for correlations to determine porosity (gas hold-up) reported in the literature with the values found in this study.

Correlation	Parameter & exponent	Literature value	Value from this study
Smith (1991) Eq. (2)	$ReFrFl_g^\alpha$	$\alpha = 0.35$	$\alpha = 0.012 \pm 0.005$
Whitton and Nienow (1993) Eq. (4)	$(P_g/V)^A$	$A = 0.26$	$A = 0.012 \pm 0.003$
Yawalkar et al. (2002) Eq. (5)	$(P_g/V)^A$	$A = 0.25$	

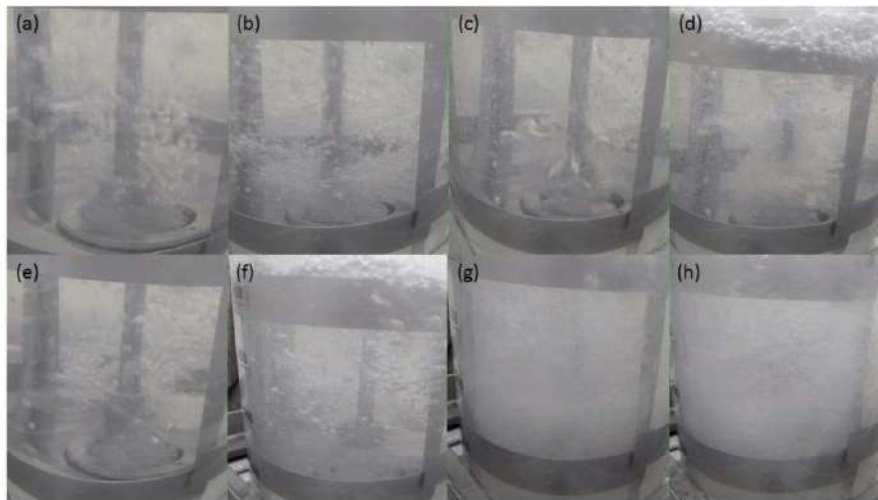


Fig. 4 – Flow regimes at different impeller speed, impeller diameter and gas flow rate. (a) D = 4 cm, G = 2 L/min, N = 200 rpm (b) D = 4 cm, G = 2 L/min, N = 1000 rpm (c) D = 4 cm, G = 20 L/min, N = 200 rpm (d) D = 4 cm, G = 20 L/min, N = 1000 rpm (e) D = 9 cm, G = 2 L/min, N = 200 rpm (f) D = 9 cm, G = 2 L/min, N = 1000 rpm (g) D = 9 cm, G = 20 L/min, N = 200 rpm (h) D = 9 cm, G = 20 L/min, N = 1000 rpm.

Monotonic relationships were found for the evaluated foams (R^2 equal to 0.68 and 0.85 for foam produced a 1' and 20' air entrainment time respectively) but again the exponent values were significantly different from the correlations determined for gas–liquid systems. In both the applied correlations, the exponent values were close to 0.3 while in this study the exponent values were in the range 0.012 ± 0.003 . Table 3 summarises the values of the exponents reported in the literature and the values proposed in this work.

The foam porosity was correlated to the different flow regimes present under the different operating conditions applied. Since a flow-regime map for an up-pumping pitched blade turbine was not found in the literature, this was determined experimentally keeping in mind that the flow patterns proposed by Nienow et al. (1978) are for gas–liquid systems. The presence of particles in the work undertaken here prevented the visual observation of the flow patterns. In addition, the rheological properties change during the foam formation process and this process could lead to transient flow patterns. Despite not being able to establish visually the flow regime in our system, an indication was obtained by using the experimental process parameters (e.g. impeller speed, impeller diameter and gas flow rate) in a particle free air–liquid (water plus additives) system. From Fig. 4 it was observed that, with the exception of case (b) where a loading pattern is observed, flooding was present when the smaller impeller was used (a,c,d); whereas in larger impeller, when increasing the gas flow rate, a transition from a loaded to a recirculating regime was observed (e–h).

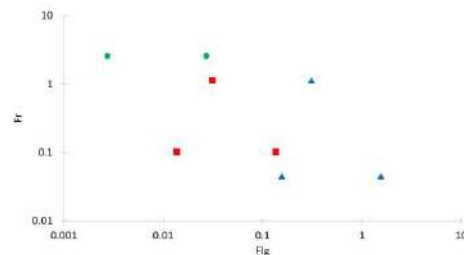


Fig. 5 – Flow regime map for the experimental system representing the different flow regimes: flooded (▲), loaded (■) and fully recirculated (●).

From the visual observation of the different flow regimes, a flow regime map was drawn for the current system by plotting the gas flow number Fl_g (abscissa) and the Froude number Fr (ordinate) in Fig. 5. The aim of this work was not to define an exact flow regime map for the impeller used; the observed flow regimes were plotted as a function of Fr and Fl_g number in order to have an indication of the operating conditions at which they occurred. The limited number of experiments do not allow absolute definition of transition regions between regimes.

Fig. 6(a) and (b) show the foam porosity as a function of the different flow regimes; the different colours and shapes of the bars indicate the flow regimes at which the specific foams were produced. Two different graphs were plotted for the short

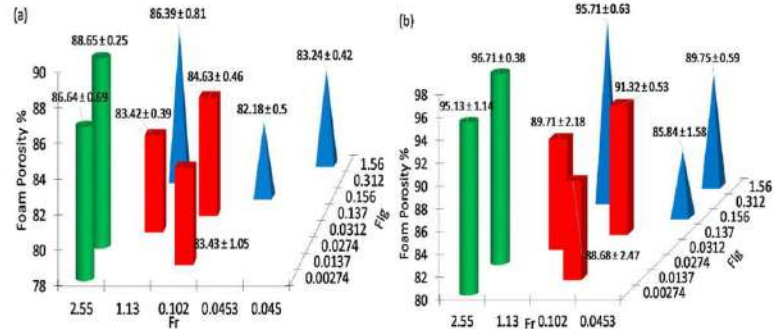


Fig. 6 – Foam porosity as a function of the flow regime conditions for (a) 1 min air entrainment time (b) 20 min air entrainment time. The different flow regimes are represented as flooded (Δ), loaded (\blacksquare) and fully recirculated (\bullet).

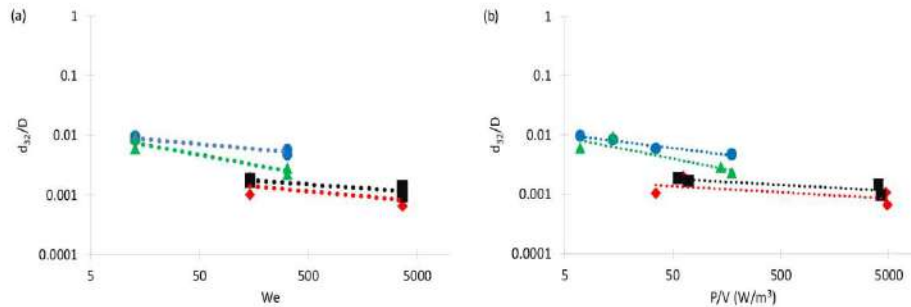


Fig. 7 – d_{32}/D as a function of mean energy dissipation for (a) We (b) P_g/V . The different sparger pore size and impeller diameter are indicated as: 40, $D = 4$ cm (\bullet); 40, $D = 9$ cm (\blacklozenge); 100, $D = 4$ cm (\blacktriangle); 100, $D = 9$ cm (\blacksquare).

and long air entrainment time since that variable affected the foam porosity.

From Fig. 6 it can be noted that a similar trend is followed for both the short and long air entrainment time, with the highest porosity observed when the foam is produced under fully recirculating conditions. It can be noted that, at both air entrainment times, a point characterized by high porosity is present in the flooded region. This point occurs at high Fr and Fl_g numbers which correspond to operating conditions where high flow rate and high impeller speed are used resulting in higher air entrainment and hence porosity. As discussed in Section 4.1, air entrainment time has an effect on the foam porosity; it can be noted that all the foam produced at longer entrainment times had consistently higher porosity values.

4.3. Bubble size correlations applied to ceramic foams

Bubble size correlations presented in the literature were applied to ceramic foams. In particular, the Sauter mean bubble size, d_{32} , was plotted as a function of the mean energy dissipation and Weber number. It is worth noting that the correlations, as in the case of the gas hold-up correlations, refer to liquid–liquid systems or gas–liquid systems. In addition, as previously stated, the physical properties of the slurry change over the duration of the experiment due to foam formation so the density and viscosity of the initial slurry were used for the calculation of the Weber number. The Weber number is expected to increase during the course of the experiment due to the reduction in surface tension as the modified particles attach at the air–water interface; a quantification of the reduc-

tion in surface tension was not possible due to the nature of the system. Given these limitations, it was expected that the relationships would still describe the change in bubble size under the different operating conditions, although some discrepancies in terms of the exponent values were forecast.

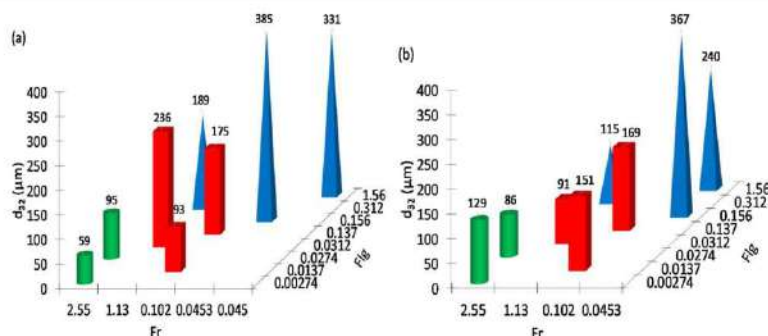
Fig. 7 shows the normalised Sauter mean diameter, d_{32}/D , plotted as a function of both the mean energy dissipation and Weber number. Since the bubble size is affected by both the mean sparger pore size and the impeller diameter, different symbols were used for each enabling the effects to be examined separately.

Fig. 7 shows that the experimental data were fitted by the relationships proposed in the literature (Eqs. (6) and (7)) but, as expected, different values of the mean energy dissipation and Weber number exponents were necessary to correlate the data. The exponents derived in this work ranged from 0.10 to 0.33; these values are not significantly different from the value observed by Hu et al. (2006,2003) in systems where the presence of solvents strongly suppressed coalescence; the authors proposed a value of 0.35 for the exponent. The stability of the foams under consideration is due to the attachment of hydrophobic particles at the air–liquid interface which prevent coalescence. Table 4 summarises the values of the exponents reported in the literature and the values proposed in this work.

In Section 4.1, it was shown that the flow regime affects the porosity of the foam; a similar effect was observed for bubble size. Fig. 8(a) and (b) show the values of d_{32}/D for the different flow regime conditions for the 40 μm and 100 μm sparger disks respectively.

Table 4 – Comparison between the exponent values in correlations reported in the literature for bubble size (d_{32}) with values found in this study.

Correlation	Parameter & exponent	Literature value	Value from this study
Kolmogoroff (1949) Eq. (6)	ε^β	$\beta = -0.4$	$\beta = -0.22 \pm 0.12$
Hinze (1955) Eq. (7)	We^γ	$\gamma = -0.6$	$\gamma = -0.22 \pm 0.08$
Hu et al. (2006, 2003) Eq. (7)	We^γ	$\gamma = -0.35$	$\gamma = -0.22 \pm 0.08$

**Fig. 8 – d_{32}/D depending on the different flow regimes conditions for (a) 40 μm sparging disk (b) 100 μm sparging disk. The different flow regimes are represented as flooded (▲), loaded (■) and fully recirculated (●).**

From Fig. 8, it can be seen that a clear trend exists with smaller bubbles obtained under fully recirculating conditions and larger bubbles progressively formed when moving from loaded to flooded. It is notable that, contrary to expectation, the smaller porosity sparger disk produces bigger bubbles for foams made at Fr higher than ~ 0.02 . At high gas flow rates, a higher level of coalescence is exhibited in the smaller porosity sparger; this is mostly due to the close proximity of the smaller pores and results in the formation of larger bubbles than those initially formed by the large porosity sparger.

4.4. Rheological characterization of wet ceramic foams

The effect of drop size and their distribution on the rheology of emulsions is well reported in the literature (Derkach, 2009; Masalova and Malkin, 2007). Due to the similarities between ceramic foams and emulsions, a correlation between the rheology of the foams produced under different mixing conditions and bubble size distribution was expected. The existence of such a correlation would allow an at-line measurement technique to be developed to control the foam structure during manufacture. The foams rheology was determined using the procedures described in Section 2.6 with all the measured samples presenting shear thinning behaviour. Fig. 9(a) compares the upwards (increasing shear rate) rheology curves for the 16 foams evaluated. There is a notable “kink” present in all the curves. Fig. 9(b) shows the upward (increasing shear rate) and downward (decreasing shear rate) rheology curve for the foam produced in run 4. The downward curve does not reach the initial viscosity of the fresh foam suggesting that the structure of the foam was irreversibly changed at the higher shear rates. In addition, the “kink” appears at lower shear rates in the down curve compared to the up curve. The different position of the “kink” might be used to develop a correlation if it could be shown that was not an artefact of the test procedure. One possibility was that slip was developing during the test despite the upper hatched plate geometry being used.

To investigate the nature of the inflection, the rheology of a foam was measured using three different geometries;

a 40 mm steel plate, a 40 mm acrylic hatched plate and a rotor-vane geometry. In this case, a 20%_{w/w} titania foam was produced using DL-phenylalanine as amphiphile. This change was implemented because the original amphiphile gave an unpleasant odour. In the phenylalanine system titania replaced the original alumina particles due to its better performance. Although the measured system was different from the original foams, the aim of the comparison was to evaluate the nature of the observed “kink”. It was found that the extent of the inflection was geometry dependent, reducing when the vane was used compared with the parallel plate, suggesting that slip is occurring. Given the limitations of the experiment (odour and volume) the vane geometry could not be used for the DoE formulations. The stabilized bubbles in ceramic foams can be assumed to behave as soft spheres, thus, at high concentrations and low shear stress, they exhibit viscoelastic and solid-like behaviour but yield and flow above a yield stress (Fernandez-Neives et al., 2011). Slip of soft particles has been widely investigated in the literature; this occurs when particles are depleted from a solid surface giving a low viscosity boundary layer between the surface and the particles in the bulk of the suspension (Barnes et al., 1995).

The data presented in Fig. 9(a) can be extended allowing study of both the upward and downward shear rate ramp data; the samples can be divided into three groups where their behaviours are similar based on the kink location in terms of the slip onset shear rate and stress. This analysis is shown in Fig. 10 along with the corresponding bubble size data. Fig. 10 shows the sets of rheology curves having similar behaviour and the bubble size distribution of the corresponding foams; the figure indicates that foams having similar bubble size distribution present comparable shear rate values at which the “kink” appears. Table 3 reports the properties of the foam; the span values reported in the table refers to the width of the bubble size distribution calculated using (Merkus, 2009):

$$\text{Span} = \frac{D_{v0.9} - D_{v0.1}}{D_{v0.5}} \quad (17)$$

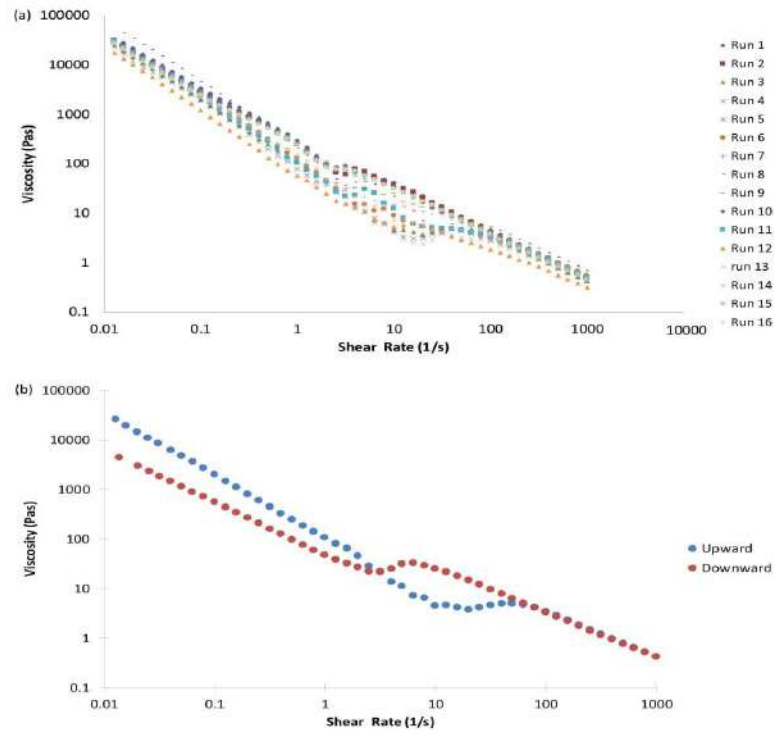


Fig. 9 – (a) Comparison of the upward rheology curve for the produced foams (b) details of the upward and downward rheology curve for foam made in run 4.

Table 5 – Summary of the foams properties divided by overlapping series.

	Exp.	d_{32} (μm)	Distribution span	Shear rate (s^{-1})	Shear stress (Pa)
1st set	1	367	4.08	2.51	214.9
	2	150	2.48	2.51	162.4
	5	236	5.08	2.51	195.0
	7	169	2.74	3.16	235.6
	10	331	2.95	2.51	210.7
Average	15	93	1.62	2.51	173.1
		224	3.16	2.62	198.6
	3	95	1.56	9.99	44.9
	4	189	2.31	12.59	42.1
	12	129	1.50	10.01	53.6
2nd Set	13	86	1.60	19.97	39.9
	14	114	1.70	12.59	73.6
		123	1.73	13.03	50.8
	6	59	1.26	5.01	70.8
	8	240	2.43	3.98	118.9
3rd Set	9	91	1.89	3.98	89.3
	11	175	1.83	3.16	71.1
	16	384	5.13	3.16	112.9
		190	2.51	3.86	92.6
	Average				

It can be seen that slip occurs at different shear rate values in the three sets. In the first, slip appears at around 2.60 s^{-1} , in the second slip occurs at approximately 13.00 s^{-1} and in the third one slip occurs at around 3.90 s^{-1} . Although, the slip of the foams belonging to the same set occurs at very similar shear rates, due to the differences in viscosity among the compared foams, it is more indicative to compare the shear stresses at which slip occurs; these are summarized in Table 5.

Fig. 11 shows the dependence of the shear stress at which slip occurs on both Sauter mean diameter and distribution span.

Fig. 11 shows that a higher shear stress is necessary to generate slip when larger bubbles with wider distribution spans are present, thus onset of slip depends on the structural properties of the foam. Meeker et al. (2004a, 2004b) proposed that slip in soft particles systems is based on an elastohydrodynamic lubrication (EHL) mechanism which occurs when soft particles deform and develop flat facets at hard surfaces under

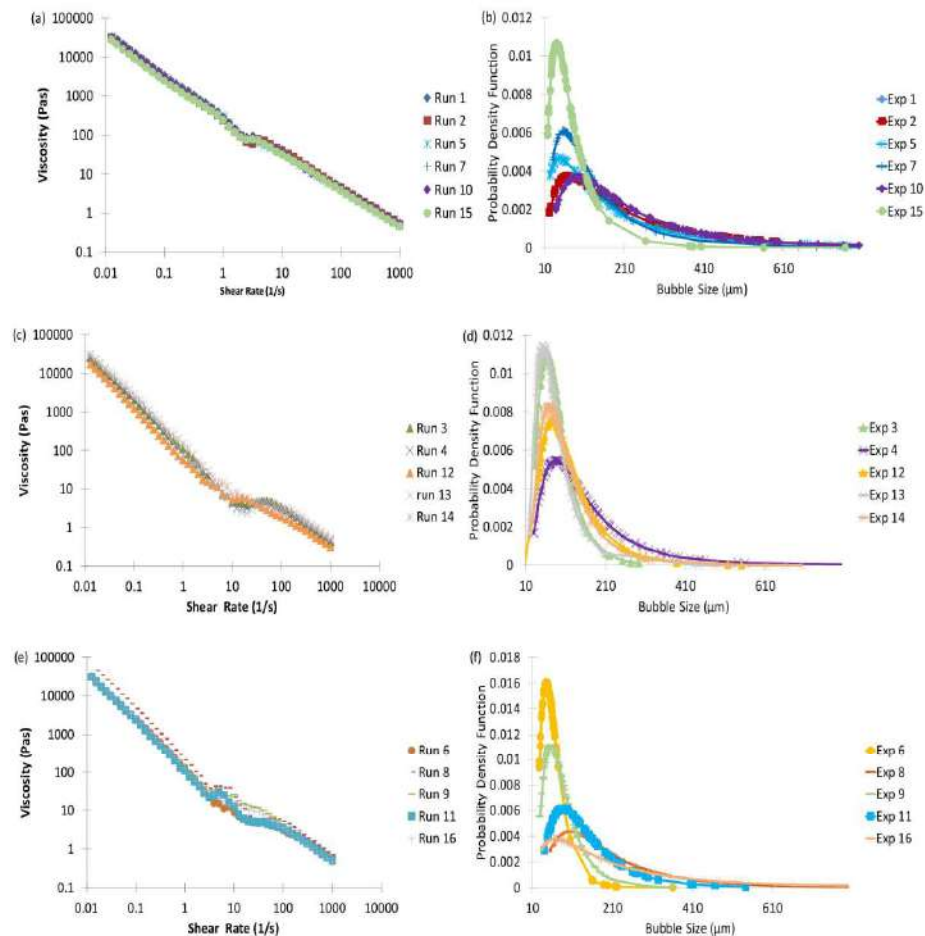


Fig. 10 – Series of rheology curves presenting similar behaviour and corresponding bubble size distribution: (a) first series of rheology curves (b) bubble size distribution of the foams in the first series (c) second series of rheology curves (d) bubble size distribution of the foams in the second series (e) third series of rheology curve (f) bubble size distribution of the foams in the third series.

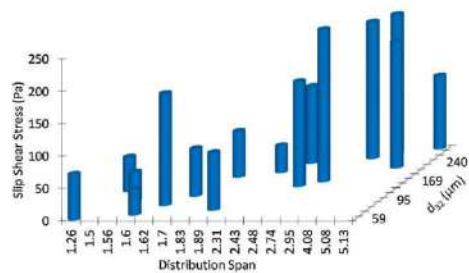


Fig. 11 – Slip shear stress as a function of bubble size and distribution span.

shear. The increased effective area of the particles promotes hydrodynamic lubrication with the thickness of the slip layer depending on the balance between lift force and the repulsive forces generated by the tendency of the particles to regain sphericity; these forces are dependent on the particles elastic

modulus. The elastic modulus of bubbles can be described by the Gibbs elasticity term expressed as (Bianco and Marmur, 1993):

$$E = 2 \frac{d\sigma}{d \ln A_t} \quad (18)$$

where σ is the gas–liquid interfacial tension and A_t is the total surface area of the bubble which is, in turn, radius dependent. Although it was not possible to determine the value of the elasticity modulus due to the nature of the system, these relationships describe the dependence of slip on bubble size and appear to support the observed behaviour.

The viscoelastic properties of the foams were determined following the testing procedure reported in Section 2.6. All the foams presented a similar trend so, for brevity, only oscillation curve for foam produced in run 4 is presented in Fig. 12.

It should be noted that ceramic foams present quite an extensive linear viscoelastic region (LVER). In the LVER G' presents higher values with respect to G'' indicating that the

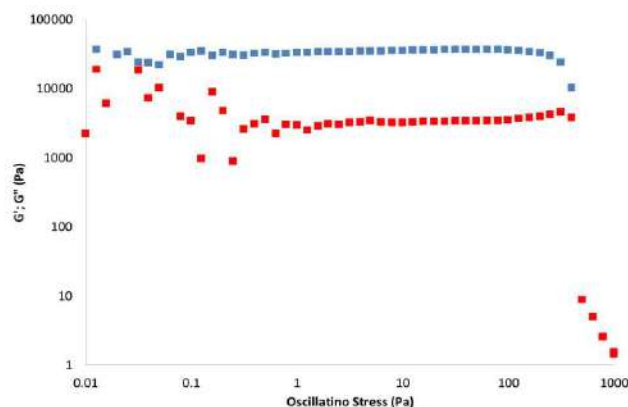


Fig. 12 – Amplitude sweep curve for the foam produced in run 4.

ceramic foams behave more like an elastic solid. All the foams presented a LVER which extended beyond 100 Pa with the foam from experiment 8 extending to 500 Pa. The end of the LVER can be used as an indication of the maximum stress at which the foam can be subjected without destroying its structure. In fact, it has already been mentioned that particles stabilised foams behave like soft spheres giving a solid-like behaviour to the foam. It is expected that as the stabilized bubbles are broken, the foams behaves more like a viscous fluid. This aspect could be particularly relevant in the foam post-processing (e.g. extrusion or forming), where the material could be subjected to stresses higher than those experienced during its manufacture. In these operations knowing the maximum stress at which the foam can be subjected without destroying its structure is fundamental to retain the required product specifications.

5. Conclusions

In this work, the manufacturability of ceramic foams has been studied; in particular, the process parameters affecting the foam properties have been identified and include porosity and bubble size distribution. The effects of impeller speed, impeller diameter, gas flow rate, sparging time and sparging disk mean pore size have been investigated through design of experiment (DoE) in which foam density, foam porosity, foam stability and bubble size distribution were selected as responses. From the experimental work, it was established that foam stability is not dependent on its manufacturing process but is only affected by the initial ceramic slurry formulation. It was determined that sparging time, air flow rate and impeller speed are the major factors affecting foam density and porosity while impeller speed, impeller diameter and the interactions between sparging time and air flow rate and between impeller diameter and the mean pore diameter of sintered disk have an impact on bubble size. To facilitate the process scale-up, foam porosity and foam bubble size distribution were plotted as functions of different global mixing parameters. Correlations capable of describing the investigated system were not found in the literature, this was due to the transient flow behaviour of the investigated system and the change in its physical properties during the foaming. The system was better described by equations valid for turbulent systems and those were used to correlate foam porosity and

bubble size to dimensionless numbers describing the studied system. As expected, in both cases, differences in the exponent values were found compared to literature but the used relationships were well correlated by the experimental data. It is important to remark that, due to the complexity of the system and the number of assumptions made during the study, the new exponents are relevant exclusively for the current system and future work is necessary to identify a general correlation.

To characterize the structure of the foam, rheological measurements were carried out. Slip was observed in the rheological data whose onset was dependent on foam structure as measured by the mean Sauter diameter and distribution span. The viscoelastic properties of the foams were also investigated through an amplitude sweep test showing that foams behave more like viscoelastic solids with the end of the linear viscoelastic region occurring over 100 Pa.

This study highlighted the complexity of the manufacturing process of ceramic foams. Nonetheless, relationships proposed in the literature were shown to be able, upon adjustment of the exponents, to correlate the experimental data. This allows the manufacturing process to be tuned to the desired foam structure. The existence of a correlation between foam rheology and its structural properties, such as bubble size and distribution, could be the starting point to develop an at-line measurement to check the evolution of the foam structure during its manufacture.

Acknowledgements

AC was funded by an EngD studentship from the EPSRC Industrial Doctorate Centre in Formulation Engineering at the University of Birmingham (EP/G036713/1) and Johnson Matthey plc. The authors would like to acknowledge Dr Chandresh Malde and Dr Sam Wilkinson at Johnson Matthey for useful discussion and input on the rheology work.

References

- Albright, L.F., 2009. *Albright's Chemical Engineering Handbook*. Taylor & Francis Group LLC.
- Anon, 2012. *JMP 10 Modeling and Multivariate Method*. SAS Institute, Cary.

- Bach, H.F., Pilhofer, T., 1978. Variations of gas hold-up in bubble columns with physical properties of liquids and operating parameters of column. *Ger. Chem. Eng.* 1, 270–275.
- Barnes, H.A., Bonnecaze, R.T., Cloitre, M., 1995. A review of the slip (wall depletion) of polymer solutions, emulsions and particles suspensions in viscometers: its cause, character, and cure. *J. Non-Newton. Fluid Mech.* 56, 221–251.
- Benkhish, A., Lemoine, R., Sehabiague, L., Oukaci, R., Morsi, B.I., 2007. Gas holdup and bubble size behaviour in a large-scale slurry bubble column reactor operating with an organic liquid under elevate pressures and temperatures. *Chem. Eng. J.* 128 (2–3), 69–84.
- Bhaga, D., Pruden, B.B., Weber, M.E., 1971. Gas holdup in bubble column containing organic liquid mixtures. *Can. J. Chem. Eng.* 49, 417–420.
- Bianco, H., Marmur, A., 1993. Gibbs elasticity of a soap bubble. *J. Colloid Interface Sci.* 158, 295–302.
- Buffo, A., Alopaeus, V., 2016. Experimental determination of size distribution: analyzing proper sample size. *Meas. Sci. Technol.* 27, 1–6.
- Calabrese, R.V., Francis, M.K., Mishra, V.P., Phongikaroon, S., 2000. Measurements and analysis of drop size in a batch rotor-stator mixer. In: 10th European Conference on Mixing, Delft, The Netherlands, pp. 149–156.
- Colombo, P., Sheffield, M., 2005. *Cellular Ceramics: Structure, Manufacturing, Properties and Applications*. Wiley-VCH, Weinheim.
- Derkach, S.R., 2009. Rheology of emulsions. *Adv. Colloid Interface Sci.* 151, 1–23.
- Fernandez-Neves, A., Wyss, H., Mattson, J., Weitz, D.A., 2011. *Microgel Suspensions: Fundamentals and Applications*. Wiley-VCH Verlag.
- Frohn, A., Roth, N., 2000. *Dynamics of Droplets*. Springer Science & Business Media.
- Gauckler, L.J., Waeber, M.M., Contand, C., Jacobduliere, M., 1985. Ceramic foam for molten-metal filtration. *J. Metals* 37 (9), 47–50.
- Gonzenbach, U.T., Studart, A.R., Tervoort, E., Gauckler, L.J., 2006. Stabilization of foams with inorganic colloidal particles. *Langmuir* 22, 109383–109388.
- Gonzenbach, U.T., Studart, A.R., Tervoort, E., Gauckler, L.J., 2007. Tailoring the microstructure of particle-stabilized wet foams. *Langmuir* 23, 1025–1032.
- Greaves, M., Barigou, M., 1990. Estimation of gas hold-up and impeller power in a stirred vessel reactor. *Fluid Mixing III* 108, 235–255.
- Harnby, N., Edwards, M.F., Nienow, A.W., 2001. *Mixing in the Process Industries*, 2nd Edition. Butterworth-Heinemann, Oxford.
- Heijnen, J.J., Van't Riet, K., 1984. Mass transfer, mixing and heat transfer phenomena in low viscosity bubble column reactors. *Chem. Eng. J.* 28, B21–B42.
- Hikita, H., Asai, S., Tanigawa, K., Segawa, K., Kitao, M., 1980. Gas hold-up in bubble columns. *Chem. Eng. J.* 20, 59–67.
- Hinze, J.O., 1955. Fundamentals of the hydrodynamic mechanism of splitting in dispersion processes. *AIChE J.* 1, 289–295.
- Hu, B., Nienow, A.W., Pacek, A.W., 2003. The effect of sodium caseinate concentration and processing conditions on bubble sizes and their break-up and coalescence in turbulent, batch air/aqueous dispersions at atmospheric and elevated pressures. *Colloids Surf. B Biointerfaces* 31, 3–11.
- Hu, B., Pacek, A.W., Stitt, E.H., Nienow, A.W., 2005. Bubble sizes in agitated air-alcohol systems with and without particles: turbulent and transitional flow. *Chem. Eng. Sci.* 60, 6371–6377.
- Hu, B., Nienow, A.W., Stitt, E.H., Pacek, A.W., 2006. Bubble size in agitated solvent/reactant mixtures used in heterogeneous catalytic hydrogenation of 2-butyne-1,4-diol. *Chem. Eng. Sci.* 61, 6765–6774.
- Hughmark, G.A., 1967. Holdup and mass transfer in bubble columns. *Ind. Eng. Chem. Process. Des. Dev.* 6, 218–220.
- Kasprzyk-Hordern, B., 2004. Chemistry of alumina, reactions in aqueous solution and its application in water treatment. *Adv. Colloid Interface Sci.* 110, 19–48.
- Kastanek, F., Zahradnik, J., Kratochvil, J., Cermak, J., 1984. Modelling of large-scale bubble column reactors for non-ideal gas-liquid systems. In: *Frontier in Chemical Reaction Engineering*. John Wiley and Sons, New Delhi, India, pp. 330–344.
- Khopkar, A.R., Kasat, G.R., Pandit, A.B., Ranade, V.V., 2006. Computational fluid dynamics simulation of the solid suspension in a stirred slurry reactor. *Ind. Eng. Chem. Res.* 45, 4416–4428.
- Kolmogoroff, A.N., 1949. *Dokl. Akad. Nauk S.S.S.R. (N.S.)* 66, 825.
- Lau, R., Peng, W., Valazquez-Vargas, G., Yang, G.Q., Fan, L.S., 2004. Gas-liquid mass transfer in high-pressure bubbles columns. *Ind. Eng. Chem. Res.* 43, 1302–1311.
- Lenth, R.V., 1989. Quick and easy analysis of unreplicated factorials. *Technometrics* 31, 469–473.
- Machon, V., Pace, A.W., Nienow, A.W., 1997a. Bubble sizes in electrolyte and alcohol solutions in a turbulent stirred vessel. *TransChemE* 75 (A), 339–348.
- Machon, V., Pacek, A.W., Nienow, A.W., 1997b. Bubble sizes in electrolyte and alcohol solutions in a turbulent stirred vessel. *TransChemE* 75 (A), 339–348.
- Masalova, I., Malkin, A.Y.A., 2007. Peculiarities of rheological properties and flow of highly concentrated emulsions: the role of concentration and droplet size. *Colloid J.* 69 (2), 185–197.
- Meeker, S.P., Bonnecaze, R.T., Cloitre, M., 2004a. Slip and flow in pastes of soft particles: direct observation and rheology. *J. Rheol.* 48, 1295–1320.
- Meeker, S.P., Bonnecaze, R.T., Cloitre, M., 2004b. Slip and flow in soft particles pastes. *Phys. Rev. Lett.* 92 (19), 4.
- Merkus, H.G., 2009. *Particles Size Measurements: Fundamentals, Practise, Quality*. Springer.
- Montante, G., Magelli, F., 2005. Modelling of solids distribution in stirred tanks: analysis of simulation strategies and comparison with experimental data. *Int. J. Comput. Fluid Dyn.* 19 (3), 253–262.
- Nienow, A.W., Wisdom, D.J., Middleton, J.C., 1978. *Proceedings of 2nd European Conference on Mixing*. BHRA Fluid Engineering, Cranfield, pp. pp. F1-1-F1-16 and X54.
- Nienow, A.W., Hu, B., Pacek, A.W., 2003. Bubble sizes in stirred reactors: what can we predict? Annual Meeting, Paper 361a.
- Ozturk, S.S., Schumpe, A., Deckwer, W.D., 1987. Organic liquids in bubble column: holdups and mass transfer coefficients. *AIChE J.* 33, 1473–1480.
- Paul, E.L., Atiemo-Obeng, V.A., Kresta, S.M., 2004. *Handbook of Industrial Mixing: Science and Practice*. Wiley-Interscience, Hoboken, NJ.
- Pinelli, D., Nocentini, M., Magelli, F., 2001. Solids distribution in stirred slurry reactors: influence of some mixer configurations and limits to the applicability of a simple model for predictions. *Chem. Eng. Commun.* 00, 1–18.
- Rewatkar, V.B., Deshpande, A.B., Pandit, A.B., Joshi, J.B., 1993. Gas hold-up behaviour of mechanically agitated gas-liquid reactors using pitched blade downflow turbines. *Can. J. Chem. Eng.* 71, 226–237.
- Sada, E., Kamazawa, H., Lee, C.H., 1983. Chemical absorption in bubble column loading concentrated slurry. *Chem. Eng. Sci.* 38, 2047–2051.
- Sarrafi, A., Jamialahmadi, M., Muller-Steinhagen, H., Smith, J.M., 1999. Gas holdup in homogeneous and heterogeneous gas-liquid bubble column reactors. *Can. J. Chem. Eng.* 77, 11–21.
- Shinnar, R., 1961. On the behaviour of liquid dispersions in mixing vessels. *J. Fluid Mech.* 10, 259.
- Smith, J.M., 1991. Simple performance correlations for agitated vessels. *Proc. 7th Euro Congress on Mixing*, 233–241.
- Sprow, F.B., 1967. Drop size distributions in strongly coalescing agitated liquid-liquid systems. *AIChE J.* 13 (5), 995–998.
- Studart, A.R., Gonzenbach, U.T., Tervoort, E., Gauckler, L.J., 2006. Processing routes to macroporous ceramics: a review. *J. Am. Ceram. Soc.* 89 (6), 1771–1789.
- Whitton, M.J., Nienow, A.W., 1993. Scale-up correlations for gas hold-up and mass transfer coefficients in stirred tank

- reactors. *Proc. 3rd Int. Conference on Bioreactor and Bioprocess Fluid Dynamics*, 135–149.
- Wilkinson, P.M., Spek, A.P., van Dierendonck, L.L., 1992. Design parameters estimation for scale-up of high-pressure bubble columns. *AIChE J.* 38, 544–554.
- Williams, A., Garner, C.P., Binner, J.G.P., 2008. *Measuring Pore Diameter Distribution of Gelcast Ceramic Foams from Two-Dimensional Cross Sections*. Loughborough's Institutional Repository.
- Wong, J.C.H., Tervoort, E., Busato, S., Gauckler, L.J., Ermanni, P., 2011. Controlling phase distributions in macroporous composite materials through particle-stabilized foams. *Langmuir* 27, 3254–3260.
- Yawalkar, A.A., Pangarkar, V.G., Beenackers, A.A.C.M., 2002. Gas hold-up in stirred tank reactors. *Can. J. Chem. Eng.* 80, 158–166.
- Ye, K.Q., Hamada, M., 2000. Critical values of the length method for unreplicated factorial designs. *J. Qual. Technol.* 32 (1), 57–66.
- Zou, R., Jiang, X., Li, B., Zu, Y., Zhang, L., 1988. Studies on gas holdup in a bubble column operated at elevated temperatures. *Ind. Eng. Chem. Res.* 27, 1910–1916.

Patents

(12) INTERNATIONAL APPLICATION PUBLISHED UNDER THE PATENT COOPERATION TREATY (PCT)

(19) World Intellectual Property

Organization
International Bureau



(43) International Publication Date
6 October 2016 (06.10.2016)

WIPO | PCT

(10) International Publication Number

WO 2016/156789 A1

(51) International Patent Classification:

B01J 23/75 (2006.01) C04B 38/00 (2006.01)
B01J 35/04 (2006.01) C10G 2/00 (2006.01)
B01D 39/20 (2006.01) C07C 1/04 (2006.01)
C04B 35/46 (2006.01)

(74) Agent: RIDLAND, John; Johnson Matthey Process Technologies, PO Box 1, Belasis Avenue, Billingham Cleveland TS23 1LB (GB).

(21) International Application Number:

PCT/GB2016/050696

(22) International Filing Date:

15 March 2016 (15.03.2016)

(25) Filing Language:

English

(26) Publication Language:

English

(30) Priority Data:

1505556.9 31 March 2015 (31.03.2015) GB

(71) Applicant: JOHNSON MATTHEY PUBLIC LIMITED COMPANY [GB/GB]; 5th Floor, 25 Farringdon Street, London EC4A 4AB (GB).

(72) Inventors: CELANI, Andrea; Johnson Matthey Process Technologies, PO Box 1, Belasis Avenue, Chilton, Billingham Cleveland TS23 1LB (GB). DAVIES, Laura Helen; Johnson Matthey Process Technologies, PO Box 1, Belasis Avenue, Chilton, Billingham Cleveland TS23 1LB (GB). HOLT, Elizabeth Margaret; Johnson Matthey Process Technologies, PO Box 1, Belasis Avenue, Chilton, Billingham Cleveland TS23 1LB (GB). KELLY, Gordon James; Johnson Matthey Process Technologies, PO Box 1, Belasis Avenue, Chilton, Billingham Cleveland TS23 1LB (GB).

(81) Designated States (unless otherwise indicated, for every kind of national protection available): AE, AG, AL, AM, AO, AT, AU, AZ, BA, BB, BG, BH, BN, BR, BW, BY, BZ, CA, CH, CL, CN, CO, CR, CU, CZ, DE, DK, DM, DO, DZ, EC, EE, EG, ES, FI, GB, GD, GE, GH, GM, GT, HN, HR, HU, ID, IL, IN, IR, IS, JP, KE, KG, KN, KP, KR, KZ, LA, LC, LK, LR, LS, LU, LY, MA, MD, ME, MG, MK, MN, MW, MX, MY, MZ, NA, NG, NI, NO, NZ, OM, PA, PE, PG, PH, PL, PT, QA, RO, RS, RU, RW, SA, SC, SD, SE, SG, SK, SL, SM, ST, SV, SY, TH, TJ, TM, TN, TR, TT, TZ, UA, UG, US, UZ, VC, VN, ZA, ZM, ZW.

(84) Designated States (unless otherwise indicated, for every kind of regional protection available): ARIPO (BW, GH, GM, KE, LR, LS, MW, MZ, NA, RW, SD, SL, ST, SZ, TZ, UG, ZM, ZW), Eurasian (AM, AZ, BY, KG, KZ, RU, TJ, TM), European (AL, AT, BE, BG, CH, CY, CZ, DE, DK, EE, ES, FI, FR, GB, GR, HR, HU, IE, IS, IT, LT, LU, LV, MC, MK, MT, NL, NO, PL, PT, RO, RS, SE, SI, SK, SM, TR), OAPI (BF, BJ, CF, CG, CI, CM, GA, GN, GQ, GW, KM, ML, MR, NE, SN, TD, TG).

Published:

- with international search report (Art. 21(3))
- before the expiration of the time limit for amending the claims and to be republished in the event of receipt of amendments (Rule 48.2(h))



WO 2016/156789 A1

(54) Title: CATALYST PRECURSOR, METHOD OF PREPARATION AND USE THEREOF

(57) Abstract: Acatalyst precursor suitable for the Fischer Tropsch reaction is described comprising cobalt oxide supported on a porous support wherein the porous support is a ceramic foamcomprising a closed cell structure.

CATALYST PRECURSOR, METHOD OF PREPARATION AND USE THEREOF

The present invention relates to cobalt based Fischer-Tropsch catalysts, in particular cobalt based Fischer-Tropsch catalysts on foamed supports.

- 5 The Fischer-Tropsch reaction uses synthesis gas comprising carbon monoxide and hydrogen to generate hydrocarbons, particularly long-chain hydrocarbon products and oxygenates. Suitable catalysts comprise cobalt supported on a metal oxide support. The cobalt is typically provided in oxidic form and reduced in-situ to the active metal form or the catalyst may be pre-reduced and passivated. The metal oxide support may be in the form of a spray-dried powder,
10 granules or shaped extrudates.

- US6558634 and US6750258 disclose a microchannel reactor for the Fischer-Tropsch reaction in which a preferred catalyst structure within the microchannels is made using a metal foam support with an open cell structure to permit the flow of gas through the catalyst. The metal
15 foam structure was coated with a slurry of a Fischer-Tropsch catalyst and dried to form the catalyst structure. Metal foam supports are however of limited utility and it is necessary to pre-treat the metal to ensure the necessary adhesion of the catalyst slurry.

- CN102728359(A) discloses a cobalt-based Fischer-Tropsch catalyst prepared using a
20 mesoporous silicon oxide foam as carrier. The mesoporous carrier has a three-dimensional ordered pore structure having a pore size in a range of 20 to 50 nm and a pore volume of 1.5 to 3.0 cm³/g. The foam has an open cell structure wherein the spherical pores are communicated through windows.

- 25 US5217939 discloses a cobalt oxide-coated ceramic foam, where the ceramic foam is a reticulated ceramic foam, made for example by polyurethane casting. Such foams possess an open cell structure.

- We have found that surprisingly effective cobalt based Fischer Tropsch catalysts may be
30 supported on a ceramic foam support comprising a closed cell structure.

- Accordingly the invention provides a catalyst precursor suitable for the Fischer Tropsch reaction comprising cobalt oxide supported on a porous support wherein the porous support is a ceramic foam comprising a closed cell structure.
35

The invention further provides a catalyst produced from the catalyst precursor, methods for the manufacture of the catalyst and catalyst precursor, and the use of the catalyst in a Fischer-Tropsch process.

The cobalt oxide in the catalyst precursor may be Co_3O_4 and/or CoO , although Co_3O_4 is more suitable. The cobalt oxide may be present on the porous catalyst support as crystallite, with an average crystallite size in the range 5-25 nm.

- 5 The cobalt content of the catalyst precursor, expressed as Co, may be in the range 5-50% by weight, preferably 10-40% by weight, more preferably 10-30% by weight.

- The catalyst precursor may further comprise one or more promoter metals or metal compounds to enhance the activity or selectivity of the catalyst and/or to enhance the reduction of the cobalt oxide to cobalt metal. Suitable promoter metals include one or more of Pt, Pd, Ru and Re. The promoter metal may be included in the catalyst precursor in an amount in the range 0.01-1.0%, preferably 0.01 to 0.50% by weight.
- 10

- A ceramic foam is a solid porous material generally having many gas-filled cells or voids formed therein, such that the support has a lower density than conventional catalyst supports. Open cell ceramic foams may be manufactured by impregnating open-cell polymer foams internally with a ceramic slurry and then firing in a kiln, leaving only a ceramic material. In the present invention the ceramic foam comprises a closed cell structure and is therefore prepared by different methods. By the term, "closed cell structure", we mean that the cells or voids within the foam are generally not inter-connected, although a small proportion, e.g. up to about 20% of the cell volume, but preferably less than 10% of the cell volume, may be interconnected. In a closed cell structure, unlike an open-cell structure, there is generally no open flow-path through the foam from one side to another such that a gas passing through the foam has to diffuse through a cell wall from one cell to the next. The shape of the cells in the closed cell structure will vary depending upon the manufacturing method and conditions, but typically are spheres or distorted spheres having a circular cross section. The cells may have a diameter in the range 0.1-500 μm , although the majority (i.e. >50% in number) of the cells desirably have a diameter in the range 0.1-250 μm . The average cell diameter may be in the range 0.2-150 μm , preferably 1-100 μm . The cell diameters may be determined using microscopy.
- 15
- 20
- 25

- The void fraction of the foams may be in the range 50-95% by volume, preferably 75-90% by volume. Hence the solids content of the foams may be 5-50%, preferably 10-25% by volume.
- 30

- Because the support has a closed cell structure, there are walls between the cells. The cell walls are porous, i.e. the cell walls may comprise pores through which a gas may pass. The pore size or width may be >50 nm in diameter although preferably the pores are \leq 50 nm in diameter. Cobalt oxide is present on the cell walls and in at least a portion of the pores in the cell walls, which upon activation, is able to catalyse the Fischer-Tropsch reaction. Fischer-Tropsch reactions are influenced by the contact time of the reacting gases and therefore the
- 35

thickness of the cell walls may be controlled to provide an optimum diffusion path for reacting gases through the catalyst in order to maximise selectivity. The thickness of the cell walls may also be controlled to impart a desired strength to the final catalyst. Cell wall thicknesses may be up to 500 μm , preferably up to 200 μm , with an average in the range 10-100 μm , preferably 5 25-85 μm . The control of wall thickness may, for example, be performed by controlling the void fraction in the ceramic foam during its manufacture.

The ceramic in the ceramic foam may be formed using a metal oxide or other ceramic material suitable for supporting a Fischer-Tropsch catalyst, such as SiC. Metal oxides are preferred and 10 suitable metal oxide foams may be prepared using alumina, metal-aluminates, silica, ceria, titania, zirconia and mixtures of these. Silica is less preferred. Alumina can form cobalt-aluminate by reaction with cobalt compounds used to produce the cobalt oxide. Cobalt aluminate is less reducible than cobalt oxide, and so where alumina is present in the catalyst support it is preferably coated with a layer of another metal oxide, such as silica, titania or 15 zirconia, or the alumina may be converted into another metal aluminate by reaction with a suitable divalent metal, such as Ni. Titania is particularly preferred because of its low interaction with cobalt and its ability for being formed into foamed structures. The titania may comprise variable amounts of rutile and anatase. High anatase materials are preferred, e.g. with an anatase content >60% by weight. .

20 The invention further provides a method for preparing a catalyst precursor comprising the steps of (i) forming a ceramic foam comprising a closed cell structure, (ii) applying a cobalt compound to the ceramic foam and (iii) heating the cobalt-containing ceramic foam to form the catalyst precursor.

25 Various known methods may be used to form the ceramic foam comprising a closed cell structure. For example, a sacrificial template method may be used wherein a ceramic precursor in liquid form is mixed with a sacrificial template material, often another liquid, and the resulting composition heated to decompose the sacrificial material and create voids in the 30 final ceramic foam. A preferred method for preparing the ceramic foam is a direct foaming method, in which a liquid ceramic precursor or suspension of a ceramic powder in a suitable liquid is foamed by addition of a gas to create a wet foam, which is subsequently heated to give the final ceramic foam. A particularly preferred method includes (i) forming a suspension of a ceramic powder in a liquid (ii) adding a gas to the liquid to create a wet foam, and (iii) heating 35 the wet foam to form the ceramic foam. The suspension may contain one or more surfactant-type molecules, which may be termed "amphiphiles" that act with the ceramic powder to stabilise the wet foam. Thus preferably a stabilised wet foam may be prepared using a suspension of a ceramic powder containing an amphiphile. Methods for producing such particle-stabilised foams are known.

EP1960097-A1 describes a method to prepare wet foams exhibiting long-term stability wherein partially lyophobic colloidal particles are used to stabilize the gas-liquid interface. In one aspect, the particles are partially lyophobic in-situ by treating initially hydrophilic particles with amphiphilic molecules of specific solubility in the liquid phase of the suspension. This method has been found to be particularly useful for preparing catalyst precursors according to the present invention.

Thus a suitable method for preparing a ceramic foam support may include steps where:

1. A ceramic powder is suspended in an aqueous phase;
2. An amphiphile is included in the suspension. This adsorbs at the particles surfaces forming modified particles that are less hydrophilic.
3. Air or another gas is then included into the suspension forming bubbles and causing attachment of the modified particles at the gas/aqueous phase interface in the wet foam, thereby stabilising the wet foam, and,
4. The wet foam is further processed, e.g. by shaping, drying and/or calcination.

Powdered forms of the ceramic support materials listed above may therefore be used to prepare the wet foams. The mean particle size of the ceramic particles in the suspension may be in the range 1 nm to 20 μm , but is preferably in the range 2 nm – 10 μm , more preferably 2 nm – 2 μm . Where ceramic powders with larger mean particle sizes are used, preferably the suspension is subjected to milling to attain the desired mean particle size in these ranges. Good foams can be obtained with narrow as well as with broad particle size distributions. Ceramic powders that have been subjected to pre-treatment with a surface modifier may be used, including ceramic powders that have been pre-treated with an amphiphile.

The stabilizing colloidal particles of ceramic are initially hydrophilic and are partially hydrophobized, preferably in-situ, by the adsorption of amphiphilic molecules on the particle surface.

The amphiphilic molecules consist of a tail part coupled to a head group. The tail part may generally be described as non-polar and can be aliphatic (linear alkyl or cycloalkyl) or aromatic (phenyl or naphthyl) and can carry one or more substituents. Such substituents may be an alkyl group, e.g. $-\text{C}_n\text{H}_{2n+1}$ with $n < 8$, an aryl group (such as phenyl or substituted phenyl), $-\text{OH}$, or $-\text{NH}_2$. Preferred tail parts are optionally substituted linear carbon chains comprising 2 to 8 carbon atoms. The head group that is coupled to the tail part is preferably an ionic or polar group and may be selected from phosphates, phosphonates, phosphinates, sulphates, sulphonates, carboxylates (i.e. COOH), carboxylate esters, gallate esters, amides, amines including cyclic amines, and $-\text{OH}$. For Fischer-Tropsch catalysts carboxylic acids and esters are preferred to head groups that introduce sulphur or phosphorus.

Particularly preferred amphiphiles are C2-C6 carboxylic acids and esters thereof, such as valeric acid, butyric acid and propionic acid, and C2-C6 gallate esters such as propyl gallate. Furthermore we have found that particularly stable foams may be prepared using amino-acids, especially alpha-amino acids, where the amine group is attached to a carbon atom adjacent the carboxylate head group. Preferred alpha-amino acids include one or more of valine, isoleucine, leucine, phenyl alanine and tryptophan. Methionine may be used where the sulphur content of the resulting foam can be tolerated. Less preferred alpha-amino acids include alanine and tyrosine. Particularly preferred alpha-amino acid amphiphiles include one or more of leucine, isoleucine and phenylalanine. D, L or DL forms of each may be used. An especially suitable amino acid is phenyl alanine. DL-phenyl alanine may be used. Using amino acid amphiphiles has the advantage of producing stable foams with small bubbles without the handling difficulties of the carboxylic acids or problems caused by the acidic pH of carboxylic acids.

The pH of the suspension may be adjusted before the amphiphile is included, although may not be necessary. For example, the pH may be adjusted to a pH at which the surface charge of the ceramic powder is high enough for electrostatic stabilization. An acid, such as nitric acid, or a base may be added, but pH adjustment with alkali metals is not desirable for Fischer-Tropsch catalysts as alkali metals reduce the catalyst activity.

Dependent on the charge of the surface to be coated either a negatively charged or positively charged head group may be chosen. For e.g. Al_2O_3 , a negatively charged head group is suitable at low pH conditions, i.e. pH lower than the isoelectric point, here $\text{pH} < 9$, in particular pH 4-5. The above mentioned head groups and further similar groups can be used to modify a broad variety of ceramic particles, in particular metal oxides.

Surface modification can be achieved through the physical or chemical adsorption of negatively or positively charged amphiphile molecules onto a suitable, preferably an oppositely charged surface leaving the hydrophobic tail in contact with the aqueous phase. For e.g. positively-charged alumina particles the adsorption may be carried out with carboxylic acids in water at pH 4.75. By changing the anchoring polar head group of the amphiphile, the alumina surface can also be modified at alkaline pH conditions using for instance alkyl gallates as adsorbing molecule. This amphiphile can also be used to lyophobicize the surface of a variety of other amphoteric and basic oxides. Alternatively, the surface of acidic-like oxides such as silica, silicon carbide and silicon nitride can be lyophobicized employing amine-containing head group amphiphiles.

For the in-situ lyophobicization of particles, the amphiphile may be applied in amounts of less than 1 % by weight of the particles, preferably in amounts of < 0.8 % by weight. The minimum

amount of amphiphile that should be present may be about 0.001%, preferably about 0.1%. Amounts in the range 0.2 – 1.0 mmol amphiphile/g particles may be used. Since the amphiphile, besides of other ingredients of the suspension, also influences the viscosity of the foam, the actual amount of modifier used is chosen dependent on the desired final viscosity.

5

It has been found that ceramic particles with different shapes can be used as foam stabilizers, i.e. the ceramic particles may be spherical, polygonal plates, needles, fibres, rods, single crystals etc., provided that their particle size is within suitable dimensions. The particles themselves may be dense, i.e. non-porous, or porous, or mixtures of dense and porous particles may be used.

10

The particles are preferably present in amounts of at least about 5 % v/v in the suspension. The upper limit is provided by the viscosity that must not be too high. In general said viscosity should not exceed 10 Pa.s at a shear rate of 100 s⁻¹. The minimum amount needed to foam the whole suspension depends on the particle size and can easily be determined by the skilled person. In general the smaller the particles are, the lower the amount of particles to produce the stabilised wet foam will be. In the present invention, the solids concentration of the suspension is preferably in the range 10-45% by weight, preferably 25-35% by weight.

15

The wet foams are suitably formed at temperatures up to 90°C. The lower temperature is limited by freezing of the aqueous phase. The method appears to perform best where it is operated below the Krafft temperature for the amphiphile in question. The Krafft temperature (also known as Krafft point, or critical micelle temperature) is the minimum temperature at which surfactants form micelles. Below the Krafft temperature, there is no value for the critical micelle concentration (CMC), i.e., micelles cannot form.

20

The wet foam can be prepared using different methods, for example by incorporating bubbles of gas into the suspension. The incorporated bubbles may be small bubbles, or they may be big bubbles that upon shearing of the suspension are divided into the desired amount of small bubbles.

25

The air or another gas such as nitrogen, oxygen, argon and carbon dioxide, may be introduced to the suspension to generate the wet foam by any suitable means. For example foams may be produced by subjecting the suspension to a high intensity and/or high speed agitation while exposed to the atmosphere. The agitation may be carried out using a mixer, e.g. a mechanical mixer rotated at high speed. The agitation is carried out for a sufficient period to introduce bubbles of air into the suspension until expansion has been achieved according to the desired physical and other properties of the end product. The expansion ratio, i.e. the volume of foam formed compared to the volume of the starting suspension, can be between about 1.5 and

30

35

about 15. Hence dip tubes or sparger apparatus may be used. In one embodiment, a gas-inducing impeller may be used. A gas-inducing impeller introduces gas bubbles from the blades of the impeller as it rotates within the suspension. Gas-inducing impellers are known, but do not appear previously to have been used for producing ceramic foam materials.

- 5 Alternatively, the gas may be introduced by bubbling it through a filter of a defined pore size into the suspension while being stirred. In this case the final pore size of the foam may be dependent on the pore size of the filter. In a variation, high pressure gas is forced through a fine filter, then intimately mixed with the suspension in a suitable chamber and the aerated mixture is then ejected from a nozzle. Alternatively an aerosol method may be used, in which
- 10 the suspension is placed in a pressurised vessel and gas such as air or carbon dioxide is injected under pressure into the suspension to produce a foam when the pressure is released, e.g. via a nozzle.

- Bubbles may also be formed in the suspension by including a gas-forming reagent in the suspension and activating it by heat or chemical reaction to evolve a gas. Such gas forming reagents include sodium azide and hydrogen peroxide.
- 15

- The formation of bubbles in the suspension may be accomplished in a batch-wise manner or continuously.
- 20

- The aqueous phase comprises water, e.g. mains water or demineralised water, which may further comprise a hydrophilic solvent such as alcohols, glycols, etc. and mixtures thereof. Further additives, such as acids or bases can be added e.g. to adjust the pH and/or the ionic strength.
- 25

- As already mentioned above, the preferred pH or pH range is dependent on the head group used for in-situ lyophobicization and the particle surface to be modified. It should be such that at least about 1.5 %, preferably at least about 10 %, much preferred about 50 % of the head groups are negatively charged (deprotonated) or positively charged (protonated).
- 30

- The ionic strength can be adjusted to favour the close-packing of the attached particles at the interface and the attraction of particles within the foam lamella. However, the ionic strength should be kept low enough to ensure a sufficiently low viscosity of the suspension exists to allow sufficient introduction of air or good foaming.
- 35

- The viscosity of the suspension preferably is such that the viscosity is less than the level at which the introduction of gas cannot take place and above the level at which entrapped gas bubbles will tend to escape. In the absence of amphiphile addition, the viscosity may be 5 mPas to 1000mPas at a shear rate of 100 s^{-1} . The viscosity of the suspension when the

amphiphile is present may be in the range of about 5 mPa.s to about 10,000 mPa.s at a shear rate of 100 s^{-1} , preferably 25 mPa.s to about 5000 mPa.s. The preferred range is dependent on the method of gas entrapment.

- 5 The bubble size of the wet foam is dependent on all the above parameters, in particular the viscosity, the amount of additives, the amount of particles and the apparatus or the apparatus dependent method parameters used to get air into the suspension. The bubble size, e.g. diameter, may range from $1\text{ }\mu\text{m}$ to 1 mm , preferably from $1\text{ }\mu\text{m}$ to $500\text{ }\mu\text{m}$. The bubbles ultimately provide the cells in the catalyst precursor.
- 10 The wet foams may be cast into moulds for shaping or may be shaped by extrusion using conventional extrusion equipment suitably adjusted for the wet foam viscosity. The cast or extruded foams may then be subjected to a drying step to create a solid foam with sufficient green strength for further processing.
- 15 The drying can be carried out using a conventional oven at up to about 120°C . The drying time may be varied from 0.1-48 hours as desired to preserve the foam structure. The drying may be done at atmospheric or reduced pressure. At reduced pressure the foam may expand before the green strength is developed. The degree of expansion and hence the cell size of the foam
- 20 will depend on the pressure selected. Drying at elevated temperature may also cause a slight expansion of the foam. It is preferred to control the humidity during the drying step, to prevent uneven shrinkage and drying cracks. Temperature-assisted or vacuum-assisted unidirectional drying leads to an even shrinkage of the sample without inducing stresses which would result in cracks. Freeze drying may also be used.
- 25 The suspension may include other ingredients, which play a role at the drying stage. Examples of such ingredients include binders such as resins, e.g. polyvinylchloride, gums, cellulose, starch, polyvinyl alcohol, oligo- and poly-saccharides to increase green strength. Polymerisable materials may also be included although this is less preferred. Although the
- 30 addition of binders in general is not needed to produce suitable wet foams, such additives may have advantages if high green strength after drying is desired. The body formed in the presence of binders or polymerizable materials after drying is relatively robust, and the addition of binders or polymerizable materials can be preferred when the article to be formed is of a complex shape.
- 35 The cast or extruded foams may be subjected to additional shaping steps, including for example milling or grinding the ceramic foam to a desired particle size, sieving, granulating pelleting and other shaping procedures known in the art.

The foam may be subjected to a heating step or calcination in which the ceramic particles are fused together to form a porous catalyst support material. Such heating may be done at temperatures in the range 500-1600°C or higher depending on the ceramic, although to retain a suitable pore structure in the cell walls, it may be desirable to calcine the ceramic foams below about 1200°C. The calcination may be performed for 1-24 hours, preferably 1-8 hours, depending on the temperature chosen. The heating step may be performed under air or an inert atmosphere such as nitrogen or argon. The latter may be preferred where decomposition of organic residues is expected.

- 10 The invention includes the step of applying cobalt oxide, or a precursor thereof, to the ceramic foam. This may be accomplished by applying a wash-coat slurry containing cobalt oxide, but this is less preferred because the foam comprises a closed cell structure and so the cobalt will not be able to penetrate the foam beyond the surface cells. Therefore preferably the catalyst precursor is prepared using one or more soluble cobalt compounds in solution. The cobalt
- 15 compound may be an organic cobalt compounds such as cobalt acetylacetonate, a cobalt complex such as cobalt ammine carbonate, or may be a cobalt salt such as cobalt acetate and/or cobalt nitrate. One or more soluble cobalt compounds may be used. Thus in a preferred method, a soluble cobalt compound is dissolved in a suitable solvent, such as water, to form a cobalt solution and the cobalt solution applied to the ceramic foam, e.g. by spraying
- 20 or dipping, to impregnate the cells and cell wall pores. In addition to soluble cobalt compounds, one or more soluble promoter compounds may be included in the cobalt solution or may be applied to the foam in a separate impregnation step. Soluble compounds of Pt, Pd, Ru and Re are preferred.
- 25 The impregnated ceramic foam may then be subjected to drying to remove the solvent and leave the cobalt deposited within the foam. The cobalt may be deposited as a salt or complex or may be cobalt oxide depending upon the method used to impregnate the ceramic foam. The cobalt and any promoters are preferably uniformly deposited within the ceramic foam. A particularly suitable method for depositing cobalt uses a cobalt ammine carbonate complex,
- 30 which upon oxidation and heating deposits cobalt oxide directly within the cells and pores of the ceramic foam.

- The cobalt compounds may if desired be subjected to a heating step or calcination to cause their decomposition to form cobalt oxide. This may accompany the drying step, or the
- 35 calcination step may be performed separately. The conversion of cobalt compounds to cobalt oxide may conveniently be accomplished by heating the impregnated or dried cobalt-containing ceramic foam to temperatures up to about 800°C, preferably 200-800°C, more preferably 200-600°C, most preferably 200-400°C under air or an inert gas such as nitrogen or argon. The

calcination of the cobalt compounds may be performed over 0.5-8 hours depending on the temperature.

5 The catalyst precursor, where the cobalt is in oxidic form, may be provided for use in a Fischer-Tropsch process. Before use, the catalyst precursor is activated to produce a catalyst suitable for the Fischer-Tropsch reaction by reducing the cobalt oxide in the catalyst precursor to cobalt metal.

10 Alternatively the catalyst precursor may be pre-reduced and encapsulated to provide a catalyst product for use in the Fischer Tropsch process.

15 Reduction may be performed by passing a hydrogen-containing gas such as hydrogen, synthesis gas or a mixture of hydrogen with nitrogen, methane or other inert gas over the catalyst precursor at elevated temperature, for example by passing the hydrogen-containing gas over the composition at temperatures in the range 150-600°C, preferably 250-600°C, preferably 275-500°C for between 1 and 24 hours. Reduction may be performed at atmospheric or higher pressures up to about 25 bar abs.

20 Catalysts in the reduced state can be difficult to handle as they can react spontaneously with oxygen in air, which can lead to undesirable self-heating and loss of activity. For catalysts suitable for Fischer-Tropsch processes, the reduced catalyst is preferably protected by encapsulation of the reduced catalyst particles with a suitable barrier coating. In the case of a Fischer-Tropsch catalyst, this may suitably be a FT-hydrocarbon wax. Alternatively, the catalyst can be provided in the unreduced state and reduced in-situ with a hydrogen-containing gas.

25 Cobalt catalysts prepared on the ceramic foam supports may have cobalt surface areas (as determined by hydrogen chemisorption at 150°C following reduction at 425°C) of $\geq 1\text{m}^2/\text{g}$ catalyst. The cobalt surface area may suitably be determined by H_2 chemisorption. The preferred method is as follows; approximately 0.2 to 0.5 g of sample material is firstly degassed and dried by heating to 140°C at 10°C/min in flowing helium and holding it at 140°C for 60 mins. The degassed and dried sample is then reduced by heating it from 140°C to 425°C at a rate of 3°C/min under a 50 ml/min flow of hydrogen and then holding it under the same hydrogen flow, at 425°C for 6 hours. Following reduction and under vacuum, the sample is heated up to 450°C at 10°C/min and held under these conditions for 2 hours. The sample is then cooled to 150°C and held for a further 30 minutes under vacuum. The chemisorption analysis is carried out at 150°C using pure hydrogen gas. An automatic analysis program is used to measure a full isotherm over the range 100 mmHg up to 760 mmHg pressure of hydrogen. The analysis is carried out twice; the first measures the "total" hydrogen uptake (i.e.

includes chemisorbed hydrogen and physisorbed hydrogen) and immediately following the first analysis the sample is put under vacuum (< 5mm Hg) for 30 mins. The analysis is then repeated to measure the physisorbed uptake. A linear regression may then be applied to the "total" uptake data with extrapolation back to zero pressure to calculate the volume of gas chemisorbed (V).

Cobalt surface areas were calculated in all cases using the following equation;

$$\text{Co surface area} = (6.023 \times 10^{23} \times V \times \text{SF} \times A) / 22414$$

where V = uptake of H₂ in ml/g

SF = Stoichiometry factor (assumed 2 for H₂ chemisorption on Co)

A = area occupied by one atom of cobalt (assumed 0.0662 nm²)

This equation is described in the Operators Manual for the Micromeritics ASAP 2010 Chemi System V 2.01, Appendix C, Part No. 201-42808-01, October 1996.

The catalysts may be used for the Fischer-Tropsch synthesis of hydrocarbons. Accordingly, the invention further provides a process for the Fischer-Tropsch synthesis of hydrocarbons comprising contacting a gas mixture containing hydrogen and carbon monoxide over a cobalt-catalyst comprising a ceramic foam support comprising a closed cell structure

The Fischer-Tropsch synthesis of hydrocarbons with cobalt catalysts is well established. The Fischer-Tropsch synthesis converts a mixture of carbon monoxide and hydrogen to hydrocarbons. The mixture of carbon monoxide and hydrogen is typically a synthesis gas having a hydrogen: carbon monoxide ratio in the range 1.6-3.0:1, preferably 1.7 – 2.5:1. The reaction may be performed in a continuous or batch process using one or more fixed bed reactors, stirred slurry-phase reactors, jet-loop reactors, bubble-column reactors, or fluidised bed reactors. The process may be operated at pressures in the range 0.1-10Mpa and temperatures in the range 150-350°C, preferably 200-250°C. The gas-hourly-space velocity (GHSV) for continuous operation is in the range 100-25000hr⁻¹. A preferred operating range is 1000-15000hr⁻¹.

The catalysts of the present invention are able to provide exceptionally high selectivity to the desired C5+ hydrocarbons, for example C5+ selectivity for titania-foam-supported FT catalysts maybe over 90%.

The invention will now be further described by reference to the following examples.

Example 1 Titania foam preparation

- a) A ceramic foam was prepared using a titania suspension containing 30% wt solids. 128 g titania powder (P25 available from Evonik) were added slowly to 300 ml demineralised water in a stirred vessel. Then, without pH adjustment, 0.36 mmol DL-phenylalanine were added per gram of titania (7.6 g DL-phenylalanine). The pH of the suspension was 4.59. Air was then introduced into the suspension to form bubbles using a gas inducing impeller for 30 minutes. The foam was cast into a tray and dried at room temperature and at atmospheric pressure. It was then calcined with a nitrogen purge by heating at 2 °C/ min to 600 °C. After 45 minutes at 600 °C the nitrogen flow was replaced by air. The total dwell at 600 °C was 4 hours. The resulting ceramic foam support was crushed and sieved to 0.5 mm.

A porosity measurement was made by immersing the ceramic foam in demineralised water at room temperature for 4 days and measuring the water up-take by the increase in weight. The porosity measured in this way includes the volume of the cells and accessible pores and indicates the volume of cobalt solution that may be used to prepare the catalyst. The porosity of the foamed titania was 0.8 cm³/g after 4 days.

- b) The method was repeated for different titania contents in the suspension as follows;

Titania weight %	DL-phenylalanine mmol/g titania	pH	Porosity cm ³ g ⁻¹
17.5	0.82	4.65	2.2
20.0	0.36	4.50	1.6
20.0	0.54	4.52	1.5
20.0	0.72	4.56	1.4
25.0	0.39	4.56	0.9
25.0	0.54	4.58	1.0

20

- c) The method was repeated, replacing the phenyl alanine with n-butyric acid. pH adjustment was required before air entrainment using potassium hydroxide.

Titania weight %	Butyric Acid mmol/g titania	pH after butyric acid addition	Foaming	pH after KOH addition	Porosity cm ³ g ⁻¹
20	0.36	3.86	Not Observed	4.65	2.3
20	0.54	3.71	-	4.65	2.2
20	0.72	3.66	-	4.40	1.8

25	0.36	3.71	-	4.50	1.8
25	0.54	3.68	-	4.50	1.5
25	0.72	3.56	-	4.00	1.4
30	0.36	3.66	-	4.30	1.2
30	0.54	3.60	-	4.30	1.4
30	0.72	2.46	-	3.20*	1.1

*pH was not increased further since an increase in viscosity was observed

- d) The method was repeated, replacing the phenylalanine with other alpha-amino acids. Unless otherwise indicated, no pH adjustment was performed prior to air entrainment.

5

Example	Titania weight %	DL-amino acid mmol/g titania	pH	Porosity cm^3g^{-1}
1(d)(i)	30	0.21 DL-leucine	3.66	0.62
1(d)(ii)	30	0.54 DL-valine	4.02	0.47
1(d)(iii)	30	0.43 DL-phenyl alanine	1.60*	0.45
1(d)(iv)	25	0.36 DL-Leucine	0.93*	0.52
1(d)(v)	20	0.22 DL-tryptophan	3.25	0.50
1(d)(vi)	20	0.74 DL-leucine	3.96	2.84
1(d)(vii)	25	0.72 DL-isoleucine	1.28*	0.63
1(d)(viii)	25	0.72 DL-methionine	1.21*	0.44

*pH adjusted by addition of nitric acid

Example 2: Catalyst precursor preparation

- a) Cobalt nitrate impregnation of titania foam of Example 1(a).
- 10 7 g of cobalt nitrate hexahydrate ($\text{Co}(\text{NO}_3)_2 \cdot 6\text{H}_2\text{O}$) and 2.2 ml demineralised water were heated until the melting and dissolution of the salt were complete. This was added in aliquots to 15 g of the ceramic foam product of Example 1(a) in a plastic bag. After each addition the material was kneaded into the support. The impregnated foam was dried for 2 hours at 105°C and calcined for 2 hours at 300°C. The process was then repeated. 5.5 g $\text{Co}(\text{NO}_3)_2 \cdot 6\text{H}_2\text{O}$ and
- 15 2.74 ml demineralised water were heated until the melting and dissolution of the salt were complete. This was added in aliquots to 16.5 g of the impregnated ceramic foam product from the first impregnation in a plastic bag. After each addition the material was kneaded into the support. The resulting material was dried for 2 hours at 105°C and calcined for 2 hours at 300°C. The cobalt content of the catalyst precursor by ICPAES was 10.8 %wt. The cobalt
- 20 surface area as determined by hydrogen chemisorption was 1.0 m^2/g catalyst.

b) Cobalt ammine-carbonate impregnation of titania foam of Example 1(a).

A cobalt ammine carbonate solution was prepared as follows; 198 ml of a 28% ammonia solution was added to 20.4 g ammonium carbonate in a round bottomed flask and diluted with 193.4 ml demineralised water. The resulting solution was stirred for 20 minutes then 23.7 g of cobalt basic carbonate was added over 15 minutes and the solution stirred at 150 rpm for a further 2.5 hr to give a purple solution. 30% hydrogen peroxide solution was added drop wise while the solution was stirred at 234 rpm until the Oxido-reduction potential (Mettler Toledo transmitter M 700) was near to -100 mV. Stirring was continued for a further 10 minutes and then the solution was filtered.

385 ml of the Co ammine carbonate solution (2.6% w/w Co) was added to a 2 L four-necked round bottom flask. A stirrer, temperature probe, lute and condenser were fitted to the flask. 52 g of the ceramic foam product of Example 1(a) was added. This mixture was then diluted with 385 mL water and 165 mL ammonia before being heated and agitated for 80 minutes to cause evolution of the ammonia and deposition of cobalt oxide in the cells and pores of the ceramic foam. The mixture was filtered and washed with 80 ml demineralised water. The catalyst precursor was dried at 105°C for 8 hours. It was not calcined. The cobalt content of the catalyst precursor by ICPAES was 11.2 %wt. The cobalt surface area as determined by hydrogen chemisorption was 1.1 m²/g catalyst.

c) Cobalt ammine-carbonate impregnation of titania foams of Examples 1(d) (i) – (iv).

The method of Example 2(b) was repeated using instead the titania foams obtained in Examples 1(d) (i) – (iv). The target cobalt content in each case was 13% by weight. The cobalt surface areas for the catalyst precursors, as determined by hydrogen chemisorption, are set out below.

Foam	Cobalt Surface Area (m ² / g catalyst)
1(d)(i)	3.9
1(d)(ii)	1.6
1(d)(iii)	1.5
1(d)(iv)	1.5

Example 3 Catalyst testing

0.5 g of the catalyst from Example 2(a) was tested for catalytic performance in Fischer-Tropsch synthesis. The reaction conditions were syngas (H₂:CO of 2:1) flow rate 30 ml_N/min, 20 bar and 210°C with GHSV 3590 ml_N sygas.g catalyst⁻¹.h⁻¹ and a target conversion of 50%. The selectivity to C5+ was 92%.

0.25 g of the catalyst from Example 2(b) was tested for catalytic performance in Fischer-Tropsch synthesis. The reaction conditions were syngas ($H_2:CO$ 2:1) flow rate 44 ml_N/min , 20 bar and 210°C with GHSV 10338 ml_N syngas.g catalyst⁻¹.h⁻¹ and a target conversion of 50%. The selectivity to C5+ was 91%.

5

0.25 g of each of the catalysts from Example 2(c) was tested for catalytic performance in Fischer-Tropsch synthesis. The reaction conditions were syngas ($H_2:CO$ of 2:1), 20 bar and 210°C and a target conversion of 50%. The remaining reaction conditions and selectivity to C5+ for the catalysts based on the different foam materials were as follows;

10

Foam	Flow Rate (ml_N/min)	Pressure (bar)	Temperature (°C)	GHSV (ml_N syngas.g catalyst ⁻¹ .h ⁻¹)	Selectivity to C5+
1(d)(i)	49.48	20	210	12082	89.51
1(d)(ii)	33.98	20	210	7816	89.90
1(d)(iii)	15.20	20	210	3461	86.71
1(d)(iv)	15.13	20	210	3642	90.02

Claims.

1. A catalyst precursor suitable for the Fischer Tropsch reaction comprising cobalt oxide supported on a porous support wherein the porous support is a ceramic foam comprising a closed cell structure.
2. A catalyst precursor according to claim 1 wherein the cobalt content of the catalyst precursor, expressed as Co, is in the range 5-50% by weight, preferably 10-40% by weight, more preferably 10-30% by weight.
3. A catalyst precursor according to claim 1 or claim 2 wherein up to 20% of the cell volume, preferably less than 10% of the cell volume, is interconnected.
4. A catalyst precursor according to any one of claims 1 to 3 wherein the average cell diameter is in the range 10-150 μm , preferably 10-100 μm .
5. A catalyst precursor according to any one of claims 1 to 4 wherein the cell fraction of the foams is in the range 50-95% by volume, preferably 75-90% by volume.
6. A catalyst precursor according to any one of claims 1 to 5 wherein the cell wall thicknesses is up to 500 μm , preferably up to 200 μm , with an average in the range 10-100 μm , preferably 25-85 μm .
7. A catalyst precursor according to any one of claims 1 to 6 wherein the ceramic foam comprises titania.
8. A method for preparing a catalyst precursor according to any one of claims 1 to 7, comprising the steps of (i) forming a ceramic foam comprising a closed cell structure, (ii) applying a cobalt compound to the ceramic foam and (iii) heating the cobalt-containing foamed metal oxide to form the catalyst precursor.
9. A method according to claim 8 wherein the ceramic foam is formed by steps comprising (i) forming a suspension of a ceramic powder in a liquid (ii) adding a gas to the liquid to create a wet foam, and (iii) heating the wet foam to form the ceramic foam.
10. A method according to claim 9 wherein the ceramic powder particle size in the suspension is in the range 1 nm to 20 μm , preferably in the range 2 nm – 10 μm , more preferably 2 nm – 2 μm .

11. A method according to claim 9 or claim 10 wherein the suspension contains one or more amphiphiles that act with the ceramic powder to stabilise the wet foam.
12. A method according to claim 11 wherein the amphiphiles comprise one or more of C2-C6 carboxylic acids and esters thereof, C2-C6 gallate esters and alpha amino acids.
13. A method according to claim 11 or claim 12 wherein the amphiphile comprises one or more of valine, isoleucine, leucine, phenylalanine or tryptophan, preferably one or more of leucine, isoleucine and phenyl alanine, more preferably phenyl alanine.
14. A method according to any one of claims 9 to 13 wherein the wet foam is shaped before heating.
15. A method according to claim 14 wherein the shaped foam is subjected to a heating step at temperatures in the range 500-1600°C.
16. A method according to any one of claims 8 to 15 wherein the cobalt compound applied to the ceramic foam is an organic cobalt compound, a cobalt complex or a cobalt salt.
17. A catalyst prepared using a catalyst precursor according to any one of claims 1 to 7 or prepared according to any one of claims 8 to 16 comprising cobalt in elemental form supported on a porous support, wherein the porous support is a ceramic foam comprising a closed cell structure.
18. A catalyst according to claim 17 encapsulated in a hydrocarbon wax.
19. A method for the preparation of a catalyst according to claim 17 or claim 18 comprising the steps of preparing a catalyst precursor according to any one of claims 9 to 16 and applying a reducing gas stream to the catalyst precursor to convert at least a portion of the cobalt oxide to elemental form.
20. A process for producing hydrocarbons by the Fischer-Tropsch reaction comprising contacting a synthesis gas comprising carbon monoxide and hydrogen with a catalyst according to claim 17 or claim 18.

(12) INTERNATIONAL APPLICATION PUBLISHED UNDER THE PATENT COOPERATION TREATY (PCT)

(19) World Intellectual Property
Organization
International Bureau



WIPO | PCT



(10) International Publication Number
WO 2016/156790 A1

(43) International Publication Date
6 October 2016 (06.10.2016)

- (51) International Patent Classification:
C04B 35/01 (2006.01) C04B 38/10 (2006.01)
- (21) International Application Number:
PCT/GB2016/050697
- (22) International Filing Date:
15 March 2016 (15.03.2016)
- (25) Filing Language: English
- (26) Publication Language: English
- (30) Priority Data:
1505558.5 31 March 2015 (31.03.2015) GB
- (71) Applicant: JOHNSON MATTHEY PUBLIC LIMITED
COMPANY [GB/GB]; 5th floor, 25 Farringdon Street,
London EC4A 4AB (GB).
- (72) Inventors: CELANI, Andrea; Johnson Matthey Process
Technologies, PO Box 1, Belasis Avenue, Chilton, Billin-
gham, Cleveland TS23 1LB (GB). HOLT, Elizabeth Mar-
garet; Johnson Matthey Process Technologies, PO Box 1,
Belasis Avenue, Chilton, Billingham, Cleveland TS23 1LB
(GB).
- (74) Agent: RIDLAND, John; Johnson Matthey Process Tech-
nologies, PO Box 1, Belasis Avenue, Billingham, Cleve-
land TS23 1LB (GB).

(81) Designated States (unless otherwise indicated, for every
kind of national protection available): AE, AG, AL, AM,
AO, AT, AU, AZ, BA, BB, BG, BH, BN, BR, BW, BY,
BZ, CA, CH, CL, CN, CO, CR, CU, CZ, DE, DK, DM,
DO, DZ, EC, EE, EG, ES, FI, GB, GD, GE, GH, GM, GT,
HN, HR, HU, ID, IL, IN, IR, IS, JP, KE, KG, KN, KP, KR,
KZ, LA, LC, LK, LR, LS, LU, LY, MA, MD, ME, MG,
MK, MN, MW, MX, MY, MZ, NA, NG, NI, NO, NZ, OM,
PA, PE, PG, PH, PL, PT, QA, RO, RS, RU, RW, SA, SC,
SD, SE, SG, SK, SL, SM, ST, SV, SY, TH, TJ, TM, TN,
TR, TT, TZ, UA, UG, US, UZ, VC, VN, ZA, ZM, ZW.

(84) Designated States (unless otherwise indicated, for every
kind of regional protection available): ARIPO (BW, GH,
GM, KE, LR, LS, MW, MZ, NA, RW, SD, SL, ST, SZ,
TZ, UG, ZM, ZW), Eurasian (AM, AZ, BY, KG, KZ, RU,
TJ, TM), European (AL, AT, BE, BG, CH, CY, CZ, DE,
DK, EE, ES, FI, FR, GB, GR, HR, HU, IE, IS, IT, LT, LU,
LV, MC, MK, MT, NL, NO, PL, PT, RO, RS, SE, SI, SK,
SM, TR), OAPI (BF, BJ, CF, CG, CI, CM, GA, GN, GQ,
GW, KM, ML, MR, NE, SN, TD, TG).

Published:

— with international search report (Art. 21(3))

(54) Title: METHOD FOR PREPARING PARTICLE-STABILIZED FOAMS COMPRISING AMINO ACIDS

(57) Abstract: A method is described for preparing a particle-stabilised foam comprising the steps of (i) forming a suspension of a particulate material in an aqueous medium containing an amphiphile and (ii) introducing a gas into the dispersion to generate a foam, wherein the amphiphile is an amino acid.



WO 2016/156790 A1

**METHOD FOR PREPARING PARTICLE-STABILIZED FOAMS COMPRISING
AMINO ACIDS**

The present invention relates to a method for preparing particle-stabilised foams, in particular particle-stabilised foams suitable for use as catalysts or sorbents or supports therefor.

5

WO2007/068127 A1 discloses a method to prepare wet foams exhibiting long-term stability wherein partially lyophobic colloidal particles are used to stabilize the gas-liquid interface of a foam. In one aspect, the particles are partially lyophobicized in-situ by treating initially hydrophilic particles with amphiphilic molecules of specific solubility in the liquid phase of the

10

suspension. Amphiphiles specifically disclosed were C2-C6 carboxylic acids, including butyric acid and propionic acid, and propyl gallate. The carboxylic acids are unpleasant to handle and attack pH-sensitive materials. The low pH may also require adjustment in order to generate foams.

15

We have found that surprisingly effective foams may be produced using amino acid amphiphiles.

Accordingly the invention provides a method for preparing a particle-stabilised foam comprising the steps of (i) forming a suspension of a particulate material in an aqueous medium containing

20

an amphiphile and (ii) introducing a gas into the dispersion to generate a foam, wherein the amphiphile is an amino acid.

The invention further provides a method for preparing a solid foam from the particle-stabilised foam, and a solid foam obtained by the method.

25

The method for preparing the particle-stabilised foam is a direct foaming method, in which a suspension of a particulate material in a suitable liquid is foamed by addition of a gas to create a wet particle-stabilised foam, which may be subsequently heated to remove liquid and form a solid foam material.

30

The particulate material may be a ceramic material, a catalyst material or a sorbent material. (By "sorbent" we include adsorbent and absorbent). Thus the particle-stabilised foam may be prepared using a suspension of a ceramic powder, a catalyst powder or a sorbent powder. The foam may also be prepared using a metal powder.

35

Thus, the particulate material may be a ceramic powder, such as a metal oxide or other ceramic material, such as SiC. Metal oxides are preferred and suitable foams may be prepared using alumina, metal-aluminates, magnesia, silica, lanthana, ceria, titania, zirconia and mixtures of these. Zeolite powders may also be considered herein to be a ceramic

material. The particulate ceramic materials are preferably those suitable for use as supports for catalysts and sorbents. The resulting ceramic foams may be treated with catalyst or sorbent materials in subsequent processing steps.

- 5 The particulate material may be a catalyst powder. A catalyst powder may be any composition containing a catalytically active metal or a precursor thereto. Catalyst powders include one or more of the oxides, hydroxides, carbonates and/or hydroxycarbonates of metals. The metals may be supported or unsupported. Suitable catalytic metals may comprise one or more metals selected from Na, K, Mg, Ca, Ba, Al, Si, Ti, V, Cr, Mn, Fe, Co, Ni, Cu, Zn, Y, Zr, Nb, Mo, Ru, Rh, Pd, Ag, Sn, Sb, La, Hf, W, Ag, Re, Ir, Pt, Au, Pb, or Ce. Hence the catalyst powder may
- 10 comprise one or more transition metals such as nickel, cobalt, iron or copper, and/or one or more precious metals such as silver, gold, platinum, palladium, rhodium iridium or ruthenium that are present in the form of the metal, an oxide, hydroxide, carbonate or hydroxycarbonate. Such catalyst materials may be supported on a refractory oxide such as alumina, calcium
- 15 aluminate, magnesium aluminate, titania or zirconia. Examples of particulate transition metal catalyst powders include copper/alumina compositions, copper/zinc oxide/alumina compositions, cobalt/alumina compositions, cobalt titania compositions, nickel/alumina compositions, nickel/metal aluminate compositions, iron/copper/alumina compositions, iron/molybdenum compositions and zinc oxide/alumina compositions. Examples of particulate
- 20 precious metal compositions include platinum/alumina compositions, palladium alumina compositions and ruthenium alumina compositions. The transition metal and precious metal content in such catalysts may be up to 85% by weight, but is preferably in the range 0.1-60% by weight.
- 25 The sorbent powder may be a zeolite material or a reactive composition that is capable of adsorbing contaminants such as sulphur compounds, mercury or arsenic compounds and halogen or halogen compounds from gaseous or liquid process fluids. Sorbent compositions suitable for adsorbing sulphur compounds may comprise one or more metals selected from Mn, Fe, Cu and Zn, which may be present as an oxide, hydroxide, carbonate and/or
- 30 hydroxycarbonate of the metals. Sorbent compositions suitable for adsorbing mercury and/or arsenic compounds may comprise one or more metals selected from Mn, Fe, Cu and Zn, which may be present as a sulphide of the metals. Pd supported on an metal oxide support may also be used. Sorbent compositions suitable for adsorbing mercury and/or arsenic compounds may comprise one or more metals selected from Mn, Fe, Cu and Zn, which may be present as a
- 35 sulphide of the metals. Sorbent compositions suitable for adsorbing halogen, particularly chlorine compounds may comprise one or more metals selected from Na, K, Ca and Mg, which may be present as an oxide, carbonate or hydrogen carbonate.

The mean particle size of the particles in the suspension may be in the range 1 nm to 20 μm , but is preferably in the range 2 nm – 10 μm , more preferably 2 nm – 2 μm . Where powders with larger mean particle sizes are used, preferably the suspension is subjected to milling to attain the desired mean particle size in these ranges. Good foams can be obtained with narrow
5 as well as with broad particle size distributions. Particulate materials that have been subjected to pre-treatment with a surface modifier may be used, including powders that have been pre-treated with an amphiphile.

Thus a suitable method for preparing a foam may include steps where:

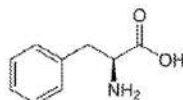
- 10 1. A particulate material is suspended in an aqueous phase;
2. An amino acid amphiphile is included in the suspension. This adsorbs at the particles surfaces forming modified particles that are less hydrophilic.
3. Air or another gas is then included into the suspension forming bubbles and causing attachment of the modified particles at the gas/aqueous phase interface in the wet
15 foam, thereby stabilising the wet foam, and,
4. The particle-stabilised foam is further processed, e.g. by shaping, drying and/or calcination.

The stabilizing colloidal particles are initially hydrophilic and are partially hydrophobized,
20 preferably in-situ, by the adsorption of amino acid amphiphilic molecules on the particle surface.

The amphiphilic amino acid molecules consist of a tail part coupled to a head group. The tail part may generally be described as non-polar and can be aliphatic (linear alkyl or cycloalkyl) or
25 aromatic (phenyl or naphthyl) and can carry one or more substituents. Such substituents may be an alkyl group, e.g. $-\text{C}_n\text{H}_{2n+1}$ with $n < 8$, and/or an aryl group (such as phenyl or substituted phenyl). Preferred tail parts are optionally substituted linear carbon chains comprising 2 to 8 carbon atoms. The head group that is coupled to the tail part may be generally described as polar and comprises a carboxylate group (i.e. COOH). In the present invention amphiphile
30 comprises an amino group (i.e. an $-\text{NH}_2$ substituent) such that the amphiphile is an amino-acid.

Particularly preferred amphiphiles are alpha-amino acids, where the amine group is attached to a carbon atom adjacent the carboxylate head group. The amphiphile may then be considered to be of formula; $\text{R}^1-\text{CR}^2(\text{NH}_2)\text{COOH}$, where R^1 is the tail group and R^2 is H, alkyl or aryl.
35 Preferred alpha-amino acids include one or more of valine, isoleucine, leucine, phenyl alanine and tryptophan. Methionine may be used where the sulphur content of the resulting foam can be tolerated. Less preferred alpha-amino acids include alanine and tyrosine. Particularly preferred alpha-amino acid amphiphiles include one or more of leucine, isoleucine and

phenylalanine. D, L or DL forms of each may be used. An especially suitable amino acid is phenyl alanine. DL-phenyl alanine may be used.



- 5 Using an alpha-amino acid amphiphile has the advantage of producing stable foams with small bubbles without the handling difficulties of the carboxylic acids or problems caused by the acidic pH of carboxylic acids.

- The pH of the suspension may be adjusted before the amphiphile is included. For example,
10 the pH may be adjusted to a pH at which the surface charge of the particulate material is high enough for electrostatic stabilization. However one advantage of the amino acid amphiphile is that pH adjustment is not usually necessary. Preferably the foaming stage is performed without pH adjustment of the suspension.

- 15 For the in-situ lyophobicization of particles, the amino acid amphiphile may be applied in amounts of less than 1 % by weight of the particles, preferably in amounts of <0.8 % by weight. The minimum amount of amphiphile that should be present may be about 0.001%, preferably about 0.1%. Amounts in the range 0.2 – 1.0 mmol amphiphile/g particles may be used. Since
20 the amphiphile, besides of other ingredients of the suspension, also influences the viscosity of the foam, the actual amount of modifier used is chosen dependent on the desired final viscosity.

- It has been found that particles with different shapes can be used as foam stabilizers, i.e. the particles may be spherical, polygonal plates, needles, fibres, rods, single crystals etc., provided
25 that their particle size is within suitable dimensions. The particles themselves may be dense, i.e. non-porous, or porous, or mixtures of dense and porous particles may be used.

- The particles are preferably present in amounts of at least about 5 % v/v in the suspension. The upper limit is provided by the viscosity that must not be too high. In general said viscosity
30 should not exceed 10 Pa.s at a shear rate of 100 s⁻¹. The minimum amount needed to foam the whole suspension depends on the particle size and can easily be determined by the skilled person. In general the smaller the particles are, the lower the amount of particles to produce the stabilised wet foam will be. In the present invention, the solids concentration of the suspension is preferably in the range 10-45% by weight, preferably 25-35% by weight.

- 35 The wet foams are suitably formed at temperatures up to 90°C. The lower temperature is limited by freezing of the aqueous phase. The method appears to perform best where it is

operated below the Krafft temperature for the amphiphile in question. The Krafft temperature (also known as Krafft point, or critical micelle temperature) is the minimum temperature at which surfactants form micelles. Below the Krafft temperature, there is no value for the critical micelle concentration (CMC), i.e., micelles cannot form.

5

The wet foam can be prepared using different methods, for example by incorporating bubbles of gas into the suspension. The incorporated bubbles may be small bubbles, or they may be big bubbles that upon shearing of the suspension are divided into the desired amount of small bubbles.

10

The air or another gas such as nitrogen, oxygen, argon and carbon dioxide, may be introduced to the suspension to generate the wet foam by any suitable means. For example foams may be produced by subjecting the suspension to a high intensity and/or high speed agitation while exposed to the atmosphere. The agitation may be carried out using a mixer, e.g. a mechanical mixer rotated at high speed. The agitation is carried out for a sufficient period to introduce bubbles of air into the suspension until expansion has been achieved according to the desired physical and other properties of the end product. The expansion ratio, i.e. the volume of foam formed compared to the volume of the starting suspension, can be between about 1.5 and about 15. Hence dip tubes or sparger apparatus may be used. In one embodiment, a gas-inducing impeller may be used. A gas-inducing impeller introduces gas bubbles from the blades of the impeller as it rotates within the suspension. Alternatively, the gas may be introduced by bubbling it through a filter of a defined pore size into the suspension while being stirred. In this case the final pore size of the foam may be dependent on the pore size of the filter. In a variation, high pressure gas is forced through a fine filter, then intimately mixed with the suspension in a suitable chamber and the aerated mixture is then ejected from a nozzle. Alternatively an aerosol method may be used, in which the suspension is placed in a pressurised vessel and gas such as air or carbon dioxide is injected under pressure into the suspension to produce a foam when the pressure is released, e.g. via a nozzle.

30

Bubbles may also be formed in the suspension by including a gas-forming reagent in the suspension and activating it by heat or chemical reaction to evolve a gas. Such gas forming reagents include sodium azide and hydrogen peroxide.

35

The formation of bubbles in the suspension may be accomplished in a batch-wise manner or continuously.

The aqueous phase comprises water, e.g. mains water or demineralised water, which may further comprise a hydrophilic solvent such as alcohols, glycols, etc. and mixtures thereof. Further additives, such as acids or bases can be added e.g. to adjust the pH and/or the ionic

strength. The ionic strength can be adjusted to favour the close-packing of the attached particles at the interface and the attraction of particles within the foam lamella. However, the ionic strength should be kept low enough to ensure a sufficiently low viscosity of the suspension exists to allow sufficient introduction of air or good foaming.

5

The viscosity of the suspension preferably is such that the viscosity is less than the level at which the introduction of gas cannot take place and above the level at which entrapped gas bubbles will tend to escape. In the absence of amphiphile addition, the viscosity may be 5 mPas to 1000mPas at a shear rate of 100 s^{-1} . The viscosity of the suspension when the amphiphile is present may be in the range of about 5 mPas to about 10,000 mPa.s at a shear rate of 100 s^{-1} , preferably 25 mPa.s to about 5000 mPa.s. The preferred range is dependent on the method of gas entrapment.

15 The bubble size of the wet foam is dependent on all the above parameters, in particular the viscosity, the amount of additives, the amount of particles and the apparatus or the apparatus dependent method parameters used to get air into the suspension. The bubble size, e.g. diameter, may range from $1 \mu\text{m}$ to 1 mm , preferably from $1 \mu\text{m}$ to $500 \mu\text{m}$. The bubbles ultimately provide the cells in the solid foam.

20 The wet foams may be cast into moulds for shaping or may be shaped by extrusion using conventional extrusion equipment suitably adjusted for the wet foam viscosity. The cast or extruded foams may then be subjected to a drying step to create a solid foam with sufficient green strength for further processing.

25 The drying can be carried out using a conventional oven at up to about 120°C . The drying time may be varied from 0.1 to 48 hours as desired to preserve the foam structure. The drying may be done at atmospheric or reduced pressure. At reduced pressure the foam may expand before the green strength is developed. The degree of expansion and hence the cell size of the foam will depend on the pressure selected. Drying at elevated temperature may also cause a slight expansion of the foam. It is preferred to control the humidity during the drying step, to prevent uneven shrinkage and drying cracks. Temperature-assisted or vacuum-assisted unidirectional drying leads to an even shrinkage of the sample without inducing stresses which would result in cracks. Freeze drying may also be used.

35 The suspension may include other ingredients, which play a role at the drying stage. Examples of such ingredients include binders such as resins, e.g. polyvinylchloride, gums, cellulose, starch, polyvinyl alcohol, oligo- and poly-saccharides to increase green strength. Polymerisable materials may also be included although this is less preferred. Although the addition of binders in general is not needed to produce suitable wet foams, such additives may

have advantages if high green strength after drying is desired. The body formed in the presence of binders or polymerizable materials after drying is relatively robust, and the addition of binders or polymerizable materials can be preferred when the article to be formed is of a complex shape.

5

The cast or extruded foams may be subjected to additional shaping steps, including for example milling or grinding the foam to a desired particle size, sieving, granulating pelleting and other shaping procedures known in the art.

- 10 The foam may be subjected to a heating step or calcination in which the particles are fused together. Such heating may be done at temperatures in the range 200-1600°C or higher depending on the particulate material, although to retain a suitable pore structure in the cell walls, it may be desirable to calcine the foams below about 1200°C. The calcination may be performed for 1-24 hours, preferably 1-8 hours, depending on the temperature chosen. The heating step may be performed under air or an inert atmosphere such as nitrogen or argon. The latter may be preferred where decomposition of organic residues is expected.

- A solid foam results from the drying and/or calcination of the particulate-stabilised wet foam. The solid foam is a solid porous material comprising many gas-filled cells or voids formed therein. In the present invention the ceramic foam comprises a closed cell structure. By the term, "closed cell structure", we mean that the majority of the cells or voids within the foam are generally not inter-connected, although a proportion, e.g. up to 50% of the cell volume, but preferably less than 20% of the cell volume, may be interconnected. In a closed cell structure, unlike an open-cell structure, there is generally no open flow-path through the foam from one side to another such that a gas passing through the foam has to diffuse through a cell wall from one cell to the next. The shape of the cells in the closed cell structure will vary depending upon the manufacturing method and conditions, but typically are spheres or distorted spheres having a circular cross section. The cells may have a diameter in the range 0.1-500 µm, although the majority (i.e. >50% in number) of the cells desirably have a diameter in the range 0.1-250 µm.
- 20 25 30 The average cell diameter may be in the range 0.2-150 µm, preferably 1-100 µm. The cell diameters may be determined using microscopy.

- The void fraction of the foams may be in the range 50-95% by volume, preferably 75-90% by volume. Hence the solids content of the foams may be 5-50%, preferably 10-25% by volume.

35

Because the foam comprises a closed cell structure, there are walls between at least some of the cells. The cell walls are porous, i.e. the cell walls may comprise pores through which a gas may pass. The pore size or width may be >50 nm in diameter although preferably the pores are ≤ 50 nm in diameter. The thickness of the cell walls may be controlled to provide an

optimum diffusion path for reacting gases through the catalyst or sorbent. The thickness of the cell walls may also be controlled to impart a desired strength to the final product. Cell wall thicknesses may be up to 500 μm , preferably up to 200 μm , with an average in the range 10-100 μm , preferably 25-85 μm . The control of wall thickness may, for example, be performed by
5 controlling the void fraction in the foam during its manufacture.

The solid foam may be subjected to treatment with one or more metal compounds to form a catalyst or sorbent. This may be accomplished by applying a wash-coat slurry containing an insoluble metal compound such as a metal oxide, but this is less preferred because the solid
10 foam comprises a closed cell structure and so the wash-coat will not be able to penetrate the foam beyond the surface cells. Therefore preferably the solid foam is treated using one or more soluble metal compounds in solution. One or more of the metals recited above may be used to treat the solid foam. The metal compound may be an organic metal compounds such as metal acetylacetonate, a metal complex such as metal ammine complex, or may be a metal
15 salt such as metal acetate and/or metal nitrate. One or more soluble metal compounds may be used. Thus in a preferred method, a soluble metal compound is dissolved in a suitable solvent, such as water, to form a metal solution and the metal solution applied to the solid foam, e.g. by spraying or dipping, to impregnate the cells and cell wall pores. One or more treatments using the same or different metal compounds may be applied to the foam. The treated foam may
20 then be subjected to drying to remove the solvent and leave the metal deposited within the foam. The metal may be deposited as a salt or complex or may be metal oxide depending upon the method used to impregnate the foam. The metals are preferably uniformly deposited within the ceramic foam.

25 The metal compounds in the solid foam may if desired be subjected to a heating step or calcination to cause their decomposition to form the corresponding metal oxide. This may accompany the drying step, or the calcination step may be performed separately. The conversion of metal compounds to metal oxide may conveniently be accomplished by heating the impregnated or dried metal -containing foam to temperatures up to about 800°C, preferably
30 200-800°C, more preferably 200-600°C under air or an inert gas such as nitrogen or argon. The calcination of the metal compounds may be performed over 0.5-24 hours depending on the temperature.

The foams may be subjected to various treatments such as reduction with a hydrogen- and/or
35 carbon monoxide-containing gas stream or sulphidation, e.g. with hydrogen sulphide, to render them active in use. The post treatment may be carried out ex-situ or in-situ, i.e. before or after installation in the vessel where it is to be used.

- Foams containing one or more catalytic metals prepared according to the present invention may be applied to any heterogeneous catalytic process, but are preferably applied to processes using gaseous reactants. The catalytic process may comprise contacting a reactant mixture, preferably a gaseous reactant mixture, with the catalyst under conditions to effect the catalysed reaction. The catalytic process may be selected from hydroprocessing including hydrodesulphurisation, hydrogenation, steam reforming including pre-reforming, catalytic steam reforming, autothermal reforming and secondary reforming and reforming processes used for the direct reduction of iron, catalytic partial oxidation, catalytic cracking, water-gas shift including isothermal-shift, sour shift, low-temperature shift, intermediate temperature shift, medium temperature shift and high temperature shift reactions, methanation, hydrocarbon synthesis by the Fischer-Tropsch reaction, methanol synthesis, methanol oxidation to formaldehyde, ammonia synthesis, ammonia oxidation and nitrous oxide decomposition reactions.
- Foams containing one or more sorbent metals may be used to trap sulphur compounds, halogen compounds or heavy metals such as mercury and arsenic from contaminated gaseous or liquid fluid streams.

The invention will now be further described by reference to the following examples.

Example 1 Titania foam preparation

- a) A ceramic foam was prepared using a titania suspension containing 30% wt solids. 128 g titania powder (P25 available from Evonik) were added slowly to 300 ml demineralised water in a stirred vessel. Then, without pH adjustment, 0.36 mmol DL-phenylalanine were added per gram of titania (7.6 g DL-phenylalanine). The pH of the suspension was 4.59. Air was then introduced into the suspension to form bubbles using a gas inducing impeller for 30 minutes. The foam was cast into a tray and dried at room temperature and at atmospheric pressure. The cast foam was then calcined under a nitrogen purge by heating at 2 °C/ min to 600 °C. After 45 minutes at 600 °C the nitrogen flow was replaced by air. The total dwell at 600 °C was 4 hours. The resulting ceramic foam support was crushed and sieved to 0.5 mm.

A porosity measurement was made by immersing the ceramic foam in demineralised water at room temperature for 4 days and measuring the water up-take by the increase in weight. The porosity measured in this way includes the volume of the cells and accessible pores and indicates the volume of metal solution that may be incorporated into the foam. The porosity of the foamed titania was 0.8 cm³/g after 4 days.

- b) The method was repeated for different titania contents in the suspension as follows;

Titania weight %	DL-phenylalanine mmol/g titania	pH	Porosity cm^3g^{-1}
17.5	0.82	4.65	2.2
20.0	0.36	4.50	1.6
20.0	0.54	4.52	1.5
20.0	0.72	4.56	1.4
25.0	0.39	4.56	0.9
25.0	0.54	4.58	1.0

- c) The method was repeated, replacing the phenyl alanine with other alpha-amino acids as follows;

Titania weight %	DL-amino acid mmol/g titania	pH	Porosity cm^3g^{-1}
20	0.22 DL-tryptophan	3.25	0.50
20	0.74 DL-leucine	3.96	2.84
30	0.54 DL-valine	4.02	0.47

- 5 d) The method was repeated but with nitric acid adjustment of the pH of the slurry prior to air entrainment as follows:

Titania weight %	DL-amino acid mmol/g titania	pH	Porosity cm^3g^{-1}
25	0.72 DL-leucine	1.29	1.11
25	0.72 DL-tryptophan	1.20	0.38
25	0.72 DL-phenylalanine	1.36	0.78
25	0.72 DL-isoleucine	1.28	0.63
25	0.72 DL-methionine	1.21	0.44
25	0.72 DL-valine	1.34	0.41

- The results suggest that the pH adjustment does not enhance porosity. The order of effectiveness of the amphiphiles at an amphiphile concentration of 0.20-0.25 mol/litre at a pH 1.0-1.4 is DL-leucine >DL-phenylalanine >DL-isoleucine >DL-methionine >DL-valine \geq DL-tryptophan.

Example 2: Catalyst preparation

- a) Cobalt nitrate impregnation of titania foam of Example 1(a).
- 15 7 g of cobalt nitrate hexahydrate ($\text{Co}(\text{NO}_3)_2 \cdot 6\text{H}_2\text{O}$) and 2.2 ml demineralised water were heated until the melting and dissolution of the salt were complete. This was added in aliquots to 15 g of the ceramic foam product of Example 1(a) in a plastic bag. After each addition the material

was kneaded into the support. The impregnated foam was dried for 2 hours at 105°C and calcined for 2 hours at 300°C. The process was then repeated. 5.5 g $\text{Co}(\text{NO}_3)_2 \cdot 6\text{H}_2\text{O}$ and 2.74 ml demineralised water were heated until the melting and dissolution of the salt were complete. This was added in aliquots to 16.5 g of the impregnated ceramic foam product from the first
5 impregnation in a plastic bag. After each addition the material was kneaded into the support. The resulting material was dried for 2 hours at 105°C and calcined for 2 hours at 300°C. The cobalt content of the catalyst by ICPAES was 10.8 %wt.

b) Cobalt ammine-carbonate impregnation of titania foam of Example 1(a).

10 A cobalt ammine carbonate solution was prepared as follows; 198 ml of a 28% ammonia solution was added to 20.4 g ammonium carbonate in a round bottomed flask and diluted with 193.4 ml demineralised water. The resulting solution was stirred for 20 minutes then 23.7 g of cobalt basic carbonate was added over 15 minutes and the solution stirred at 150 rpm for a further 2.5 hr to give a purple solution. 30% hydrogen peroxide solution was added drop wise
15 while the solution was stirred at 234 rpm until the Oxido-reduction potential (Mettler Toledo transmitter M 700) was near to -100 mV. Stirring was continued for a further 10 minutes and then the solution was filtered.

385 ml of the Co ammine carbonate solution (2.6% w/w Co) was added to a 2 L four-necked
20 round bottom flask. A stirrer, temperature probe, lute and condenser were fitted to the flask. 52 g of the ceramic foam product of Example 1(a) was added. This mixture was then diluted with 385 mL water and 165 mL ammonia before being heated and agitated for 80 minutes to cause evolution of the ammonia and deposition of cobalt oxide in the cells and pores of the ceramic foam. The mixture was filtered and washed with 80 ml demineralised water. The
25 catalyst was dried at 105°C for 8 hours. It was not calcined. The cobalt content of the catalyst by ICPAES was 11.2 %wt.

Example 3. Direct foaming of catalyst powder

a) $\text{CuO}/\text{ZnO}/\text{alumina}$ catalyst. 99.7 g of a co-precipitated copper/zinc oxide/alumina
30 catalyst powder comprising 45% wt CuO , 45% wt ZnO and 10% wt silica-doped alumina were dispersed in 300 ml of water using a Silverson L 5M mixer at 6000 rpm. The initial pH was 7.18. The suspension was subsequently stirred with an impeller and, without pH adjustment, 8.2 g of DL-phenylalanine were dissolved into the suspension. The pH of the resulting suspension was 6.48. Air was introduced into the suspension using a gas inducing impeller at
35 2000 rpm for 20 minutes. Some stable foam was produced. The foam was poured into a tray and dried at room temperature. The sample was subsequently heated to 590°C under a nitrogen purge and held at 590°C for 2 hours to produce a catalyst foam.

Example 4: Comparative Example

The method of Example 1 was repeated, replacing the phenyl alanine with n-butyric acid.

a) Without pH adjustment.

A 20% suspension was prepared by adding 75 g titania powder (P25 available from Evonik) to 300 ml demineralised water in a beaker stirred with an impeller. The suspension pH was 4.49. 2.5 ml of butyric acid were added to provide 0.36 mmol butyric acid/g titania. The resulting pH was 3.86. Air was entrained with a gas inducing impeller for 20 minutes but no foaming was observed. The pH upon addition of the butyric acid was too low for a stable foam to be produced.

b) With pH adjustment.

Example 4(a) was repeated. 0.54 ml of KOH were added to increase the pH of the suspension to 4.65. Air was then entrained with a gas inducing impeller for 20 minutes. The foam was dried at room temperature. It was calcined with a nitrogen purge by heating at 2 °C/ min to 600 °C. After 45 minutes at 600 °C the nitrogen flow was replaced by air. The total dwell at 600 °C was 4 hours. The porosity of the foamed titania was 2.2 cm³/g.

The method was repeated for different titania contents in the suspension as follows. pH adjustment was required before air entrainment using potassium hydroxide.

Titania weight %	Butyric Acid mmol/g titania	pH after butyric acid addition	pH after KOH addition	Porosity cm ³ g ⁻¹
20	0.54	3.71	4.65	2.1
20	0.72	3.66	4.40	1.7
25	0.36	3.71	4.50	1.7
25	0.54	3.68	4.50	1.5
25	0.72	3.56	4.00	1.4
30	0.36	3.66	4.30	1.2
30	0.54	3.60	4.30	1.4
30	0.72	2.46	3.20*	1.1

*pH was not increased further since an increase in viscosity was observed

Claims.

1. A method for preparing a particle-stabilised foam comprising the steps of (i) forming a suspension of a particulate material in an aqueous medium containing an amphiphile and (ii) introducing a gas into the dispersion to generate a foam, wherein the amphiphile is an amino acid.
2. A method according to claim 1 wherein the particulate material is a ceramic powder, a catalyst powder or a sorbent powder.
3. A method according to claim 2 wherein the ceramic powder comprises a metal oxide selected from alumina, metal-aluminates, magnesia, silica, lanthana, ceria, titania, zirconia and mixtures of these; or a zeolite.
4. A method according to claim 2 wherein the catalyst powder comprises an oxide, hydroxide, carbonate or hydroxycarbonate of one or more metals selected from the group consisting of Na, K, Mg, Ca, Ba, Al, Si, Ti, V, Cr, Mn, Fe, Co, Ni, Cu, Zn, Y, Zr, Nb, Mo, Ru, Rh, Pd, Ag, Sn, Sb, La, Hf, W, Ag, Re, Ir, Pt, Au, Pb, and Ce.
5. A method according to claim 2 wherein the sorbent powder comprises an oxide, hydroxide, carbonate, hydroxycarbonate or sulphide of one or more metals selected from Na, K, Ca, Mg, Pd, Mn, Fe, Cu and Zn.
6. A method according to any one of claims 1 to 5 wherein the mean particle size of the particles in the suspension is in the range 1 nm to 20 μm , preferably in the range 2 nm – 10 μm , more preferably 2 nm – 2 μm .
7. A method according to any one of claims 1 to 6 wherein the amino acid consists of a non-polar tail part, a carboxylate head group and an amino group.
8. A method according to any one of claims 1 to 7 wherein the amino acid is an alpha-amino acid, where the amine group is attached to a carbon atom adjacent a carboxylate head group.
9. A method according to any one of claims 1 to 8 wherein the amino acid is of formula; $\text{R}^1\text{-CR}^2(\text{NH}_2)\text{COOH}$, where R^1 is a tail group and R^2 is H, alkyl or aryl.
10. A method according to any one of claims 1 to 9 wherein the amino acid is one or more of valine, isoleucine, leucine, phenylalanine or tryptophan, preferably one or more of leucine, isoleucine and phenyl alanine, more preferably phenylalanine.

11. A method according to any one of claims 1 to 10 wherein the pH of the suspension is not adjusted by addition of an acid or a base.
12. A method according to any one of claims 1 to 11 wherein the foam contains bubbles having a diameter from 1 μm to 1 mm, preferably from 1 μm to 500 μm .
13. A method for making a solid foam comprising the steps of (i) preparing a particle-stabilised foam according to any one of claims 1 to 12, (ii) shaping the particle stabilised foam and (iii) drying and/or calcining the shaped foam.
14. A method according to claim 13 wherein the solid foam is prepared from a ceramic powder and is subjected to treatment with one or more metal compounds to form a catalyst or sorbent.
15. A solid foam obtainable by the method of claim 13 or claim 14.

Conferences

- *14th International Conference European Ceramic Society*; held at Toledo, Spain, 21-25 June 2015 – Poster

Characterization and Comparison of the Microstructural Properties of Catalyst Support Materials

Andrea Celani^{1,2}, Stuart Blackburn¹, Mark Simmons¹, Liz Holt², Hugh Stitt²

¹School of Chemical Engineering, University of Birmingham, B15 2TT

²Johnson Matthey Technology Centre, Billingham, TS23 1LB

Abstract:

Ceramic materials have an outstanding role in catalysis due to their use as catalyst supports. Recently, ceramic foams produced by different routes have been increasingly employed in this area in addition to traditional catalyst supports. These materials are characterized by a high porosity that, coupled with an economic production route, makes them particularly suitable as supports.

In this work, a combination of characterization techniques has been applied to a range of conventional and foam catalyst supports, in order to generate an insight into the mass transport properties of these materials. In particular, conventional catalyst supports such as alumina pellets and positive/negative replicas of polyurethane foams have been analysed and characterised. The results obtained for the different samples have been compared in order to establish the difference in term of microstructure, porosity and pore size distribution of these catalyst support materials.

In particular, analysis of SEM and X-ray tomography images has been conducted in order to investigate the samples microstructures as well as to provide information on the three-dimensional spatial distribution of porosity. Finally, mercury porosimetry has been employed to obtain the pore size distribution and the specific pore volume of the samples.

- *Formula VIII Congress*; held at Barcelona, Spain, 4-7 July 2016 - Presentation

Formulation of Ceramic Foams: a New Class of Amphiphiles

Andrea Celani^{a,b,*}, Stuart Blackburn^a, Mark Simmons^a, Liz Holt^b, Hugh Stitt^b

^aSchool of Chemical Engineering, University of Birmingham, B15 2TT

^bJohnson Matthey Technology Centre, Billingham, TS23 1LB

*corresponding author. Email: andrea.celani@matthey.com

Abstract:

Ceramic materials have a key role in catalysis due to their use as catalyst supports. Recently, there has been a significant growth in interest in their use as an alternative to traditional catalyst supports due to the increased macro-porosity of the foam leading to reduced transport resistance. Ceramic foams can be produced by different methods such as replica technique and direct foaming [1]. In the latter, air is directly introduced into a ceramic slurry leading to the formation of a stable wet foam. The structural properties of this foam (e.g. porosity, pore size distribution) are strongly affected by the initial formulation of the ceramic slurry [2]. In particular, the surface properties of the ceramic particles are modified by the addition of an amphiphile resulting in different foam structures depending on the degree of particle hydrophobisation.

In this work, a new class of amphiphiles is proposed and assessed that is more environmentally benign and present a wider operational window than those reported in the literature. The effects of the amphiphile concentration and structure on the foam properties were investigated. Water pick up experiments and image analysis of SEM images were used to determine the foam porosity and pore size distribution respectively.

Surface tension measurements were used to establish a hydrophobicity index for the different amphiphiles. A linear relationship between the hydrophobicity index and the maximum porosity obtainable was found. This strong correlation allows a priori selection of the most appropriate amphiphile depending on the desired foam properties opening up to the possibility of tailoring the structure of ceramic materials.

References

- [1] Studart A. R., Gonzenbach U. T., Tervoort E., Gauckler L. J.; J. Am. Ceram. Soc., **89** [6] (2006) 1771-1789.
- [2] Gonzenbach U.T., Studart A.R., Tervoort E., Gauckler L.J.; Langmuir, **22** (2006) 10983-10988.

- *International Symposium on Mixing in Industrial Processes IX*; held at Birmingham, UK, 25-28 June 2017 – Presentation

Effect of Mixing Conditions on the Wet Preparation of Ceramic Foams

Andrea Celani^{1,2}, Stuart Blackburn¹, Mark Simmons¹, Hugh Stitt²

¹*School of Chemical Engineering, University of Birmingham, B15 2TT*

²*Johnson Matthey technology Centre, Billingham, TS23 1LB*

Abstract:

Ceramic foams constitute a promising alternative to conventional catalyst supports thanks to their macro-porosity which enhances the mass transport properties of the catalyst. Among the techniques for the production of ceramic foams (e.g. replica technique, sacrificial template, etc.), direct foaming is a straightforward method to generate macroporous ceramic materials. Although the effect of the initial slurry formulation (e.g. amphiphile concentration, solid content, etc.) on the foam properties have been widely investigated, little attention has been given to the effect of mixing parameter on the foam and product properties. Rather, the use of kitchen mixers to froth the initial ceramic slurry is commonly reported in the literature. This study thus reports a systematic investigation of the impact of mixing parameters in an aerated stirred vessel on the product foam properties.

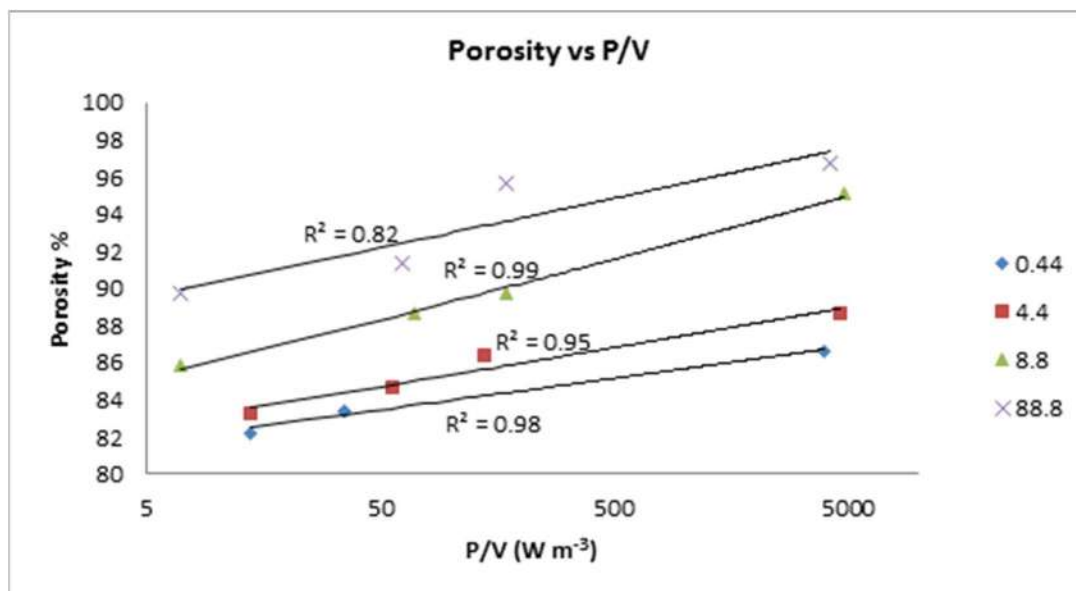


Figure.1 Foam porosity as a function of P/V for different ratios of entrained gas volume/slurry initial volume.

Design of Experiment (DoE) was employed to generate a series of screening experiments from which the process parameters (e.g. impeller speed, impeller diameter, gas flow rate, etc.) that mostly affect the foam properties (e.g. porosity, bubble size distribution, etc.) were identified. The mixing in the sparged stirred tank was described by the calculation of a series of adimensional

numbers (e.g. Re, Fr, Fl_g, etc.) while the flow regime map was experimentally estimated by direct observation of a ceramic particles free system. The properties of the foams obtained at the different operating conditions were evaluated as a function of global mixing parameters, regime maps and dimensionless numbers. The statistical approach also allows a rigorous ranking of the process variable importance. The paper will present the detail of this analysis. Figure.1 gives an exemplification of the dried foam porosity as a function of P/V. This study starts to give a deeper insight into the effects of mixing and process variables on the preparation of the foam precursors, many of which do not correspond well with conventional gas-liquid mixing theory due to higher gas hold up and complex rheology.

- *UK Colloids 2017*; held at Manchester, UK, 10-12 July 2017 – Presentation

Hydrophobic Amino Acids as Amphiphiles in the Formulation of Ceramic Foams

Authors: Andrea Celani^{1,2}, Stuart Blackburn¹, Mark Simmons¹, Hugh Stitt², Liz Holt²

¹*School of Chemical Engineering, University of Birmingham, B15 2TT*

²*Johnson Matthey Technology Centre, Billingham, TS23 1LB*

Email: andrea.celani@matthey.com

Abstract:

Ceramic materials have a key role in catalysis due to their use as catalyst supports. Recently, there has been a significant growth in interest in their use as an alternative to traditional catalyst supports due to the increased macro-porosity of the foam leading to reduced transport resistance. Ceramic foams can be produced by different methods such as replica technique and direct foaming [1]. In the latter, air is directly introduced into a ceramic slurry leading to the formation of a stable wet foam (Figure.1). The structural properties of this foam (e.g. porosity, pore size distribution) are strongly affected by the initial formulation of the ceramic slurry [2]. In particular, the surface properties of the ceramic particles are modified by the addition of an amphiphile resulting in different foam structures depending on the degree of particle hydrophobisation.

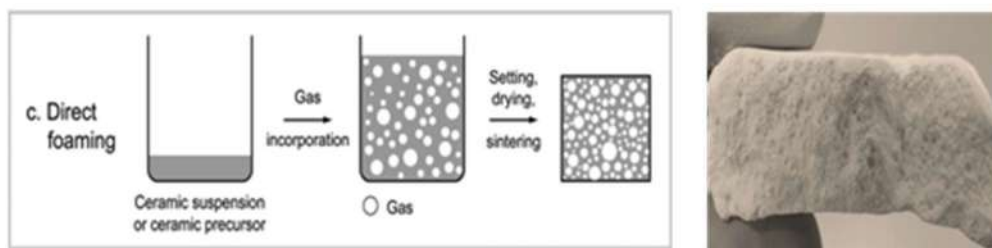


Figure.1 Direct Foaming Process and ceramic foam respectively [1]

In this work, a new class of amphiphiles is proposed and assessed that is more environmentally benign and present a wider operational window than those reported in the literature. The effects of the amphiphile concentration and structure on the foam properties were investigated. Water pick

up experiments and image analysis of SEM images were used to determine the foam porosity and pore size distribution respectively (Figure.2).

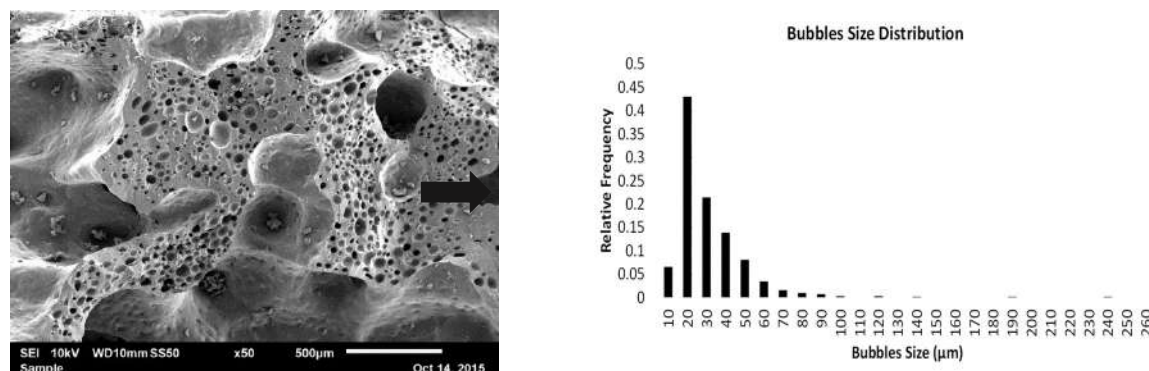


Figure.2 SEM image of a ceramic foam and correspondent bubble size distribution

Surface tension measurements were used to establish a hydrophobicity index for the different amphiphiles. Relationships between the hydrophobicity index and the foam structural properties (e.g. porosity, bubble size) were found; Figure.3 shows the correlation between hydrophobicity index and foam porosity. These correlations allow a priori selection of the most appropriate amphiphile depending on the desired foam properties opening up to the possibility of tailoring the structure of ceramic materials.

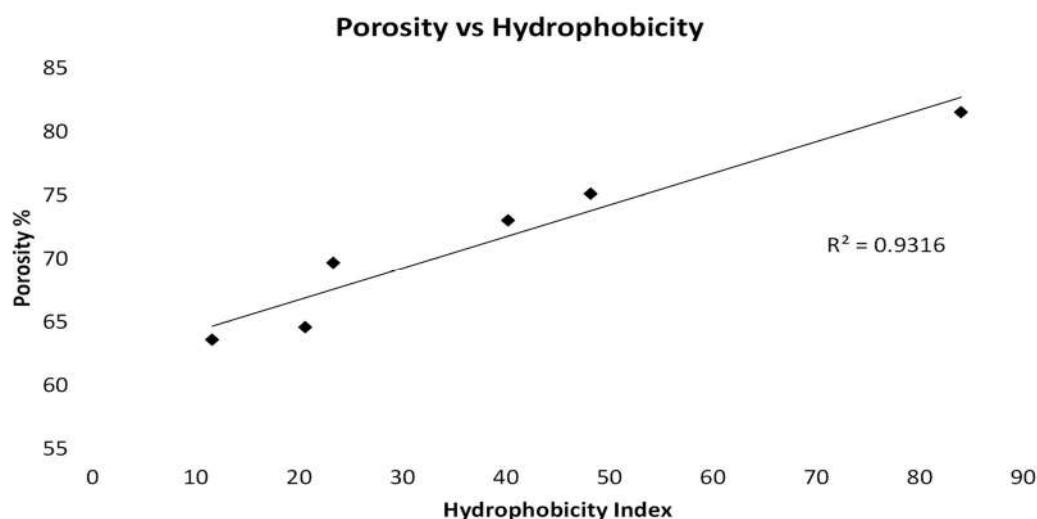


Figure.3 Linear relationships between porosity and amphiphile hydrophobicity

References

- [1] Studart A. R., Gonzenbach U. T., Tervoort E., Gauckler L. J.; J. Am. Ceram. Soc., 89 (2006) 1771-1789.
- [2] Gonzenbach U.T., Studart A.R., Tervoort E., Gauckler L.J.; Langmuir, 22 (2006) 10983-10988